Modeling and analysis of material behavior during cavitation erosion

Samir Chandra Roy

▶ **To cite this version:**

Samir Chandra Roy. Modeling and analysis of material behavior during cavitation erosion. Materials. Université Grenoble Alpes, 2015. English. NNT : 2015GREAI081 . tel-01267573

HAL Id: tel-01267573
https://theses.hal.science/tel-01267573

Submitted on 4 Feb 2016

HAL is a multi-disciplinary open access archive for the deposit and dissemination of scientific research documents, whether they are published or not. The documents may come from teaching and research institutions in France or abroad, or from public or private research centers.

L'archive ouverte pluridisciplinaire **HAL**, est destinée au dépôt et à la diffusion de documents scientifiques de niveau recherche, publiés ou non, émanant des établissements d'enseignement et de recherche français ou étrangers, des laboratoires publics ou privés.

UNIVERSITÉ GRENOBLE ALPES

THÈSE

Pour obtenir le grade de

DOCTEUR DE L'UNIVERSITÉ GRENOBLE ALPES

Spécialité : **Matériaux, Mécanique, Génie civil, Electrochimie**

Arrêté ministériel: 7 août 2006

Présentée par

Samir Chandra ROY

Thèse dirigée par **Marc FIVEL** et **Jean-Pierre FRANC**

préparée au sein du **Laboratoire SIMaP : Science et Ingénierie des Matériaux et Procédés**
dans **l'École Doctorale I-MEP2 : Ingénierie – Matériaux Mécanique Energétique Environnement Procédés Production**

Analyse et modélisation du comportement de divers matériaux en érosion de cavitation

Thèse soutenue publiquement le **11 Décembre 2015**,
devant le jury composé de :

Mme. Régiane FORTES-PATELLA
Professeur, Univ. Grenoble Alpes, LEGI, Président
Mme. Véronique FAVIER
Professeur, Arts et Métiers ParisTech, PIMM, Rapporteur
Mr. Sofiane KHELLADI
Professeur, Arts et Métiers ParisTech, DynFluid, Rapporteur
Mr. Ayat KARIMI
Docteur, Ecole Polytechnique Fédérale de Lausanne, ICMP, Examinateur
Mr. Marc FIVEL
Directeur de Recherche CNRS, Univ. Grenoble Alpes, SIMaP, Encadrant
Mr. Jean-Pierre FRANC
Directeur de Recherche CNRS, Univ. Grenoble Alpes, LEGI, Encadrant
Mr. Christian PELLONE
Chargé de Recherche CNRS, Univ. Grenoble Alpes, LEGI, Invité

UNIVERSITÉ GRENOBLE ALPES

THESIS

For obtaining the grade of

DOCTORATE OF THE UNIVERSITY GRENOBLE ALPES

Speciality : **Materials, Mechanical, Civil Engineering, Electrochemistry**

Ministerial order : 7 August 2006

Presented by

Samir Chandra ROY

Thesis directed by **Marc FIVEL** et **Jean-Pierre FRANC**

Prepared within the **Laboratory SIMaP : Science and Engineering of Materials and Processes**
in the **Doctoral School IMEP2 : Engineering – Materials Mechanical Energy Environmental Processes Production**

Modeling and analysis of material behavior during cavitation erosion

Thesis defended publicly on **11 December 2015**,
before the jury composed of :

Mrs. Regiane FORTES-PATELLA
Professor, Univ. Grenoble Alpes, LEGI, President
Mrs. Veronique FAVIER
Professor, Arts et Métiers ParisTech, PIMM, Reviewer
Mr. Sofiane KHELLADI
Professor, Arts et Métiers ParisTech, DynFluid, Reviewer
Mr. Ayat KARIMI
Doctorate, Ecole Polytechnique Fédérale de Lausanne, ICMP, Examiner
Mr. Marc FIVEL
Director of Research CNRS, Univ. Grenoble Alpes, SIMaP, Supervisor
Mr. Jean-Pierre FRANC
Director of Research CNRS, Univ. Grenoble Alpes, LEGI, Co-supervisor
Mr. Christian PELLONE
Researcher CNRS, Univ. Grenoble Alpes, LEGI, Invited

Acknowledgements

It has been a long 21 years of continuous study, starting from class-I to the completion of PhD. I remember the first day of my school life when I was at the age of 6. The Journey started from a broken classroom without having enough chairs to sit, in a remote village in India. Finally obtaining a PhD in France, one of the world's developed countries, developed in all aspects- socially, culturally and most importantly scientifically. The journey have been a great challenge. However, the journey would have not been possible without adequate support, encouragement and motivation from my family members, especially my parents, brothers, sister and others. So, at first, I take the opportunity to thank and express my gratitude to them.

I feel blessed that I got the opportunity to work with **Prof. Marc FIVEL** (SIMaP) and **Prof. Jean-Pierre FRANC** (LEGI) under their supervision. I have no word to express my gratitude to them, for all kinds of helps rendered by them. Without their consistent scientific and moral supports, encouragements and motivations I would have not been able to finish my PhD. I especially thank them for their innovative and unique ideas and directions, and many discussions in solving different issues during the research that led to the work to a unique level.

I feel honor to thank **Mr. Christian PELLONE** (LEGI) for his help during these years, especially for many fruitful discussions, suggestions and ideas to overcome some problems encountered during the research. I deeply express my gratitude to him.

I express my sincere thanks to **Mr. Ludovic CHARLEUX** (SYMME) for providing lectures on Python programming, **Mr. Hyung-Jun Chang** (SAFRAN) for his help regarding ABAQUS modeling, **Mr. Nicolas RANC** (ENSAM) for his help in conducting the compression and split Hopkinson pressure bar tests, **Mr. Renaud PFEIFFER** (ENSAM) for his help in coding to analyze the SHPB test data, **Mr. Marc VERDIER** (SIMaP) for his help in conducting the nanoindentation tests, **Mr. Michel RIONDET** (LEGI) for conducting the cavitation pitting tests and **Dr. Michel SUERY** (SIMaP) and **Mr. Charles JOSSEROND** (SIMaP) for the tensile tests. I wish to thank **Mr. Jean-Yves Cavaille**, (MATEIS), **Mr. Olivier LAME** (MATEIS), **Mr. Giovanni GHIGLIOTTI** (LEGI) and **Mr. Pierre LHUISSIER** (SIMaP) for their valuable suggestions at some points in time during these years. I also thank **Mr. Xavier Bataillon** (SIMaP) and **Mr. Franck Pelloux** (SIMaP) for their help regarding sample preparation for various tests.

This research was conducted under a NICOP (Naval International Cooperative Opportunities in Science and Technology Program) project funded by the Office of Naval Research (ONR). I wish to thank **Dr. Ki-Han Kim** from the Office of Naval Research (ONR) and **Dr. Woei-Min Lin** from the Office of Naval Research Global (ONRG) who supported this work. I also express my sincere thanks to all other members of the NICOP program, especially from the France, Germany and USA, for having the fruitful meetings and discussions in every 6 months. These meetings had been very innovative where I got many ideas and feedbacks that helped to raise the level of my work.

I would like to extend my greatest respect and gratitude to the Jury members for accepting the invitation to be present during the defense and evaluate the work. I am grateful to the referees: **Mme. Véronique FAVIER** (PIMM) and **Mr. Sofiane KHELLADI** (DynFluid) for their careful reading, valuable comments and evaluation of the thesis. I have the honor to get **Mme. Régiane FORTES-PATELLA** (LEGI) and **Mr. Ayat KARIMI** (EPFL) as the examiners of the thesis. I also acknowledge the presence of **Prof. Marc FIVEL** (SIMaP), **Prof. Jean-Pierre FRANC** (LEGI) and **Mr. Christian PELLONE** (LEGI) as a part of the jury members.

In this special moment I would like to take the opportunity to thank and express my warmest gratitude to a few others who helped me directly or indirectly during the completion of the work.

Special thanks to **Mme. Claire THOMASSON** (SIMaP) for her numerous supports regarding all kinds of administrative works during these years. In these regards I would also like to thank **Mme. Claude GHIOTTI** (SIMaP)**, Mme. Elisabeth LUSSI** (SIMaP) and **Mme. Augustine ALESSIO** (I-MEP2) for their help.

I also thank all the members of the **GPM2** (**Génie physique et mécanique des matériaux)** group for their cooperation and social integration that provided me a workable environment during the last three years. I remember the ski-weekends and thank the organizers for that.

I would also like to thank the Grenoble INP, IMEP-2 and SIMaP, especially the people in the administrative service for their voluntary help whenever needed.

It would be disgraceful if I do not mention about the hospitality and affection that **Prof. Marc FIVEL**, **Mme. Claire THOMASSON** and their family members delivered upon my arrival in France. I sincerely appreciate and thank for that, especially the delicious French cuisine.

At this point I also remember my previous teachers from the **Metallurgical and Material Engineering** department of **Jadavpur University, Kolkata, India,** especially **Prof. Saradindukumar Ray**, **Prof. Pravash Chandra Chakraborti** and **Prof. Tapan Kumar Pal,** and from the **Fatigue Studies Section** of **Indira Gandhi Center for Atomic Research (IGCAR), Kalpakkam, India, Dr. Sunil Goyal** and **Dr. R Sandhya** for their invaluable teaching and encouragements. I feel the pleasure to express my gratitude to them.

During these three years I came across many people but few of them made my stay really memorable in some or other ways. I would like to thank them, especially by nick name **Christian** (Germany), **Oscar** (Spain), **Remy** (France), **Vicky** (India), **Miller** (Vietnam), **Ernest** (Ghana), **Hareesh** (India) and **Cindy** (China).

I also apologize if I forgot to mention any name who helped me during the course of my work. Finally I beg pardon for anything that made any inconvenience to anybody during the last three years.

Dated, 11th December 2015.

Samir Chandra ROY

Génie physique et mécanique des matériaux (GPM2)

Laboratoire de Science et Ingénierie des Matériaux et Procédés (SIMaP)

Ingénierie – Matériaux Mécanique Energétique Environnement Procédés Production (I-MEP2)

Université Grenoble Alpes, Grenoble, France.

A favorite quote

Bengali poem:

যদি তোর ডাক শুনে কেউ না আসে তবে একলা চলো রে।
একলা চলো, একলা চলো, একলা চলো, একলা চলো রে॥

যদি কেউ কথা না কয়, ওরে ও অভাগা,
যদি সবাই থাকে মুখ ফিরায়ে সবাই করে ভয়—
তবে পরান খুলে
ও তুই মুখ ফুটে তোর মনের কথা একলা বলো রে॥

যদি সবাই ফিরে যায়, ওরে ওরে ও অভাগা,
যদি গহন পথে যাবার কালে কেউ ফিরে না চায়—
তবে পথের কাঁটা
ও তুই রক্তমাখা চরণতলে একলা দলো রে॥

যদি আলো না ধরে, ওরে ওরে ও অভাগা,
যদি ঝড়-বাদলে আঁধার রাতে দুয়ার দেয় ঘরে-
তবে বজ্রানলে
আপন বুকের পাঁজর জ্বালিয়ে নিয়ে একলা জ্বলো রে।

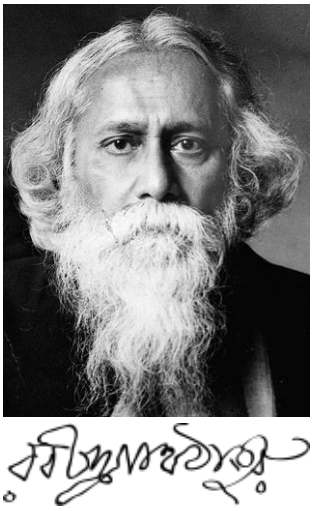

– রবীন্দ্রনাথ ঠাকুর

English translation:

If they answer not to your call walk alone
If they are afraid and cower mutely facing the wall,
O thou unlucky one,
open your mind and speak out alone.
If they turn away, and desert you when crossing the wilderness,
O thou unlucky one,
trample the thorns under thy tread,
and along the blood-lined track travel alone.
If they shut doors and do not hold up the light when the night is troubled with storm,
O thou unlucky one,
with the thunder flame of pain ignite your own heart,
and let it burn alone.

− Rabindranath Tagore

Indian Bengali polymath (1861 –1941), Nobel Prize in Literature in 1913.

Contents

Abstract

Numerical prediction of cavitation erosion requires the knowledge of flow aggressiveness, both of which have been challenging issues till-date. This thesis proposes to use an inverse method to estimate the aggressiveness of the flow from the observation of the pits printed on the surface in the first moments of the cavitation erosion. Three materials were tested in the same experimental conditions in the cavitation tunnel PREVERO available in LEGI Grenoble. The geometry of the pits left on the surface is precisely measured using a systematic method to overcome the roughness effect. Assuming that each pit was generated by a single bubble collapse whose pressure field is treated as a Gaussian shape, finite element calculations are run for estimating the load that created each residual imprint. It is shown that the load distribution falls on a master curve independent of the tested material; the softer material (aluminum alloy) measuring the lowest impacts while the most resistant material (duplex stainless steel) provides access to the largest impact pressures. It is concluded that the material can be used as a pressure sensor measuring the level of aggressiveness of the flow. The inverse method is based on a material characterization taking into account strain rate effects. It is shown that nanoindentation tests are more suitable than compression tests to determine the parameters of the behavior law, particularly for the aluminum alloy for which the microstructure is very heterogeneous. High-speed compression tests with split Hopkinson pressure bars complement the constitutive law giving the sensitivity to the strain rate. Simulations considering the dynamic loading show that impacts of strong amplitude but applied in a short time do not leave any residual pit if the frequency is higher than the natural frequency of the material treated as a damped oscillator. A dynamic mechanism of plastic strain accumulation that could eventually lead to fatigue failure is proposed. Finally, the mass loss curve of cavitation erosion is simulated by applying randomly on a 3D mesh, the impact force population estimated by the inverse method.

Key Words: Cavitation erosion; Finite element modeling; Material characterization, Impact load measurement; Cavitation fatigue, Mass-loss prediction.

Résumé

A ce jour il n'est toujours pas possible de prédire avec exactitude le phénomène d'érosion par cavitation. La raison principale est qu'il est difficile de caractériser l'agressivité de l'écoulement. Cette thèse propose d'utiliser une méthode inverse pour estimer l'agressivité de l'écoulement à partir de l'observation des cratères (pits) imprimées sur la surface dans les premiers instants de l'érosion de cavitation. Trois matériaux ont été testés dans la veine d'écoulement PREVERO disponible au LEGI de Grenoble dans les mêmes conditions expérimentales. La géométrie des pits laissés sur la surface est précisément mesurée à l'aide d'une méthode systématique permettant de s'affranchir de l'effet de rugosité. Supposant que chaque pit a été généré par une bulle unique dont le champ de pression est assimilé à une forme Gaussienne, des calculs par éléments finis permettent d'estimer le chargement qui a créé l'empreinte résiduelle. On montre que la distribution des chargements suit une loi universelle indépendante du matériau testé; le matériau le plus tendre (alliage d'aluminium) mesurant les plus faibles impacts tandis que le matériau le plus résistant (Acier inoxydable) donne accès aux plus grandes pressions d'impact. On en conclu que le matériau peut être utilisé comme capteur de pression mesurant le niveau d'agressivité de l'écoulement. La méthode inverse repose sur une caractérisation mécanique des matériaux prenant en compte la sensibilité de la contrainte à la vitesse de déformation. On montre que les essais de nanoindentation sont mieux adaptés que les essais de compression pour déterminer les paramètres de la loi de comportement, notamment pour l'alliage d'aluminium pour lequel la microstructure est très hétérogène. Des essais de compression à haute vitesse par barres de Hopkinson complètent la loi de comportement en donnant la sensibilité à la vitesse de déformation. Des simulations prenant en compte la dynamique du chargement montrent que des impacts de fort amplitude mais appliqués sur un temps court ne laissent pas d'empreinte résiduelle si la fréquence est plus élevée que la fréquence naturelle du matériau assimilé à un oscillateur amorti. Un mécanisme d'accumulation dynamique de la déformation plastique pouvant conduire à la rupture par fatigue est proposé. Finalement, la courbe de perte de masse est simulée en appliquant aléatoirement sur un maillage 3D, la population d'impacts estimée par la méthode inverse.

Mots Clefs: Erosion de cavitation; Modélization par éléments finis; Caractérisation des matériaux; Mesure de la charge d'impact, Fatigue de cavitation, Prédiction de perte de masse.

Preface

This thesis deals with the study of cavitation erosion from both experimental and numerical point of view. Cavitation erosion is a type of wear that occurs due to repeated high impacts caused by cavitation bubbles collapses near a solid surface. Cavitation generally occurs in fluid machineries including pumps, pipes, turbines, marine propellers, pistons and fuel injectors etc. It requires a multi-disciplinary approach that consists in the knowledge of fluid dynamics and material dynamics along with the other branches of science and engineering to deal with the problem. The fluid could be anything not necessarily water. Cavitation usually causes performance breakdown, noise, vibration and erosion in components. Sometimes, the consequence of cavitation erosion could be catastrophic, as the damage involved is very localized and confined into a micro-region that is difficult to detect easily. This region could act as a stress concentrator leading to formations of micro-cracks which may propagate with the speed of sound if the local stress exceed a threshold critical stress. Finally, many such cracks may join together leading to premature and sudden failure.

Though cavitation is undesirable for structural or design engineering, it has got popularity in some specific fields like in chemical industry for mixing or homogenizing suspended particles in a colloidal liquid like paint mixture or milk, in medical science for breaking kidney stones by shock wave lithotripsy, sometimes it is also used for cleaning in industry. Cavitation mechanism is also used as survival tools by mantis shrimps and pistol shrimps.

Since mid-17th century (after Euler in 1754 [1] first conjectured the problem of cavitation erosion in his memoir on the theory of hydraulic machines), cavitation erosion has been a challenging issue till date. R E Froude, a naval architect was the first to introduce the term "Cavitation" in about 1895, though Reynolds in 1873 had carried out for the first time a fundamental study of cavitation in tubular constrictions. Since then a large number of research works have been done on the field of cavitation, many books have been written. Many symposiums, national and international conferences like "*international symposium of cavitation*" are being held periodically to understand the mechanism of cavitation erosion, develop cavitation resistant materials and techniques, access cavitation flow conditions, develop numerical tools for simulation and so on.

Both experimental and numerical studies are being done to estimate cavitation erosion of materials or structures. Accelerated cavitation tests are performed following standardized method to determine cavitation erosion resistance of a material since real cavitation erosion occurs slowly over long period of time. There are two American Society for Testing and Materials (ASTM) standards G-32 and G-134. Both of these standards provide guidelines for specimen preparation, test conditions, test procedure and interpretation of results. Calibration of the testing apparatus is done using a reference material and comparison of erosion resistances of materials are made to select a suitable candidate for application.

Despite of having standardized techniques for testing, there is no reliable analytical tool or method for prediction of cavitation erosion. Various empirical methods are widely used in industry to predict cavitation erosion damage. Empirical methods consist in- 1) conducting pitting tests on a model to evaluate the flow

aggressiveness, 2) conducting erosion tests to classify materials based on their erosion resistance and to correlate as far as possible with material properties and flow aggressiveness, and finally 3) transposition of erosion data from model to prototype. Besides the method being very tedious, there are some serious short comings- like the way the flow aggressiveness is measured, the dependencies of erosion data on the test facility and working fluid, and also the scaling laws used for transposition are not fully determined.

Difficulties in the measurement of flow aggressiveness come from the typical nature of cavitation bubble collapse, which is often associated with complex mechanisms involving formation of shock waves and micro jets. Each or both of which lead to a high impact (~GPa) of very short duration (~µs) over a very confined region (~µm) that make it difficult to capture them by using conventional pressure transducers. Computational fluid dynamics (CFD) simulations are also being used by many researchers to estimate flow aggressiveness. The main limitations in CFD simulation come in as all the parameters related to the fluid side like air contents, phase change, bubble sizes and location etc. cannot be defined accurately, moreover there are many difficulties associated with the fluid and structure interaction. All these aspects related to the measurement of flow aggressiveness are discussed in details in this thesis. A new method based on cavitation pitting tests and finite element method (FEM) simulations of the material response is developed and successfully implemented in this thesis to estimate the cavitation impact loading conditions. This method is believed to provide a better estimation of the flow aggressiveness over the existing methods in literature. This is a major contribution of the current research work.

Characterization of the material properties relevant for cavitation pitting is also a very difficult task since there is no specific testing method dedicated to cavitation. Moreover the deformation is confined, compressive and inhomogeneous, where size effect or microstructural dependencies of the material properties might be unavoidable. This is why nanoindentation is generally preferred for probing the material properties. However, the impact duration is very short and hence the strain rate is very high (could be as high as 10^5 or 10^6 s^{-1}), which is out of the scope of nanoindentation testing available today. Thus we never know the real mechanical behavior of the material at such high strain rate. A method by integrating nanoindentation material properties with strain rate sensitivity obtained by compression and Split Hopkinson Pressure Bar (SHPB) tests is presented to take into account strain rate effects involved in cavitation pitting.

Cavitation erosion is a kind of fatigue phenomenon, where the structure initially undergoes plastic deformation if the local stress due to cavitation impact exceeds the yield strength of the material. Repetition of such impacts leads to strain accumulation and failure in terms of material removal. Prediction of cavitation erosion has been an active field of research for last decades. The mechanism of strain accumulation is not very clear. Indeed, there is no reversed cycling of the loading so that after one impact the structure may get stabilized if the next impact load is equal or less than the previous one. That will of course depend on the choice of hardening law (like isotropic or kinematic) and also on the strain rate sensitivity of the material. This thesis provides a detailed analysis of potential mechanisms of strain accumulation in cavitation pitting from the material point of view, and a possible mechanism of strain accumulation is presented.

Finally this thesis provides a new way of predicting cavitation erosion of materials based on FEM simulations. The impact loads which characterize the flow conditions, obtained by the newly developed method based on pitting tests and FEM simulations of material response, are applied repetitively and randomly onto the material surface to estimate mass loss with time. This is also an important contribution of the thesis, which provides a new background for cavitation erosion prediction, even if more efforts are needed to improve the method and validate against experimental results. But preliminary results provide a first step towards that direction.

Apart from those mentioned above, several phenomena observed by FEM simulation of material response to cavitation pitting are presented. Both FEM static and dynamic explicit analyses were done using the commercial FEM code ABAQUS. It should be mentioned that no fluid structure interaction has been considered in the current study. This is justified because the materials under consideration in this thesis are metallic alloys that are much stiffer than compliant materials such as polymers that may be used to mitigate damage. The pressure field associated with a single cavitation bubble collapse is represented by a Gaussian type of distribution both in space and time. This choice for the pressure profile is justified by comparing experimental and simulated pit shapes.

Dynamic behavior of cavitation pitting is analyzed in details by FEM simulations and some interesting results are presented. It is found that the mechanism of pit formation is not only controlled by the magnitude of the cavitation impact load, but most importantly by the impact duration compared to a characteristic time of the material based on its natural frequency. This provides a new key point to account for in the mechanism of cavitation pit formation.

The thesis is divided into different chapters and each chapter is subdivided into different section and sub-sections to assemble the suitable scientific facts together. However a clear link has always been maintained to correlate different scientific theories or technical facts together. All the appendices and list of references are provided in the end of the thesis.

The orientation and contents of the thesis are as follows-

Chapter-1:

This chapter provides a detailed literature review required to understand the results or contents of the research. The physics of cavitation bubble formation and collapse leading to high impact load have been explained. Special emphasize is given to understand the mechanisms of micro-jets and shock-waves formation upon bubble collapse that highlight the complex type of loading condition both in space and time associated with cavitation bubble collapse. The following topics are also presented from a detailed literature survey of cavitation erosion-

- Mechanism of damage under cavitation impact
- Experimental techniques available for evaluating cavitation erosion resistance of a material
- Different methods available for estimating cavitation impact loads

- Different methods dedicated to cavitation erosion predictions

Chapter-2:

In this chapter a numerical simulation technique has been developed and verified in order to be used for all similar analyses in the subsequent studies. Cavitation pitting/erosion testing method and characterization of cavitation pits are also presented. Some conclusions have been drawn from numerical simulations of cavitation pitting. The "numerical inverse method" or the "inverse FE technique" based on pitting tests and numerical simulations to estimate cavitation impact load from cavitation pit geometry is presented in details. An analytical method, so-called "analytical inverse method" is also developed to the predict impact load from the cavitation pit geometry. A shorter version of this chapter has been accepted for publication in Wear in 2015 [2]

Chapter-3:

In this chapter, the so-called "numerical inverse method" or "inverse FE technique" have been implement on three materials under identical cavitation flow condition. The aim is to verify if the estimated impact loads by using different materials are material independent or not. The statistical analyses show that the estimated loads are material independent, which indicate that the target material can be used as a pressure sensor in cavitation pitting/erosion. In this regards, the proper way of characterization of material properties has been established by conducting a comparative study using compression, nanoindentation and split Hopkinson pressure bar tests. The importance of microstructural consideration on the characterization of material properties has also been established and presented in details. Main results of this chapter has been collected in a paper accepted by the Journal of Applied Physics in September 2015 [3].

Chapter-4:

In this chapter, a dynamic explicit analysis of cavitation pitting was conducted on the three metallic alloys selected for the current study. Their dynamic behavior was characterized by the popular Johnson-Cook plasticity model. Dynamic behavior of material under cavitation impact has been compared with the analytical response of a spring-mass-damper system. A special focus is made on investigating the effect of impact duration, in relation with the natural duration (based on the natural frequency of the materials), to the cavitation pitting mechanism. The role of density and strain rate sensitivity of the materials into the mechanism of cavitation pitting has also been investigated. Finally, the feasibility of both the "numerical inverse method" and the "analytical inverse method" to implement with the dynamic behavior of the materials has been investigated. These results were published in Wear in 2015 [4].

Chapter-5:

In this chapter a framework has been established for a new method of cavitation erosion prediction. The method could potentially be able to simulate the incubation period as well as the more advanced stages of mass-loss with time in cavitation. The mechanism of fatigue under cavitation impacts has been investigated in details, and the role of strain rate sensitivity and kinematic type of hardening is found to be important to account for

strain accumulation under repeated impacts. A mechanism of strain accumulation based on reduction of strain rate with successive impact has been proposed and verified numerically. Numerical simulation of cavitation erosion is conducted, where the impact load chosen randomly from a statistical population of impact loads estimated in the previous chapter by using the "numerical inverse method", has been applied repeatedly on the material surface at random locations. The results qualitatively represent the basic nature of cavitation erosion curve that i.e. incubation period followed by mass-loss stages. Some of the results in this chapter have been published in Interface Focus in 2015 [5].

Chapter-6:

In this chapter some scopes for future research work has been highlighted.

The thesis also contains two Appendices-

Appendix-A:

The details of Split Hopkinson Pressure Bar (SHPB) test and data analysis technique have been explained. Verification of the estimated material properties based on SHPB data has also been provided.

Appendix-B:

The traditional method of material properties determination, especially the stress-strain curve, from spherical nanoindentation tests has been explained.

This research was conducted under the Naval International Cooperative Opportunities in Science & Technology Program (NICOP, Grant No. N62909-12-1-7112) funded by the Office of Naval Research and the PhD grant was funded by the Ecole Doctorale **I-MEP2** (Ingénierie – Matériaux Mécanique Energétique Environnement Procédés Production). We thank both the ONR and I-MEP2 for their support.

***Note to the reader**

The thesis is written based on four articles published in different journals. Each chapter of the thesis contains results of a particular article, however some modifications were done to make a continuity and to avoid too many repetitions. The thesis represents a complete story of cavitation erosion predition, however each chapter represents a part of the whole story and could be read independently.

Samir Chandra Roy

Email: roysam.nita@gmail.com

Dated 11th December 2015.

Grenoble, France.

Chapter-1

1. Overview of Cavitation Erosion

This chapter provides in brief the theoretical background required to understand the main results presented in the thesis. As the thesis deals with cavitation erosion, an introduction to cavitation erosion is provided in Sec. 1.1. The mechanisms of formation and subsequent collapse of cavitation bubbles are discussed from both theoretical and engineering viewpoints. Complexities involved in the mechanism of formation of high intense impact loads due to the formation of high velocity micro-jets and shock-waves caused by cavitation bubble collapse are discussed in details. The effect of such repetitive impact loadings on the solid surface leading to fatigue type of failure has also been discussed. The experimental techniques commonly used for cavitation erosion study are discussed in Sec. 1.2 with a special emphasis on ASTM standardized techniques (G32 and G134) and high speed cavitation tunnel (used in the current study). Primary aim of the current study is to estimate cavitation impact loads from cavitation pit geometries obtained by cavitation pitting test. In this regard the other techniques available or used for estimating cavitation impact loads are discussed in Sec. 1.3. Ultimate goal of the current study is numerical prediction of cavitation erosion based on the estimated population of the impact loads. Hence, Sec. 1.4 provides a brief review of the most recent cavitation erosion prediction methods that are commonly used for industrial or research purposes. Finally the aim of the thesis is elaborated in Sec. 1.5.

1.1. Introduction to cavitation

1.1.1. Cavitation- theoretical view

Cavitation is defined as the appearance of vapor cavities inside a continuous and homogeneous liquid medium. The generation of vapor cavities could be driven by different situations, though the underlying cause remains to be the same i.e. a drop of the local pressure below the vapor pressure. During cavitation the continuum liquid medium breaks down to form vapor cavities. The ideal mechanism of cavitation could be explained by phase diagram, as an example for water is explained below. Fig. 1.1 shows the schematic of phase diagram of water. If the liquid, in static or dynamic condition, has a state defined by ambient pressure, p and temperature, T as shown by point 1 in Fig. 1.1, it can be vaporized by two different ways. Vaporization by increasing the temperature at constant pressure (i.e. following path 1-3) is called boiling, whereas vaporization due to pressure drop at constant temperature is called cavitation (i.e. when state changes from 1 to 2). These are the ideal

definitions, but in reality both temperature and pressure may change, though one could be dominant over the other, deciding the phenomenon. When pressure drops below the vapor pressure (solid line connecting T_r and T_c), which is a function of temperature, the liquid phase changes to its vapor phase. When it happens locally inside a continuum medium of liquid, a cavitation bubble is generated. It should be mentioned that the boundaries between different phases are not very rigid, in reality deviation may occur depending on the liquid and the environment. Sometimes phase changes may occur at temperature below the intended one, called as thermal delay in cavitation. Similarly, static delay is- when phase changes at pressure below the vapor pressure [6–8].

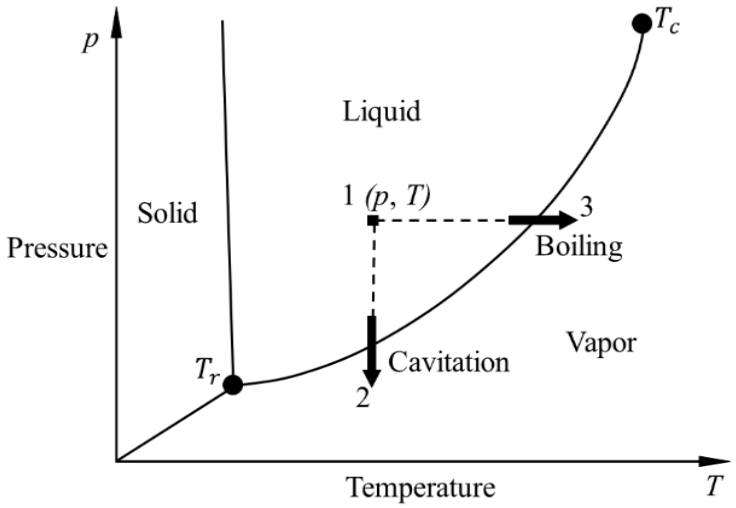

Fig. 1.1 Schematic of phase diagram of water. In the figure, T_r represents temperature corresponding to triple point and T_c corresponding to critical point.

The steps involved in cavity formation are- breaking down of liquid phase to create voids, filling up these voids with vapor of the liquid and finally saturation of the voids with vapor. Practically the steps are almost simultaneous and so rapid that the voids saturate almost instantaneously.

1.1.2. Cavitation- engineering view

The definition given above is ideally true, but not sufficient to explain the cavitation that occurs in reality, like in a flowing fluid in hydraulic machineries. In reality, liquid always contains a large number of micron air bubbles or gas particles that act as cavitation nuclei, which may not be visible to the naked eyes. Cavitation easily initiates at those bubble nuclei or other favorable locations like suspended micron solid particles or discontinuities on the solid surfaces. A pure liquid free from any nuclei is able to sustain a very large tension, in the order of hundreds of atmospheres (tens of MPa), before a cavity can be generated through breaking the liquid molecules [9–12].

Cavitation is defined as the explosive growth and intense collapse of bubble nuclei in a liquid due to rapid and large variations of ambient pressure [7]. In presence of nuclei, cavitation inception is defined in terms of a critical pressure below which they grow explosively. This critical pressure depends on the vapor pressure and is significantly reduced by the surface energy of any existing nucleus [7,13]. Thus, practically it is always

necessary that the liquid pressure has to drop below its vapor pressure for unstable growth. Cavitation manifests itself either in terms of visible cavities or acoustical emission of high-pressure recognizable sound produced by these cavities. Because of micron sizes of bubble nuclei, sometimes, especially at low speed and/or high local pressure of flowing fluid, sound emission occurs before the bubbles become visible in relatively low pressure regions [7,9–12,14,15].

1.1.3. Mechanism of cavitation bubble collapse

When the local pressure inside a flowing liquid drops suddenly below a critical value, say due to the geometry of the wall, cavitation nuclei grow rapidly forming visible cavities. Theoretically, cavities will grow until the pressure inside falls below the ambient liquid pressure. Moreover the growth is also driven by the inertia of the interface. The cavities are then again compressed in the high pressure region in the fluid and finally collapse. Depending upon the flow condition, the compression of such cavities could be very strong and, so rapid that they may collapse very violently. Such collapses are often associated with the formation of high velocity micro-jets [16–20] and recognizable intense shock waves [21,22]. Rayleigh in 1917 [21] has theoretically explained the generation of shock waves by explosion of spherical bubble and Harrison in 1952 [22] has provided the first experimental evidences of shock waves emission during cavitation bubble collapse. The idea of formation of micro-jet hitting the solid surface was first introduced by Kornfeld & Suvorov [16] and many authors like [17–20][23][24] have observed it experimentally. As an example, Fig. 1.2 shows the evolution of a bubble shape as it collapses nearby a solid boundary, experimentally observed by Crum [18] with a pulsating bubble illuminated stroboscopically. Though the pulsating bubble collapse is different form the hydrodynamic bubble collapse, it describes well the micro-jet formation and asymmetrical bubble collapses in real cavitating flow.

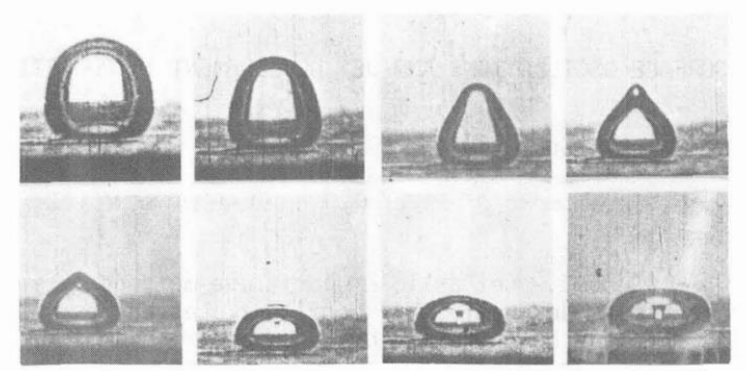

Fig. 1.2 Micro-jet formation during the collapse of a pulsating bubble filmed under stroboscopic illumination. The maximum diameter of the bubble is approximately 1 mm. Experimental observation of Crum [18].

Ideally the bubbles growth should stop when the pressure inside the bubble is equal to the liquid pressure. But, due to the dynamics involved in high velocity liquid and/or the inertial effect of the liquid, cavities/bubbles may grow excessively, and when they again enter into a high pressure region in the liquid, experience a high pressure gradient toward the center of the cavities that leads to violent collapses. Practically, the liquid pressure

on the whole surface of a cavity is not necessarily the same, for many reasons like turbulence, location of near-by solid surface, liquid-liquid or liquid-solid friction, solid particles contamination in the liquid etc. All of these factors contribute to the asymmetrical growth and collapse of cavitation bubbles. Wherever the pressure is maximum, the surrounding liquid is driven in from that point in the form of a micro-jet, toward the center of the cavity during its collapse. Asymmetrical growth and collapse of bubbles close to a solid boundary was first numerically solved by Plesset & Chapman [25]. Thereafter extensive works like [26–28] have been done to understand the mechanism and Fig. 1.3 [28] shows a typical evolution of bubble shape with time during collapse.

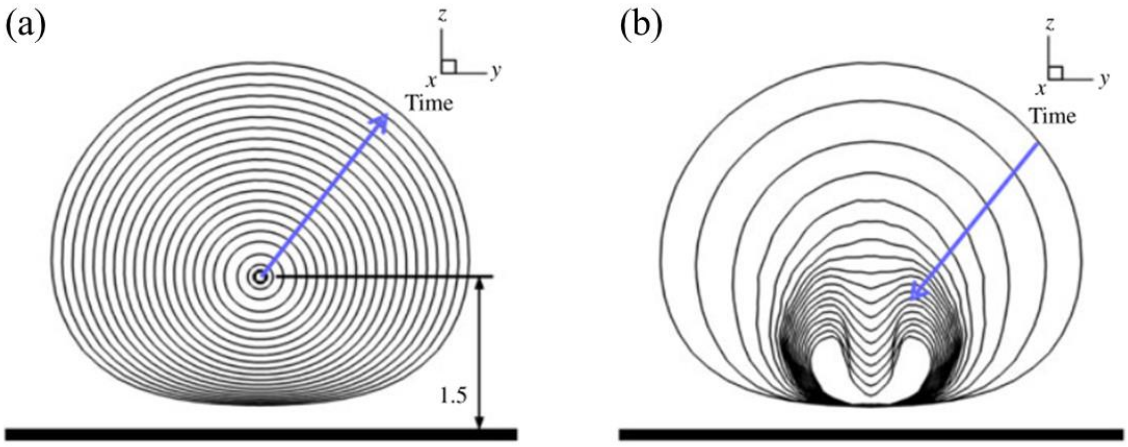

Fig. 1.3 Evolution of bubble shape with time showing (a) bubble growth and (b) bubble collapse. The arrow indicate increase in time. 3D boundary element method (BEM) simulation of initial nuclei of 50 µm at a distance of 1.5 mm undergoes a pressure difference of 10 MPa in a period of 2.415 ms. Standoff distance at maximum bubble radius is 0.75 [28].

When a bubble collapse occurs nearby a solid boundary the micro-jet is always found to be directed towards the solid boundary [7,17–20]. This is because the radial flow of liquid is prevented by the solid boundary below the bubble wall. As a result the liquid pressure at the bubble wall close to the solid surface is minimum whereas, the pressure at the bubble wall farthest from the solid surface is maximum. Philipp and Lauterborn [19] have done extensive experimental works along with literature review on the mechanism of cavitation bubble collapse and presented in details the influences of solid boundaries. According to them the pressure gradient along the boundary leads to different accelerations of the closer and farthest bubble wall which ultimately drives the bubble towards the boundary. This kind of translational movement of bubbles during collapse was first introduced by Shutler & Mesler [29] and is considered to be able to enhance the damaging effect of bubbles collapsing relatively away from the solid boundary.

Benjamin & Ellis [11] first pointed out the ‘virtual mass’ induced by the fluid flow surrounding the bubble that acquires a Kelvin impulse due to the Bjerknes force [30] resulting from the pressure gradient across the bubble. During the final stages of collapse, the Kelvin impulse becomes almost constant and, as the bubble size gets reduced, to maintain the conservation of impulse, the velocity of the bubble center has to increase. This leads to the increased velocity of the wall farthest from the solid boundary compared to the wall closer to the boundary. As a result, liquid close to the bubble wall farthest from the solid boundary is focused and

accelerated towards the bubble wall closer to the solid boundary, in the form of a micro-jet. The velocity of such micro-jet could be very high, about few hundreds m s^{-1} [7,19,25,31], as observed experimentally. Though numerical studies suggest even higher jet velocity as high as 1500 m s^{-1} [28]. This micro-jet initially hits the bubble wall leading to a toroidal and then hits the solid surface. The presence of water layer between the bubble wall and the solid boundary dampens the impact velocity of the micro-jet. The intensity of the impact increases with the decrease in the water layer thickness, which can never be eliminated totally.

When the micro-jet hits the bubble wall before hitting the solid boundary a shock wave (called jet shock wave) is emitted and immediately afterwards the collapse of the bubble also leads to the formation of another shock wave (collapse shock wave), as the gas contents of the bubble is highly compressed. Fig. 1.4 shows these shock waves captured by Phillipp and Lauterborn [19] using high speed photography with shadowgraph method, for two different stand-off distances (γ) which is defined as the ratio of initial bubble distance from the solid surface to the maximum bubble radius. Intensity of shock waves becomes weaker with decreasing the bubble stand-off distance, as the collapse becomes more asymmetrical.

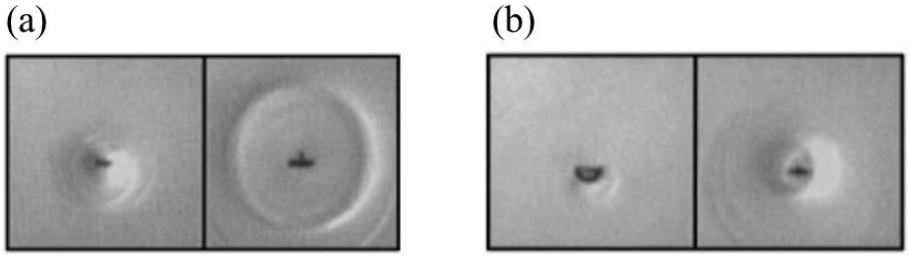

Fig. 1.4 Emission of two shock waves during a bubble collapse: (a) γ =1.9; (b) γ =1. 7, frame width 4.0 mm [19].

Both experimental and numerical studies suggest that after the first collapse the bubble produces a vortex ring like shape (see the last frame in Fig. 1.2) which subsequently collapses and produces a second impact onto the solid surface [19,28], if the bubble standoff distance is very small (typically $\gamma < 1$). This can be followed by subsequent impacts. Thus in general we can understand the complexity involved with hydrodynamic bubble collapses.

1.1.4. Cavitation pitting and erosion

As mentioned earlier, in a high velocity liquid violent growth and collapse of cavitation bubbles lead to formation of high velocity micro-jets and shock waves. If the bubble collapse occurs near the solid surface, both the micro-jet and shock wave result in a high impact onto the solid surface. Magnitude of such impacts depends on the bubble size, distance of bubble collapse from the surface and collapse driving pressure gradient [7,28]. The magnitude could be so high that the material would undergo local plastic deformation, resulting in the formation of cavitation pit. Though the accurate estimation of impact stresses remains a challenge, many authors like [19,20,32] have estimated the impact pressures to be in the range of a few GPa (as high as 6 GPa or more is also reported [33,34]). The formation of cavitation pit due to cavitation bubble collapse is called

cavitation pitting. Repetition of such impacts due to cavitation bubble collapses leads to strain accumulation and hardens the surface layer of the target material. Eventually damage initiates and propagates leading to complete failure in terms of material removal. Material removal due to repeated impacts of cavitation bubble collapses is called cavitation erosion. Cavitation erosion is commonly observed in hydraulic turbines, ump impellers, ship propellers, valves, heat-exchanger tubes, and other hydraulic structures [6,7,35]. Fig. 1.5 shows two examples of cavitation erosion- a) cavitation erosion in rotary plug valve body [36] and b) cavitation erosion in marine propellers [37]. The figure clearly shows the extent of damage that cavitation bubble collapses may induce. Hence protection against such damage is unavoidable.

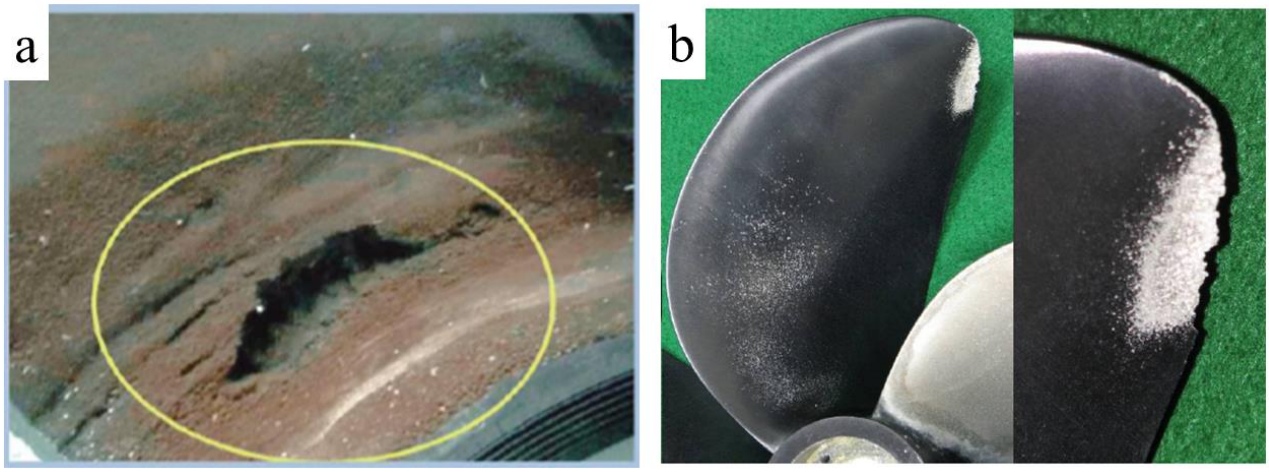

Fig. 1.5 *Typical example of cavitation erosion damage- (a) rotary plug valve body* [36] *and (b) marine propellers* [37].

1.1.5. Fatigue aspect of cavitation impact

Response of a material under cavitation impacts could be compared with random cycle fatigue. The impact loads vary between zero and compressive peaks, with random intervals, magnitudes and random locations of impacts on the surface. Fig. 1.6 below shows a typical signal recorded by a conventional piezoelectric pressure sensor (PCB 108A02) subjected to cavitation erosion [38], which highlights the randomness in cavitation impact loads. Each peak in the positive direction represents an impact due to cavitation bubble collapse. Negative peaks are due to ringing of the transducer and the red dotted line represents a threshold value (0.8 V) to avoid background noise and weak pulses which might not result in cavitation pits. Unlike completely reversed cycle fatigue [39,40], there is no tension loading or in other words no reversing of the applied loading cycle. Although, there is no reversal of the applied impact load cycle, complex surface geometry induced by previous impacts and random location of impacts may result in reverse straining of the material close to the surface or at least to stress triaxiality fluctuations. Under such scenario, the strain accumulation may not occur evenly with successive impacts.

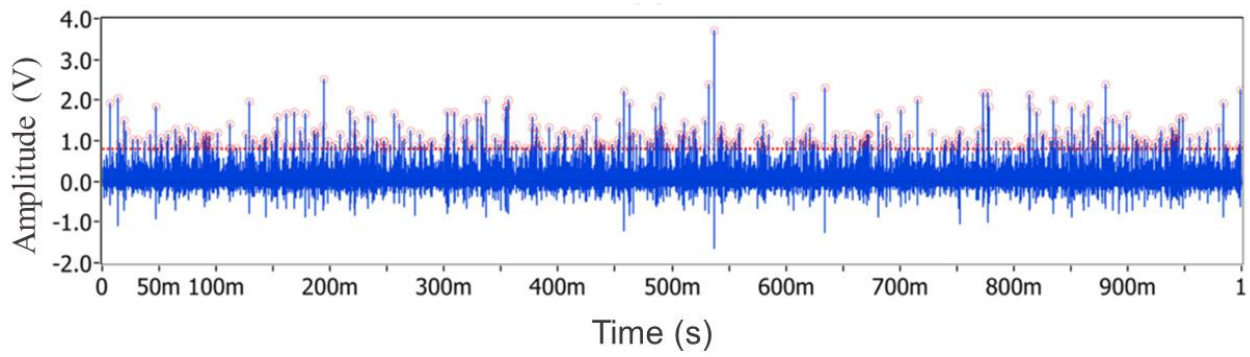

Fig. 1.6 Impact load signals recorded by a piezoelectric pressure sensor in a cavitation tunnel operating at flow pressure of 40 bar. The circles show the signals above a threshold of 0.8 V [38].

Cavitation is a special type of fatigue phenomenon since the frequency of impacts is usually very high and the magnitude is very random, leading to local stresses into the material that vary in a wide range from elastic to plastic domain. The impact loads of large amplitude have a smaller frequency and may cause damage by a low cycle fatigue (LCF) mechanism, whereas impact loads of small amplitude have a high frequency and may cause damage by a high cycle fatigue (HCF) mechanism. Hence, the type of fatigue mechanism involved in cavitation erosion strongly depends upon the flow aggressiveness and it can be expected that it will be different for vibratory cavitation which is generally less aggressive than hydrodynamic cavitation at very high flow velocity that may be highly aggressive. The research work presented in this thesis is related more especially to the latter for which LCF is expected to play an important role. Thus for the modeling of cavitation damage, fatigue aspect should be considered with special attention, so that the mechanism of strain accumulation is represented correctly.

Fatigue type of failure mechanism of cavitation pitting has been studied by many authors, for example [32,41–46]. Presumption of fatigue in cavitation is mainly based on the fatigue striations or tire tracks like structures on the fracture surface [32,41–46], as shown in Fig. 1.7(a-b)[32]. Though fatigue is considered to be the dominant failure mechanism, the complete picture is not yet clear in the literature. The role of the very high strain rate involved in cavitation pitting and shock waves that propagate through the material is not understood well. Karimi [43] has highlighted that the appearance of cross-slips in cavitation of duplex stainless steel could be due to high rate of cavitation impact. The large number of dislocations evidenced far from the surface is considered to be due to shock waves that propagate through the material [43]. The presence of residual stress relatively deeper inside the material is attributed to shock waves by [47].

Ambiguity, regarding the fatigue crack initiation, arises from the fact that, experimental investigations of cavitation eroded surface show that the crack initiates at the surface [32,43,45], as shown in Fig. 1.7(c), whereas numerical studies of material response under cavitation impact of a single bubble collapse show that maximum stress occurs inside the material [7,28,48,49], as shown in Fig. 1.8(a-b). Thus it is necessary to understand the influence of intervals between impacts, impact locations and sequence of impact magnitude etc. on the cavitation erosion mechanism, possibly by means of numerical simulation, if they could explain the reason of such differences.

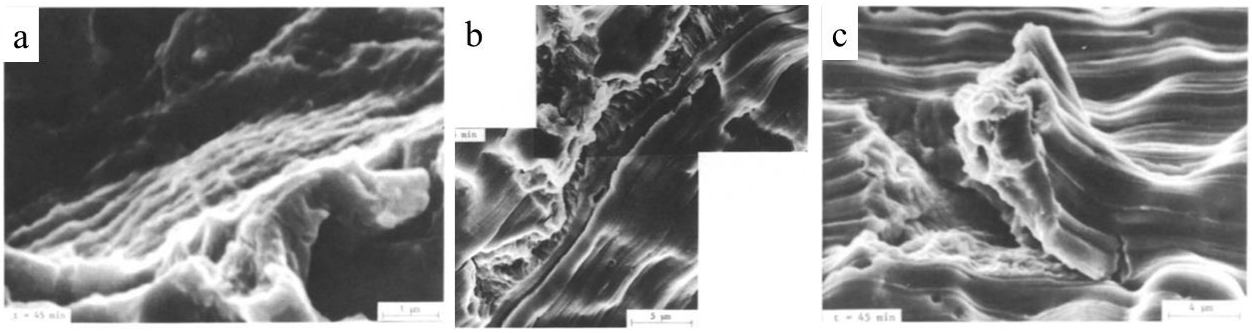

Fig. 1.7(a-c) Cavitation erosion study of SUS 304 stainless steel [32], *(a) fracture surface showing fatigue striations, (b) tire tracks on fracture surface and (c) initiation and progress of the fatigue crack.*

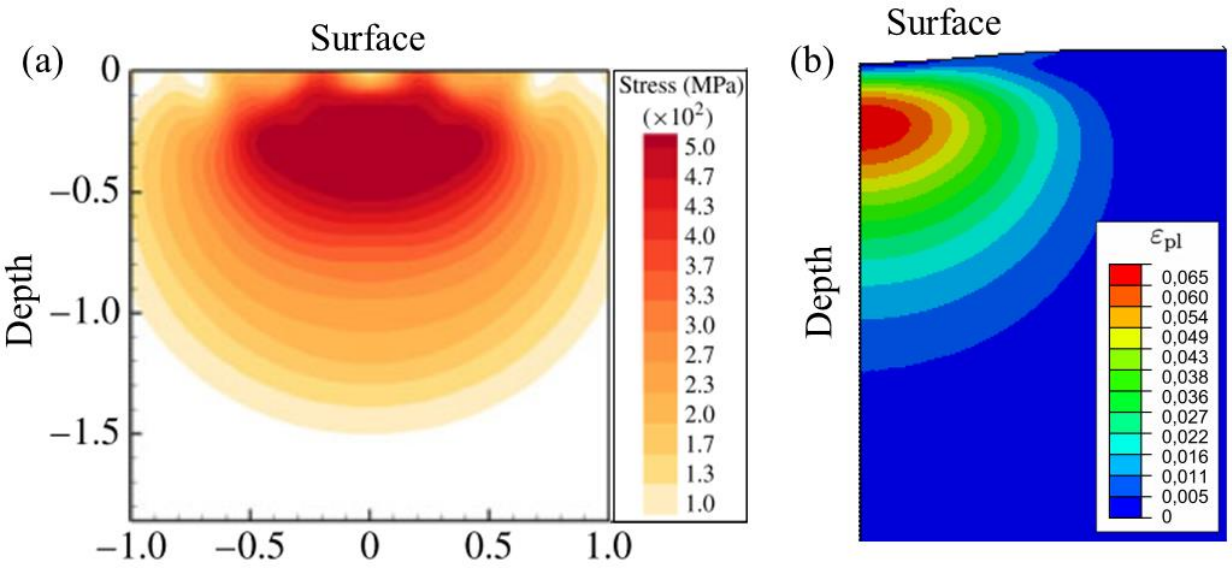

Fig. 1.8 Numerical simulation of material response under hydrodynamic impact of single bubble collapse, (a) contours of equivalent stress into the material (7075 aluminum alloy), obtained by fluid structure interaction simulation [28] *and (b) contour of plastic strain into a pure polycrystalline copper (99.99%), obtained by simulating material response to a representative pressure field* [49].

1.1.6. Cavitation number

Cavitation potential of a flowing liquid is measured by using the cavitation number (σ_{ca}). This is defined as the ratio between the local pressure drop (Δp) and the kinetic energy (E_k) per volume of the liquid [6,7], as given by Eq. (1.1). Drop in local pressure is estimated with respect to the saturated vapor pressure (p_V) of the liquid, which is a function of temperature (T).

$$\sigma_{ca} = \frac{\Delta p}{E_k} = \frac{p_l - p_V(T)}{\frac{1}{2}\rho_l v_l^2} \tag{1.1}$$

Here, p_l is the absolute local pressure, ρ_l is the density and v_l is the flow velocity of the liquid.

The cavitation number is used to guess or presume the extent of cavitation erosion in test facilities like cavitating liquid jet, cavitation tunnel, vibratory device and others. The cavitation number is also used for hydraulic devices like pump, pipe and turbine as an indicator of the development or extent of cavitation.

As shown by Eq. (1.1), increasing the velocity or reducing the flow pressure, which commonly occurs in a high velocity liquid that comes in contact with structural discontinuities, have the same effect on σ_{ca}. Cavitation extent in a flow varies inversely with σ_{ca}. For a given system, with reduction in σ_{ca}, the cavitation starts to appear at some particular value called the incipient cavitation number (σ_i). A smaller value of σ_i is often desirable in order to delay the inception of cavitation. For a flow to be non-cavitating, σ_{ca} should be greater than σ_i. This could be achieved by eliminating surface discontinuities to avoid local pressure drops.

1.1.7. Fluid-Structure interaction

When a cavitation bubble collapses, it produces high intensity shock waves along with micro-jets. When the shock wave propagating through the liquid hits the solid structure, the wall recoils elastically and the wave loses part of its energy. Simultaneously a part of the shock wave gets reflected back into the liquid and a part gets transmitted through the solid [6]. Transfer of the energy or the solid-liquid interface velocity depends on the ratio of acoustic impedances of the liquid and solid. Similarly the effective load on the solid surface also gets affected by the acoustic impedances of the liquid and solid. Acoustic impedance could be estimated simply as the product of density by the speed of sound through the medium.

The interaction of the micro-jet/shock-wave with the solid structure could be explained by analogy with the water hammer phenomenon, where a water jet of diameter d_{jet} at velocity v_{jet} (density ρ_l and speed of sound c_l) hits normally a solid surface (density ρ_s and speed of sound c_s). Then based on the conservation of mass and momentum the actual impact pressure can be estimated as follows [6]-

$$P_{imp} = \left(\rho_l c_l v_{jet}\right)/\left(1 + (\rho_l c_l)/(\rho_s c_s)\right) \tag{1.2}$$

For a perfectly rigid body Young's modulus E_s is infinite and hence $c_s = \sqrt{E_s/\rho_s}$ is also infinite, so the impact pressure would be $\rho_l c_l v_{jet}$. In case of metallic alloys the acoustic impedance is very high compared to water, thus attenuation of impact pressure is negligible. This means that- impact load measurements using pressure transducers made of metallic or ceramic piezo-electric material would give the actual impact pressure, whereas polymeric transducer would not give the real pressure. However, as discussed in Sec. 1.3.3.1, polyvinylidene fluoride (PVDF) transducers are widely used to measure cavitation impact loads [50,51]. For the same reason, ultra-high molecular weight polyethylene (UHMWPE) that has a lower acoustic impedance compared to 2205 stainless steel alloy shows high damping effect and excellent resistance to cavitation erosion [52]. This effect should be considered in the numerical modeling of the material behavior, if polymeric materials are used as pressure sensors to estimate hydrodynamic impact loads from cavitation pit geometries by using the inverse finite element method proposed in this thesis, as discussed in Sec. 2.5.

1.2. Experimental techniques for cavitation erosion tests

Cavitation erosion tests are done to evaluate the erosion resistance of a material or component in a cavitating flow. Practically field erosion tests as well as small scale accelerated laboratory tests are done to deduce erosion

resistance. Field erosion tests have been conducted for hydraulic turbine and pumps but they are expensive and not so commonly used, whereas the laboratory experimental studies are commonly used for marine applications [7].

There are several laboratory testing methods:- ultrasonic vibratory devices, rotating discs, cavitating liquid jets and cavitating flow loops [7,34,53–56]. Though the experimental setup is different for all the above mentioned methods, the main objective remains the same- generation of explosive cavitation bubbles. Some of these testing methods are standardized by the American Society for Testing and Materials (ASTM). The vibratory test method (ASTM G-32) and cavitating liquid jet method (ASTM G-134) are most commonly used. In the current study high-speed cavitation tunnel is used, though not standardized yet but extensively used the field of cavitation erosion study.

The following section provides a brief introduction to the vibratory test method, cavitating liquid jet method and cavitation tunnels. Special focuses was made on the cavitation tunnel that has been used in the current study.

1.2.1. Vibratory cavitation erosion testing

In this method the test sample is generally attached to a suitably designed 'horn' or velocity transformer that is attached to an ultrasonic transducer (magnetostrictive or piezoelectric type) which vibrates at high frequency (a few tens of kilohertz, typically 20 kHz). Fig. 1.9 below shows the schematic of a vibratory erosion test apparatus [57].

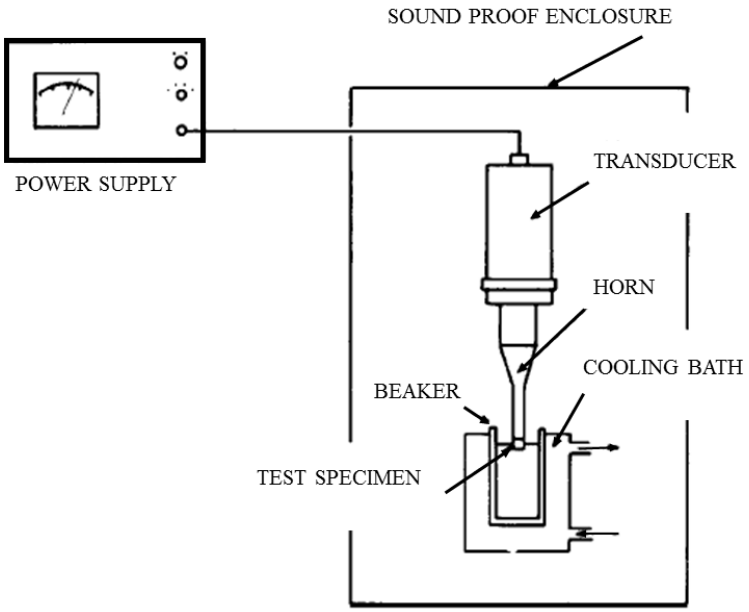

Fig. 1.9 Schematic of vibratory cavitation erosion apparatus [57].

The specimen along with the horn-tip is axially vibrated at a specified amplitude while immersed into a liquid (generally distilled water) whose temperature is maintained constant throughout the test. The cyclic pressure fluctuations produced by the high frequency vibrations of the transducer-horn-sample assembly lead to the

generation of cavitation bubbles. Bubbles are generated during the tension part of the imposed cyclic pressure (i.e. negative pressure) and subsequently collapse during the compression part (i.e. positive pressure) leading to cavitation erosion.

The diameter of the sample should be similar to the horn tip and the thickness should be chosen properly to avoid excessive mass. The sample surface should be smooth without any scratches or pits and the preparation method should be as close as possible to that of intended field application [57]. Each time the specimen size and mass is changed, the amplitude and frequency of vibration should be calibrated. Periodically erosion tests are done on a standard reference material (99.5% pure nickel product commercially known as annealed wrought Nickel 200 (UNS N02200)) to verify the normal performance of the apparatus.

In this method the mechanism of cavity generation differs from that of flowing liquid systems or hydraulic machines, but the basic mechanism of material erosion is believed to be same. Moreover, small scale and rapidness of the method makes it popular, which enables to analyze and rank relative cavitation erosion resistance of different materials. This method is not recommended for elastomeric or compliant coatings, because of their high compliance which could reduce the aggressiveness of the cavitation [57]. An alternative approach for such compliant materials is to use a stationary specimen, while the horn equipped with a highly resistant tip vibrates close to the specimen. Complete details about the specimen dimensions, vibration amplitude, shape and size of the beaker and cooling bath etc. can be found in [57,58].

1.2.2. Cavitating liquid jet system

The cavitating liquid jet testing method is standardized as ASTM G134 [59]. In this method cavitation erosion is produced by a submersed cavitating jet which impinges upon a test specimen which is also submerged and stationary. The high velocity liquid jet is issued from a suitably designed cylindrical-bore nozzle and, cavities are generated in the vena contracta region of the jet which later on collapse on the specimen surface. Vena contracta region is the smallest locally occurring diameter of the flowing jet where the flow velocity is maximum leading to lowest flow pressure, which encourages the generation of unstable cavities. This method provides greater flexibility to control different parameters and study their effects on cavitation erosion. The parameters are generally the type of the jet, its velocity, diameter, angle of impingement, standoff distance, and downstream pressure [53]. Fig. 1.10 below shows the schematic of the test chamber of a cavitating liquid jet apparatus [59]. Unlike vibratory device, this test method provides more realistic clouds of cavitation bubbles of various sizes along with shear flows with vortices.

The cavitating liquid jet is issued through a long cylindrical nozzle (item 6 in Fig. 1.10) and the button shape specimen (item 8) is mounted coaxially with the nozzle. The standoff distance between the sample and the nozzle inlet edge can be adjusted through the micrometer head (item 10). The test chamber is filled with a test liquid that is maintained at a specific temperature and pressure throughout the test. Depending on the purpose and the type of the test liquid, it can be recirculated for reuse or disposed. The jet interrupter (item 11) can be used to protect the specimen while the test conditions are being set up and the perspex widow (item 3) enables

to observe the erosion process. The nozzle must be made of highly erosion and corrosion resistant material (generally Nitronic 60 is used). Consistent performance of the test apparatus should be verified by conducting periodical test on a standard material (could be Nickel 200) at standard test condition [59].

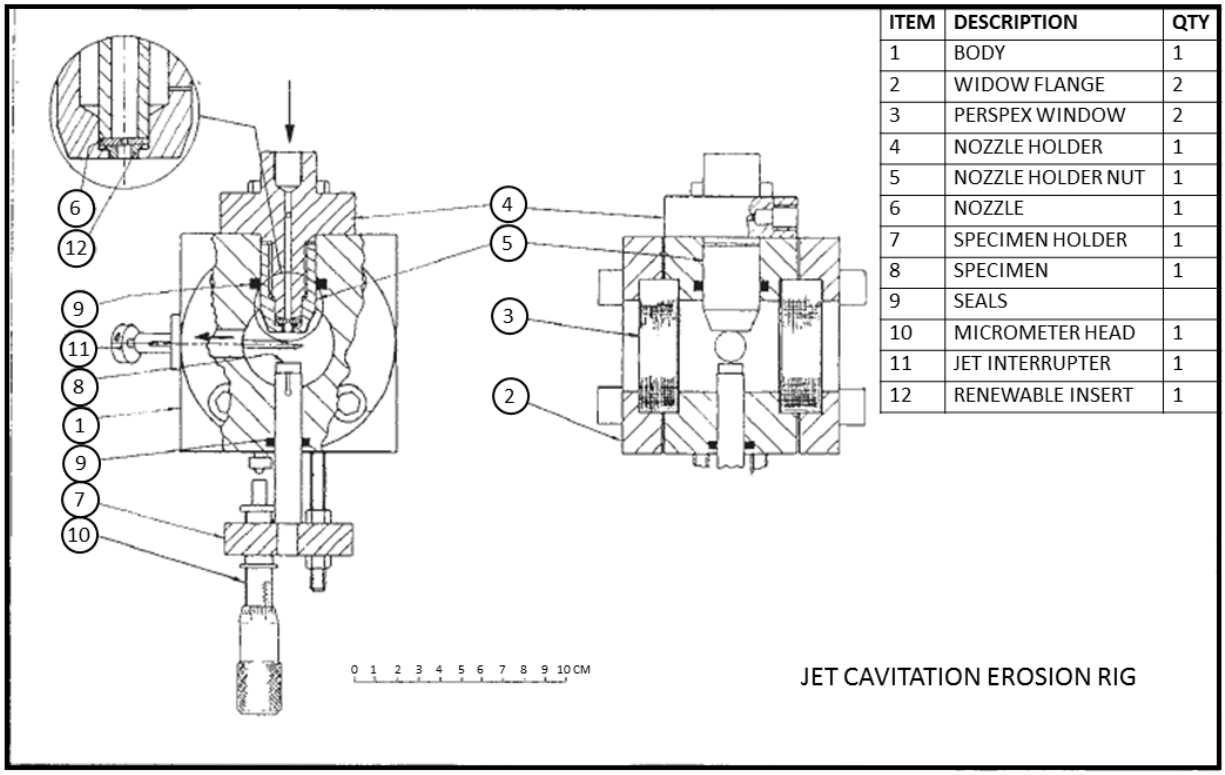

Fig. 1.10 Test chamber assembly of cavitating liquid jet apparatus [59].

1.2.3. High speed cavitation tunnel

High speed cavitation tunnel is also preferred for erosion test of hard materials as it produces more realistic cavitation erosion. This apparatus has been extensively used by many authors like [60–63] for cavitation erosion studies. This method is not yet standardized by ASTM. Fig. 1.11 shows a typical example of a cavitation tunnel that is used for the current study (PREVERO device built in 2003 at LEGI). The 80 kW electric motor driven centrifugal pump (maximum flow rate of 11 l/s at 40 bar pressure) drives the test liquid to the test section through a flow meter. After the test section the liquid comes into a downstream tank (of size 1 m^3) maintained at a specified pressure. The liquid is pressurized in the tank with nitrogen by using a pressurization bottle. The heat exchanger controls the temperature of the liquid before it is recirculated for use again. The apparatus has a radially divergent cross section. The test liquid (generally tap water) comes in through the axial inlet where it faces the test specimen (generally cylindrical in shape), and goes out radially through the passage between the test specimen and the supporting wall. Cavities are generated in the divergent section just after the axial inlet due to sudden change in cross sectional area. The already existing cavitation nuclei undergoes sudden pressure fluctuations in this region along the flow path, which causes explosive growth and collapse of these bubbles leading to cavitation erosion.

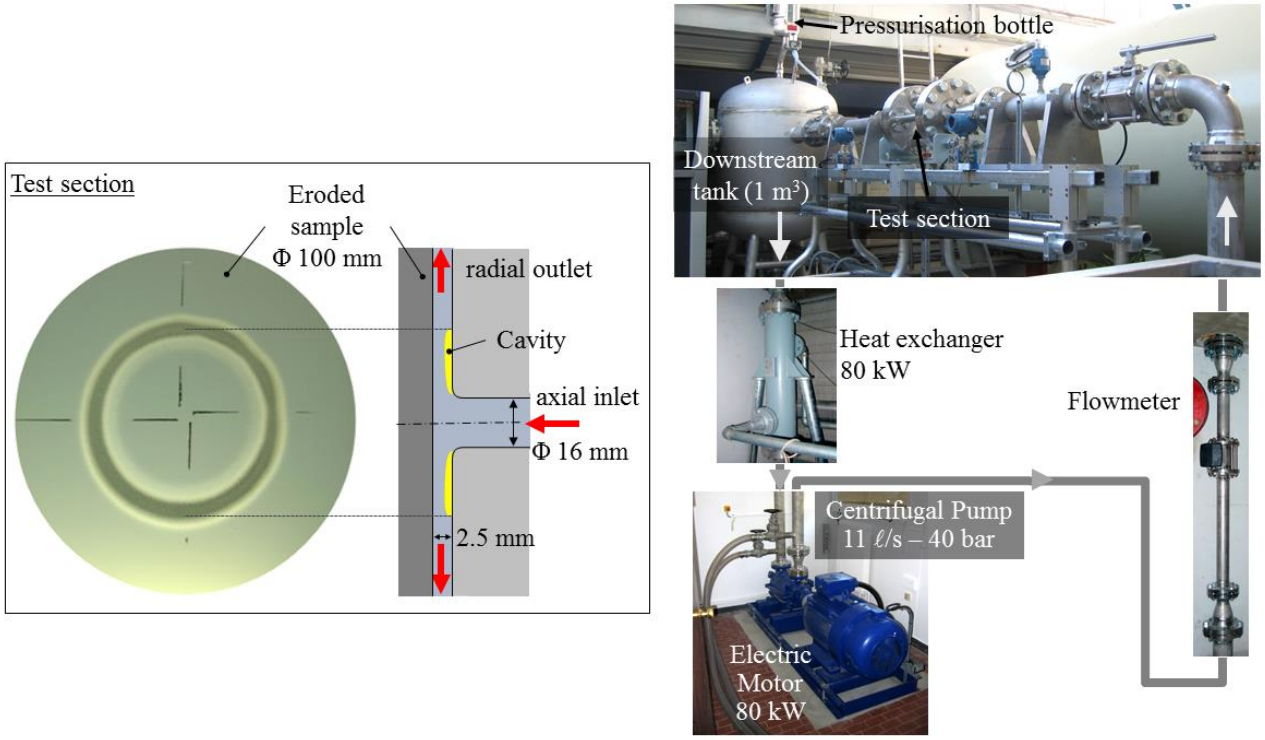

Fig. 1.11 The high speed cavitation tunnel PREVERO used for the current study. The apparatus is made of stainless steel and has been installed in 2003 in the Laboratory of Geophysical and Industrial Flows (LEGI), University Grenoble Alpes, France. It can operate at maximum pressure of 4 MPa (40 bar) with flow velocity of 90 m/s.

The apparatus is designed for a maximum flow pressure of 4 MPa (40 bar) corresponding to a maximum flow velocity of 90 m/s. The test section can be changed to investigate cavitation erosion through different channels like Venturi with or without central body, slot cavitator, cylindrical specimen spanning the tunnel or radial divergent [7]. In the current study radially divergent test section is used and hence the maximum erosion is concentrated around a ring as can be seen on the left in Fig. 1.11.

For this apparatus, the cavitation number is defined as [62]-

$$\sigma_{ca} = \frac{p_d - p_V(T)}{p_u - p_d} \tag{1.3}$$

Where p_u and p_d are upstream and downstream pressure respectively, measured by pressure sensors at the inlet and outlet ducts of larger diameter (90 mm), away from the test section. The cavitation number defines the erosion potential as well as the location of erosion on the sample surface. Pressurization of the liquid in the downstream tank helps in maintaining a constant cavitation number that enables us to investigate the effect of flow velocity independent of cavitation number or cavity length. Test duration depends on the erosion resistance of the material being tested and cannot be rigorously predicted in advance.

1.2.4. Test procedure and interpretation of results

Irrespective of the testing apparatus being used, the basic test procedure remains to be the same. First of all, the weight of the test specimen should be measured. Set up all the test parameters (like standoff distance, flow

velocity, upstream and downstream pressures etc. in the case of cavitation tunnel apparatus) and perform all the calibration required for the particular apparatus being used. Then perform the cavitation test on test specimen.

The results of a cavitation erosion test cannot be defined by a term with single value. The primary output of any cavitation erosion test is the cumulative mass loss versus cumulative exposure time. The mass loss depends on the erosion resistance of the material being tested and, may also vary depending on the test apparatus being used. The test should be stopped periodically and the test specimen should be removed, cleaned and dried carefully and, the mass loss should be determined by reweighing the specimen. As the rate of mass loss of a material varies with exposure time, to obtain a better accuracy sufficient data points should be recorded with periodic intervals, though it is difficult to rigorously specify the test intervals in advance.

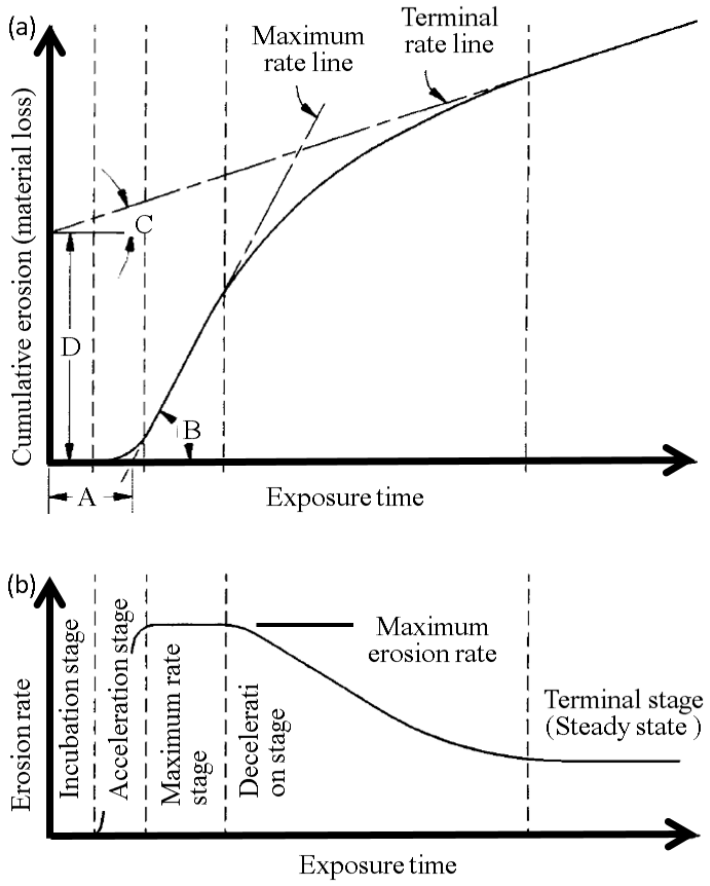

Fig. 1.12 Primary results of cavitation erosion test [57] *(a) Characteristics of typical cumulative erosion versus exposure time curve. A = nominal incubation time; tan (B) = maximum erosion rate; tan(C) = terminal erosion rate; and D = terminal line intercept. (b) Characteristics of an erosion rate versus exposure time curve corresponding to Fig 12(a).*

Fig. 1.12(a-b) shows the general behavior of cavitation erosion of a material with time [57]. Fig. 1.12(a) shows the characteristics of cumulative mass loss versus cumulative exposure time curve and Fig. 1.12(b) shows the variation of erosion rate in the different regions with time. The incubation stage is the period when no mass loss occurs and material undergoes plastic deformation only. It is followed by a period of accelerated material

loss rate (because of damage initiation and propagation) and then an almost constant erosion rate for a certain period of time. Sometimes it is difficult to clearly distinguish this constant erosion rate stage [7]. After this short constant mass loss period the material surface topology changes significantly and fluid-structure interaction gets modified leading to decreasing erosion rate. Finally the material reaches a state where again the erosion rate is constant; this period is called terminal stage or steady-state period. All of the different phases of cavitation erosion curve depend on the material being tested and the apparatus being used. The initial four stages are very dynamic in nature and change with the fluid-structure interaction, which varies with apparatus and the progressive damaged surface topology of the material. Thus all the phases may not be observed all the time in any cavitation test.

1.3. Cavitation pitting and impact loads measurement

In the early stage of cavitation erosion the target material undergoes elasto-plastic deformation (especially for metals) due to hydrodynamic impact loads caused by cavitation bubble collapses. As a result cavitation pits are formed, which are micro-indents of various sizes (depths and diameters). These cavitation pits could be considered as the signatures of impact loads caused by cavitation bubble collapses, and controlled by the materials constitutive behavior. Estimation of the impact loads generated by the bubble collapses is important to determine the cavitation flow aggressiveness. Estimation of aggressiveness of a cavitating flow is an essential step for accessing the cavitation erosion resistance of a material or for prediction of such damage. Despite of having serious limitations, use of different types of pressure transducers [23,27,38,50,64–66] have been the common practice to estimate the cavitation impact loads and is discussed in the following Sec. 1.3.3.1. Recently authors in [7,67,68] have developed a method to estimate cavitation impact loads from the cavitation pit dimensions by combining cavitation pitting tests and nanoindentation, which is discussed in the following Sec. 1.3.3.2. Other popular methods of estimating flow aggressiveness or impact loads within the scope of computational fluid dynamics (CFD) simulations or experimental fluid dynamics are discussed in Sec. 1.3.3.3.

Knapp [8,69,70] was the first to introduce cavitation pitting tests to characterize the intensity or aggressiveness of a cavitating flow by counting the number of pits per unit surface area of the test sample and per unit time of exposure to cavitation. He proposed this definition of cavitation intensity as an alternative to the earlier used rate of material removal per unit surface area, which does not only depend on the flow aggressiveness but also on the corrosion potential of the particular liquid-solid system [70]. However, the proper measurement of impact loads would provide better quantification of flow aggressiveness in terms of impact stresses, their radial extents and frequencies. This is still a challenging issue even after many decades of active research in this field of cavitation erosion.

Continuous progresses in the surface analysis techniques such as contact profilometry [62], laser profilometry [60], optical interferometry [71], scanning electron microscopy [72], atomic force microscopy [49] and so on have enabled more detailed and precise analysis of cavitation pits, especially in terms of individual pit shape, depth, diameter and volume. These detailed analyses, in turn, enabled better quantification of cavitation flow

aggressiveness from cavitation pitting tests. In this thesis a new method is proposed to estimate the cavitation impact loads from cavitation pit geometries by combining cavitation pitting test and inverse finite element simulation of the material response to cavitation impacts. This new method is discussed in Sec. 2.5 in Chapter-2.

1.3.1. Cavitation pitting test

Cavitation pitting tests are nothing but cavitation erosion tests conducted for a short duration of time that falls within the incubation period of the target material. The similar test apparatus and testing methods as explained in Sec. 1.2 are used. The test specimen should be very finely polished, otherwise separation of pits from surface roughness would be difficult as the dimensions are in the micron range [62]. The purpose is to produce cavitation pits which are undamaged and non-overlapped or isolated from each other. With increase in exposure time the cavitation pits become more connected with each other and also the material starts to damage. Thus, the counting of pits and the analyses of pit parameters become difficult. Determination of optimum exposure time, which depends on the flow condition (especially velocity [70]), should be such that a sufficient number of pits is obtained with no or negligible overlapping of pits. Large number of pit data are required for accurate statistical analysis of cavitation intensity or flow aggressiveness.

1.3.2. Characterization of cavitation pits

Characterization of cavitation pits involve detection of individual pits, estimation of pit depth, diameter, volume and pit shapes. As surface roughness cannot be avoided completely during sample preparation or in practical situation, a cut-off depth is required to detect cavitation pits, rather than surface roughness or defects. Moreover it reduces the chances of detecting overlapped pits, if there is any [63,67]. Franc *et al*. in [63] have used a 0.5 μm of cut-off depth to detect cavitation pits on metallic alloys tested in cavitation tunnel, while the surface roughness of the test specimen was about 0.1 μm. Once the pits are detected, the estimation of the pit depth is simply measured from the virgin surface. Pit diameters are measured as the equivalent diameter of a circle corresponding to the pit areas on the cut-off plane. Thus the estimated pit diameter is cut-off depth dependent, though it can be minimized by choosing as minimum cut-off depth as possible. This method of pit depth and diameter estimation is discussed in Fig. 1.13.

In this thesis we have proposed a slightly different way of pit diameter estimation by using a cut-off depth which is proportional to the pit depth. This method which overcomes the dependencies of the pit diameter on the cut-off depth is discussed in Sec. 2.4 in Chapter-2.

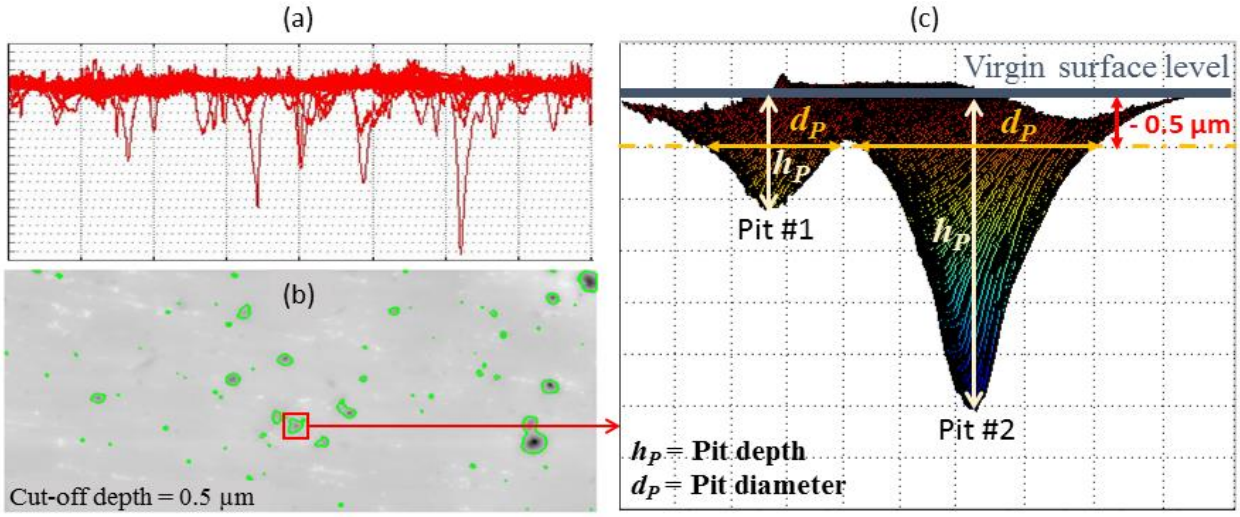

Fig. 1.13 Illustration of the method of pit dimensions determination using a contact profilemeter. The surface topology of a pitting tested sample is obtained by measuring the depth profiles along different lines, as shown in (a). The depth profiles along only 20 lines are shown in (a), the total number of lines will depend on the spatial resolution of the testing apparatus. Then assembling them numerically to produce the three dimensional topology of the tested surface. This surface consists in the geometrical information of the cavitation pits. Then by using a numerical cut-off depth (say 0.5 µm) the pits boundaries are detected, as shown in (b). Then on the basis of the area within each boundary, circular equivalent diameter is computed as the pit diameter. This is shown in (c) highlighting two pits.

1.3.3. Measurement of impact loads

Measurement of impact loads in a cavitating flow is required to estimate the flow aggressiveness. There are different ways of measuring the impact loads as discussed below.

1.3.3.1. Direct measurement by using pressure sensors

Measurement of impact loads by using pressure sensors has been the most widely used method. There are different types of transducers available and used by many authors to study the cavitation flow intensity or aggressiveness. Tomita and Shima [23] and Franc *et al*. [38] have used commercial pressure transducers made of piezoelectric material, that has a rise time of about 1 µs and a natural frequency of 400 kHz, to measure the impact loads and highlighted the associated difficulties due to different factors. The transducers were flush-mounted onto the test specimen or onto a solid wall that was exposed to cavitation erosion. Fig. 1.6 shows the output signals obtained by Franc *et al*. [38] using a piezoelectric pressure transducer (PCB 108A02). The main problem with this type of transducers is their sensitive area, which is significantly bigger (normally a few mm) than that of the impact loading area corresponding to a single cavitation bubble collapse, which could presumably be as small as a few microns. Because of the larger sensitive area, recordings of individual single bubble collapses cannot be ensured and the pressure sensor response could be due to multiple collapse events.

The pressure transducers can provide only the temporal evolution of impact loads, but the radial extent of these impact loads cannot be obtained from the transducer's output readings. Moreover, the output of these transducers is in terms of force (expressed as Newton or other similar unit), which is then converted to stress by dividing with transducer's sensitive area, along with other calibrations if necessary as per manufacturer or

design specifications. Thus there is always an error associated with this conversion, which assumes that the load is applied uniformly on the transducer's exposed surface. In reality the applied stress has a complex spatial distribution as can be understood from the mechanism of bubble collapse discussed in Sec. 1.1.3 and also from the resulting cavitation pit geometries [62,63].

The loading under cavitation bubble collapse is a shock-like event and hence to accurately measure the temporal evolution of the impact load it is necessary to use a transducer with a very short rise time along with a high natural frequency. Often the commercially available transducers have limited rise time and natural frequency. Apart from all these difficulties, the high intensity impact loads could possibly damage the transducers, if not, the elastic or plastic deformation would lead to a loss of energy, or in other words, lead to a biased response of the transducer.

As there is no other alternative established yet for the precise estimation of cavitation impact pressures and their radial extent, researchers continued to use pressure sensors. However, many researchers have tried to use specially designed transducers made of ceramic piezoelectric material [73,74], magnesium oxide single crystal along with piezoelectric ceramic discs [75], piezoelectric polyvinylidene fluoride (PVDF) polymer films [24,34,36,38,50,64,76]. PVDF transducers are preferred over others especially because of their high resonant frequency, typically 10 MHz, with a rise duration of about 30-50 ns [50,76]. Thus PVDF provides the required sensitivity to capture impacts of duration as short as 1 μs. Moreover, PVDF material as a transducer has other benefits like (i) a better reproducibility of the material behavior under sharp dynamic impacts in a wide range, (ii) an acoustic impedance close to the water which provides a better energy transfer, (iii) a large piezo stress coefficient leading to a better sensitivity and (iv) a better resistance to cavitation erosion.

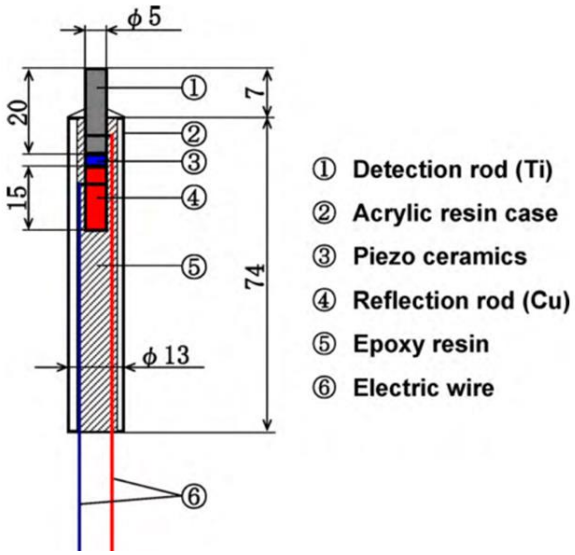

Fig. 1.14 Pressure sensor designed for cavitation impact load measurement [74]. *All dimensions are in mm.*

Because of the aggressive nature of cavitation erosion, the design of the transducers is associated with different accessories to protect the sensor from cavitation damage. Fig. 1.14 shows an example of pressure transducer designed by Hattori *et al*. [74] to measure cavitation impact loads. Usually the piezo-electric material is not

exposed directly to the cavitation environment but protected by a suitably designed material layer (detection rod in Fig. 1.14), especially metallic material that is more resistant to cavitation damage.

Because of the composite structure of the sensors, a thorough calibration is always necessary and it is usually cumbersome. This calibration stage is also seen as a drawback of these sensors [7]. The calibration is usually done by using a dropping ball test technique, pencil lead breaking test technique, gas shock tube technique or pendulum type ball impact technique [34,38,51,76]. By solving the laws of conservation of energy and momentum, impact load corresponding to such tests are estimated analytically and, then by analyzing the impact load versus output voltage the sensitivity constant (usually defined as volt (V)/newton (N) for materials with linear piezoelectric behavior) is determined. This calibrated sensitivity constant is used to estimate the cavitation impact loads from the output voltage readings of the pressure sensors. Once the output voltage signal of the transducer is recorded, it is required to filter out the background noise from the actual cavitation impact events. Different algorithms can be used, the use of a threshold value of amplitude (such as 0.8 V used in Fig. 1.6) is the simplest one.

As the present thesis is intended to present a new method of estimating cavitation impact loads, the details regarding the calibration technique, signal processing or other types of pressure transducers are not discussed further in this thesis.

1.3.3.2. Estimation by nanoindentation approach

After Knapp [8,69,70] in 1950s, cavitation pitting test has gained a lot of interest especially for characterizing the cavitation flow intensity. Carnelli *et al*. [67,68] have proposed a new indirect method for estimating cavitation impact loads by using cavitation pitting tests along with the theory of nanoindentation and materials constitutive laws. This method is discussed here in details since our study is also aimed towards the use of cavitation pitting test to measure the impact loads and their radial extent.

Cavitation pits are generated on metallic alloys by conducting pitting tests in a high speed cavitation tunnel. Surface of the test samples were mirror polished before the tests were done in order to enable better/clear recordings of cavitation impact events. Each pit printed on the surface is considered to be resulted from an individual bubble collapse. The individual cavitation pit shape is then compared with the indent shape of a spherical indenter, as shown schematically in Fig. 1.15. For spherical indentation, the equivalent true strain (ε) is given by the Tabor's [77] empirical relationship as Eq. (1.4).

$$\varepsilon = 0.2\frac{a_c}{R_{ind}} \tag{1.4}$$

Here, a_c is the indentation contact radius and R_{ind} the indenter radius.

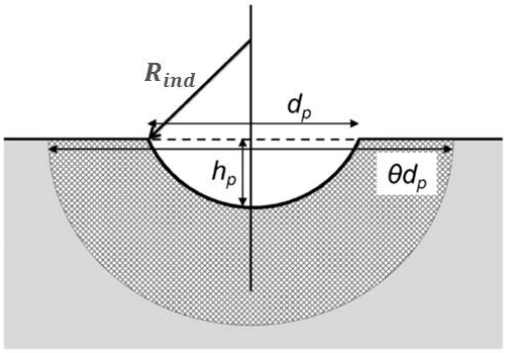

Fig. 1.15 Schematics of spherical representation of cavitation pits. The extended region beneath the pit is a qualitative representation of plastically deformed region [67]. *Here d_P and h_P represent pit diameter and depth respectively.*

From the geometrical relationship as presented in Fig. 1.15, for cavitation pit $a_c = d_P/2$ and R_{ind} is related to pit depth and diameter as given by Eq. (1.5).

$$R_{ind} = \frac{(d_P/2)^2 + (h_P)^2}{2h_P} \tag{1.5}$$

In order to compute the plastic strain, Eq. (1.4) can be written as Eq. (1.6) and, the authors in [67,68] referred this computed strain, (ε_P), as the '*pitting strain*'.

$$\varepsilon = \varepsilon_P = 0.2\frac{h_P d_P}{(d_P/2)^2 + (h_P)^2} \tag{1.6}$$

Further simplifying Eq. (1.6) for cavitation pits where the pit depth is usually smaller compared to the pit diameter, the pitting strain can be estimated as given by Eq. (1.7).

$$\varepsilon_P \approx 0.8\frac{h_P}{d_P} \tag{1.7}$$

Now, by using the constitutive law of the material on which the pitting tests were done, the stress σ_P corresponding to pitting strain ε_P can be estimated. The estimated value of stress σ_P is considered, by the authors, to be a relevant estimate of the cavitation impact stress. It should be mentioned that neither Tabor's equation (Eq. (1.4)) is universal and could be used unambiguously, nor the spherical representation of the cavitation pits is fully justifiable. Moreover, the estimated stress, so called '*impact stress*' or '*pitting stress*', may not necessarily correspond to the maximum stress generated during the cavitation bubble collapse as highlighted in [67]. This point is also investigated in the current thesis and explained in details in Sec. 2.3 in Chapter-2. Finally, this method does not provide the actual radial or spatial extents of the impact loads realized by the targeted material surface. Instead, as often done, the pit diameters are considered as the radial extents of the impact loads, which may not be true as the values will depend both on the shape of the applied loads and on the elastic recovery of the tested material.

Despite having these ambiguities, the proposed method is interesting as it represents a thought slightly out of track of using pressure sensors and may also encourage other researchers to think of other possible ways of

estimating cavitation impact loads. The current research is strongly motivated by this work and intended for improvement.

1.3.3.3. Other popular methods for estimation of impact loads

- There exist several others methods as well. Many researchers [19,26,27] have utilized hydrophones to estimate cavitation impact loads generated from cavitation bubble collapse. By listening the sound of shock wave that is produced during each bubble collapse, which is nothing but a propagating pressure wave, the hydrophone measures the impact load. A hydrophone is also a transducer that transforms acoustic waves into an electric signal, but mainly dedicated to capture the impact loads due shock waves. But when a cavitation bubble collapses near a solid boundary, which is more severe, the direct impact load produced by the high velocity micro-jet plays a more important role than the shock waves. Indeed, in this type of collapses the shock waves are weak due to the asymmetrical or non-spherical shape of the collapse. Thus hydrophones may not provide a real signature of the impact loads.

- A large number of researches is being conducted in the field of fluid engineering, few examples cited here are [78–80], where particle image velocimetry (PIV) technique is being utilized to measure instantaneous spatial distribution of pressure in a flowing liquid. The principle of the method is based on measurement of distribution of material acceleration and then integrating them to obtain the local pressure distribution in a flowing fluid. For this purpose, high resolution cameras with high frame rates are generally used to capture the instantaneous positional distribution of the fluid material. There is a great potential for such techniques to be implemented in the future for measuring the spatial and temporal evolution of cavitation impact loads in a cavitating flow. However, a major difficulty to implement this technique for a cavitating flow is that the solid wall on which the impact loads are to be measured needs to be transparent and cavitation damage resistant.

- Another most commonly used method for estimating the cavitation intensity is computational fluid dynamics (CFD) simulation. As CFD simulation is out of scope of the present study, this is not explained here in details. Rather a brief introduction along with some interesting publications are reported. Many authors, a few examples are [26–28,81–86], have done an extensive research on the numerical simulation of cavitation bubble collapse in a static or dynamic flowing fluid.

  Many researchers like Chahine [81], Hsiao *et al*. [28] and Jayaprakash *et al*. [27] have been developing a two-way coupled fluid-structure interaction (FSI) method to simulate cavitation bubble collapse near a deformable solid boundary. Attention is paid on the mechanism of bubble collapse to capture the relevant physics of the fluid-structure interaction, with special emphasis to capture the impact loads generated during the bubble collapse. To accomplish the goal they couple different numerical solvers:- the boundary element method code 3DYNAFS-BEM (an incompressible flow solver), the finite difference method code GEMINI (a compressible flow solver) and the finite element code DYNA3D for simulating the material's dynamic behavior. But these researches are mainly focused on a single bubble collapse, where the initial bubble size is predefined as well as the temporal variation of ambient pressure in the liquid medium. But

in real flows, the location and initial size of such a bubble, along with the local pressure gradient and possible interaction with neighboring bubbles which affect the impact pressure are not known.

Bubble collapse in reality may not necessarily always be driven by the ambient pressure variation, it could well be driven by the interaction with shock waves generated from the neighboring bubble collapses. Johnsen & Colonius [26] and Johnsen [82] have been developing numerical methods and tools to simulate shock-induced bubble collapse as well as Rayleigh bubble collapse where, as stated by them, the collapse is driven by the pressure difference between the bubble and the liquid. These studies are also mostly focused on a single bubble collapse to estimate the impact loads and their effect on cavitation erosion. This type of study is very encouraging and suitable to explain the mechanism of a static bubble that undergoes a violent collapse under the collision with a traveling shock wave, such as utilized in shock-wave lithotripsy to break kidney stone. However, these studies did not consider any fluid-structure interaction and the impact loads were estimated numerically on a rigid surface. For all these simulations, the initial bubble size, distance from the solid surface and properties of the incident shock waves must be predefined.

The authors in [85–87] have developed a density based 3D finite volume method flow solver CATUM (CAvitation Technische Universität München) that can simulate cavitation phenomena in a flowing fluid around real geometries like hydrofoil or high speed cavitation tunnel. The fluid can be defined as a homogeneous mixture of liquid and vapor (of given volume fraction), or liquid filled with cluster of bubbles. CATUM takes into account the coalescence and formation of bubbles or clouds of bubbles whose collapse is interpreted in terms of resulted shock waves. The method does not take into account the formation of micro-jets (that is considered to be the dominating factor for cavitation erosion) nor the fluid-structure interaction. However, the method is very encouraging and could be used for the prediction of cavitation prone zones of a solid structure such as ship propellers, pipes, gear pumps etc. Although this method has some intrinsic limitations, the distribution of impact loads due to shock-waves generated by bubble collapses, their location and loading duration etc. that are essential to characterize the flow aggressiveness can be estimated reasonably well.

There is a large number of papers or books available in the literature addressing all aspects of cavitation erosion based on numerical approaches like computational fluid dynamics (CFD) simulations. Significant improvements have also been made over the years especially to simulate multi-phase flow behaviors (such as the flow around hydrofoils [87]), finding out critical locations of cavitation erosion prone zone (such as for ship propeller blades, [88]), estimating impact pressures due to cavity collapses (such as in a high speed cavitation tunnel [86]) and so on. However, as stated above, well established and validated models or methods are not yet available. Such a realistic model should take into account all the physics involved in the mechanism of cavitation bubble collapse, such as the fully multi-scale modeling in both space (for representing bubble of all possible sizes) and time (for capturing all possible impact durations), multi-phase fluid, bubble-bubble interaction, bubble-shock wave interaction, viscosity, surface tension, gas content, compressibility and bubble-structure interaction that requires coupling between solid and fluid

dynamics and so on. Thus the problem is very complex; moreover, it is always difficult to accurately define the nuclei distribution, locations and initial sizes in the liquid.

1.4. Cavitation erosion and mass loss prediction

1.4.1. Introduction

Cavitation erosion is the removal of material from the surface when exposed to a cavitating flow environment. It occurs due to repeated impact loadings caused by cavitation bubble collapses. It is often observed on ship propeller blades as shown in Fig. 1.5(b) and thus received a lot of attention from the marine industries. As explained in Sec. 1.1.4, strain accumulation under repeated cavitation impact loadings leads to damage and material loss with time. Cavitation erosion has extensively been studied by many researchers [32,42–46,64] as it gives reliable information about cavitation erosion resistance of a material, which is very important for design and life or performance prediction of hydraulic machineries. Moreover, metallurgical analysis of the eroded specimen provides useful information about the damage mechanism and helps in developing new materials more resistant to cavitation erosion.

There are different testing methods available as discussed in Sec. 1.2 and some of them are standardized and some are not. There are many quantities or terminologies used to interpret cavitation erosion test data [57–59]. The main result of cavitation erosion test is however the evolution of mass loss with respect to time, which shows different distinct regions (as shown in Fig. 1.12) depending on the target material, test fluid and test apparatus and condition etc. Another very commonly used term to quantify cavitation erosion is the mean depth of erosion (MDE) [45,89,90] with respect to time. The MDE is calculated from mass-loss by dividing with the material density and exposed surface area of the test specimen [57–59,91]. Mass loss or material removal starts just after the incubation period. The estimation of the incubation period (or nominal incubation period) is important, as correlations have been developed between mass-loss in the steady-state period and incubation time [90,92], which in other words provide an estimation of life of a component before any significant amount of mass-loss occurs. The extent of the incubation period itself could be used as an indicator of materials resistance to cavitation erosion. However, comparative analysis of cavitation erosion results of different materials is usually recommended to be done in terms of exposure time required to reach a given level of cavitation erosion or MDE, the vice-versa (i.e. constant duration tests) would not be meaningful as different materials have different incubation periods.

Prediction of cavitation erosion has been a challenging issue as it encounters with different aspects of fluids and solids like- hydrodynamics, solid mechanics, chemical and metallurgical behaviors etc. Taking into account all these factors is essential to establish a life prediction model, but often difficult mostly because of their complex interactions. For example cavitation erosion of 316 stainless steel (a nuclear grade material) in mercury is 3-7 times higher than that in water [91], which is believed to be related to the higher density of mercury but not fully understood, because adsorption of liquid onto the metal surface or Liquid Metal

Embrittlement (LME) like phenomenon (of solid structure assisted by the tri-axial state of stress generated due to cavitation impacts) may also play a role especially for mercury [90]. Sometimes it is also difficult to quantify some environmental or chemical factors to be considered into such predictive model. Thus many researchers have been developing simplified correlative empirical, phenomenological or other models to predict cavitation erosion resistance.

1.4.2. Different methods of cavitation erosion prediction

1.4.2.1. Correlative empirical methods

Because of the complexity of cavitation erosion, correlative empirical methods are preferably being used by industries. The empirical methods generally focus on *conducting cavitation erosion test* on a material using a laboratory test apparatus. Then *classifying materials* as per their erosion resistance and *correlating with classical mechanical properties* such as hardness, yield strength, resilience or toughness etc. There are also empirical methods that do not consider any classical material property: erosion resistance is then correlated with cavitation pitting rate or flow aggressiveness [74,90,92] that is obtained by cavitation pitting tests. However it should be mentioned that pitting rate does depend on material strength. In addition, the definition of the flow aggressiveness is not unique since it could be pitting rate, distribution of impact loads, cumulative impact force and so on. Finally, *establishing scaling laws* for transposing the empirical laws from model to prototype [6]. There are numerous empirical methods available in the literature; some of them are discussed here to have a general overview.

Hattori [93] has provided a review of cavitation erosion test results conducted on a large number of materials using standardized test methods (ASTM G32 and G134) at the University of Fukui, Japan since more than 40 years. He found a linear relationship (on log-log scale) between the erosion resistance of metallic alloys and the Vickers hardness (HV), as shown by Eq. (1.8). The erosion resistance is then defined as the inverse of the maximum of mean depth of erosion rate ($MDER_{max}$) of a given material.

$$MDER_{max}^{-1} = 2.6 \times 10^{-7} \times HV^{2.4} \tag{1.8}$$

The constants: coefficient 2.6×10^{-7} and exponent 2.4 are almost indifferent for all the materials tested under standard test condition (ASTM G32). However, for materials that have high work hardening effect, the hardness value should be calculated from the eroded sample.

Okada *et al*. [94] have developed a pressure transducer mounted with test specimen that enables simultaneous recordings of impact forces and erosion damages (indent size or volume loss) due to cavitation bubble collapses. By correlating the impact loads with indent sizes in decreasing order of magnitudes, an empirical relationship between cumulative volume loss and cumulative impact energy has been established, which is linear in nature and independent of test apparatus and test condition. Although the arbitrariness in correlating impact loads with indent size could be argued, the method provides a simple way to predict cavitation erosion based on the measurement of cavitation impact loads.

Futakawa *et al*. [90] have developed an experimental technique called Magnetic IMpact Testing Machine (MIMTM) to study the cavitation erosion behavior of materials, where the target specimen which is in contact with the test liquid in a closed chamber is cyclically impacted to produce cavitation bubbles that collapse subsequently. Their device is designed to study the cavitation erosion of a solid container of mercury in a high intensity neutron beam generator. Cavitation erosion occurs when the liquid mercury in the solid container is bombarded with a high energy proton beam. By conducting experiments on various materials for a large number of mechanical impacts (N_{imp}) of about 10^7 cycles, a linear relationship (on log-log scale) between mean depth of erosion (MDE) and N_{imp} has been verified, as given by Eq. (1.9).

$$\log(MDE) = A\log\left(N_{imp}\right) + B \tag{1.9}$$

Where, A and B are constants. A = 1.27 for mercury and does not depend on the material, and B is representative of the incubation period that depends on the material surface property, temperature, imposed pressure amplitude of the impacts etc.

The authors probably took advantage of almost similar observations made by Kass *et al*. [91], for which a polynomial relationship between the erosion rate (with respect to the steady state region) of stainless steel in mercury and the power applied to a vibratory test apparatus has been established whereas a linear relationship was found for water as the test liquid.

Motivated by these findings, Futakawa *et al*. [90], Soyama and Futakawa [92] have conducted cavitation erosion tests on a variety of materials (pure metals, metallic alloys, polymers and ceramics) using two types of test apparatus: the cavitating liquid jet and the rotating disk. They found that all the plots of non-dimensional mass loss (Δm) vs. non-dimensional exposure time (Δt) within the steady sate periods follow a unique linear behavior on a log-log scale, irrespective of the materials and test apparatus being used. Thus, they modified Eq. (1.9) and proposed the following Eq. (1.10), which is more convenient to interpret cavitation test results.

$$\log(\Delta m) = A'\log(\Delta t) + B' \tag{1.10}$$

Where, A' and B' are constants having the same meaning as A and B. The constant $A'$is A'= 1.3 for deionized water and tap water.

Eq. (1.10) provides the ability to predict the cavitation erosion resistance in terms of the incubation period. The incubation period can be estimated from a single test data of mass loss vs. exposure time by fitting Eq. (1.10) with the known value of A'(= 1.3 for water). The intercept on the time axis would be the measure of incubation time.

Hattori *et al*. [74] have proposed a different method to predict the cavitation incubation period based on the measurement of cavitation impact forces. Cavitation erosion is considered to be a fatigue phenomenon (as discussed in Sec. 1.1.5) where a relationship between the impact force and the number of impacts at failure is represented by the following Eq. (1.11), similar to the Basquin equation commonly used to represent the fatigue behavior of a material in terms of stress amplitude and number of cycles at failure.

$$F_i^{\alpha} N_i = C_1 \tag{1.11}$$

Where, N_i is the number of impacts at failure for impact force of F_i amplitude, and α and C_1 are two empirical constants depending on material. In Eq. (1.11) impact force is considered instead of impact stress, as the latter one cannot be measured accurately in cavitation pitting test due to unknown impacted area and distribution. Number of impacts at failure N_i is assumed to correspond to the end of the incubation period after which mass loss occurs. Then, under repeated amplitude of loadings the erosion damage is given by the Miner's linear cumulative damage law as given by Eq. (1.12).

$$D = \sum \frac{n_i}{N_i} \tag{1.12}$$

Where n_i is number of impacts at an amplitude of F_i . It should be emphasized that none of the standard test methods for cavitation erosion (ASTM G32 and G134) can produce impacts of constant force, thus N_i corresponding to a given level of F_i cannot be estimated experimentally. However, use of controlled single bubble collapse (such as spark or laser generated bubble) in a cyclic manner until damage is observed remains to be a subject of future research.

Now if n_i is defined as number of impacts per unit time, $\sum n_i/N_i$ gives a measure of cumulative damage per unit time. At the end of incubation period (t_{incb}) when $D = 1$, total damage is $t_{incb} \times \sum n_i/N_i$. Thus, Hattori [74] proposed the following Eq. (1.13) to estimate incubation period.

$$t_{incb} = \frac{1}{\sum n_i/N_i} \tag{1.13}$$

Substituting Eq. (1.11) for N_i in Eq. (1.13), they further improved the prediction model as the following Eq. (1.14).

$$\frac{1}{t_{incb}} = \frac{1}{C_1} \sum (F_i^{\alpha} \times n_i) \tag{1.14}$$

The incubation period for a given material can be predicted by using Eq. (1.14) if the constants C_1 and α are known. These constants can be determined by trial-and-error method by conducting cavitation tests at different conditions such as two different flow velocities that would provide the values of t_{incb} , n_i and F_i.

As presented above all these empirical methods for prediction of cavitation erosion are based on experimental data obtained under a particular type of experimental conditions. These types of models provide information for the transposition of erosion resistance from one velocity to another, one fluid to another etc. But the transposition from model test to prototype or real geometry is not yet fully established and remains a great challenge.

1.4.2.2. Phenomenological models

Another popular method of cavitation erosion prediction is based on phenomenological models. There are many models proposed by different authors, a few of them are: Karimi and Leo [95], Kato *et al*. [96], Berchiche *et al*. [97]. The phenomenological models proposed by Karimi and Leo [95], Berchiche *et al*. [97] and Franc

and Michel [6] consist in different parameters that account for different phenomena associated with cavitation erosion both from the material and fluid sides, hence discussed in details below. Kato *et al*. [96] have presented a similar scenario to predict cavitation erosion without model test, by estimating the distribution of impact forces/pressures based on some empirical relationships for the generation rate of cavities.

The model of Karimi and Leo [95] simplified by Franc and Michel [6] is applicable in the steady state region of cavitation erosion. It assumes that the cavitation impacts of magnitude lower than the yield strength (σ_Y) do not lead to any strain accumulation or damage. The long term effect of those impacts, cannot be considered by this model which does not account for the High Cycle Fatigue damage. Under the impacts of higher magnitude ($>\sigma_Y$), the material undergoes plastic deformation and when the accumulated plastic strain reaches the rupture strain (ε_R) corresponding to the rupture stress (σ_R), a complete damage resulting in material removal is assumed.

To take into account the fluid effect, the flow aggressiveness is defined by three parameters: a mean value of the impact stresses (σ_{mean}), a mean value of the impacted areas (A_{mean}) and their rate ($\dot{N}$) per unit time and unit surface area. Thus, the random amplitudes of impact stresses and pit areas are not considered in the model, and only mean values are taken for simplicity. These flow parameters can be estimated by using pressure transducers along with the target material.

The time required (t_{cov}) for such a mean impact load of (σ_{mean} , A_{mean}) at a rate of $\dot{N}$ to completely cover the material surface is $1/(\dot{N}A_{mean})$. This is called one cycle time, after which a layer of the material is considered to have hardened uniformly. The strain profile into the hardened layer is given by the following Eq. (1.15).

$$\varepsilon = \varepsilon_s \left(1 - \frac{x}{L}\right)^{\theta} \tag{1.15}$$

Where, ε_s is the strain at the surface of the material, x indicates distance or depth from the surface, L is the thickness of the hardened layer and θ is a measure of the steepness of the hardening gradient.

After each cycle time or each complete coverage, the thickness of the hardened layer will increase. Thus values of ε_s and L will increase continuously following the same strain profile until damage is initiated at the surface. Once damage is initiated the thickness of the hardness layer (L) will remain constant. Now considering that the plastic strain varies from zero (0) to the rupture strain (ε_R) in the thickness L, and in the steady-state period the material is being subjected to a mean impact load of (σ_{mean} , A_{mean}) eroding ΔL thickness of the material from the surface, the strain profile Eq. (1.15) would give-

$$\varepsilon_R = \varepsilon_{mean}\left[1 - \frac{\Delta L}{L + \Delta L}\right]^{\theta} \tag{1.16}$$

In the above Eq. (1.16) $\varepsilon_{\text{mean}}$ represents the value of the strain on the surface of the removed layer which corresponds to σ_{mean}. Now the thickness of the eroded layer can be estimated as-

$$\Delta L = L\left[\left(\frac{\varepsilon_{\text{mean}}}{\varepsilon_R}\right)^{1/\theta} - 1\right] \tag{1.17}$$

If the material is considered to follow a Ludwik's type constitutive behavior as given by Eq. (1.18),

$$\sigma = \sigma_Y + K\varepsilon^n \tag{1.18}$$

where, K and n are the strain hardening coefficient and strain hardening exponent of the material respectively, then we can deduce the following Eq. (1.19) from Eq. (1.18).

$$\varepsilon_{mean} = \varepsilon_R\left(\frac{\sigma_{mean} - \sigma_Y}{\sigma_R - \sigma_Y}\right)^{1/n} \tag{1.19}$$

From Eq. (1.17) the thickness of the eroded layer can be estimated as-

$$\Delta L = L\left[\left(\frac{\sigma_{mean} - \sigma_Y}{\sigma_R - \sigma_Y}\right)^{1/n\theta} - 1\right] \tag{1.20}$$

Erosion rate, in the steady-state region, in terms of mean depth of penetration rate (*MDPR*) or in other words volume loss per unit surface area of the material is given as Eq. (1.21).

$$MDPR = \frac{\Delta L}{t_{cov}} = \dot{N}A_{mean}L\left[\left(\frac{\sigma_{mean} - \sigma_Y}{\sigma_R - \sigma_Y}\right)^{1/n\theta} - 1\right] \tag{1.21}$$

The parameters L and θ can be estimated from micro-hardness measurements.

This model represents very well the shape of the mass-loss vs. time or erosion rate vs. time curves but a large discrepancy has been observed between experimental and predicted values [95]. Given the complex mechanism of cavitation erosion the discrepancy is not very surprising. Moreover, many important phenomena like dynamic behavior of the material, strain rate sensitivity and fatigue aspect etc. have not been included into the model. The strain profile (Eq. (1.15)) used to describe the hardening behavior of the material assumes that the maximum stress or strain occurs at the surface of the material and decreases with depth. Whereas, numerical simulation of cavitation pitting (as shown in Fig. 1.8 under Sec. 1.1.5) shows maximum stress or strain occurs at the subsurface region into the material. This inconsistency would also lead to some error.

Berchiche *et al*. [97] have proposed almost a similar model, but, unlike a mean value for the impact stresses and diameters these values were calculated analytically from the pit geometries by using the hardening profile (Eq. (1.15)) and materials constitutive relationship. But their model also suffers from the poor predictability of cavitation erosion.

There are many more models like [98–100] that represent different phenomenological approaches to predict cavitation erosion. The models, Steller [98] and Steller and Kaczmarzyk [99], take into account mainly the material parameters like Young's modulus, ultimate strength, and some other parameters related to the cavitation resistance of materials. The model of Dular *et al*. [100] explains the different physical phenomena like cavitation cloud implosion, pressure wave emission and its attenuation, micro-jet formation and finally pit formation involved in cavitation erosion. Despite continuous effort since many decades and the large number

of models that have been developed, it is very difficult to include all the phenomenological aspects into a single model to predict cavitation erosion, and hence none of these models can accurately predict cavitation erosion that might occur in a real situation. This remains a challenging issue till date.

1.4.2.3. Numerical methods

There are different numerical approaches sought by many researchers to predict cavitation erosion. A fully predictive computational method that takes into account the fluid-structure interaction and simultaneously solves fluid dynamics and solid dynamics phenomena by a two-way coupled approach would have been the ideal one. Ideally, such a model could be applied to a real industrial case such as a propeller. Although numerous studies have been conducted by many authors (as discussed in Sec. 1.1.5) to understand the damage mechanism of cavitation erosion, most of them were focused on metallurgical or microstructural aspects. Less attention has been paid to understand the damage mechanism from the solid mechanics point of view. This would imply first to identify reliable hardening laws taking into account the strain rate effect and also to establish a damage initiation and evolution criteria as well. However, as mentioned in Sec. 1.3.3.3, numerical studies of cavitation are mostly focused on identifying the locations of erosion prone zones in a flowing fluid around a solid structure (generally considered as a rigid body). Although, coupled fluid-structure approaches with deformable solid have also been developed, they are mostly limited to single bubble collapse for the time being. Given these limitations, researches have been developing alternative numerical or semi-numerical methods to predict cavitation erosion. As an example one such model is discussed in below.

Patella *et al*. [44,64,101] have developed a numerical tool based on the finite element method that simulates cavitation erosion with the number of impacts especially dedicated to capture the incubation period. However the tool, for the time being, is limited to a two dimensional (2D) axisymmetric frame-work. Their one dimensional cavitation damage model seems to be encouraging as it represents a different view towards the cavitation erosion damage modeling. In their model cavitation damage is attributed to the repeated impact loading caused by the high intensity shock waves due to cavitation bubbles collapse. The characteristics of impact loadings were obtained from pit geometries (obtained by pitting test) using the following simple relation (as shown by Eq. (1.22)) they established.

$$E_{wave} = C_2 V_{pit} \tag{1.22}$$

Where, E_{wave} is the energy of the incident shock wave, V_{pit} is the volume of resulted pit and C_2 is a material constant. For 316L stainless steel $C_2 = 24$ J/mm^3.

They have adopted an energy based fatigue criterion to model cavitation damage, which assumes that after each impact the material stores an amount of energy (ΔE, defined as the increment of internal energy density). Failure is supposed to occur when the accumulated energy, after a particular number of impacts (say N_r), reaches a critical value. The relation between N_r and ΔE is represented by a Basquine type equation as given by the following Eq. (1.23).

$$\Delta E \times N_r^{\beta} = C_3 \tag{1.23}$$

Where, β and C_3 are constants that depend on the test material.

Considering Miner's linear cumulative damage law and assuming damage accumulates evenly with repeated cavitation impacts of given amplitude, the damage increment (ΔD) is given by the following Eq. (1.24).

$$\Delta D = 1/N_r \tag{1.24}$$

In case of impact loadings of variable amplitudes that exist in real flow, the above equation can be written in general form as Eq. (1.25), where i is used to indicate repeated loadings of different amplitudes and N_i is the number of impacts at failure corresponding to a particular load level.

$$\Delta D = \frac{1}{N_i} = \left(\frac{\Delta E}{C_3}\right)^{1/\beta} \tag{1.25}$$

Thus when the total damage ($\sum \Delta D$) at a point reaches 1, the material is assumed to fail at that particular location. Patella *et al*. [44] have proposed a relationship (Eq. (1.26)) to estimate the maximum ΔE_{max}.

$$\Delta E_{max} = \frac{\eta \bar{\gamma} E_{wave}}{10 L'^3} \tag{1.26}$$

The parameter η depends on the pressure wave and defines the fraction of impacted shock-wave energy utilized for plastic deformation to form a cavitation pit. The parameter L' is related to the distance between metal surface and the source of the shock wave emission. The correction factor ($\bar{\gamma}$) accounts for cyclic hardening or softening behavior of a material with number of impacts as commonly observed in fatigue. It is given by:

$$\bar{\gamma} = \frac{\Delta E_{max}(n)}{\Delta E_{max}(1)} \tag{1.27}$$

Where, $\Delta E_{max}(n)$ stands for maximum increment of internal energy density after n impacts and $\Delta E_{max}(1)$ stands for maximum increment of internal energy density after 1 impact.

Using the above mentioned method, the statistical population of the impact loads in a cavitating flow can be obtained by pitting test results (mainly pit volume and radius). These in turn can be used to simulate the mass loss with time, using Eq. (1.26) to estimate increment of internal energy density, from which damage increment can be estimated by using Eq. (1.25).

The main limitations of this method are: till now the model is limited to a 2D axisymmetric configuration and experimental methods (or data) for the parameters (like η, C_2 and L') related to the model are still not available. Moreover, in reality cavitation erosion occurs due to repeated impacts variable amplitudes at random locations on to the 3-dimensional surface of the test specimen.

In Sec. 1.4 various methods of cavitation erosion prediction have been discussed and associated limitations and difficulties have also been highlighted to have a general overview of the state-of-art. As can be understood cavitation erosion and its prediction is a complex subject that required multi-disciplinary approach and remains a big challenge since many decades. In this thesis we propose a new method to numerically simulate cavitation

erosion with time using cavitation pitting tests and finite element simulations of the material behavior. Initially, the cavitation flow aggressiveness, defined as the statistical distribution of the impact loads generated by the cavitation bubbles collapses, has been obtained from the cavitation pit geometries. However, the method used for the impact loads determination strongly differs from what has been published up to now (see discussion in Sec. 2.5 in Chapter-2). Then those estimated impact loads are applied repeatedly at random locations onto a 3D material surface to simulate mass-loss with time as discussed in Sec. 5.4 in Chapter-5. Complete dynamic behavior of the material, which includes inertial and strain rate sensitive effects, has been taken into account in the numerical simulation. The purpose of this method is to capture the incubation period as accurately as possible. Although the fluid-structure interaction is not considered into the modeling, simulation of advance stages of erosion like steady-state period could be possible. Simulation of more advance stages like attenuation period, where the erosion rate decreases with time due to the modification of the specimen surface topology that alters the aggressiveness of a cavitating flow, may not be possible. Given the complexities involved in fluid-structure interaction simulation for cavitation erosion prediction, our proposed method provides a simple frame-work to predict cavitation erosion only by simulating the material response to a statistical population of impact loads derived from pitting tests.

1.5. Aim of the thesis

The ultimate goal of the present research is numerical prediction of cavitation erosion with time. As discussed above in Sec. 1.1 to Sec. 1.4, cavitation erosion is a complex phenomenon and for the time being numerical prediction of erosion including fluid-structure interaction is out of scope. In this thesis focus is made on the response of the material to a statistical population of cavitation impact loads supposed to represent the cavitation erosion potential of the fluid. Thus it is required first to estimate the impact loads due to cavitation bubbles collapses in a cavitating fluid, that are difficult to measure accurately using transducers or to compute numerically using computational fluid dynamics (CFD) simulations. In this thesis a new technique is proposed that is based on cavitation pitting tests and numerical finite element simulations. The aim is to use the target material as a pressure sensor. Pitting tests are aimed at generating cavitation pits that are characteristics of the cavitation impact loads due to bubbles collapses. The dimensions of the cavitation pits are related to the constitutive behavior of the target material and the level of the applied impact load. Now if we can numerically reproduce each cavitation pit with a representative pressure field relevant to the bubble collapse pressure field, then we have access to the cavitation impact loading condition. The representative pressure field used here is assumed to have a Gaussian type of distribution both in space and time. This inverse method is reliable provided the material properties are characterized properly.

The primary aims of the thesis can be outlined as follows-

1. Better characterization of cavitation pits obtained by cavitation pitting test in order to overcome the dependency of pit diameters on the choice of the arbitrary cut-off depth usually used to avoid surface roughness effect on the measured pit dimensions.

2. Numerical study of cavitation pitting/erosion based on single impact and multiple impacts. Analyzing both static and dynamic aspects of the material behavior under a loading condition similar to that of hydrodynamic impact loading caused by a cavitation bubble collapse.
3. Estimation of cavitation impact load corresponding to a cavitation pit. In other words to develop a numerical inverse method based on finite element simulations, where the input parameters would be the cavitation pits obtained by pitting test and the output results should be the corresponding impact loads and their radial extents.
4. Answering the crucial question of this thesis: whether the target material in cavitation pitting itself can be used as pressure sensor or not. For that purpose different materials will be used as pressure sensors to get material independent response under a given cavitation flow condition.
5. Characterization of the material properties. This step is required for accurately estimating the impact load from the cavitation pit geometry. Cavitation impact is a very dynamic phenomenon that occurs for a very short duration of time in a confined region at a very high level of pressure. Thus the characterization requires special attention.
6. Once the statistical distribution of impact loads corresponding to cavitation pits is obtained, the aim is to apply those impact loads repeatedly and randomly on to a 3D solid surface to track the mass-loss with time.
7. Understanding the mechanism of damage accumulation in cavitation pitting. The final step is required for accurate modeling of mass loss with time.

The above-mentioned items were the primary aims of the thesis. However, the thesis deals with more aspects of cavitation pitting or erosion and provides some conclusions on different issues/questions that came across during the progress of the work:

(i) Especially, some microstructural analyses were done to answer a question, which existed for a long time, related to the erosion resistance of the materials considered for the current study. The question was: “Why Aluminum alloys A2206 is more sensitive to cavitation damage than stainless steels or bronze alloys whereas its load-displacement curve is above that of the other two materials?”

(ii) In order to answer Item 5 on the material characterization, we have conducted dynamic explicit analysis of cavitation pitting including strain rate sensitivity of the materials, which is very rare in literatures related to cavitation erosion. This, provided a unique description of cavitation pitting mechanism based on natural frequency analysis of the material volume affected by cavitation pitting. Aim here is to understand the effect of material inertia and strain rate sensitivity towards the mechanism of cavitation pitting/erosion.

1.6. Some highlights and remarks

Some highlights of the chapter:

- Cavitation occurs only when mean pressure of fluid at high velocity falls below a critical value.
- Cavitation bubble collapse leads to formation of micro-jets and shock-waves along with a translational movement towards solid boundary. All these result in a high impact loading to the solid wall.
- Intense collapse of a cavitation bubble leads to the formation of a cavitation pit on the solid wall, if the local stress into the material exceeds the yield strength.
- Cavitation pits are plastically deformed localized regions on the solid surface.
- Repetition of cavitation impacts lead to fatigue type damage accumulation, failure and mass-loss.
- Cavitation pitting tests and cavitation erosion tests are usually done to determine cavitation erosion resistance of a material.
- However various testing methods are in use, ASTM-32 and ASTM-134 standard testing methods.
- High speed cavitation tunnel is used in the current study.
- Measurement of cavitation impact loads is important for cavitation erosion prediction.
- Transducers are commonly used to estimate impact load, but results are not error-proof.
- An alternative method to the estimate impact loads is presented in this thesis.
- Empirical methods are commonly used for cavitation erosion prediction in industries, but the scaling laws to transpose the prediction method from model to prototype are not well established.
- A numerical technique is proposed in the current thesis for prediction of cavitation erosion.

Remarks:

In this chapter (Chapter-1) a brief literature review is provided to understand the contents of the thesis. The subsequent chapters deal with the objectives presented in Sec. 1.5. Each chapter deals with one or more of the objectives. The problem definition, adopted methodology to deal with the problems or objectives under consideration, main results and discussion of the investigations, and summary and conclusions etc. have been presented separately in the end of each chapter. Irrespective of the chapter of reference, all the appendices are provided in the end of the thesis.

Chapter-2

2. An inverse finite-element method for estimating cavitation impact loads from pitting tests– Static approach

This chapter contains the results of a journal paper [2] accepted for publication in Wear whose details are given below. However, additional data and results are given here which could not be included in the paper.

Determination of cavitation load spectra – Part 1: Static finite element approach

Samir Chandra Roy[a,1], Jean-Pierre Franc[b], Christian Pellone[b], Marc Fivel[a]

[a]Science and Engineering of Materials and Processes (SIMaP-GPM2), University Grenoble Alpes/CNRS, F-38000 Grenoble, France
[b]Laboratory of Geophysical and Industrial Flows (LEGI), University Grenoble Alpes/CNRS, F-38000 Grenoble, France

Abstract

Numerical prediction of cavitation damage strongly relies on the determination of the loading conditions applied to the wall. In this paper, an inverse method is proposed to identify the pressure field that could generate individual pits as observed experimentally on eroded samples of Aluminum alloy 7075-T651. The pits are defined by the diameter and depth of the imprints. Assuming each pit was generated by a single bubble collapse, the pressure load is defined by two parameters, the peak pressure (σ_H) and its radial extent (r_H). Two methods are proposed based on finite element modeling. The first one uses analytical expression of the unknown parameters built from a parametric simulation campaign. The second one is based on an optimization loop of the finite element simulations to best fit the experimental measures for a given error limit. Both methods give access to the load distributions relevant to the flow aggressiveness of the cavitation test.

Keywords: Cavitation pitting; Pit dimensions; Hydrodynamic impact parameters; Analytical inverse method; Numerical inverse method

[1] Corresponding author:
E-mail address: roysam.nita@gmail.com or samir-chandra.roy@simap.grenoble-inp.fr (S. C. Roy)

2.1. Introduction

It is well known that the repeated collapse of cavitation bubbles may erode solid walls [6,102,103]. The collapse of a cavitation bubble is generally associated with the formation of a micro-jet and/or shock waves, which impact the nearby solid surface resulting in a cavitation pit, if the load is high enough to exceed the local yield strength of the material. In order to predict the erosion damage including the long-term damage and mass loss, it is essential to know the loading conditions generated by bubble collapses and analyze the response of the material to these loads.

The determination of the loading conditions due to the combined or solo effect of micro-jet and shock waves during cavitation bubble collapse is a major issue in cavitating flows. Numerical approaches may be used to compute the pressure pulses due to the collapse of a single bubble or bubble clusters that may develop in real flows such as the flow around a cavitating foil or in a cavitating hydraulic device (see e.g. [81,85,87]). The difficulties in such approach arise from the complex fluid-structure interaction and also from the large number of parameters involved on the fluid side such as bubble content, bubble size, distance to the wall, pressure history to which the bubble is subjected, potential interactions between bubbles, etc.

Pressure pulses may also be measured in cavitation facilities. One option is to use pressure transducers flush mounted in the region of bubble collapses. The pressure signal generally shows successive pulses of various amplitudes caused by bubble collapses [38,104,105]. This method allows determination of impact loads in force units (typically in Newton) but the determination of the pressure or stress amplitude (in MPa) is difficult because the loaded surface area is unknown and usually much smaller than the transducer sensitive surface. Moreover, conventional pressure transducers, because of their limited natural frequency, may not capture accurately the cavitation pressure pulses whose rise time and duration are quite small. Finally, the impact could plastically deform or even damage the transducer leading to faulty responses.

In order to avoid these measurement difficulties, another option may be used. It consists in using the material itself as a transducer. The measuring technique is based on pitting tests as introduced by [69,70]. The idea behind pitting tests is that each pit is the signature of a single bubble collapse. Then, it can reasonably be expected that the loading conditions be derived from the geometry of the pit and the material properties.

Such a technique has been used by [67,68]. The authors have taken advantage of the similarity between a cavitation erosion pit and a spherical nanoindentation to estimate the amplitude of the pressure pulse responsible for a cavitation pit. The method is based on the use of Tabor's equation [106] that makes it possible to estimate the mean strain associated to a plastic deformation of given depth and diameter. It is easy to deduce the stress from the estimated strain using the stress-strain relationship of the material.

In the present work, another technique is investigated for deriving the loading conditions from pitting tests conducted during the incubation period. It is based on finite element (FE) computations of the response of the material to a representative pressure pulse. The pressure pulse considered here has a Gaussian shape and is defined by two parameters, namely its maximum amplitude and radial extent. The Gaussian shape profile used

for the FE simulations is found to produce non-dimensional pit shapes that are close to that experimentally observed, as discussed in Sec. 2.4. An inverse technique is proposed to derive these two parameters from the depth and diameter of the pit, both deduced from an appropriate analysis of the pitted surface.

This kind of approach, combining FE simulations and pitting test is relatively new and the authors have noticed only few publications. To our knowledge, such an inverse technique has only been used by Phol *et al.* [49] using a different bell-shape pressure profile into the framework of static FE (no time dependencies) analysis of material response using 2D axisymmetric modeling. We are proposing here a simple and fast technique based on interpolation that optimizes the pressure parameters for given error limits in pit dimensions. Moreover, we show that a given pit shape could be optimized with a unique set of parameters for the assumed pressure profile. Note that in order to simplify the problem, Phol *et al.* [49] have ignored dynamic effect that include inertia and strain rate sensitivity of the material, as we are doing in this current Part 1 study.

The event of cavitation hydrodynamic impact is very dynamic in nature since the impact duration is very short, in the order of a microsecond, as observed experimentally and/or by computational fluid dynamics (CFD) simulation of cavitation bubble collapse [28,48,81,107,108]. In a companion paper ((Part 2) [4] or Chapter-4 of this thesis), we have performed dynamic explicit FE analysis of the cavitation impact using similar Gaussian pressure field with a temporal evolution of Gaussian type. By decoupling the effect of inertia and strain rate sensitivity into the simulation, it was found that for impact duration of 1 μs or more the inertial effect becomes insignificant and, static and dynamic explicit FE analyses yield the same solution in terms of resulted pit dimensions. Similar observation was reported by Choi *et al.* in [48]. However, strain rate effect at such high rate of loading in cavitation pitting cannot be avoided if the material is strain rate sensitive. For more details see [4], where it is shown that for duplex stainless steel (A-2205) which has a high strain rate sensitivity, although inertial effect is negligible for impact durations as small as 1 μs, the dynamic effect associated with strain rate sensitivity is unavoidable till 10^5 μs (or 0.1 s) of impact duration; thus care should be taken as described in [4]. In order to avoid the effects of strain rate in our modeling approach, the current study is conducted on Aluminum alloy 7075-T651 (Al-7075) which has a very weak strain rate sensitivity [3] so that a static approach appears fully appropriate for this particular alloy even for impact durations as short as 1 μs.

As discussed in Sec. 3.2 in Chapter-3, the strain rate sensitivity coefficient of Al-7075 was estimated by using the well-known Johnson-Cook plasticity model, for which compression and Split Hopkinson Pressure Bar (SHPB) tests were done for strain rates ranging from 0.001 to ~2000 s^{-1}, details of which can be found in [3]. A value $C = 0.0068$ for the strain rate parameter was found which demonstrates negligible strain rate sensitivity.

Although in the current study, static analysis was adopted for the inverse FE technique, it is shown in Chapter-4 [4] that this inverse technique could be transposed to dynamic explicit analysis as well and then applied to strain rate sensitive materials by considering the complete dynamic behavior including inertia and strain rate sensitivity. The question of impact duration corresponding to each cavitation pit remains however unsolved. The authors [81,107,108] have both experimentally and numerically determined the impact durations

corresponding to cavitation bubble collapses. However, the geometry and the cavitation conditions considered in these studies are significantly different from the conditions considered in the present study, so that the transposition of these data to the present case is not straightforward. To our knowledge, the impact duration cannot be determined from the sole pit shape that represents the final plastic deformation and time sensitive transducers are required to provide details on the time evolution of the impact load including its duration. In the case, the impact duration is unknown; it may be difficult to use a fully dynamic approach. For strain rate sensitive material, one option could be to use a static approach and extrapolate the material properties to a high strain rate that would correspond to the typical strain rates involved in cavitation impacts (for more details see [3]).

The inverse FE technique has been implemented in [3] for different cavitation flow conditions and impact loads were estimated by using three different materials as sensors. Very interestingly, statistical analyses of the estimated impact loads show a material independent response for a given flow condition. This is very encouraging and proves the reliability of the estimated impact loads.

Generally cavitation pit diameter is measured by using a cut-off depth to avoid surface roughness artefacts. Here, experimental pit dimensions, especially the diameter was estimated by using a cut-off depth fractional to the pit depth. This way of measurement overcomes the cut-off depth dependence and enables better estimation of the characteristic pit diameter (δ) and coverage time (t_{cov}), two important parameters associated with the statistical analysis of pitting test results. Extensive analysis of FEM computations were done and discussed throughout the chapter. The pit shape factor (ratio of pit depth to diameter) is found to follow a logarithmic behavior with σ_H, whereas, the pit diameter is proportional to r_H. During unloading that follows a given hydrodynamic impact, the material is found to undergo deformation, which could be plastic if the impact load is high enough.

In this chapter, the FE computation technique is first presented and validated against the Hertzian elastic contact theory in Sec. 2.2. Typical results of FE pitting calculations are presented and discussed in Sec. 2.3 for the aluminum alloy Al-7075 and an approximate analytical inverse technique is presented. The Sec. 2.4 is devoted to the technique of analysis of pitting tests for the determination of pit depth and diameter. In Sec. 2.5, the principle of the inverse FE technique termed here as numerical inverse method is presented. Typical results of the inverse technique are given and discussed in Sec. 2.6, which provide a kind of validation to the estimated impact loads.

2.2. Numerical method

2.2.1. Model considerations and verification

In the current study, as well as in [49] most of the experimental pit shapes are found to be nearly axially symmetric. Such a pit shape is shown in Fig. 2.17. So the effective pressure field could also be assumed

symmetric and hence a semi-infinite 2D axisymmetric model as shown in Fig. 2.1 is used for the current study. As explained in the introduction, the study reported in this Chapter is limited to static FE analyses. In reality, some impacts may have collapse durations of less than a microsecond so that the dynamic effect due to material inertia becomes unavoidable (as discussed in details in Chapter-4 [4]). In such cases, which is expectable for the collapse of very small bubbles, the estimated impact loads would be different from this static FE approach. Moreover, if the target material is strain rate sensitive, the strain rate dependence should be taken into account for better estimation of impact loads, at least by extrapolating the material properties at higher strain rate corresponding to cavitation impact (as discussed in [3,4]). Chapters-3 and 4 will try to answer to these points.

Two types of elements CAX4R (continuum axisymmetric 4 nodes reduced integration element) and CINAX4 (continuum infinite axisymmetric 4 nodes element) were used for meshing. Zero radial displacement and symmetry axis rotation constraints have been used on the axis of symmetry. Infinite element at the bottom and right most side imposes condition of zero stress and zero strain at infinity. Fig. 2.1(a) shows meshing details. Bold black lines separate different sections. Fig. 2.1(b) shows magnified view of the loading region. The material behavior is modeled as elastic-plastic isotropic hardening and a Gaussian type of distribution models the impact pressure due to cavitation bubble collapse. FE computations are made using ABAQUS standard (version 6.11-2). A brief introduction to the finite element analysis procedure along with material constitutive modeling for axisymmetric model is given in the Appendix C.

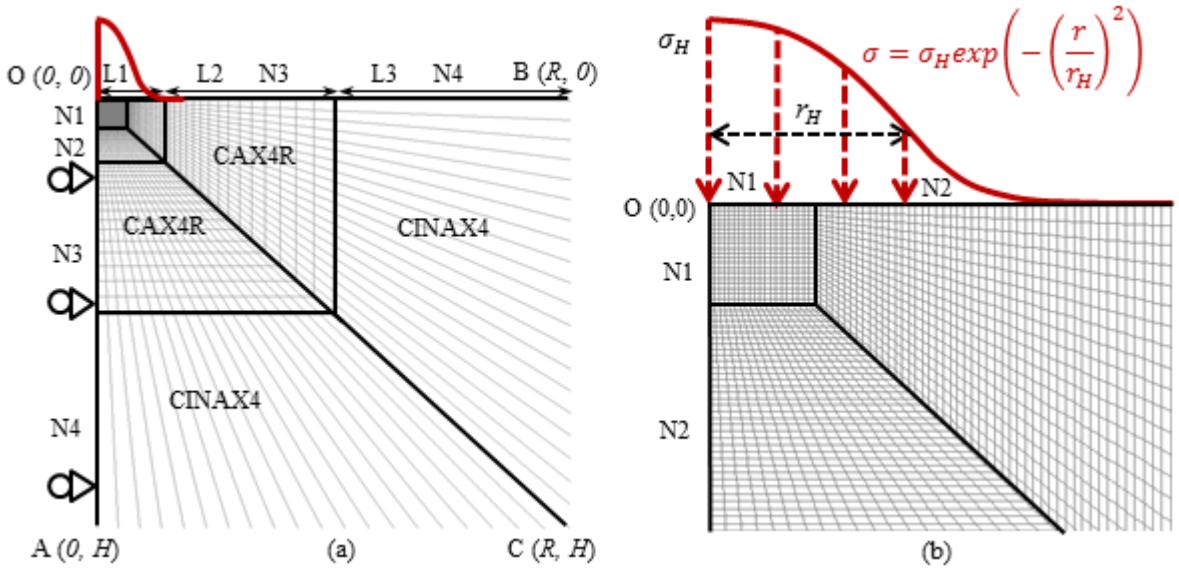

Fig. 2.1 (a) 2-D axisymmetric mesh used for numerical simulation. L represents length of one or more section as shown by arrow. N represents number of elements on the surface of different section. Number of elements (N1, N2, N3 and N4) in different section is always constant, but section lengths (L1, L2 and L3) are parameterized from radius of hydrodynamic pressure field, r_H, e.g. if $r_H = 10$ µm, N1 = 20, N2 = 60, N3 = 40 and N4 = 1 then, L1 = 1.5× r_H=15 µm, L1+L2 = L3 = R/2 = 8×L1= 120 µm, H = R = 240 µm using geometric progression with common ratio of 1.01. (b) Shows magnified view of the loading region. Minimum element size is 0.123 µm for $r_H = 10$ µm.

The mesh has been verified against Hertz theory by applying Hertzian type of load [109] on to a purely elastic material (Young's modulus = 200 GPa and Poisson's ratio = 0.3) for which the analytical solution is known.

According to Hertz theory [109], during elastic indentation of a spherical indenter of radius R_{ind} by an amount of δ' (as shown in Fig. 2.2), the radial distribution of pressure (P) applied by the indenter to a flat substrate surface of a semi-infinite medium is given by

$$P = P_0 \sqrt{1 - \left(\frac{r}{r_c}\right)^2}, \tag{2.1}$$

Where the maximum pressure P_0 is given as:-

$$P_0 = \frac{2E^*}{\pi} \sqrt{\frac{\delta'}{R_{ind}}}, \tag{2.2}$$

Where the effective modulus E^* is given as:-

$$\frac{1}{E^*} = \frac{1 - \nu_1^2}{E_1} + \frac{1 - \nu_2^2}{E_2} \tag{2.3}$$

Here, ν and E stands for Poison's ratio and Young's modulus respectively (1: substrate and 2: indenter).

The contact radius r_c is given as-

$$r_c = \sqrt{R_{ind}\delta'} \tag{2.4}$$

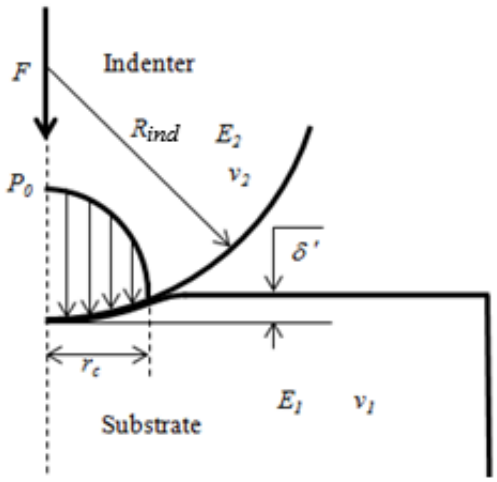

Fig. 2.2 Hertzian type of elastic contact of a spherical indenter with flat surface

For the simulation, the equivalent Hertz pressure (defined by Eq. (2.1)) has been applied for different values of δ' and R and the resultant depth of indentation, contact radius, maximum shear stress and location of maximum shear stress have been verified with the analytical solution. The influence of different types of elements, number of elements in the loading and other sections, the effect of the boundary conditions, the size of the model and the use of infinite element on the accuracy of simulation results have been investigated in details in order to optimize the mesh. No significant influence of the number of elements has been observed but the element size in the loading section appears to influence the accuracy. Hence, a large number of elements of smaller size have been used in the loading section (as indicated by N1 and N2 in Fig. 2.1). Fig. 2.3 shows

the variation of the normalized shear stress, τ/P_0 (as given by Eq. (2.5)) into the material plotted along the direction of the thickness (z) corresponding to the axis of symmetry. Results are very consistent with the analytical solution. As expected, the maximum shear stress $\tau_{max} = 0.31P_0$ occurs at a depth of $z_{max} = 0.48r_c$ along the axis of symmetry (OA) as defined in Fig. 2.1. The Fig. 2.4 shows the effects of the domain size relative to the indenter radius and depth of indentation. The use of infinite element eliminates the error in prediction of δ' by preventing stress reflections from the boundaries. As found by Hertz, the force-displacement relationship is given by Eq. (2.6) as plotted in Fig. 2.4.

$$\frac{\tau}{P_0} = \left[(1+\nu)\left(1 - \frac{z}{r_c} atan \frac{r_c}{z}\right) - 1.5\left(1 + \frac{z^2}{r_c^2}\right)^{-1}\right] \tag{2.5}$$

$$F = \frac{4}{3}E^* R^2 \left(\frac{\delta'}{R_{ind}}\right)^{\frac{3}{2}} \tag{2.6}$$

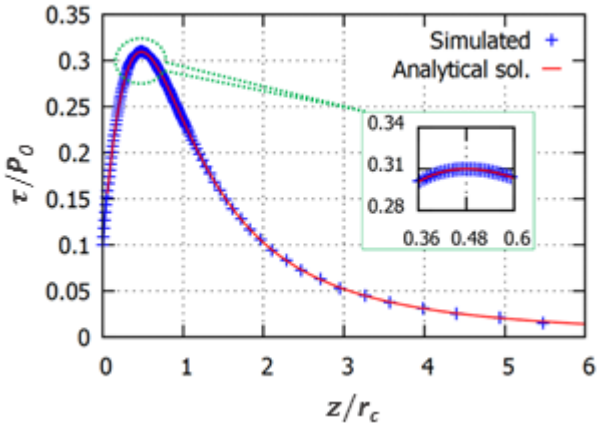

Fig. 2.3 Variation of maximum shear stress into the material along depth on the symmetry axis (OA). Maximum value of τ_{max}/P_0 *is 0.31 at* $z/r_c = 0.48$

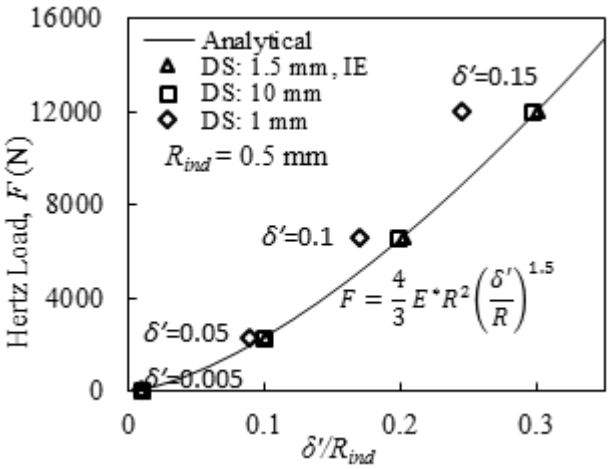

Fig. 2.4 Effect of domain size (DS) and infinite element (IE) on the accuracy of the FE simulation. Prediction of δ' *influenced by domain size and infinite elements. Here* δ' *is the estimated maximum elastic deformation depth under the action of the Hertz pressure given by the Eq. (2.1).*

The good correlation with the analytical results presented in Fig. 2.3 and Fig. 2.4 tend to validate this mesh. Finally, the parametric mesh with a constant number of elements as shown in Fig. 2.1 has been used for all simulations in this chapter.

2.2.2. Hydrodynamic impact pressure distribution

The impact pressure induced by the collapse of a cavitation bubble has a complex form in both space and time. It results from several unsteady mechanisms including the development of a micro-jet [110] and shock waves [23]. Ideally, the best option for the inverse FE technique would be to use the impact load generated from a cavitation bubble collapse, and then optimize the parameters associated with the bubble collapse in order to reproduce a given experimental pit numerically. To do so, fluid-structure interaction has to be considered and the authors in [28,81] have highlighted the difficulties associated with such simulations of cavitation bubble collapse. In industrial applications as well as for the experiment considered here [28,49], it is nearly impossible to use the impact loads deduced from CFD (Computational Fluid Dynamics) since many parameters are unknown such as the location of bubble collapse, its initial size and the local collapse driving pressure gradient corresponding to each pit produced in cavitation pitting test. All of these parameters influence the impact load. The only way to finely control these parameters would be to design single bubble collapse experiments.

In our case (cavitation tunnel in PREVERO device), the only feasible option is to use a representative pressure field and analyze the material response to this load. For sake of simplicity, a Gaussian type of distribution in space $\sigma(r)$ is considered for the hydrodynamic impact load generated by the collapse of a cavitation bubble, as given by Eq. (2.7) and shown in Fig. 2.5:

$$\sigma = \sigma_H \exp\left(-\left(\frac{2r}{d_H}\right)^2\right) \tag{2.7}$$

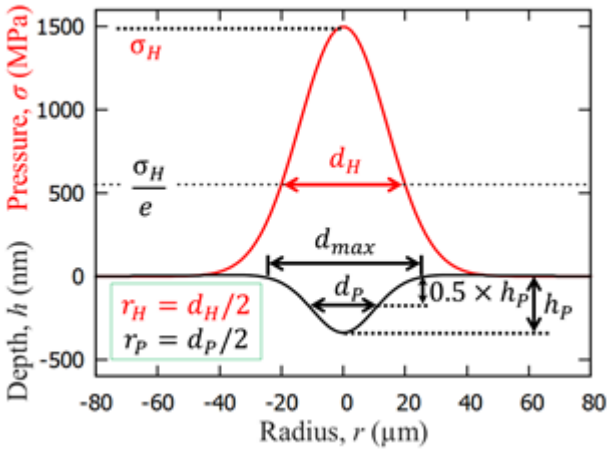

Fig. 2.5 Gaussian shape of the hydrodynamic impact pressure and resulted cavitation pit. Here d_{max} represents the maximum diameter of the pit.

Parameter σ_H is the maximum amplitude of the hydrodynamic impact pressure, whereas radius $r_H = d_H/2$ characterizes the radial extent of the load. Note that such a Gaussian law has already been used in [48,81] for

cavitation erosion studies. Moreover, in the current study it has been shown that normalized pit shapes numerically obtained by Gaussian types of pressure fields are very close to the experimental pit shapes, examined for a large number of pit, as will be discussed in Sec. 2.4.

The residual plastic deformation after unloading representing a cavitation pit is characterized mainly by two parameters, the pit depth, h_P and the pit diameter, d_P as shown in Fig. 2.5. The pit diameter is measured at 50% of pit depth to be consistent with experimental data. The reason of this definition of the pit diameter is discussed in Sec. 2.4. The pit depth, h_P, is the actual depth of the pit with respect to the original virgin surface. Since each pit is characterized here by only two parameters (depth and diameter), it seems reasonable to have only two free parameters to be optimized in the loading law.

2.2.3. Constitutive equations of the material

Numerical and experimental studies indicate that the strain rate involved in cavitation erosion process could be as high as 10^5 or 10^6 s^{-1} [4,6,85]. So it is necessary to take into account the strain rate sensitivity of a material in the FE simulations. The current material Al-7075 has a very weak strain rate sensitivity as shown in [3], which could be neglected. Hence, the deformation behavior of the material Al-7075 was characterized by quasi-static uniaxial tensile tests performed at a strain rate of 4 x 10^{-4} s^{-1}. The corresponding true stress-true strain (σ-ε) curve of the material is shown in Fig. 2.6. However, this curve corresponds to bulk tensile properties whereas we are interested in cavitation pitting which is a localized phenomenon. Depending on the microstructure, the bulk and local behavior of the material could be different, as addressed in [3,4] and in that case the material properties should be replaced by the appropriate one, typically, obtained from nanoindentation tests.

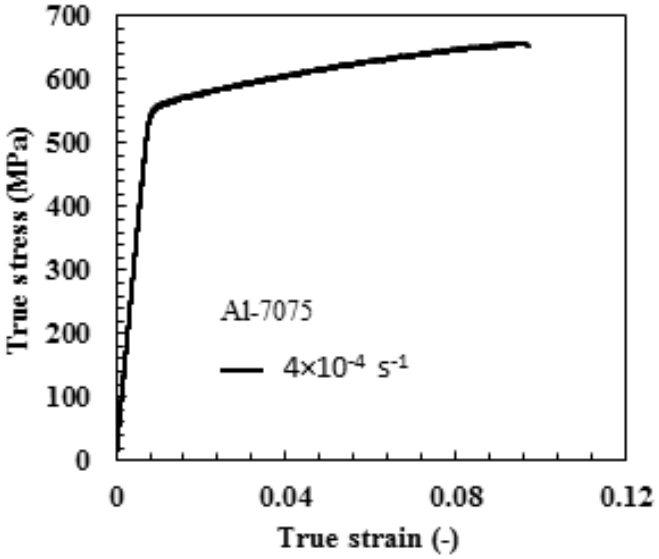

Fig. 2.6 True stress-true strain curve of Aluminum alloy 7075-T651 obtained by uniaxial tensile test.

The stress-strain curve can be represented by Ramberg-Osgood relationship [111] as given by Eq. (2.8) where the plastic part has been modified by Ludwik's equation [112] which includes yield stress (σ_y).

$$\varepsilon = \varepsilon_e + \varepsilon_p = \frac{\sigma}{E} + \left(\frac{\sigma - \sigma_y}{K_y}\right)^{m_y} \tag{2.8}$$

Here, ε_e, ε_p and E represent elastic strain, plastic strain and Young's modulus respectively. K_y and m_y are material constants obtained by least-square fitting of stress-strain curve in the plastic region. The criterion used for estimating the elastic limit corresponds to a ratio $\varepsilon_p/\varepsilon_e$ of the permanent plastic deformation ε_p to the elastic deformation ε_e equal to 5% [111]. Material properties for the aluminum alloy considered in this study are given in Table 2.1.

Table 2.1 Tensile properties of Aluminum alloy 7075-T651 (Al 7075)

Material	Al-7075
Yield strength, σ_y [MPa]	530
Ultimate tensile strength, σ_u [MPa]	645-660
Modulus of elasticity, E [GPa]	71.9
Poisson ratio, ν	0.33
Ultimate strain, ε_u	0.086-0.095
Materials parameter, K_y [MPa]	447
Materials parameter, n	0.5

To be consistent with the pitting test technique, no damage has been considered in the current study. As pitting tests were conducted within the incubation period to avoid any mass loss, pits are assumed to be formed by plastic deformation only.

2.3. Simulation of cavitation pitting

2.3.1. Primary results

A simulation campaign of 55 simulations has been carried out using the materials properties of Table 2.1 for different values of the size of the Gaussian pressure distribution, d_H (10, 20, 40, 60, 80, 100, 120, 140, 160, 200, 240 µm) and of the peak Gaussian pressure, σ_H (1.0, 1.5, 2.0, 2.5 and 3.0 GPa). The results are analyzed in terms of the deformed pit shape. Fig. 2.7 shows the applied pressure and the corresponding deformed geometry. As an example, Fig. 2.7(a) shows that pit depth and diameter both increase with size of impact loads. Whereas, with increase in peak pressure of hydrodynamic impacts of similar size as shown in Fig. 2.7(b), the pit depth increases significantly but the pit diameter does not change much. Same figure also shows that, at σ_H = 1 GPa, no pit forms i.e. the plastic deformation does not occur into the material although the yield strength of the material is 530 MPa. This is because the von Mises equivalent stress induced into the material does not exceed the yield strength, which is a direct consequence of the plasticity confinement, similar to indentation induced plasticity. At σ_H = 3 GPa when d_H > 40 µm, the pit depth becomes significantly higher than the

measured experimental maximum values of about 10 µm (for example see Fig. 2.20). The observations from Fig. 2.7 indicate that deep pits of small diameters are most probably formed by impacts of small diameter but high peak pressure.

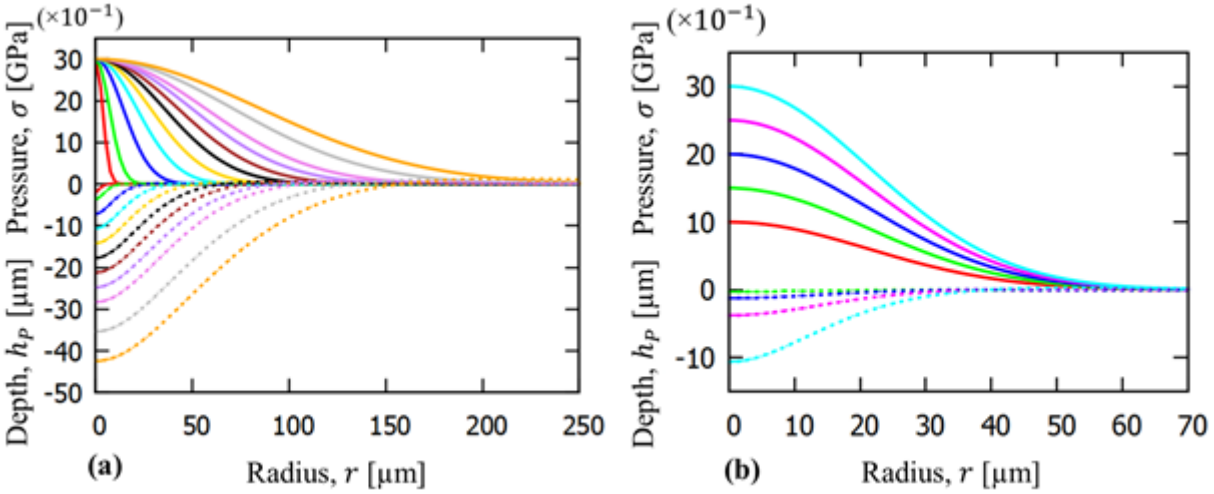

Fig. 2.7 Applied Gaussian loads and corresponding unloaded deformed geometry represent simulated pit shape. (a) At $\sigma_H = 3\ GPa$ for $r_H = 5$ to $120\ \mu m$ and (b) At $r_H = 30\ \mu m$ for $\sigma_H = 1$ to $3\ GPa$, no pit formed at 1 GPa.

In Fig. 2.8 all simulated pit depths and diameters are plotted where dotted line connects pit data for iso-r_H and continuous line connects pit data for iso-σ_H. As can be seen along the iso-σ_H, the pit depth, h_P shows a linear behavior with the pit diameter, d_P. For a given σ_H, the pit depth increases with d_H and conversely, for a given d_H the pit depth increases with σ_H. Thus, deep pits of large diameter may be caused by impacts of bigger size at relatively low pressure.

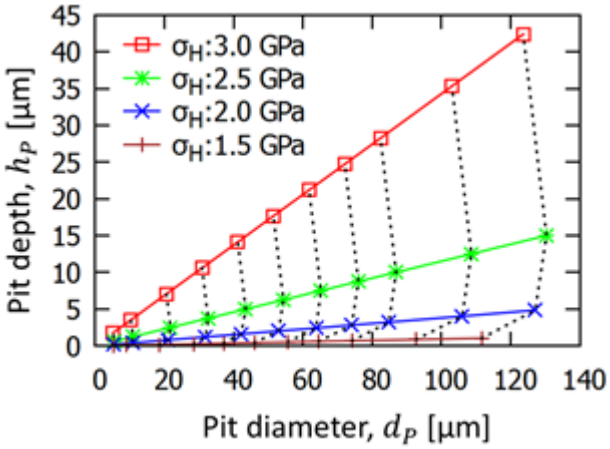

Fig. 2.8 Simulated pit depths and diameters show the effect of σ_H (solid lines) and r_H (dotted lines)

One interesting fact in Fig. 2.8 is that the solution appears to be bijective since the lines passing through different iso-σ_H or iso-r_H data points do not intersect themselves. Thus, it is evident that a pit of a particular depth, h_P and diameter, d_P is formed by a unique impact of particular size, d_H and peak pressure, σ_H. Obviously, the data lines for different σ_H converge towards zero when r_H goes to zero. Interestingly, such

bijective behavior is also observed in the case of dynamic explicit analysis of cavitation pitting as presented in Part 2 paper [4] (or in Chapter-4).

A more convenient representation of the curves in Fig. 2.8, is given in Fig. 2.9 where the ratio h_P/d_P(pit shape factor) is plotted versus the pit diameter, d_P. One should notice that the iso-σ_H curves are now horizontal and the iso-r_H curves are quasi-vertical except for the highest values of r_H.

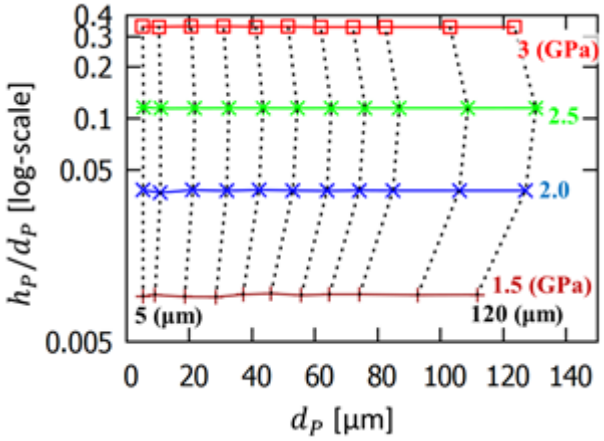

Fig. 2.9 Variation of shape factor and diameter of simulated pits with σ_H (continuous lines) and r_H (dashed lines).

From the simulation campaign (as given by Eq. (2.9)), we also observed that the ratio of pit diameter, d_P to diameter of hydrodynamic impact, d_H remains almost constant irrespective of values of σ_H and r_H.

$$\frac{d_P}{d_H} = \frac{r_P}{r_H} \approx k \tag{2.9}$$

Here *k* is a constant that depends on material only. For Al 7075, *k* is approximately 0.52.

Finally, we could establish from Fig. 2.9 that the pit shape factor, h_P/d_P follows a power law behavior which can be written by the following equation:

$$\frac{h_P}{d_P} \approx \left(\frac{\sigma_H}{\sigma^*}\right)^{\beta'} \tag{2.10}$$

Here σ^* and β' are two constants that depend on the material only. The material parameter σ^* has same unit as σ_H and β' is dimensionless. For Al 7075, σ^* and β' are found to be 3600 MPa and 5.8 respectively.

Combining Eq. (2.9) and Eq. (2.10), we can write Eq. (2.11) as follows-

$$\ln\left(\frac{d_H}{h_P}\right) = \beta' \ln\left(\frac{\sigma^*}{\sigma_H}\right) + \ln\left(\frac{1}{k}\right) \tag{2.11}$$

Eq. (2.11) represents a linear equation on log-log graphs. Fig. 2.10 shows the plot of σ^*/σ_H versus d_H/h_P for all the simulated data ($\sigma_H = 1.5\ to\ 3\ GPa$ and $r_H = 5\ to\ 120\ \mu m$) and interestingly they all follow a unique linear behavior on log-log graphs. Thus, Fig. 2.10 validates Eq. (2.11) or in other words Eq. (2.9) and Eq. (2.10).

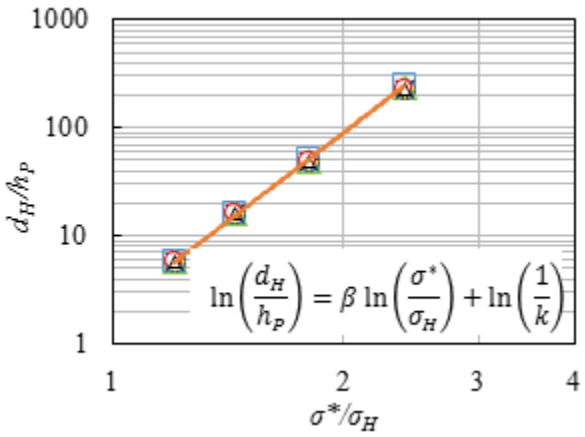

Fig. 2.10 Plot of σ^*/σ_H versus d_H/h_P for all simulated data for $\sigma_H = 1.5$ to 3 GPa and $r_H =$ 5 to 120 μm. Linear behavior on log-log scale.

Now by using Eq. (2.9) and Eq. (2.10), σ_H and d_H can be predicted when pit depth and diameter are known for experimental pits. Prediction of σ_H and d_H for a particular given pit using Eq. (2.9) and Eq. (2.10) will be termed as analytical method throughout the chapter.

2.3.2. Verification of the model predictions

In order to verify Eq. (2.10) and Eq. (2.11), six experimental pits of given depths and diameters have been chosen arbitrarily. Simulations were conducted with the input parameters of the applied pressure field σ_H and d_H estimated using Eq. (2.9) and (2.10) with the material constants obtained in Sec. 2.3.1. Fig. 2.11 shows the comparison of the simulated pit depths and diameters with the original values. It indicates a very good ability of the model although some deviations are evidenced for the biggest pits. This comes from the constant factor, k, used in Eq. (2.14). We could observe from the simulations that the pit diameter is actually a more complex function of both pressure size and peak pressure of the hydrodynamic impact. This motivates the development of an alternative and more accurate numerical inverse method to directly estimate peak pressure and pressure size for a given pit depth and diameter as discussed in Sec. 2.5, using the model predictions for the initial guess of the optimization algorithm.

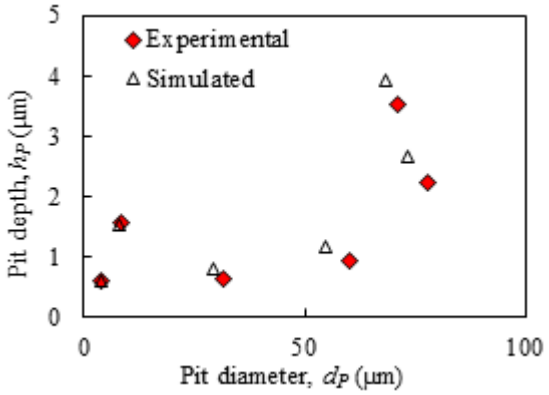

Fig. 2.11 Comparison of experimental pit depth and diameter with that of simulated. Input parameters for simulation σ_H and r_H were predicted using analytical method (Eq. (2.9) and Eq. (2.10)).

2.3.3. Residual stress under cavitation impact

Analysis of the residual stress could be an important factor to explain the degree of inhomogeneity of plastic deformation involved in cavitation pitting. Since the residual stress has significant influence in fatigue [113], its effect in cavitation pitting due to multiple impacts is inevitable and needs to be investigated.

It is observed that the residual stress (von Mises stress) field around the pit is very complex in nature. As shown in Fig. 2.12(a)-(c), the maximum stress (or strain) occurs into the material and changes its location from sub-surface to surface with the increase in peak pressure, σ_H. The maximum stress (or strain) is always found to coincide with the axis of loading or axis of symmetry. The residual stresses have been locked inside the materials after the loading-unloading cycle of the applied load. The stress mapping of these internal stresses gives an indication of the highly inhomogeneous or non-uniform deformation that occurred during the deformation. Restriction develops due to uneven hardening of material at different locations.

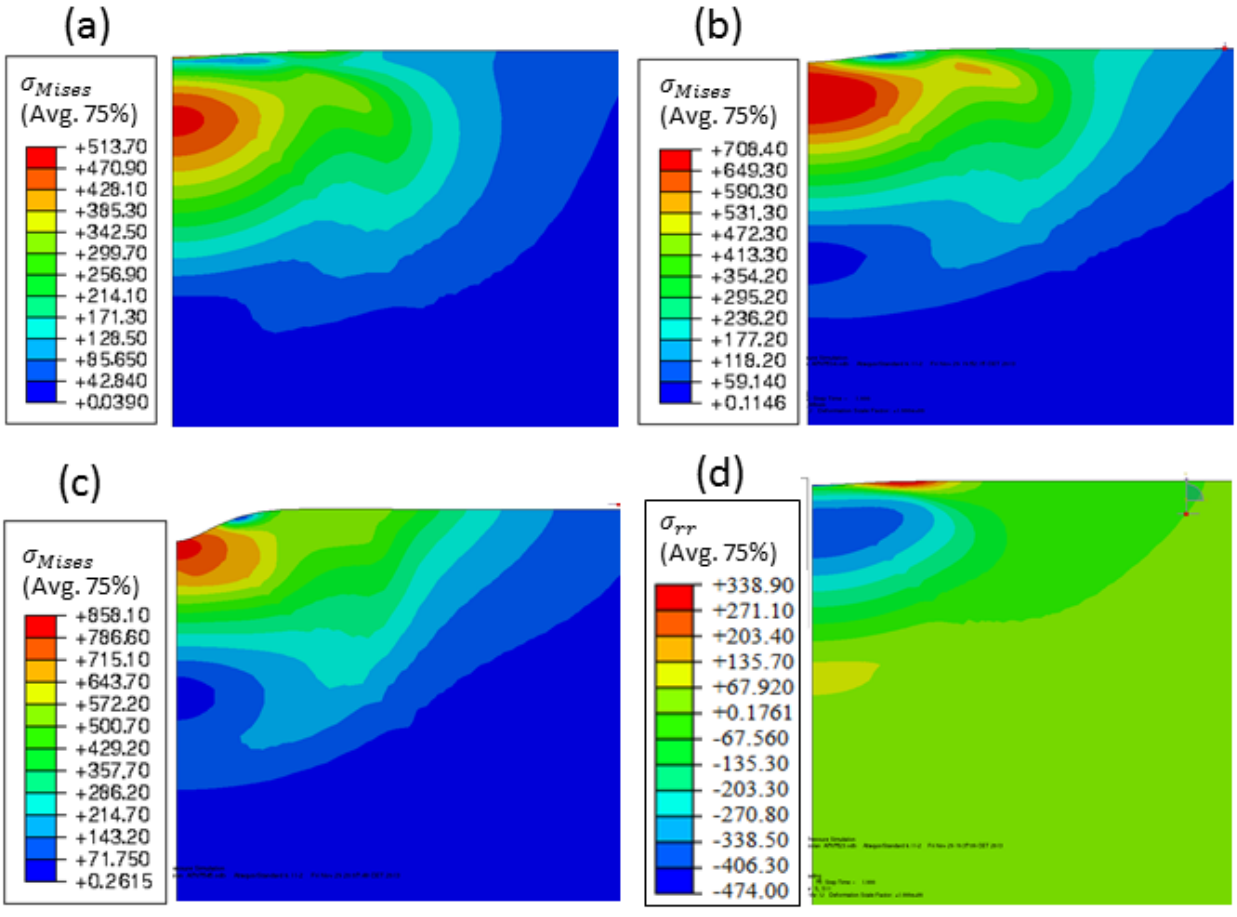

Fig. 2.12 Residual von Mises stress into the material for d_H: 10 µm and (a) σ_H: 2.0 GPa (b) σ_H: 2.5 GPa and (c) σ_H: 3.0 GPa. Zoomed views. (d) Residual stress along radial direction, σ_{rr} for σ_H: 2.0 GPa and d_H: 10 µm (magnified view)

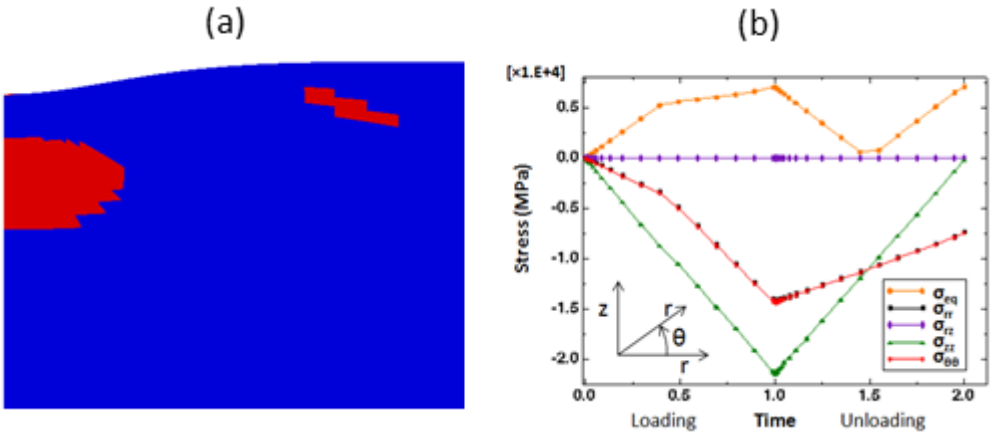

Fig. 2.13 (a) The red color indicates the regions where the material undergoes plastic deformation during unloading. The highlighted regions indicate elements for which strain exceeded the elastic limit. The simulation inputs are σ_H: 2.5 GPa, d_H: 10 µm. The figure is a magnified view. (b) Variation of the different components of stress at the point of maximum residual stress. The time scale is virtual as static simulation is time independent, so there is no unit of time. Similar to any axisymmetric model r, z and θ represents the radial, longitudinal and circumferential direction respectively (see Appendix C). Simulated data at σ_H: 2.5 GPa, d_H: 10 µm and maximum strain achieved ≈16.0%.

When the impact load is high, as shown in Fig. 2.13(a), the material is found to deform plastically during the unloading stage (i.e. during removal of the hydrodynamic impact load) at locations around the point of maximum stress and pit radius, r_p. Fig. 2.13(b) shows the variation of different components of stress during the impact loading (virtual time from 0 to 1) and the unloading (virtual time from 1 to 2). Stresses were estimated at the location of the maximum residual stress on the symmetry axis. One interesting fact is that the von Mises equivalent stress (σ_{eq}) increases during loading while during unloading, σ_{eq} initially decreases to a value well below the initial yield strength of the material and then again increases causing further deformation.

As shown in Fig. 2.13(b), the shear stress component on the radial face and longitudinal direction, σ_{rz} is always found to be zero on the symmetry axis. The normal stress on the longitudinal face, σ_{zz} (i.e. stress along thickness) increases during loading and relaxes back to almost zero during unloading. The normal stress on the radial face, σ_{rr} and circumferential face, $\sigma_{\theta\theta}$ both have the same value on the symmetry axis and then follow the same trend. As can be seen in the figure, the relaxation of σ_{rr} and $\sigma_{\theta\theta}$ was restricted probably due to non-uniform deformation of the material. Due to different rate and amount of relaxation of stresses in different directions, σ_{eq} increases and the material nearby the point of maximum stress (or strain) undergoes further deformation during unloading although there is no external load.

Fig. 2.12(d) shows the normal residual stress along the radial direction, σ_{rr}. A compressive residual stress field around the axis of symmetry has always been observed. This is probably due to the restricted on relaxation of the elastic stress of the surrounding material provided by the plastically deformed material around the surface of the pit.

Thus, the material under the pit tip and around the pit radius undergoes the maximum cumulated plastic deformation. Hence in case of multiple impacts, damage would initiate at those locations i.e. the subsurface or surface of the material on the axis of symmetry or into the material near the pit radius.

2.4. Pitting test analysis

2.4.1. Cavitation pitting test

Cavitation pitting test were conducted using the high speed cavitation tunnel as shown in Fig. 1.11 (apparatus details are given in Chapter-1 and Sec. 1.2.3). The cross sectional view of the test section and the specimen assembly is shown in Fig. 2.14. The test liquid (water) comes in through the axial inlet of diameter 16 mm and goes out through the radially divergent passage between the specimen and apparatus. Cylindrical test specimens of diameter 100 mm and thickness 25 mm have been used. The surface of the samples prior to test were prepared following conventional metallurgical polishing method down to a mirror polishing with diamond paste of 0.25 µm. A stand-off distance of 2.5 mm between the test specimen and nozzle exist has been used. Pitting tests were conducted on aluminum alloy 7075-T651 at different flow pressures (upstream pressure) of 10, 15, 20, 30 and 40 bar within the incubation period (test method can also be found [62]). The flow pressures of 10 and 40 bar correspond to flow velocities of 45 and 90 m/s respectively. The ambient (or downstream) pressure were monitored to maintain a constant cavitation number throughout the tests, which ensure only velocity effect on the test results rather than cavitation number effect. The cavitation number was set at $\sigma_{ca} = 0.98$ (see Eq. (1.3)) for all the tests.

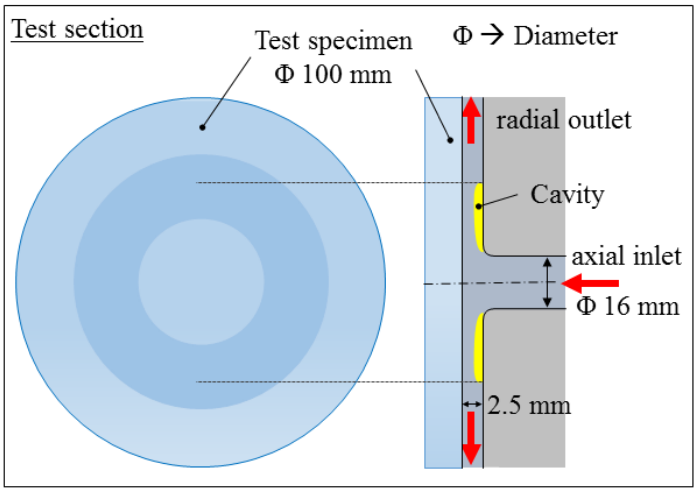

Fig. 2.14 Schematically the cross-section of the test section of the high speed cavitation tunnel (PREVERO device available at LEGI) shows the position of the test specimen during test. The dark inner ring highlights the region where most of the cavitation pits are generated.

The analysis technique of the pitting tested samples to get the pit dimensions are discussed in the following sections and the effect of the flow velocity on the cavitation erosion or pitting rate is discussed in Sec. 2.6. Extensive analysis of the test results are not done here since they are largely available in literatures (see for example [7]).

2.4.2. Pit analysis method

The surfaces of the pitting tested samples have been analyzed using a conventional contact profilometer (with a microprobe of radius 2 µm). Different regions of 2 mm × 4 mm with a mesh size of 1 µm × 1 µm had been scanned on the sample surface where maximum pitting occurs. Different regions were scanned to have a sufficient number of pit data for the statistical analysis. The scanned numerical surfaces were analyzed using a Matlab script to estimate the pit depth (h_P) and diameter (d_P). Note that the micro-probe of radius 2 µm used here might cause some errors in the estimation of the pit parameters, especially for smaller pit with bigger depth. In contrary, as can be seen in Fig. 2.20 the fact that most of the pits are far bigger in diameter than depth indicates that such an error could be negligible, at least from a statistical point of view since the number of data is rather large (typically 200 or 300 pits per sample). In [38], Franc *et al*. have done similar analysis of pits using a constant cut-off depth (0.5 µm) and highlighted the associated difficulties arising from the complex nature of the pitting. The use of a cut-off depth was necessary to avoid surface noise or roughness, while estimating the pit diameter. In the current analysis also, the same raw data as obtained by Franc *et al*. [38] using the same contact profilometer have been utilized.

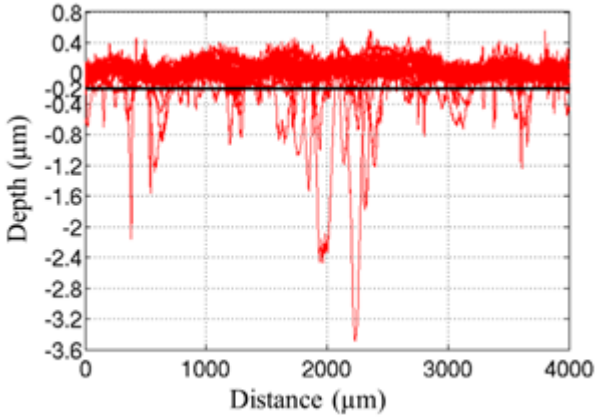

Fig. 2.15 Twenty profiles along different lines on the pitting tested surface are plotted together. Maximum noise level is approximately -0.2 µm as shown by black the line. Al-7075 material cavitation tested at flow pressure of 40 bar for 2 sec.

Firstly, the pits are detected from the part of the profiles below a cut-off depth of 0.5µm in order to avoid the surface noise. For all Al 7075 samples, the maximum level of noise was found to be approximately 0.2 µm, as shown in Fig. 2.15. Once the pits are all detected, the pit depth is always taken as the actual depth with respect to the virgin surface. The pit diameter is then measured at a depth chosen as a fraction of the pit depth (typically 50%). The use of such a fractional cut-off depth has many advantages over a fixed cut-off depth: (1) the measured pit diameter does not depend on the arbitrary cut-off depth and thereby avoids any size effect, (2) it is a more appropriate way of measuring the pit diameter as it excludes the ambiguity involved in the choice of any arbitrary the cut-off depth and (3) statistical analysis of measured pit depths and diameters provide more accurate results. Finally, the use of a fractional cut-off depth is also favorable for the numerical inverse method presented in Sec. 2.5.

2.4.3. Typical results

Systematic analyses of pits were done in order to understand the influences of two different methods namely the fractional cut-off depth (FCOD) method and the constant cut-off depth (CCOD) method. As an example, Fig. 2.16 shows the influence of the analysis method on the pit boundaries. Fig. 2.16(a) represents the pit boundaries obtained by the CCOD method using a cut-off depth of 0.5 µm. Fig. 2.16(b)-(d) represent the same pit boundaries at 20%, 40% and 50% fraction cut-off depth respectively. It is clear from the figures that with increase in FCOD, the problem of overestimation of the pit diameter due to overlapping of pits is reduced. After analyzing all the surfaces of different cavitation tests, it is found that at 50 % of FCOD there is almost no overlapping of pits, which have been detected by using CCOD of 0.5 µm. The value to retain for the FCOD is related to the CCOD used for pit detection. The condition to avoid over estimation of pit diameter (especially for shallow pit) is that the (FCOD×CCOD) or (FCOD × pit depth) should be greater than the noise level of the tested surface. This condition is fulfilled here since FCOD=50% and CCOD = 0.5 µm so that FCOD × CCOD = 0.25 µm whereas noise level was determined as 0.2 µm. This condition is not fulfilled for Fig. 2.16(b) where FCOD × CCOD = 0.1 µm, which explains the bad definition of pits.

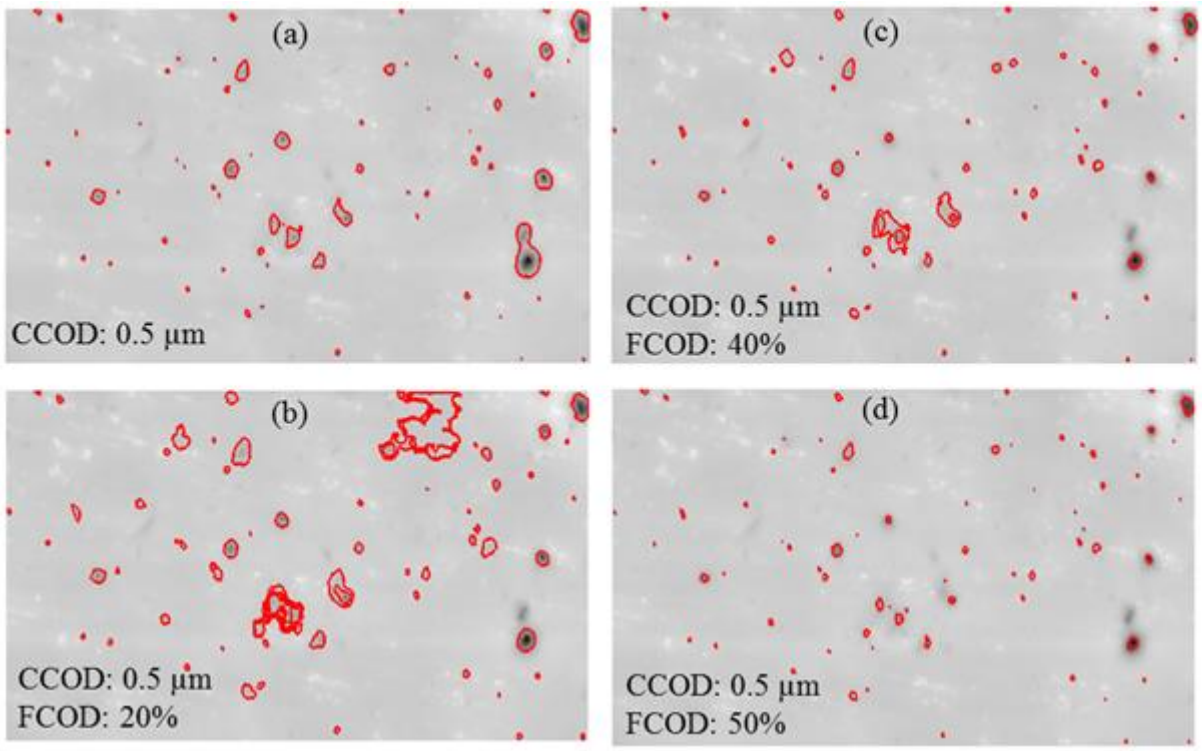

Fig. 2.16 Comparison of fractional and constant cut-off depth method for pit parameter determination, (a) CCOD method and (b)-(d) FCOD method at 20%, 40% and 50% cut-off depth respectively. Gary scale is an indicator of pit depth. Cavitation test: Al 7075 at 40 bar for 2 sec.

Since a direct measurement of the maximum pit diameter (d_{max}) at zero-level by using any of the two methods is not possible due to noise and overlapping, focuses were made to an alternative method as discussed in next Sec. 2.4.4.

2.4.4. Analysis of non-overlapping pits

In order to identify the relevance of the Gaussian pressure field assumed, simulated and experimental pit shapes have been compared. Twenty pits almost unaffected by surface noise or overlapping have been identified, one example is shown in Fig. 2.17. As can be seen, the pit profile is not closed at zero-level, this is because of the way the pit is being detected to avoid surface noise detection. Hence, the maximum pit diameter at zero-level was estimated by linear extrapolation of pit diameters at 5% and 10% of pit depth. In Fig. 2.18 normalized pit shape i.e. pit depth normalized by maximum pit depth vs. pit diameter normalized by maximum pit diameter for the 20 experimental and all (55) simulated pits have been plotted together. The normalized pit shapes are almost the same for both simulated and experimental pits. The little variation in experimental data could be due to errors associated with the measurement of the maximum pit diameter, as well as the shape correlation between the pit profile and the profilometer microprobe used for the measurement. This particular observation depicts that the Gaussian pressure field describes reasonably well the effective pressure field associated with bubbles collapse.

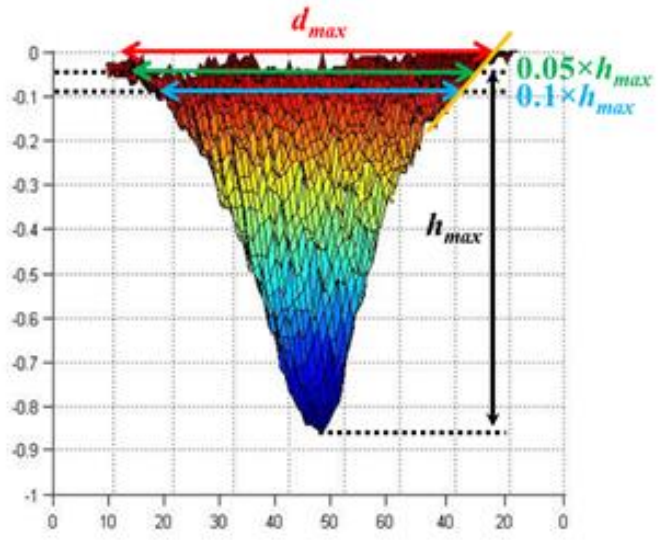

Fig. 2.17 An experimental pit obtained by contact surface profilometer with microprobe of radius 2 μm. d: diameter, h: depth, max: maximum.

Now as shown in Fig. 2.18 by the black unfilled points, a common normalized pit shape (mean of the simulated curves) could be considered to estimate d_{max} and for a particular material we can write

$$\frac{d}{d_{max}} = f\left(\frac{h}{h_{max}}\right) \tag{2.12}$$

Using Eq. (2.12) d_{max} for the experimental pit can easily be predicted, as d is already estimated by using the FCOD method. For a FCOD coefficient of 50% i.e. $h/h_{max} = 0.5$, the corresponding value of d/d_{max} is ~0.416 as can be seen in Fig. 2.18.

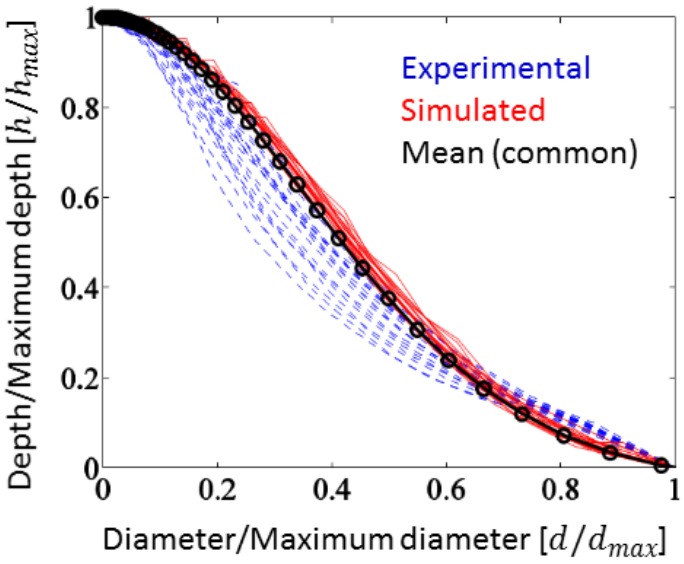

Fig. 2.18 Normalized pit shape of simulated and experimental pits. Twenty non-overlapping experimental pits were identified almost unaffected by surface roughness.

2.5. Numerical inverse method

2.5.1. Principle

The principle of the inverse FE technique, as termed here Numerical Inverse Method (NIM), to estimate impact load parameters- peak pressure (σ_H) and its radial extent (r_H) from pit parameters- depth (h_P) and diameter (d_P) is explained here. The method is based on a simple interpolation technique, but found to be very efficient to implement on a large number of data required for statistical analysis. The one-to-one correspondence between set of (σ_H, r_H) and (h_P, d_P) as mentioned in Sec. 2.3.1 makes it possible to implement the method. The basic principle of the method is to run ABAQUS simulation from an initial guess of σ_H and r_H, compare the computed pit depth and diameter with experimental values and iterate until they are optimized for a given error limit in pit dimensions. Similar to the experimental pit diameter, the simulated pit diameter was also measured at 50% of pit depth for consistency in defining the pit diameter. Let us mention here that, if we use a constant cut-off depth of 0.5 µm (instead of FCOD of 50%) to estimate the simulated pit diameter, then during the optimization if the simulated pit depth becomes smaller than 0.5 µm, there will be no value for the pit diameter and the optimization method will not work for that pit. This is one more reason for considering a fractional cut-off depth rather than a constant one.

The initial guess is an important factor that influences the number of simulations required to obtain the solution. The optimization method is discussed graphically in details in this section.

In Fig. 2.9 each data point represents a FE simulation results for which all four parameters [$d_P, h_P/d_P, \sigma_H$ and d_H] are known. Continuous solid line connects data points for iso-σ_H and dotted line connects iso-d_H data

points. More details related to the figure can be found in Sec. 2.3.1. These known simulated data have been used for the optimization method.

The optimization method starts with finding out of a triangle (such as ▲123 on the base in Fig. 2.19) from the simulated data points (from Fig. 2.9) which ensures that the experimental data point (for which only d_P and h_P/d_P is known) always lies inside the triangle. Now to predict σ_H for the experimental data point, a three dimensional (3D) plane (Fig. 2.19) is constructed from the three data points of the triangle. The 3D space is characterized by d_P as x-axis, h_P/d_P as y-axis and σ_H as z-axis. For the prediction of σ_H for the experimental data point, it is assumed that the point would lie on the 3D plane, hence can be estimated easily by linear interpolation.

Recalling that the equation of a plane through three points is given by Eq. (2.13), where ‹a', b', c'› is the vector ($\overrightarrow{ON}$) normal to the plane and d' is a constant. Vector ‹a', b', c'› was obtained by cross product of two vectors $\overrightarrow{OA}$ and $\overrightarrow{OB}$ as shown in Fig. 16. Constant d was obtained from Eq. (2.13) by substituting the values of x, y and z at point O.

$$a'x + b'y + c'z + d' = 0 \tag{2.13}$$

Now assuming the experimental data point lies on the 3D plane, in Eq. (2.13) only z ($= \sigma_H$) is unknown and can be estimated easily.

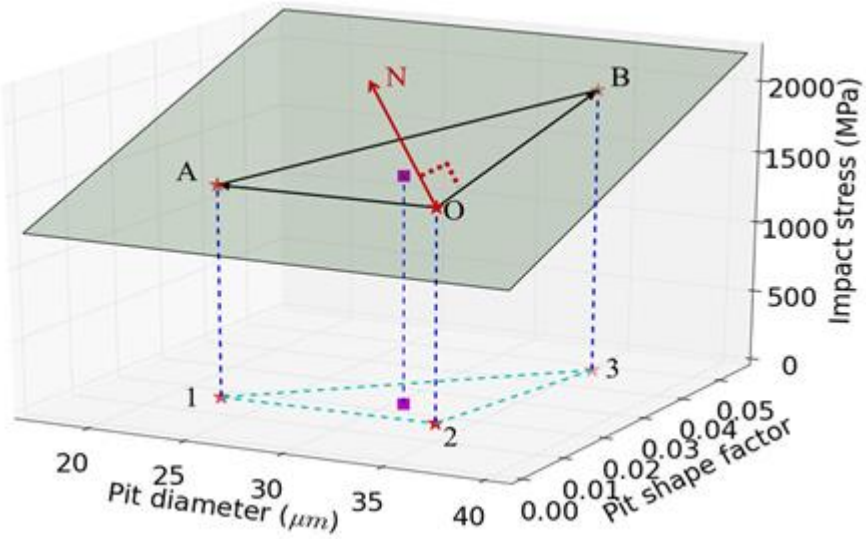

Fig. 2.19 Method of construction of 3D plane through three points from the known results of simulated data points for the prediction of σ_H. Similar plane is also constructed to predict d_H by considering the z-axis as σ_H.

Similarly, for the prediction of d_H the 3D space is characterized by d_P as x-axis, h_P/d_P as y-axis and d_H as z-axis. Once σ_H and d_H are predicted, one FE simulation will be done and two errors are evaluated: error in pit depth and in pit diameter. If both errors are below a given value (typically 1µm in diameter and 0.05µm in depth) then the solution is assumed to be achieved, otherwise the process will continue by the selection of a new triangle for the prediction of σ_H and d_H until an acceptable solution is obtained. It should be noted that

each time an FE simulation is done a new data point is added up into the database i.e. Fig. 2.9, for which the solution is known. Thus, the new triangle would become smaller and closer to the experimental data point, thereby the error domain is reduced improving the prediction accuracy.

2.5.2. Convergence and accuracy

It was observed that on average three simulations were needed for a given error limit of 1.5 µm in pit diameter and 0.05 µm in pit depth. Time required for a typical ABAQUS simulation to be completed varies from 1-3 minutes depending upon the size of the problem. Thus the average time required to obtain the optimized set σ_H and d_H for a given experimental pit varies from 3-9 minutes. This is fairly economic since to optimize 200 pits, the total time required varies from 10-30 hours on a computer system with 24 GB ram and 2.8 GHz Intel X5660 processor. Two hundred pits is a typical number of pits necessary for a reliable statistical analysis of a pitting test.

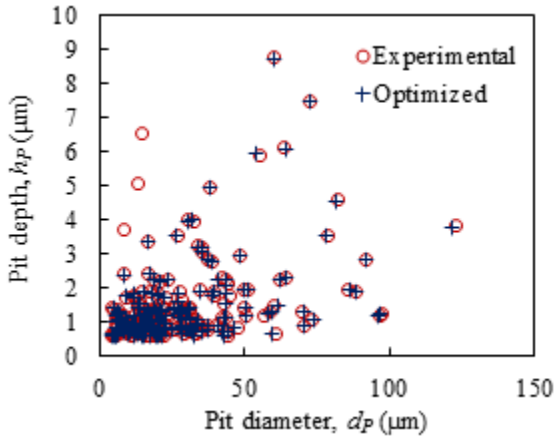

Fig. 2.20 Comparison of pit depth and diameter for experimental and optimized pit, cavitation test condition: upstream pressure 40 bar and exposure time 2 sec.

As an example, Fig. 2.20 shows a comparison of experimental and simulated pit depth and diameter. Simulated data represent the pit depth and diameter when the solution is optimized. Out of 178 pits, all pits were solved very accurately other than three pits, which are difficult to solve. The difficulty arises when a pit has a very high shape factor. In such cases, the strain into the material goes beyond the maximum strain defined in the material property for the simulation and crashes the simulation. Occurrence of this problem is rare provided the exposure time in cavitation pitting test was sufficiently less to avoid overlapping of pits.

2.6. Discussion

The hydrodynamic peak pressure (σ_H) and size (d_H) corresponding to each pit at different flow pressures have been estimated using the numerical inverse method, as discussed in Sec. 2.5. As an example, Fig. 2.21 shows the values of σ_H and d_H corresponding to all pits at the flow pressure of 40 bar. Such a distribution of impact loads as a function of stress and size is considered here as an estimate of the cavitation intensity also called

aggressiveness of the cavitating flow. Even though it was determined using a given material on which a pitting test was carried out, it is expected to characterize the only liquid flow. This was checked in [3] by considering different materials.

Such a distribution of impact loads gives representative loading conditions for this particular flow that can later be used in a FE simulation in order to predict the long-term behavior of the material. The principle of such a simulation would be to apply repetitively, on the material surface, the whole spectrum of impact loads a large number of times by randomly choosing the impact point for each load. By introducing an appropriate damage model of the material, it should be possible to predict the evolution of mass loss versus the exposure time [114].

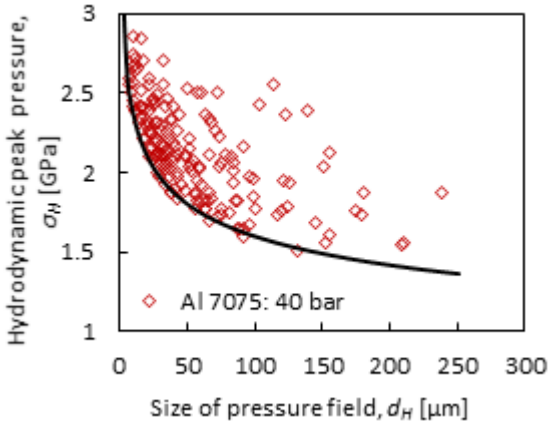

Fig. 2.21 Hydrodynamic peak pressure and sizes for all pits formed in Al 7075 under cavitating flow at 40 bar for 2 sec. Minimum depth of pit detected is greater than 0.5 µm.

As can be seen in Fig. 2.21, impacts of smaller size are associated with higher peak pressure and in most of the cases, as the impact size increases the peak pressure decreases. For a given size of impact, there exists a limit to the minimum value of the associated pressure to form a cavitation pit deeper than the detectable depth. In the current study, a 0.5 µm cut-off depth (h_{cut}) is used for the detection of pits or, in other words, the minimum measured pit depth is close to 0.5 µm. The variation of limiting minimum value of the peak pressure ($\sigma_{H\,min}$) with the impact size (d_H) for a given cut-off depth (h_{cut}) follows a power law behavior and can be derived from Eq. (2.9) and Eq. (2.10) as shown in Eq. (2.14).

$$\sigma_{H\,min} = \sigma^* \left(\frac{h_{cut}}{k d_H}\right)^{1/\beta'} \tag{2.14}$$

Eq. (2.14) is plotted in Fig. 2.21 (solid line) for $h_{cut} = 0.5$ µm with the same values of material constants σ^*, k and β' as obtained earlier in Sec. 2.3.1 and is found to clearly define the lower bound of the data points. Eq. (2.14) does not change with the flow pressure or velocity of the cavitating fluid as all the parameters depend on the material only. This can be verified from Fig. 2.22 as the distribution of σ_H and d_H for different cavitating flows, 10 bar and 40 bar, shows identical lower bound. In addition, Fig. 2.22 does not exhibit a clear

influence of the operating pressure on the values of the impact pressures and sizes since the material was the same for the two flow conditions.

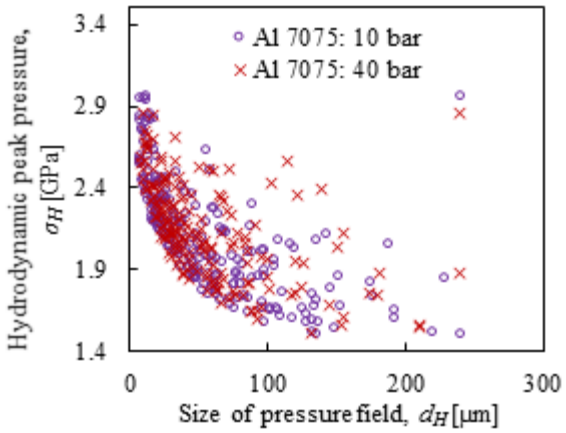

Fig. 2.22 Distribution of peak hydrodynamic pressures and corresponding sizes of pressure field associated with bubbles formed at different flow pressures, 10 bar and 40 bar.

With increase in the flow velocity, the cumulative frequency of the hydrodynamic impacts increases predominantly as shown in Fig. 2.23 and Fig. 2.24. The Fig. 2.23 represents the cumulative frequency of impacts per unit area and unit time having peak pressure σ_H greater than any given value on the horizontal axis, whereas Fig. 2.24 represents the cumulative frequency of impacts per unit area and unit time having size of the pressure field greater than any given value on the horizontal axis. On a semi-log plot, the observed linear behavior indicates an exponential expression for the cumulative frequency of impacts versus the impact diameter d_H.

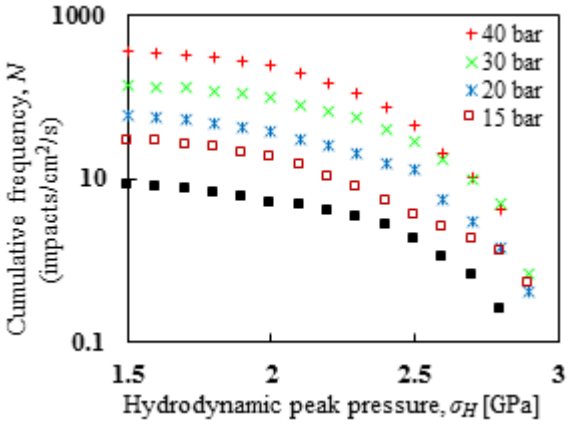

Fig. 2.23 Influence of cavitation flow pressure on cumulative frequency of impact per unit area and unit time having peak pressure σ_H greater than any given value. The vertical axis is on log scale.

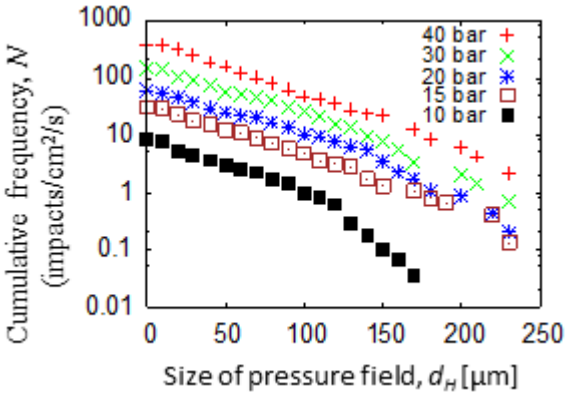

Fig. 2.24 Influence of cavitation flow pressure on cumulative frequency of bubbles per unit area and unit time having size of the pressure field greater than any given value. Almost linear plot on semi-log scale represent exponential behavior.

As discussed in Sec. 2.4, after cavitation pitting tests on Al-7075 at different flow pressures, all the measurements of cavitation pit diameters were obtained by using the FCOD method at 50% of pit depth. Then cumulative frequency of pits or cumulative pitting rate ($\dot{N}$), defined as the total number of pits per unit area and unit exposure time that have diameters greater than any given value on the horizontal axis versus pit diameter can be plotted as shown in Fig. 2.25. The cumulative pitting rate approximately follows an exponential behavior. Now we can approximate the cumulative pitting rate ($\dot{N}$) behavior with the exponential law given by Franc *et al*. [63]] as shown in Eq. (2.15).

$$\dot{N} = \frac{8}{\pi\delta^2 t_{cov}} e^{-2d_P/\delta} \tag{2.15}$$

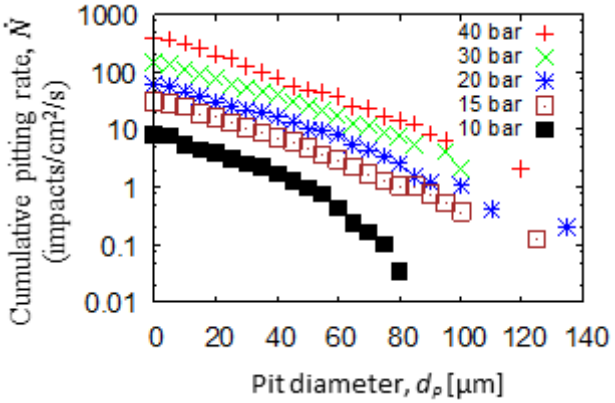

Fig. 2.25 Cumulative pitting rate of Al 7075 material as a function of pit diameter for different values of upstream pressure and constant cavitation number. Pit detected by using a constant cut-off depth of 0.5 µm and diameter measured at fractional cut-off depth of 50.0%. Straight lines on semi-log plot represent exponential distribution.

Here δ and t_{cov} are two fitting parameters known as characteristic pit diameter and coverage time respectively. These two parameters are important to describe different phenomena involved in cavitation erosion [63]. Using the constant cut-off depth method for the pit diameter determination, the parameters δ and t_{cov} could not be

measured reliably because of their dependency on the cut-off depth. The current fractional cut-off depth method of pit diameter determination overcomes this problem. Values of δ and t_{cov} are estimated and plotted in Fig. 2.26(a) and Fig. 2.26(b) respectively.

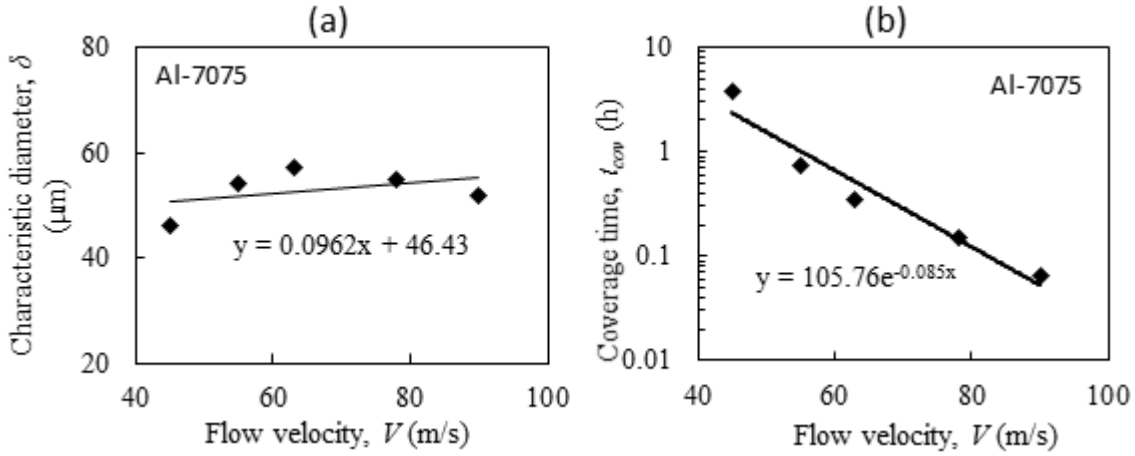

Fig. 2.26 Effect of flow velocity on- (a) characteristic pit diameter δ and, (b) coverage time t_{cov}

As shown in Fig. 2.26(a), the characteristic diameter (δ) of the pits increases very slowly with the increase in the flow velocity or upstream pressure of the cavitating fluid. The coverage time t_{cov} decreases exponentially with the increase in the flow velocity as shown in Fig. 2.26(b).

Simulation of cavitation pitting (Sec. 2.3.1) shows that no pit forms at 1 GPa peak pressure and from Fig. 2.23 it is also clear that the peak stress did not reach 3 GPa for any of the experimental pits obtained under different flow velocities. For all the pits detected by the 0.5 μm cut-off depth, the peak pressure varies from 1.5 GPa to less than 3 GPa. The probability of occurrence of pressure peaks of higher amplitude decreases rapidly. From a statistical point of view, the estimated values of impact loads are in good agreement with the previously obtained impact loads by Carnelli *et al*. [67], although the material properties were characterized differently and the method of load estimation was different.

2.7. Summary and conclusions

One of the primary aims of the current study was a better estimation of depth and diameter of cavitation pits formed under different cavitating flows. A cut-off depth is required to avoid error in the measurements of the pits due to the surface noise. The use of a fractional cut-off depth (FCOD) method to estimate the pit diameter is found to be better than the conventional constant cut-off depth (CCOD) method where the pit diameter depends on the arbitrary choice of the cut-off depth.

The second objective of the current study was to estimate the hydrodynamic peak pressure (σ_H) and the size of the pressure field (d_H) associated with a single bubble collapse that led to a pit of a given depth and diameter. Two methods namely analytical inverse method and numerical inverse method are proposed. The first analytical method predicts σ_H and d_H from pit depth and diameter using simple equations - (Eq. (2.9) and

Eq. (2.10)). The second method is based upon a numerical technique that provides σ_H and d_H after numerically reproducing a given experimental pit and is found to be more accurate than the analytical one after three iterations.

The impact load parameters (σ_H, d_H) corresponding to all pits obtained from a pitting test can be considered as the signature of the cavitating flow and a measure of its aggressiveness. Such a combination of an experimental and a numerical method based on both pitting tests and FE computations provides an alternative to direct measurement of impact loads using conventional pressure sensors that present serious limitations as mentioned in the introduction.

Apart from the above-mentioned facts, in the current study some observations related to cavitation pitting have been made as follows:-

- FE computations have shown that the hydrodynamic peak pressure is directly correlated to the pit shape factor and follows a logarithmic law. Moreover, the radial extent of the pressure distribution is virtually proportional to the pit diameter defined on the basis of the FCOD method at mid pit depth (FCOD = 50%).
- There exists a common normalized pit shape for all cavitation pits (when the pit depth is normalized by the maximum depth and the corresponding diameter is normalized by the maximum diameter).
- A Gaussian pressure distribution for the applied load appears to be realistic since it leads to a computed mean pit shape close to the measured one.
- It was also established that a one-to-one correspondence exists between the hydrodynamic load parameters (σ_H, d_H) and the pit geometrical parameters (h_P, d_P) that makes the proposed inverse technique workable in practice.
- From the FEM computations, it was found that, during the unloading phase that follows a hydrodynamic impact, the material may undergoes plastic deformation if the impact load was high enough. This way, the material could accumulate plastic strain during multiple impacts and eventually lead to fatigue failure.

2.8. Some highlights and remarks

Some highlights of the chapter:

- Gaussian pressure field profile is relevant to cavitation impact loading.
- Fractional cut-off depth (FCOD) method characterizes better the pit dimensions.
- The FCOD method provide better estimation of characteristic pit diameter (δ) and coverage time (t_{cov}).
- One to one correspondence between cavitation pits and impact loads is found.
- An analytical method is proposed for impact load prediction.
- A numerical inverse method based on pitting tests and FEM simulations accurately estimates the impact loads.
- For high impact loading, plastic deformation occurs even during the unloading stage i.e. after the impact load is removed.

Remarks:

In this chapter (Chapter-2) a few of the primary objectives (item numbers 1 and 3 as discussed in Sec. 1.5) and also some parts of the item aim number 2 have been achieved. The rests are dealt with in the following chapters.

Chapter-3

3. Using the target material as a pressure sensor in cavitation pitting

This chapter contains the results of a journal paper [3] whose details are given below. However, additional data and results are included which could not be included in the paper. The paper has been accepted for publication in the "Journal of Applied Physics" in September 2015.

Cavitation erosion: using the target material as a pressure sensor

Samir Chandra Roy[1,a)], **Jean-Pierre Franc**[2] and **Marc Fivel**[1]

[1]Science and Engineering of Materials and Processes (SIMaP-GPM2), University Grenoble Alpes / CNRS, F-38000 Grenoble, France
[2]Laboratory of Geophysical and Industrial Flows (LEGI), University Grenoble Alpes / CNRS, F-38000 Grenoble, France

Abstract

Numerical prediction of mass loss due to cavitation erosion requires the knowledge of the hydrodynamic impact loads generated by cavitation bubble collapses. Experimental measurements of such impact loads using conventional pressure sensors are not reliable (if not impossible) due to the micron size and the very small duration of the loading. In this paper, a new method to estimate these loading conditions is proposed based on cavitation pitting tests and an iterative inverse finite element modeling. The principle of the method is as follows. First, numerous pits corresponding to localized plastically deformed regions are identified from a cavitation test performed in a dedicated tunnel. Then each pit is numerically reproduced by finite element simulations of the material response to a representative Gaussian pressure field supposed to mimic a single bubble collapse. This gives the size and pressure distribution of the bubble impacts. Prime objective of this study is to find out if the target material itself could be used as a pressure sensor or not, i.e. if the cavitation pits left on the surface of the tested specimen could provide the characteristics of the cavitating flow in terms of pressure fields independently of the target material. Pitting tests were done on three materials namely 7075 Aluminum alloy (Al-7075), 2205 duplex stainless steel (A-2205) and Nickel-Aluminum Bronze (NAB) at three different flow conditions and the impact loads have been estimated for each identified pit. Very interestingly a statistical analysis shows that the estimated impact loads are material independent at all flow conditions, provided the material properties are characterized properly. It is also shown that for some materials, the constitutive parameters obtained from compression tests are not satisfactory.

Keywords: *Cavitation pitting; Material characterization; Finite element simulation; Impact load estimation; Microstructure*

[a)] Electronic mail: roysam.nita@gmail.com or samir-chandra.roy@simap.grenoble-inp.fr (S. C. Roy)

3.1. Introduction

Cavitation erosion occurs in fluid machineries, pumps, pipes, ship propellers, valves and so on [115] mainly due to rapid fluctuation of fluid pressure associated with high velocity. Life prediction of such components depends on the prediction of cavitation erosion rate which requires the estimation of the impact loads generated by cavitation bubble collapse [74] and has been a challenging issue till date. Difficulties associated with the use of pressure sensor or CFD simulations have already been discussed in Sec. 1.3.3 and Sec. 2.1 that prevent accurate estimation.

In order to avoid these measurement difficulties, we have recently proposed a method in ([2] or Chapter-2 of this thesis) to estimate the hydrodynamic impact loads. The method consists in pitting tests as introduced by Knapp [69,70] and iterative inverse finite element (FE) simulations. The idea behind pitting tests is that each pit is a localized plastically deformed region and is the signature of a single bubble collapse. The principle of the method [2] is to numerically reproduce the experimental cavitation pits (characterized by pit depth, h_P and diameter, d_P measured at mid-depth) by FE modeling of the material response to a representative Gaussian pressure field (characterized by peak stress, σ_H, and radial extent, d_H). We have shown that a Gaussian type of pressure field could be considered relevant to the cavitation impact loading. Moreover, similar Gaussian pressure field has been used by other authors [48,81] as well for cavitation pitting simulation. The material behavior is modeled as elasto-plastic isotropic hardening. In the static simulations presented in [2], the dynamic behavior of cavitation pitting is taken into account by extrapolating the material properties to a high strain rate of 10^6 s^{-1} that corresponds to an impact duration of a microsecond[4]. Dynamic simulations were also conducted in order to investigate the limitations of such a static approach and discussed in ([4] or Chapter-4). More details regarding the material model and dynamic simulations are discussed in Sec. 3.2.

In this chapter, the inverse FE method proposed in [2] is applied on three materials namely 7075 Aluminum alloy (Al-7075), 2205 duplex stainless steel (A-2205) and Nickel-Aluminum Bronze (NAB) to estimate the impact loads and their radial extent. Pitting tests were done (testing method is explained in details in [62,63] or in Sec. 2.4) on these three materials at different cavitation flow conditions as discussed in Sec. 3.3.1.

Now, if the material properties are properly characterized, the estimated impact loads should be material independent or in other words the estimated impact loads should characterize the same flow condition irrespective of the material being used to capture them. Thus the characterization of the material properties is key to the accuracy of the estimated impact loads, and a special effort is made in this study to find out the most appropriate way of material characterization with respect to cavitation erosion phenomena.

Although nanoindentation test is used by many authors [49,67,68] to characterize the deformation behavior of materials under cavitation impact, the strain rate involved in cavitation is significantly higher (typically 10^3 – 10^4 s^{-1} or even more [116]) than those achievable in conventional indentation devices. In the current study, compression and nanoindentation tests have been supported by split Hopkinson pressure bar (SHPB) tests in order to characterize the dynamic material behavior relevant to cavitation loading conditions. A special emphasis is put on the importance of local characterization (as obtained by nanoindentation test) of

heterogeneous material such as Al-7075 compared to the bulk mechanical characterization (as obtained by compression test).

Thus, this study gives an overall view on the usability of the target material as a sensor, characterization of material parameters and the difficulties associated with such methods as well. In Sec. 3.2, characterization of the material properties is discussed in details. In Sec. 3.3, the main results obtained by the inverse FE method are shown and Sec. 3.4 describes the microstructure of the three materials considered in this study in order to discuss potential differences between different testing techniques.

3.2. Constitutive laws and material characterization

3.2.1. Preview of constitutive models for high rate deformation

There are many constitutive models available for characterizing high rate deformation behavior of materials, although there is not a single universal model that can be used for all the types of material at all scales [117]. A few, for examples, physically based or phenomenological models commonly used in computational mechanics are Cowper-Symonds power law model [118], Johnson-Cook (JC) model [119,120], Zerilli and Armstrong (ZA) model [121], Khan-Huang (KH) model [122], Mechanical Threshold Stress (MTS) model [123]. These models are preferred for having a relatively low number of parameters and ease to obtain by a limited number of experiments.

Cowper-Symonds model is the simplest form of strain rate dependent hardening law, where the equivalent plastic strain rate ($\dot{\varepsilon}_p$) is defined as a power function of overstress due to strain rate and/or temperature effect, given as-

$$\dot{\varepsilon}_p = C_4\left(\bar{\sigma} - \sigma_y\right)^{C_5} \tag{3.1}$$

Were, $\bar{\sigma}$ is the flow stress, σ_y the static yield strength or strength at a reference strain rate, and C_4 and C_5 are material constants. The model is widely used in computational mechanics for large strain analysis [124,125] and also available in commonly used numerical code like ABAQUS. The model does not take into account the temperature and strain rate effects separately.

Johnson-Cook Model is the most-widely used pure empirical model for dynamic characterization [126,127] and readily available in the numerical codes like ABAQUS, LsDyna etc. This model explicitly takes into account the hardening due to strain and strain rate, and also thermal softening due to high temperature caused by adiabatic heating. The model is given as-

$$\bar{\sigma} = \left(\sigma_y + K\varepsilon_p^n\right)\left(1 + C\,\ln\frac{\dot{\varepsilon}_p}{\dot{\varepsilon}_0}\right)\left(1 - \bar{T}^{m'}\right) \tag{3.2}$$

Here, ε_p is the equivalent plastic strain, $\dot{\varepsilon}_p$ is the equivalent plastic strain rate and $\dot{\varepsilon}_0$ is the reference strain rate (generally taken as $\dot{\varepsilon}_0 = 1$ s^{-1}, but could be different as well) at which the yield strength σ_y, strength coefficient

K and strain hardening exponent *n* have been estimated. *C* is the strain rate sensitivity parameter. The material constant m' accounts for thermal softening. $\bar{T}$ is a non-dimensional temperature defined as-

$$\bar{T} = \begin{Bmatrix} 0 & , & T < T_{transition} \\ \dfrac{T - T_{transition}}{T_{melt} - T_{transition}} & , & T_{transition} \le T \le T_{melt} \\ 1 & , & T > T_{melt} \end{Bmatrix} \tag{3.3}$$

Where, T, T_{melt} and $T_{transition}$ are current, melting and transition temperatures respectively. At or below the transition temperature JC model assumes no temperature effect to the flow stress. At reference strain rate ($\dot{\varepsilon}_0$), which is generally low compared to the higher strain rate of 1000 s^{-1} or more for which the model is developed, the sample temperature remains below the transition temperature as there is enough time for the heat generated due to plastic work to dissipate. Then the flow stress depends only on plastic strain.

Another extensively used model is Zerilli-Armstrong (ZA) model, which is a dislocation dynamics-based constitutive model that uses different stress-strain relationships for different materials depending on their crystal structures like BCC (body centered cubic) or FCC (face centered cubic). Different stress-strain relationships are proposed to correctly account for dislocation characteristic that depends on the material structure. For FCC materials the flow stress is given by the following relationship-

$$\bar{\sigma} = \Delta\sigma_G' + C_6 l'^{-1/2} + C_7 \varepsilon_p^{1/2} \exp\left(-C_8 T + C_9 T \ln\left(\dot{\varepsilon}_p\right)\right) \tag{3.4}$$

Whereas for BCC materials the flow stress is given by the following relationship-

$$\bar{\sigma} = \Delta\sigma_G' + C_6 l'^{-1/2} + C_{10} \exp\left(-C_8 T + C_9 T \ln\left(\dot{\varepsilon}_p\right)\right) + C_{11} \varepsilon_p^n \tag{3.5}$$

Here $\Delta\sigma_G' + C_6 l'^{-1/2}$ is a constant that takes into account the initial state of the material. The first term accounts for solutes and the initial dislocation density, whereas the second term takes into account the grain size or boundary effect where C_6 and l' represent the microstructural stress intensity (SI unit is Pa $m^{1/2}$) and average grain diameter respectively (SI unit m). The material constants C_7, C_{10} and C_{11} have units of stress (Pa in SI) and the constants C_8 and C_9 have units of temperature (K^{-1} in absolute scale). The ZA model like the JC model takes into account the effect of strain, strain rate and temperature and initially it was considered to be an improvement over the JC model [121], however, authors in [117] have shown poor predictability of the ZA model in various cases.

The model proposed by Khan-Huang (KH) [122] is applicable for elasto-visco-plastic strain-hardening material with arbitrary loading histories. However, their model does not consider temperature effect and thus describe well the material behavior that has a very low thermal softening effect, or in other word strong work hardening at large strain rates. The authors in [123] have proposed a similar dislocation dynamics based phenomenological model to calculate the flow stress as a function of strain, strain rate and temperature. However, the model is based on the mechanical threshold stress (i.e. flow stress of a material at 0 K temperature) and popularly known as MTS model. This model is also popular but the large number of parameters and its complexity in deriving the parameters limit the use of this model. The uncertainty involved

with the ZA or MTS model increases with the complexity of the materials structure, loading histories, heat-treatments used that changes the grain sizes and orientations or presence of solute or dispersions etc. Thus in the current study, for simplicity, the slightly modified JC plasticity model is used as discussed in next Sec. 3.2.2.

3.2.2. Material and constitutive law used in the current study

Three materials- 7075 Aluminum alloy (Al-7075), 2205 duplex stainless steel (A-2205) and Nickel-Aluminum Bronze (NAB) have been considered for the current study. All the materials are commercially available and supplied by Office of Naval Research (USA). The Al-7075 alloy because of its high strength to weight ratio mostly preferred as a structural material for automobile, aircrafts or other similar applications [128]. The A-2205 has excellent resistance to general or localized corrosion, stress corrosion cracking and cavitation erosion along with high strength and low cost rendered by a reduced amount of Ni and Mo [129]. These all together makes it a favorable candidate for oil, gas, petrochemical industries and marine applications. The NAB material is widely used in marine applications such as propulsion and seawater handling systems [130,131]. It has comparable strength and good corrosion resistance attributed to the quick formation of protective double passivation layers. The microstructural details of these materials are discussed in Sec. 3.4.

The Johnson-Cook (JC) plasticity model in the form given by Eq. (3.6) (without considering the thermal softening part) is used to characterize the hardening behavior of the materials (see [120] for more details about JC plasticity model).

$$\bar{\sigma} = \left(\sigma_y + K\varepsilon_p^n\right)\left(1 + C\ln\frac{\dot{\varepsilon}_p}{\dot{\varepsilon}_0}\right) \tag{3.6}$$

At the reference strain rate $\dot{\varepsilon}_p = \dot{\varepsilon}_0$ and Eq. (3.6) becomes a simple Ramberg-Osgood type equation where the hardening is a function of plastic strain ε_p only.

Generally, nanoindentation is preferred to characterize the material behavior in cavitation pitting [49,67], whereas, the compression or tension test is commonly used to verify the material constitutive parameters obtained by nanoindentation test [132–134]. Hence in this study, both compression and nanoindentation tests were done to obtain the constitutive parameters. Young's modulus (E), Poisson's ratio (ν) and density (ρ) of the materials are considered to be same in both compression and nanoindentation, and are given in Table 3.1. Reference strain rate ($\dot{\varepsilon}_0$) is considered to be 1.0 s^{-1} for the compression tests and 0.05 s^{-1} for the nanoindentation tests. It should be emphasized that the use of different reference strain rates ($\dot{\varepsilon}_0$) are allowed in the empirical JC plasticity model.

3.2.3. Material properties obtained by compression tests

Cylindrical specimens of equal length and diameter of 8 mm have been used. Compression tests were done on the three materials at reference strain rate 1.0 s^{-1} (shown in Fig. 3.2) using a conventional servo-hydraulic compression testing apparatus as shown in Fig. 3.1 and, σ_y, K and n were estimated as shown in Table 3.1 by

fitting Eq. (3.6) with C = 0 (a numerical assumption to suppress the strain rate sensitivity, similar to putting $\dot{\varepsilon}_p = \dot{\varepsilon}_0$). The fitted curves are shown in Fig. 3.2 as the thin black lines.

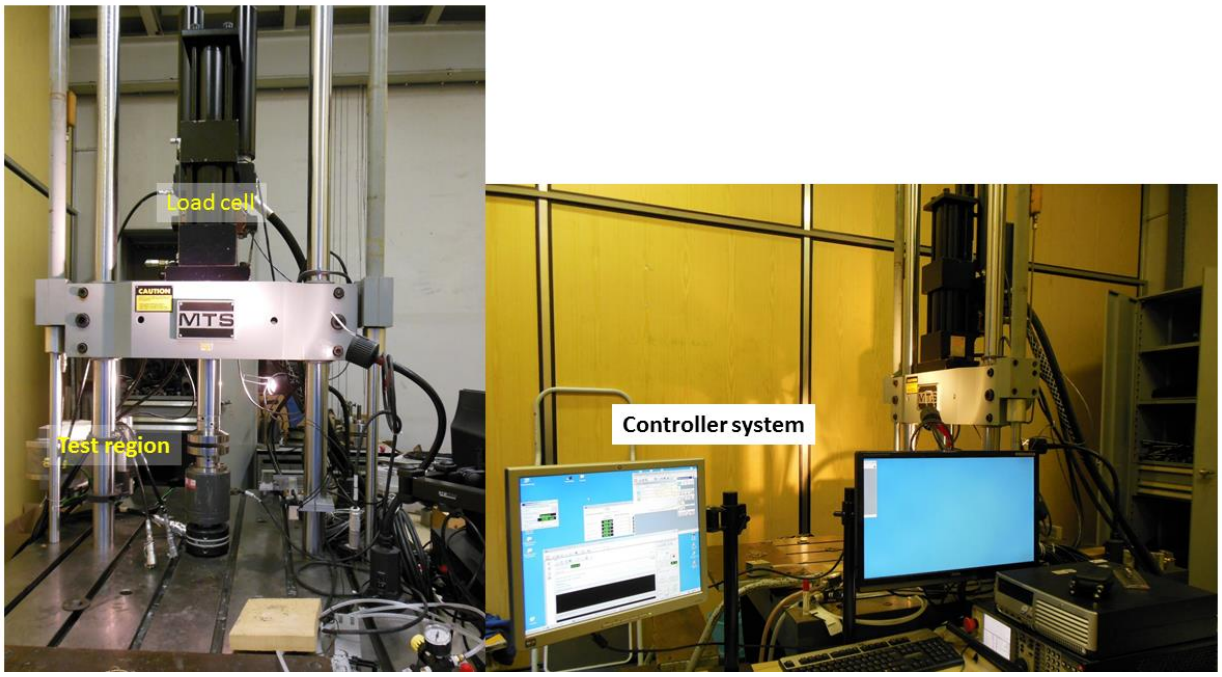

Fig. 3.1 Compression test apparatus used for the lower strain rate compression test in the current study

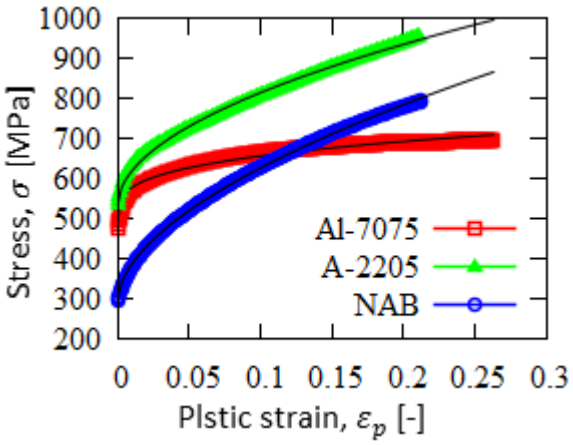

Fig. 3.2 Compression stress-strain curves (thick lines) of Al-7075, A-2205 and NAB obtained at strain rate 1.0 s^{-1} using a servo-hydraulic controlled testing machine and fitted curves (thin lines) obtained using Eq. (3.6) with C=0.

Table 3.1 Material density, Poisson's ratio, Young's modulus and compressive properties at strain rate 1.0 s^{-1}

Material	σ_y **[MPa]**	K **[MPa]**	n	E **[GPa]**	ν	ρ **(kg/m^3)**
Al-7075	500	312	0.29	71.9	0.33	2810
A-2205	560	917	0.51	186	0.30	7805
NAB	300	1205	0.56	122	0.32	7580

3.2.4. Strain rate sensitivity

In cavitation pitting, the target material deforms compressively in a confined region at a very high strain rate. Thus inertial and strain rate effect become important and should be taken into account in the simulations. Though it is debatable, typical impact duration in cavitation pitting is believed to be in the order of few microseconds [38,74] and recently authors [4,48] have shown that if the impact duration is greater than 1 μs then the inertial effect becomes insignificant. Thus we could reliably use static FE analysis for simulating cavitation impact behavior of materials, provided strain rate effect is considered. It can reasonable be assumed that the strain may exceed 30% to form a cavitation pit. Of course strain is not uniform throughout the deformed region as can be seen in Sec. 2.3.3. Thus if we consider that 30% of strain occurs in cavitation pitting in 1 μs or less time, the strain rate would be 3×10^5 s^{-1} or more. In our study to take into account the strain rate effect in cavitation pitting, the material properties were extrapolated to a strain rate of 10^6 s^{-1}, by using the JC plasticity model (Eq. (3.6)). In reality strain rate will depend on the impact duration which again depends on bubble size, pressure gradient and standoff distance [81]. However, it should be mentioned that, till date, it is not experimentally possible to know the impact duration corresponding to each pit resulted from impact loading of cavitation bubble collapse. Thus, for the inverse FE method [2] to estimate impact load parameters from cavitation pit parameters, complete dynamic explicit analysis including strain rate sensitivity where impact duration is an essential input parameter, is out of scope in the present context. From statistical point of view, static FE analysis with the extrapolated material properties seems to be a reliable option.

To verify such a high strain rate used in the inverse FE method, dynamic explicit simulations of cavitation pitting with the same material model (Eq. (3.6)), which now additionally takes into account the inertial and strain rate effects, were done on these three materials. For that purpose, the Gaussian pressure field in [2] is modified as given in Eq. (3.7) for dynamic simulation to take into account the temporal evolution of stress. It was observed that for characteristic impact duration $t_H \approx 1\ \mu s$, the maximum principle strain rates into all the three materials were close to 10^6 s^{-1}. This is discussed further in Sec. 4.4.3 in Chapter-4.

$$\sigma = \sigma_H \exp\left(-\left(\frac{2r}{d_H}\right)^2\right)\exp\left(-\left(\frac{t-t_{max}}{t_H}\right)^2\right) \tag{3.7}$$

Here, t represents the time, t_{max} is the time when $\sigma = \sigma_H$ and t_H is the characteristic impact duration in a similar sense of d_H.

In order to estimate the strain rate sensitivity, additional compression tests complemented by Split Hopkinson Pressure Bar (SHPB) tests were done on the three materials at strain rates ranging from 0.001 to ~1500 s^{-1}. The SHPB testing method and data analysis techniques to obtained stress-strain curves have been discussed in details in Appendix A. For SHPB tests also cylindrical specimens of equal length and diameter of 8 mm have been used. SHPB tests were done particularly for the highest strain rates, > 10 s^{-1} (additional details of experimental setup and analysis procedure for SHPB test can be found in [135]).

The strain rate sensitivity parameter *C* is estimated by fitting Eq. (3.8) to the experimental data as show in Fig. 3.3. To avoid thermal softening *C* is estimated at a low amount of plastic strain (<2%). As can be seen in Fig. 3.3, for all the three materials the values of C estimated at 0.5% and 1.5% of plastic strains are almost same.

$$R' = \frac{\bar{\sigma}}{\sigma_y + K\varepsilon_p^n} = 1 + C \ln \frac{\dot{\varepsilon}_p}{\dot{\varepsilon}_0} \tag{3.8}$$

In Eq. (3.8), R' represents the stress ratio at strain rate $\dot{\varepsilon}_p$ with respect to $\dot{\varepsilon}_0$. As expected for metals, the plot of R' versus strain rate follows almost a linear relationship in a semi-log plot. Values of *C* were estimated to be 0.0068, 0.031 and 0.0119 for Al-7075, A-2205 and NAB respectively. It can be seen that A-2205 has the maximum strain rate sensitivity whereas the Al-7075 has the minimum strain rate sensitivity.

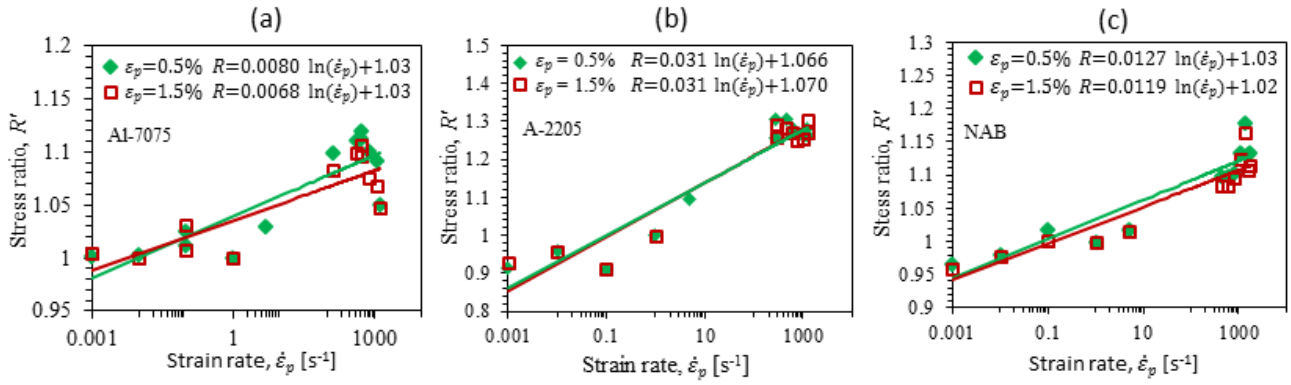

Fig. 3.3 Stress ratio versus strain rate plot on semi-log scale shows almost linear behavior for all three materials, (a) Al-7075, (b) A-2205 and (c) NAB. Strain rate sensitivity C is estimated at 0.5% and 1.5% of plastic strains.

Stress-strain curves at strain rate 10^6 s^{-1} (as shown in Fig. 3.4) were constructed from the reference curves in Fig. 3.2 by using the estimated strain rate sensitivity in Eq. (3.6). These stress-strain curves are now used for the FE simulations of cavitation pitting to estimate the hydrodynamic impact parameters σ_H and d_H from the cavitation pit geometry by using the inverse FE method.

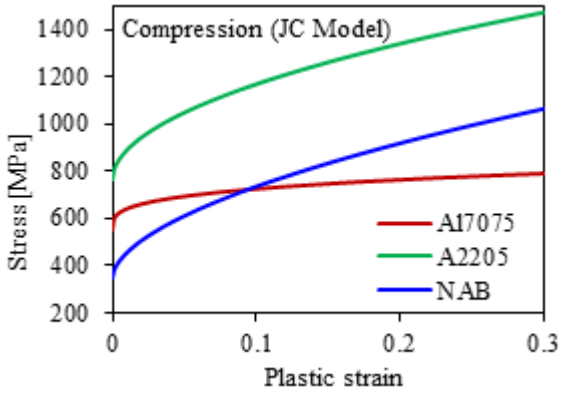

Fig. 3.4 Stress-strain curves extrapolated to a strain rate of 10^6 s^{-1} using the Johnson-Cook plasticity model (Eq. (3.6)). Reference stress-strain curves were obtained by compression tests.

3.2.5. Material properties obtained by nanoindentation tests

Because of similarity in material deformation behavior during nanoindentation and cavitation pitting, nanoindentation tests were conducted on these three materials at a strain rate of 0.05 s^{-1} using a spherical diamond (Young's modulus, E = 1141 GPa and Poisson's ratio, ν = 0.07) indenter of nominal radius, R = 9.46 µm. Sample preparation consists in mechanical polishing phases using sandpapers by gradually reducing grit size until 8.4 µm (grade P2500), followed by a polishing with diamond paste gradually reducing the size from 6 to 1 µm and finally by using colloidal silica of 0.03 µm size.

Traditionally material properties from nanoindentation test results are obtained by using popular Oliver-Pharr method along with Tabors equation for indentation strain, as discussed in Appendix B. This traditional approach suffers from serious limitations and are highlighted in Appendix B. To avoid those limitations, in the current study the material properties were obtained by FE simulations of nanoindentation with arbitrarily defined material parameters while comparing the simulated and experimental load displacement curves. The arbitrarily defined material properties also include compression test data. Now-a-days this is a very popular practice to obtain nanoindentation material properties by inverse numerical method using FE simulations [136,137]. The background of the method adopted here is as proposed by Moussa *et al.*[136]. Nanoindentation simulations were done in the FE code ABAQUS using a 2D axisymmetric model with four node quadratic elements (CAX4R). The mesh and model used is similar to that of Fig. 2.1, however no infinite element has been used, instead the domain size was kept significantly bigger 150 times larger than the indenter radius to avoid any boundary effect. Finite sliding, node-to-surface contact formulation with a coefficient of friction 0.1 between the indenter and sample material is used to model the contact. The indenter was modeled as an elastic material, whereas, the test material was modeled as an isotropic elasto-plastic material. ABAQUS static simulations were conducted.

It was found that the nanoindentation simulations performed with the material constitutive parameters estimated from the compression test conducted at a strain rate of 0.05 s^{-1}, yielded almost the same load-displacement curve for A-2205 and NAB, as shown in Fig. 3.5(a) and 4(b) respectively. Whereas, for Al-7075 the discrepancy is significant, see Fig. 3.5(c). Thus it was concluded that for A-2205 and NAB, the compression test describes well the nanoindentation behavior, which is not true for Al-7075. One important fact in Fig. 3.5(c) is that the simulated material behavior is harder than the real nanoindentation behavior of the material. The reason of this discrepancy for Al-7075 is discussed in details in Sec. 3.4.

For Al-7075, real material properties were obtained by varying the constitutive parameters (σ_y, K and n) in the FE simulations in order to fit the experimental load-displacement curve. A large number of FE simulations were done for σ_y=200-500 MPa, K=150-450 MPa and n=0.08-0.4. The root mean square error between simulated and experimental load-displacement curves was estimated as presented in [136]. Unlike what the authors found in [136], we did not get a unique solution for the constitutive parameters, but several sets of constitutive parameters yielded almost the same load-displacement curve for which the errors were smaller than 8 mN and considered as acceptable. An example is shown in Fig. 3.5(d). All the stress-strain curves for which errors are smaller than 8 mN are shown in Fig. 3.6 by dotted lines. An average curve of all of these

curves (dashed line) is taken as the characteristic of the material behavior. As can be seen, the nanoindentation strength of the material is significantly reduced compared to the compressive strength (solid line).

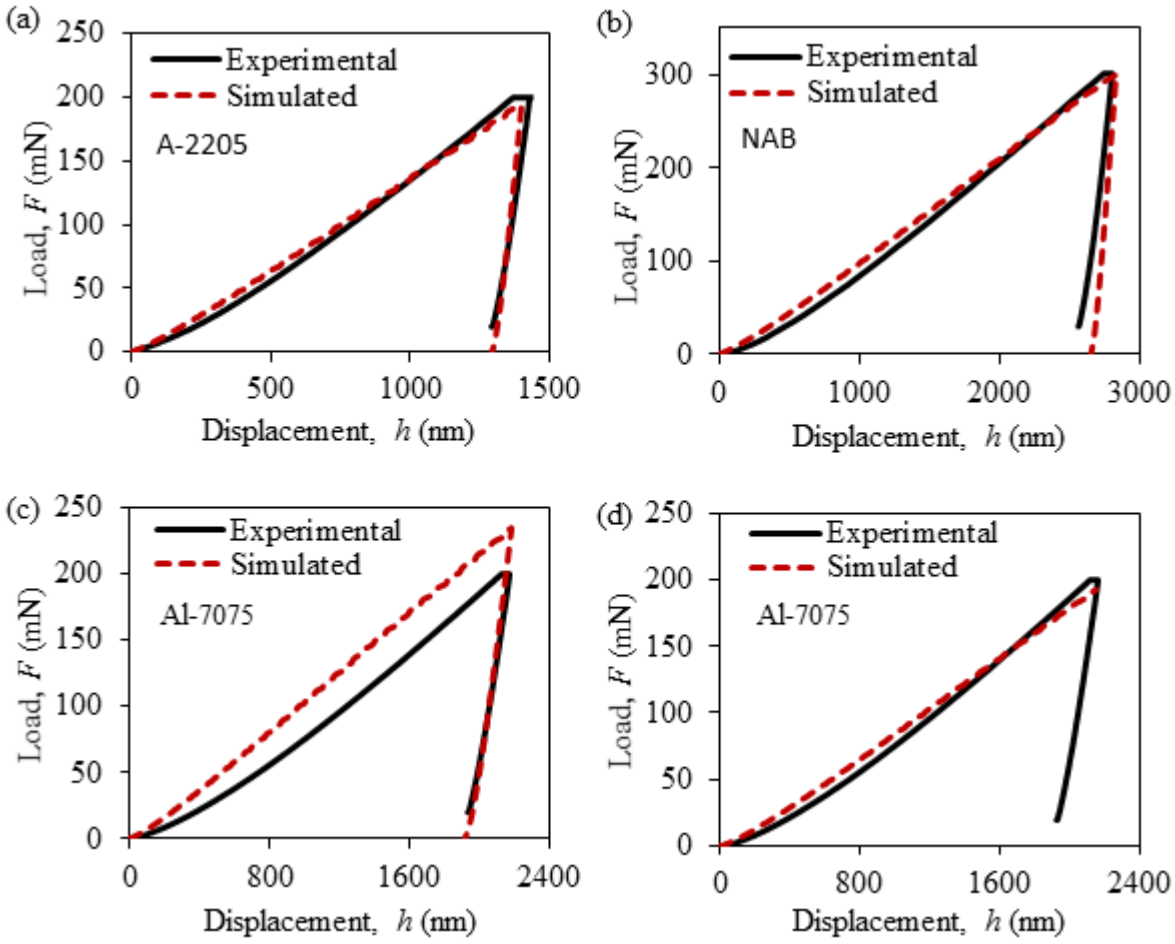

Fig. 3.5 Comparison of experimental and simulated nanoindentation load-displacement curves for all the three materials. The material properties obtained by compression tests (Table 3.1) gave the acceptable solution for (a) A-2205 and (b) NAB but not for (c) Al-7075. (d) The acceptable solution for Al-7075 is obtained by manually optimizing the constitutive parameters as discussed in Sec. 3.2.5.

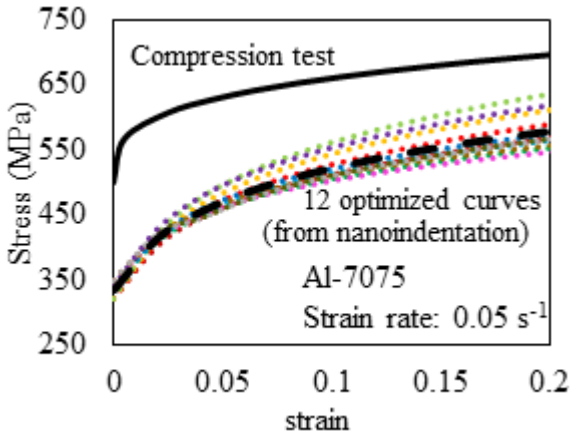

Fig. 3.6 Compression stress-strain curves at strain rate 0.05 s^{-1}. The 12 optimized curves correspond to nanoindentation stress-strain curves for which the errors between simulated and experimental load-displacement curves were < 8 mN.

The estimated material properties that are characteristics of nanoindentation behavior at a strain rate of 0.05 s^{-1} are given in Table 3.2 for all the three materials. The comparison of Table 3.1 and Table 3.2 confirms that the material properties derived from compression and nanoindentation tests are almost identical for both A-2205 and NAB (the small discrepancies are due to differences in strain rates), whereas the discrepancy is significant for Al-7075.

Table 3.2 Nanoindentation material properties at strain rate 0.05 s^{-1}

Material	σ_y **[MPa]**	K **[MPa]**	n
Al-7075	335	396	0.3
A-2205	508	832	0.51
NAB	300	1150	0.58

These properties were extrapolated to a higher strain rate of 10^6 s^{-1} by using the JC plasticity model given by Eq. (3.6) for characterizing the cavitation pitting behavior. Strain rate sensitivity parameters of the materials (C) already estimated from compression and SHPB tests were used for the extrapolation. Fig. 3.7 shows the nanoindentation stress-strain curves extrapolated to a strain rate of 10^6 s^{-1} for all the three materials.

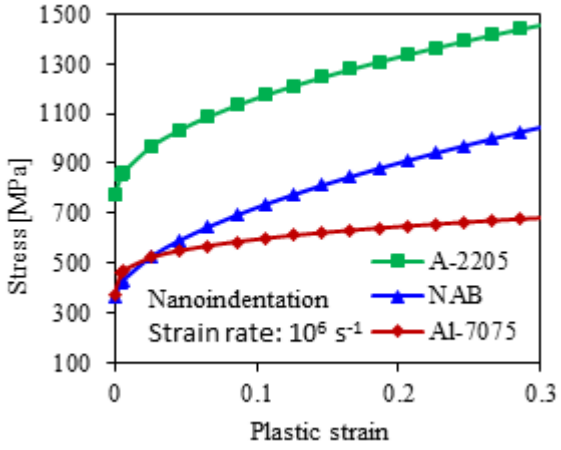

Fig. 3.7 Stress-strain curve obtained from the nanoindentation tests extrapolated to a strain rate of 10^6 s^{-1}.

In this study, the material properties were characterized in two different ways and in both the cases the strain rate sensitivity was estimated by compression tests and split Hopkinson Pressure bar tests). The influence of these two approaches on the estimated hydrodynamic impact parameters is now analyzed carefully (in the following Sec. 3.3) in order to find out the most reliable way of characterizing the material behavior for cavitation pitting.

3.3. Results

3.3.1. Estimation of hydrodynamic impact loads

Cavitation pitting tests were done on all the three materials at flow pressure of 10, 20 and 40 bar for a particular duration of time within their incubation period. All the tests were done in a high speed cavitation tunnel that produces geometrically similar flows. Details about the test sample preparation, experimental setup and testing methods are same as discussed in Sec. 2.4 in Chapter-2 (also can be found in [62,63]). The hydrodynamic impact load parameters- peak stresses σ_H and their radial extent d_H corresponding to all experimental pits have been estimated using the inverse FE method as presented in Sec. 2.5 in Chapter-2 (also presented [2]). As an example, Fig. 3.8 shows the experimental pits (circular points, for A-2205 material, pitting tested at 40 bar) that were numerically reproduced (square points) by the inverse FE method. On average, 3 simulations were required to get the optimum solution with a maximum error of 1.5 µm in pit diameter and 0.05 µm in pit depth. Fig. 3.9 shows the distribution of the hydrodynamic impact loads captured by the three materials at 40 bar. As it can be seen, the different materials depending on their strength capture different impacts. A-2205 has the maximum strength and captures the impacts of higher magnitudes. The data in Fig. 3.9 are obtained by using the material properties obtained by nanoindentation tests that were extrapolated to a strain rate 10^6 s^{-1}(see Fig. 3.7).

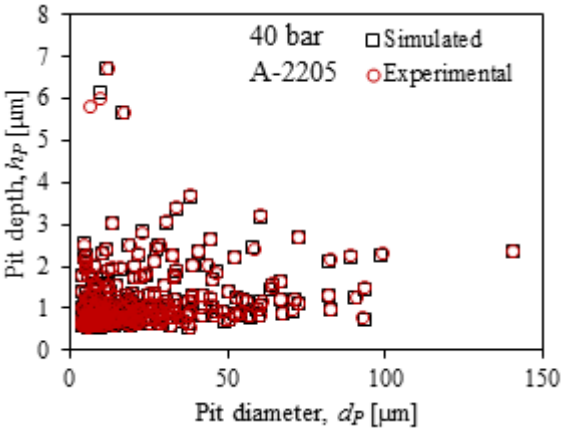

Fig. 3.8 Experimentally obtained 289 cavitation pits on A-2205 tested at 40 bar. Simulated data represent the pit dimensions when the corresponding experimental pits were optimized by the inverse FE method.

Comparing nanoindentation simulations with cavitation pits, Carnelli *et al.*[67] have estimated the strain induced in the material by the impact load required to form a cavitation pit of a given depth and diameter. Then using materials constitutive stress-strain relationship, they could estimate an equivalent stress which they refer as impact stress. Their method is based on Tabor's equation of strain [77], that they modified by assuming each cavitation pit as a spherical cap of the measured depth and diameter. Using their method, they could only estimate σ_H, but not d_H, which is also required for better characterization of the cavitating flow. Moreover it is not clear, if the stress calculated into the material could be used as a measure of the impact stress, because earlier in Chapeter-2 (or in [2]) we have seen that there is a scaling down of the stress from the hydrodynamic

impact to the material. To deform plastically a material the required stresses were few times higher than the yield strength, which could be due to triaxiality.

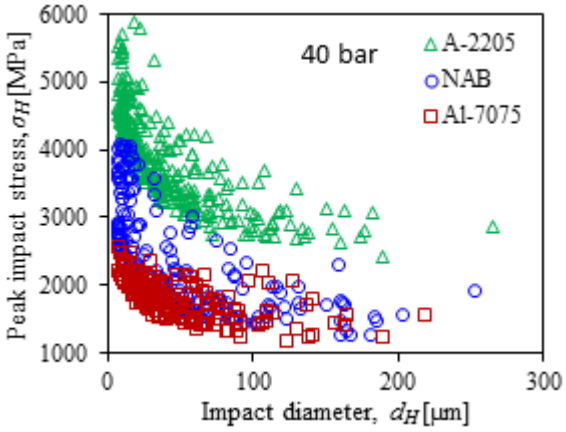

Fig. 3.9 Distribution of the hydrodynamic impact loads obtained by the inverse FE method at 40 bar of flow pressure. The impact loads for 650 pits have been shown here.

The aim here is to find out whether the target material itself can be used as a pressure sensor in cavitation pitting or not. If yes, then the question is- how to validate the estimated impact stresses, because as mentioned earlier it is not possible to accurately measure them experimentally. This is a new approach where the authors are trying to use different materials under the same flow condition to get material independent features which would characterize the flow condition only.

In a cavitating flow there would be a large number of impacts of different peak stresses and radial extents. Hence to characterize the flow, the number of impacts per unit area and per unit time for a given range of peak stress σ_H and radial extent d_H have been analyzed. This quantity in this chapter is termed as the 'normalized impact frequency', N (whose unit is impacts/cm^2/sec/µm/MPa).

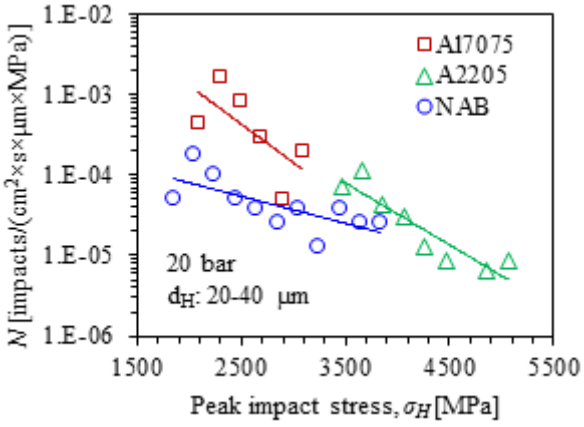

Fig. 3.10 Normalized impact frequency, N (Number of impacts/cm^2/sec/µm/MPa) is plotted as a function of peak impact stress σ_H for the hydrodynamic impact loads estimated at 20 bar. N is estimated at different ranges in the values of σ_H (with a band width of 200 MPa) for a given range of d_H=20-40 µm. The vertical axis is on log-scale. Compressive material properties extrapolated at strain rate 10^6 s^{-1} were used for FE simulations in the inverse method.

The impact load parameters σ_H and d_H have been estimated by the inverse FE method using the compressive material properties (Fig. 3.4) extrapolated to the strain rate of 10^6 s^{-1}. The normalized impact frequency N is plotted as a function of σ_H as shown in Fig. 3.10, where N is estimated for different ranges of σ_H (with a band width of 200 MPa) and for a given range of d_H = 20-40 µm. As can be seen, the data from the three materials do not follow a single trend, although all the tests were done at the same flow condition of 20 bar. Similar inconsistency was found at other flow conditions of 10 and 40 bar as well, and also for other values of d_H.

Now, by using the nanoindentation material properties extrapolated to strain rate 10^6 s^{-1} as shown in Fig. 3.7, the impact load parameters σ_H and d_H have been estimated by the inverse FE method. As before, the normalized impact frequency N is plotted as a function of σ_H for two different flow conditions of 10 and 40 bar, as shown in Fig. 3.11. As can be seen, in both the flow conditions, the normalized impact frequency N follows a unique trend in a semi-log plot (vertical axis on log-scale) irrespective of the material being used to capture them. A similar consistency is also found at flow condition of 20 bar upstream pressure, as well as for other values of d_H. This is a very conclusive result as it validates the applicability of a target material itself as a pressure sensor. We can also conclude that the impact frequency follows an exponential behavior with the impact stress. Note that a similar exponential behavior of impact load measured experimentally by using pressure transducer is reported by other authors as well [38]. The frequency of impact stress increases exponentially as the peak stress decreases. Moreover, as expected, the impact frequency also increases significantly with the flow pressure. Each material depending on its strength filters the hydrodynamic impacts, or in other word, provides the measurements of peak stresses within a certain range. It should be emphasized here, although we have used a single value of strain rate of 10^6 s^{-1} in the inverse FE method to estimate the impact load parameters, in reality the strain rate would be different depending on the bubble radius, pressure gradient, standoff distance [81]. However, as we have chosen a narrow band width of $d_H = 20 - 40$ µm in Fig. 3.11, the unique trend indicates the dynamic influence of the strain rate is not a critical issue here for such a statistical analysis.

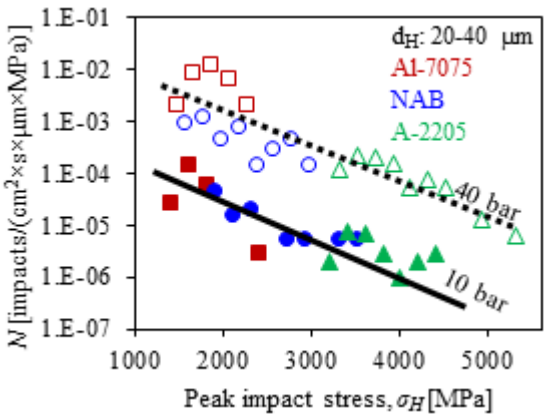

Fig. 3.11 Normalized impact frequency, N (Number of impacts/cm²/sec/µm/MPa) plotted as a function of the peak impact stress σ_H for the hydrodynamic impact loads estimated at 10 and 40 bar. N is estimated at different ranges in the values of σ_H (with a band width of 200 MPa) for a given range of d_H=20-40 µm. The vertical axis is on log-scale. Nanoindentation material properties extrapolated at strain rate 10^6 s^{-1} were used for the FE simulations in the inverse method.

We can expect some increase in the peak impact stresses with the flow pressure, but as the materials are identical we cannot capture those impacts of higher magnitudes whose frequency of occurrence is less. In order to capture them, pitting test should be carried out for a longer period of time but, by the mean time the material would get eroded out because of the repeated impacts of comparatively lower magnitudes. The only way to capture those impacts would be to use another material of even higher strength where impacts of comparatively lower magnitude would not be able to produce any cavitation pit.

In Fig. 3.12, N is plotted as a function of d_H for two different flow conditions of 10 and 40 bar. Here N is estimated at different ranges in the values of d_H (with a band width of 10 µm) for a given range of σ_H = 2400-2600 MPa. As can be seen, it is very difficult to capture impacts of similar magnitudes by using different materials as a sensor as their strengths are different. But all three materials may capture impacts of similar sizes (d_H) as shown in Fig. 3.12. The impact frequency N is found to follow an exponential behavior with d_H, as the semi-log plots of N vs. d_H in Fig. 3.12 are linear. As expected the frequency of impacts for a given d_H increases with the flow pressure.

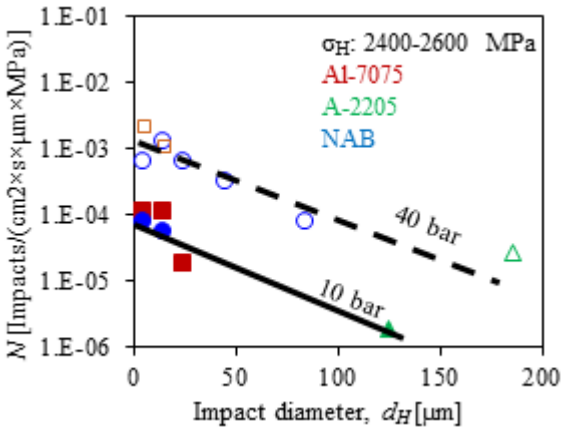

Fig. 3.12 Normalized impact frequency, N (Number of impacts/cm^2/sec/µm/MPa) plotted as a function of the impact diameter d_H for the hydrodynamic impact loads estimated at 10 and 40 bar. N is estimated at different ranges in the values of d_H (with a band width of 10 µm) for a given range of σ_H=2400-2600 MPa. The vertical axis is on log-scale. Nanoindentation material properties extrapolated at strain rate 10^6 s^{-1} were used for FE simulations in the inverse method.

Finally, the flow aggressiveness for a given flow condition can be characterized by a 3D plot as shown in Fig. 3.13, where the impact frequency N is plotted as a function of σ_H and d_H. Values of N are estimated at different points using a grid of 200 MPa × 20 µm size in σ_H-d_H space. It is observed that all the data points in Fig. 3.13 fit reasonably well the following analytical expression given by Eq. (3.9).

$$N = N^* \exp\left(-\left(\frac{\sigma_H}{\sigma_H^*}\right)\right) \exp\left(-\left(\frac{d_H}{d_H^*}\right)\right) \tag{3.9}$$

Here the characteristic impact frequency N^*, characteristic peak impact stress σ_H^* and characteristic impact diameter d_H^* are three fitting constants which characterize the flow. The σ_H^* represents a mean value of σ_H over all values of d_H and similarly the d_H^* represents a mean value of d_H over all values of σ_H. Estimated values

of N^*, σ_H^* and d_H^* at different flow pressure is given in Table 3.3. In order to get more accurate estimation of N^*, σ_H^* and d_H^* more data are required to reduce the scatter. These parameters depend on the flow condition only, irrespective of the material being used to capture them.

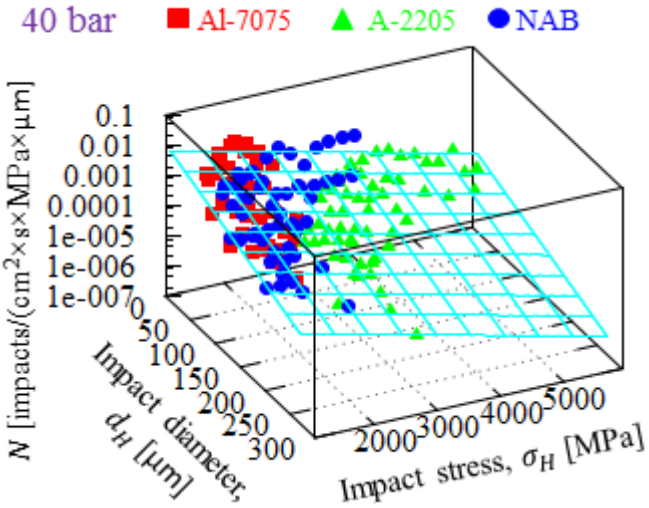

Fig. 3.13 Plot of the normalized impact frequency, N as a function of the peak impact stress σ_H and impact diameter d_H for the hydrodynamic impact loads estimated at 40 bar. N is estimated at different grids of 200 MPa × 20 µm size in σ_H-d_H space. The vertical axis is on log-scale. A total of 650 pits have been analyzed. Nanoindentation material properties extrapolated to the strain rate of 10^6 s^{-1} were used for the FE simulations in the inverse method.

Table 3.3 Values of N^*, σ_H^* and d_H^* at different flow pressures

Flow Pressure (bar)	$\boldsymbol{\sigma_H^*}$ **[MPa]**	$\boldsymbol{d_H^*}$ **[µm]**	$\boldsymbol{N^*}$
10	1000 ± 247	49.99 ± 10	0.0008904 ± 0.00052
20	575.0 ±104	57.54 ± 10	0.0194781 ± 0.01259
40	890.0 ±164	56.54 ± 10	0.0372554 ± 0.01692

This is a significant achievement as we could explain the flow aggressiveness by an analytical equation of a simple exponential form. This would enable us to predict the flow aggressiveness at different flow pressures if we analyze the behavior of N^*, σ_H^* and d_H^* with respect to flow pressure. Doing that would require a very large number of pit data for the statistical analysis. We should also be able to capture the impacts of smaller size with high peak pressure and bigger size with comparatively low peak pressure by additional cavitation pitting tests, which would be difficult as overlapping of pits would become unavoidable. So, no further analysis is done in that direction in this study. It should be mentioned that, though the errors are significant in Table 3.3, when the flow pressure increases, N^* increases significantly, whereas σ_H^* and d_H^* remains almost constant. This is interesting as the cavitation pitting tests at different flow pressures were done with a constant cavitation number [62] that essentially generates geometrically similar flows, the flow aggressiveness seems to change with the flow pressure in terms of their characteristic frequency only, whereas, σ_H^* and d_H^* seem to be not only material but flow independent as well.

3.4. Discussion

As presented in Sec. 3.3, by using the material properties obtained by compression tests extrapolated to a strain rate of 10^6 s^{-1}, we did not get a unique trend in the plot of N vs. σ_H as shown in Fig. 3.10, whereas, the properties obtained by the nanoindentation tests extrapolated to the same strain rate, gave us a unique trend as shown in Fig. 3.11. This unique trend was mandatory to conclude that the target material itself can be used as a sensor in cavitation pitting.

As discussed in Sec. 3.2, it was found that the deformation behavior of Al-7075 in compression and nanoindentation were different, whereas for both A-2205 and NAB compression and nanoindentation behaviors were similar. This difference in the behavior of Al-7075 probably led to the inconsistency in Fig. 3.10 and we concluded that nanoindentation is the proper way to characterize the materials constitutive behavior for cavitation pitting. Thus it is necessary to elucidate the reason and hence microstructural analyses were done.

As nanoindentation test is done in a confined region compared to that of compression test, distribution of different phases and their strength will decide the local and global behavior of the probed material. Thus attention was paid to reveal the different phases of the materials, rather than the grain boundaries. Samples were prepared similarly as done for nanoindentation with final polishing using colloidal silica of 0.03 µm size. If the different phases in the material have variation in strength they will be polished to different depths producing contrast under optical microscope. Fig. 3.14(a-c) show the binary images of the phase structures of the three materials, on a plane parallel to the cavitation pitting tested surface, obtained by optical microscope (Olympus BX51M).

Fig. 3.14(a) shows the phases in duplex stainless steel (A-2205) which consists of almost 50% δ-ferrite and 50% γ-austenite [129,138,139]. As can be seen, austenite is uniformly distributed into the ferrite matrix with different orientations. It is possible to selectively indent the different phases with an indenter of radius 9.46 µm (as used in this study), but the responses would not be very different. This is because the region of the material which would effectively resist the deformation could be considered as a semi-sphere of radius (R_d) 2-3 times bigger than the indenter radius R as shown in Fig. 3.15 (obtained by nanoindentation simulation of A-2205 with R=9.46), and hence this region will always contain both the phases. Therefore the local and global behavior in nanoindentation and compression tests respectively would be almost identical for A-2205. Moreover, El Mehtedi *et al.* [138] and Hay [139] have done nanoindentation tests on the different phases of 2205 duplex stainless steel and found no significant difference in their hardness or Young's modulus. Their findings also support the previous statement. These could be the reason why the FE simulation of nanoindentation using the compression test data for the constitutive equation yielded a load-displacement curve similar to the experimental one as discussed in Sec. 3.2.5.

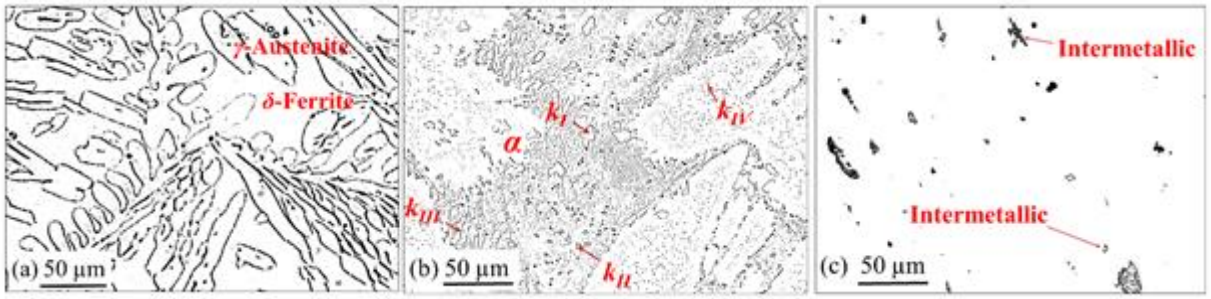

Fig. 3.14 Phase structures of all three materials obtained by optical microscopy (OLYMPUS BX51M). (a) 2205 duplex stainless-steel (A-2205) (b) Nickel-Aluminum Bronze (NAB) and (c) 7075 Aluminum alloy (Al-7075).

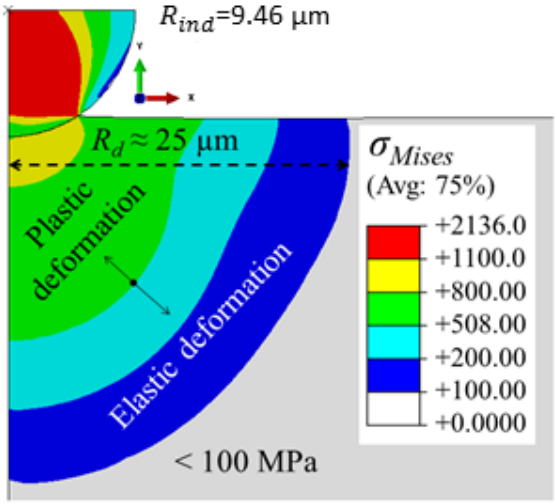

Fig. 3.15 Nanoindentation simulation of A-2205 with a spherical diamond indenter of radius R_{ind}=9.46 µm. Distribution of von Mises equivalent stress (σ_{Mises}) is shown highlighting the extent of effectively deformed region beneath the indenter.

The Fig. 3.14(b) shows the different phases in Nickel-Aluminum Bronze (NAB). The microstructure of the material is similar to that observed by several other authors [130,140,141]. The commonly observed phases are copper-rich solid solution (α-phase) matrix, different *k*-phases (iron-bearing phases k_I, k_{II} and k_{IV} are based on Fe_3Al and NiAl based k_{III} phase) and some amount of retained-β-phase which finally convert to martensite. Easily distinguishable phases have been highlighted in Fig. 3.14(b) based on their morphology. As can be seen all the phases are almost uniformly distributed into the matrix material (could be seen in [130,140,141] as well), so for NAB also we can expect that the local and global behavior would be similar. This is probably the reason for NAB also, for which the FE simulation of a nanoindentation test gives a load-displacement curve similar to the experimental one when the compression parameters are used in the FE modeling (see Sec. 3.2.5).

The Fig. 3.14(c) shows the different phases in 7075 aluminum alloy (Al-7075). Many authors [142–144] have done extensive microstructural analysis on this material, especially regarding the distribution of the second phases into the matrix. The second phases are generally Fe-bearing inclusions ($Al_7Cu_2Fe_2$, $Al_{23}Fe_4Cu$) and Si-bearing inclusions (Mg_2Si) which are uniformly distributed into the matrix, and their volume fraction could reach up to 3% [142,144]. Particle size generally varies depending on the manufacturing processes and

mechanical treatment applied. Particle size could be as big as 150 μm or even more [142] with even larger inter particle spacing. However, most of the inclusions in the current material have sizes from 10-20 μm and maximum particle size of ~50 μm is observed, as can be seen in Fig. 3.14(c). Although the volume fraction is less, the uniform distribution of these inclusions throughout the material would influence the mechanical properties of the material. Authors in [142] have done nanoindentation tests on these different phases and found huge differences in their strength compared to that of the matrix phase. Thus we can expect that in cavitation pitting or in nanoindentation the local behavior of the material would be different from the global or bulk behavior in compression. In compression the behavior would be like a composite material of soft and hard phases, whereas in nanoindentation depending on the phase we might get strong or weak response. This is probably the reason for which compressive material properties used in the FE simulation of nanoindentation did not give a load-displacement curve similar to the experimental one. So, when we optimized the constitutive parameters by the inverse nanoindentation method as discussed in Sec. 3.2.5, we got a softer stress-strain response compared to that of compression test as shown in Fig. 3.7. In cavitation test, the soft matrix of Al-7075 will get eroded out preferentially. Therefore to characterize this type of material for cavitation pitting the local behavior of the soft phases should be considered and nanoindentation test is the preferred option to get the material properties. The above hypothesis on Al-7075 is also supported by the findings in [63] which shows that cavitation erosion resistance (which is related to material strength) of Al-7075 is significantly less compared to that of NAB or A-2205, although the tension or compression strength of Al-7075 is significantly higher than NAB or A-2205.

As presented throughout the chapter, the inverse FE method is a potential technique that could be used in practice to estimate the hydrodynamic impact loads in cavitation pitting. Though improvements can be done, especially in terms of dynamic explicit FE analysis, to take into account the effect of inertia of the material and possible change in strain rates for all the hydrodynamic impacts, the method is operational. The dynamic explicit analysis of cavitation pitting performed in [4] on these same three materials has shown that for impact duration of 1μs or more, the contribution of inertial effect to the dynamics of cavitation pitting becomes negligible, it is essentially the strain rate sensitivity which influences the pit dimensions depending on the impact duration. Thus, if a material is selected carefully with a minimum strain rate sensitivity (like Al-7075), accurate measurements of the hydrodynamic impact loads could be obtained by the inverse FE method using static FE analysis. Obviously, dynamic explicit analysis of the material behavior for the inverse FE method would certainly lead to more accurate estimation of impact loads, but for that, the knowledge of impact duration corresponding to each cavitation pit is required. To the best of our knowledge there is no way to estimate impact duration based on cavitation pit dimensions and hence FE static analysis with extrapolated material properties is used here. The main difficulties to implement the method is that, this is a time consuming method as it requires several experiments and thorough analysis for calibration of material properties. Although it is found that the Gaussian profile for the pressure field is closely related to the cavitation impact loading and also used by several other authors, in practice the actual pressure field associated with cavitation bubble collapse has a more complex shape both in space and time, especially due to interaction of collapsing bubbles [81].

Despite all the difficulties, from statistical point of view the estimated values of the impact loads are quite satisfactory as they agree well with the values in literatures [38,81].

3.5. Summary and conclusions

The prime focus of this study was to answer two questions: (1) Can the target material itself be used as a sensor in cavitation pitting to estimate hydrodynamic impact loads i.e. the peak stress σ_H and radial extent d_{H}? (2) If yes, then how to characterize the material properties or constitutive behavior?

Three materials Al-7075, A-2205 and NAB were chosen on which cavitation pitting tests were done at different flow conditions (10, 20 and 40 bar) and then the resulted pit dimensions (depth, h_P and diameter, d_P) were measured. The peak stress σ_H and radial extent d_{H} of the hydrodynamic impacts corresponding to each pit have been estimated by using an inverse FE method presented in Chapter-2 (or in [2]). Very interestingly, statistical analysis of the estimated impact loads at all the flow conditions were found to be material independent. This is the most important result of this study which confirms that the target material itself can be used as a pressure sensor.

To answer the second question, the material properties required by the inverse FE method were obtained by compression and nanoindentation tests which represent the global and local behavior respectively. It was found that depending on the microstructure the global and local behavior may vary significantly. Unlike A-2205 and NAB, stress-strain curves for Al-7075 obtained by compression and nanoindentation tests were significantly different. The stress-strain curves were extrapolated to a higher strain rate of 10^6 s^{-1}, relevant to cavitation pitting. The consistency of impact load spectra between the three materials was obtained using the local material properties obtained by nanoindentation whereas the global properties led to inconsistent results. This is also a very important conclusion which proves that the characterization of material's local behavior by nanoindentation is relevant to cavitation pitting. In our approach we assumed that the strain rate sensitivity coefficient estimated from split Hopkinson bar tests could be reasonably used for the extrapolation of the nanoindentation data to strain rate as large as 10^6 s^{-1} (which are not accessible in nanoindentation).

Apart from these, it was observed that the flow aggressiveness (which effectively counts the number of impacts for a given range of σ_H and d_{H}) could be represented by a 3D surface, which follows an exponential form as given by Eq. (3.9). Such a surface can entirely be defined by three parameters, the characteristic impact frequency N^*, the characteristic peak impact stress σ_H^* and the characteristic impact diameter d_H^* which are material independent.

Chapter-5 is focused on the simulation of multiple impacts where the estimated impact loads (σ_H and d_{H}) would be applied repetitively and randomly on the material surface to estimate mass loss with time. Thus the final aim is to numerically predict mass loss evolution during cavitation erosion for which the knowledge of σ_H and d_{H} is necessary. For that reason complete dynamic analysis and additional material parameters to account for damage will be considered in the FE simulations.

3.6. Some highlights and remarks

Some highlights of the chapter:

- Three materials Al-7075, A-2205 and NAB were used to estimate cavitation impact loads.
- Material properties were characterized by a Johnson-Cook constitutive equation with parameters obtained from compression, nanoindentation and SHPB tests.
- Statistical analyses of the estimated impact loads show a consistency for the three tested materials which indicates that the target material can be used as a pressure sensor in cavitation pitting.
- Flow aggressiveness varies exponentially with both the peak impact stress and the radial extents of impact stresses.
- Nanoindentation is found to be the proper way to the characterization of material properties relevant to cavitation pitting.
- Weak cavitation erosion resistance of Al-7075 material is believed to be related to the soft matrix phase.

Remarks:

In this chapter (Chapter-3) a few of the primary objectives (item numbers 4, 5 and (i) as discussed in Sec. 1.5) have been achieved. Apart from that some interesting conclusions have been drawn. The rest of the objectives are dealt with in the following chapters.

Chapter-4

4. Dynamic behavior of material under cavitation impact loading

This chapter contains the results of a journal paper [4] whose details are given below. However, additional data and results are included which could not be included in the paper. Some data were also removed to avoid repetition of any dialogue, figures or tables etc. that were already presented in the thesis. The paper has been accepted for publication in the journal "WEAR" in 2015.

Determination of cavitation load spectra – Part 2: Dynamic finite element approach

Samir Chandra Roy[a,2], Jean-Pierre Franc[b], Nicolas Ranc[c], Marc Fivel[a]

[a]Science and Engineering of Materials and Processes (SIMaP-GPM2), University Grenoble Alpes / CNRS, F-38000 Grenoble, France.

[b]Laboratory of Geophysical and Industrial Flows (LEGI), University Grenoble Alpes / CNRS, F-38000 Grenoble, France.

[c]Laboratory Procédés et Ingénierie en Mécanique et Matériaux (PIMM), UMR CNRS 8006, Arts et Métiers ParisTech, 151 Boulevard de l'Hopital, 75013 Paris, France.

Abstract

Cavitation erosion is a well-known problem in fluid machineries which occurs due to repeated hydrodynamic impacts caused by cavitation bubble collapse. Cavitation pitting test is often used for the quantification of flow aggressiveness required for lifetime prediction of hydraulic equipment. Understanding the response of the target material under such hydrodynamic impact is essential for correctly interpreting the results obtained by cavitation pitting test. Moreover the proper knowledge of cavitation pitting mechanism would enable us to design new materials more resistant to cavitation erosion. In this paper, the dynamic behavior of three materials 7075 Aluminum alloy, 2205 duplex stainless steel and Nickel-Aluminum Bronze under cavitation hydrodynamic impact has been studied in details by using finite element simulations. The applied load due to hydrodynamic impact is represented by a Gaussian pressure field which has a peak stress and, space and time evolution of Gaussian type. Mechanism of cavitation pit formation and the effect of inertia and strain rate sensitivity of the materials have been discussed. It is found that if the impact duration is very short compared to a characteristic time of the material based on its natural frequency, no pit would form into the material even if the impact stress is very high. It is also found that strain rate sensitivity reduces the size of the deformed region and thereby could enhance the cavitation erosion resistance of the material.

***Keywords**:* Cavitation pitting; Finite element simulation; Strain rate sensitivity; Natural frequency; Cavitation pitting mechanism.

[2]Corresponding author:
E-mail address: roysam.nita@gmail.com or samir-chandra.roy@simap.grenoble-inp.fr (S. C. Roy)

4.1. Introduction

Estimation of impact loads due to cavitation bubbles collapses in hydraulic machineries or components under service condition has been a challenging issue till date. Generally transducers are used to measure impact loads in laboratory tests. Apart from the associated errors in transducer measurements (as discussed in Sec. 1.3.3.1 in Chapter-1) their use in real field is difficult and sometimes impossible. To avoid the measurement difficulties associated with transducers, a combined experimental and numerical approach has been developed as presented in Sec. 2.5 in Chapter-2 (also presented in [2,3,145]) to estimate the impact stresses as well as their radial extent. The proposed method has the potential to be used in real filed as well. The method proposed in till now in [2,3,145] is however based on static finite element computations of the material response. One of the objectives of the present chapter is to extend it to the dynamic case where density and strain rate sensitivity of the material would play a vital role into the deformation mechanism. The current paper explains in details the feasibility of such method to implement when the complete dynamics of the material deformation is considered.

Each hydrodynamic impact has characteristic size, peak stress and duration which are related to the cavitation pit parameters. Influence of these three parameters on the dynamics of cavitation pit formation is investigated in this chapter. We will focus on the influence of the impact duration on the mechanism of cavitation erosion that has been less studied in the literature, particularly when the material behavior is strain rate sensitive. Sec. 4.2 is devoted to the presentation of material properties with special emphasis on the integration of strain rate sensitivity via the Johnson-Cook model. The numerical model based on the use of the commercial finite element method (FEM) code ABAQUS is also presented in Sec. 4.2. Sec. 4.3 is devoted to presentation of results. It includes a discussion of the effect of impact duration on pit formation, an extension of the inverse FE method presented in Sec. 2.5 in Chapter-2 (or in [2]) to the dynamic case and an evaluation of the strain rate during cavitation pit formation. Discussion is largely based on the introduction of a material characteristic time evaluated on the basis of the characteristic size of the plastically deformed volume and the associated natural frequency of the material.

4.2. Simulation and experimental details

4.2.1. Materials and constitutive laws

All the three materials 7075 Aluminum alloy (Al-7075), 2205 duplex stainless steel (A-2205) and Nickel-Aluminum Bronze (NAB) have been considered for the current study here. Density (ρ), Young modulus (E) and Poisson ratio (v) of these materials are given in Table 4.1. In chapter- 3 it has been shown that the nanoindentation characterizes better the materials behavior under the hydrodynamic impact of cavitation bubbles collapses. Hence in the current study, the materials properties (σ_y, K and n) previously (in Chapter-3) obtained by nanoindentation tests (as given in Table 4.1) are utilized. Material properties were obtained by

using the Johnson-Cook (JC) plasticity model in the form given by Eq. 1, avoiding the thermal softening part (see [120] for more details about JC plasticity model).

$$\bar{\sigma} = \left(\sigma_y + K\varepsilon_p^n\right)\left(1 + C\ln\frac{\dot{\varepsilon}_p}{\dot{\varepsilon}_0}\right) \tag{4.1}$$

Here, ε_p is the equivalent plastic strain, $\dot{\varepsilon}_p$ is the equivalent plastic strain rate and $\dot{\varepsilon}_0$ is the reference strain rate at which the yield strength σ_y, strength coefficient *K* and strain hardening exponent *n* should be estimated. Parameter *C* is the strain rate sensitivity. At reference strain rate (taken as 0.05 s^{-1}) $\ln(\dot{\varepsilon}_p/\dot{\varepsilon}_0) = 0$, Eq. (4.1) becomes a simple Ramberg-Osgood type equation where hardening is a function of $\varepsilon_p$only.

Strain rate involved in cavitation pitting is expected to be very high, up to the order of ~10^6 s^{-1} [3,6], and could vary depending on the bubble size, stand-off distance and collapse driving pressure gradient. Hence it is important to consider the strain rate sensitivities of the materials to study their dynamic behavior. Strain rate sensitivities of the materials (C) previously obtained (in Chapter-3) by compression and split Hopkinson pressure bar tests (as given in Table 4.1) have been used for the current study.

Table 4.1 Strain rate sensitivity, Physical and nanoindentation mechanical properties of the materials at strain rate 0.05 s^{-1}.

Material	σ_y **[MPa]**	K **[MPa]**	n	C	E **[GPa]**	ν	ρ **(kg/m^3)**
Al-7075	335	396	0.3	0.0068	71.9	0.33	2810
A-2205	508	832	0.51	0.0310	186	0.30	7805
NAB	300	1150	0.58	0.0119	122	0.32	7580

This way of integration of strain rate sensitivity obtained by compression test with nanoindentation properties to simulate the cavitation pitting behavior is studied in details in Chapter-3 (or in [3,145]) and found to be appropriate, as the current state-of-art of nanoindentation testing does not allow test at very high strain rate to estimate strain rate sensitivity properly.

4.2.2. Simulation and mesh details

The pressure induced by cavitation bubble collapse depends on the standoff distance from the solid wall and has a complex shape in both space and time. Except for the very smaller standoff distances when double pressure pulse is expected for each bubble collapse, the pressure field can be described reasonably well by a doubly Gaussian profile [81] as given by Eq. (4.2), which is supported by experimental recordings of pressure pulses [48,107].

$$\sigma = \sigma_H \exp\left(-\left(\frac{2r}{d_H}\right)^2\right)\exp\left(-\left(\frac{t - t_{max}}{t_H}\right)^2\right) \tag{4.2}$$

In Eq. (4.2), variables t and r represent time and radial extent respectively, t_{max} is the time when $\sigma = \sigma_H$ and t_H is the characteristic impact rise duration in a similar sense to characteristic impact radius d_H represents characteristic impact diameter). The spatial and temporal evolution of the pressure field is shown in Fig. 4.1(a).

In order to investigate the dynamics of cavitation pitting/erosion, FEM simulations were done with the representative Gaussian pressure field given by Eq. (4.2) for different values of σ_H, d_H and t_H and, by using the material properties given in Table 4.1. Dynamic explicit simulations were done in the commercial FEM code ABAQUS using a 2D axisymmetric model (as shown in Fig. 4.1(b)). ABAQUS dynamic explicit solves structural momentum equation based on a lumped mass matrix corresponding to the mesh (see Appendix C for more details about finite element analysis procedure and dynamic explicit analysis). Dynamic explicit solver is preferred for simulation of high rate deformation processes where structural dynamics or stress wave propagation is important. CAX4R (continuum axisymmetric 4 nodes reduced integration) elements were used for the meshing. Model domain size is kept significantly bigger than the impact size (parametrically $150 \times r_H$), to avoid any stress wave reflection from the boundary, so that the domain could be considered infinite compared to that of impacted area. Symmetric boundary condition (XSYMM in ABAQUS) has been used on the axis of symmetry (OA) and displacement along z direction was restricted at the bottom most side (AC). Plastic behavior of the material was characterized by the Johnson-Cook plasticity model of the form given by Eq. (4.1).

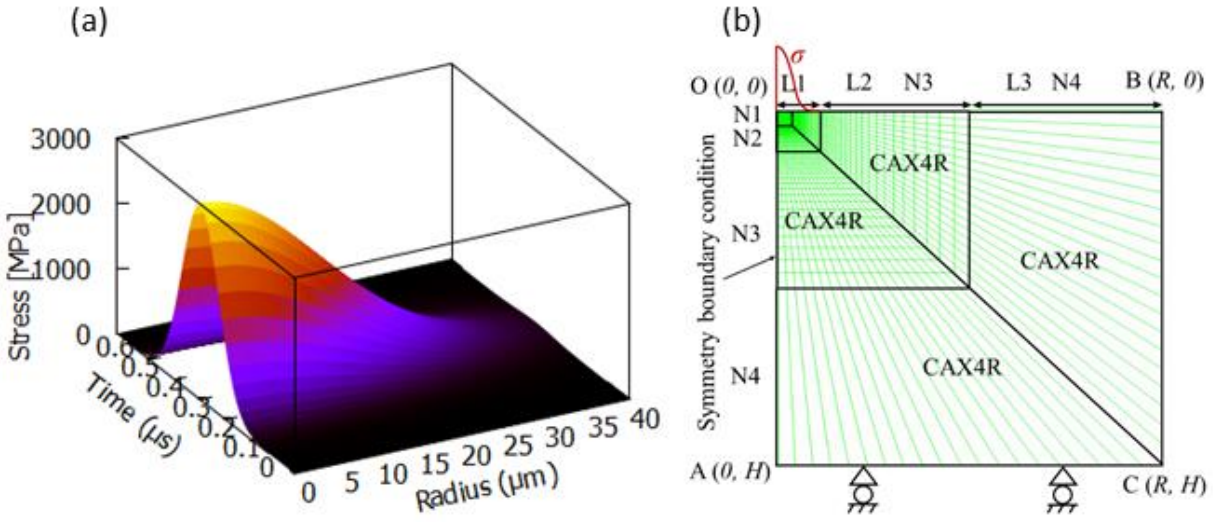

Fig. 4.1 (a) Illustration of spatial and temporal evolution of Gaussian pressure (Eq. (4.2)) and (b) the 2-D axisymmetric mesh used for the numerical simulations. Distances along radial and thickness directions are represented by r and z respectively. L represents length of one or more section as shown by the arrows. N represents number of elements on the surface of different section. R and H represent the maximum radial and vertical sizes of the simulated volume. Number of elements (N1, N2, N3 and N4) in different section is always constant, but section lengths (L1, L2 and L3) are parameterized from the radius of hydrodynamic pressure field, r_H, e.g. if $d_H = 20$ μm, N1 = 20, N2 = 60, N3 = 40 and N4 = 1 then, L1 = 0.75×d_H=15 μm, L1+L2 = L3 = R/2 = 50×L1= 750 μm, H = R = 1500 μm, using geometric progression with common ratio of 1.01.

4.3. Results

4.3.1. Preliminary results

As dynamic explicit solver does not impose any iterative procedure to converge to the solution, the time increment size should be very small for accurate dynamic response of the material. The automatic time incrementing scheme available in ABAQUS is used to avoid any such error, which essentially estimate the increment size which is always less than or equal to the time required by sound wave to propagate through the smallest element in the mesh. The accuracy of the materials dynamic response in cavitation pitting was found to be unaffected by the size of the time increment. The influences of number of elements and domain size have also been verified to get an error proof response.

Influence of impact fall duration onto the pit dimensions has been analyzed in details. As an example in the case of A-2205, Fig. 4.2(a) and Fig. 4.2(b) show the evolution of normal stress (σ_{zz}) and displacement (u_{zz}) at the top most point on the axis of symmetry for t_H = 0.005 & 1.0 µs respectively, when $\sigma_H = 2$ GPa and $d_H = 40$ µm. As can be seen in Fig. 4.2(a) for hugely dynamic impact, the material was still deforming during the unloading period of the impact, probably because of the inertial effect, and the displacement (u_{zz}) reaches the maximum and then elastic recovery takes place and continues even when the applied stress reaches its plateau region. Whereas for $t_H = 1.0$ µs (Fig. 4.2(b)), the displacement reaches the maximum almost at the same time when the applied stress (σ_{zz}) reaches its peak, and then the elastic recovery also takes place and finishes before the applied stress reaches its plateau region. Therefore to get an error free measure of the simulated pit dimensions, sufficient unloading time should be given to the structure to get stabilized, otherwise we could trap the deformation into an intermediate state. In all the cases presented in this paper impact fall duration of $12 \times t_H$ is applied and found to provide a stabilized structural response.

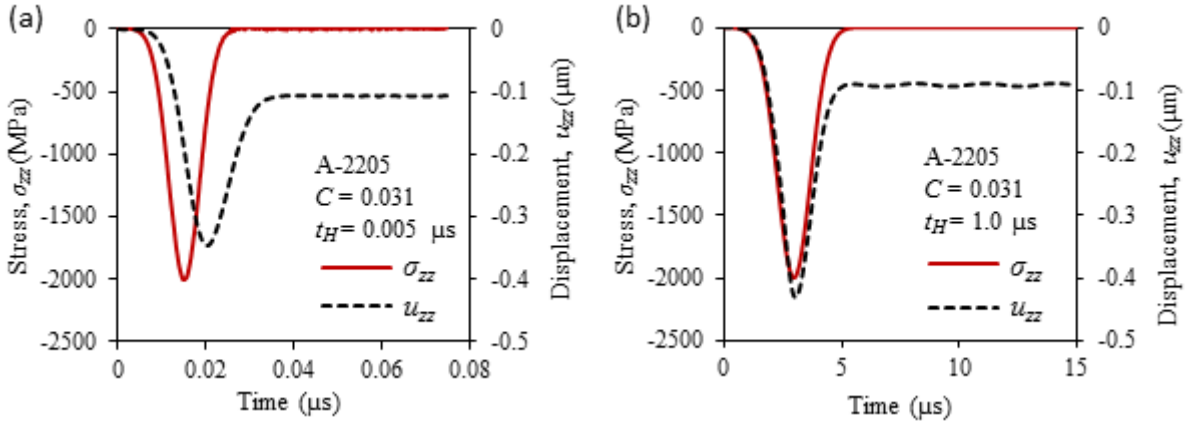

Fig. 4.2 Represents evolution of applied stress (σ_{zz}) and deformation depth (u_{zz}) with time during hydrodynamic impact. Material: A-2205, $\sigma_H = 2$ GPa and $d_H = 40$ µm (a) $t_H = 0.005$ µs (b) $t_H = 1.0$ µs.

4.3.2. Effect of impact duration on cavitation pitting

To investigate the effect of impact duration onto the mechanism of pit formation, a large number of simulations were conducted with characteristic impact rise duration t_H ranging from 1×10^{-4} to 5×10^{5} μs, which essentially covers the whole range of possible bubble collapse or hydrodynamic impact durations. Impact duration can be considered as $2 \times t_H$ which includes both the impact rise and fall duration. Moreover, to isolate the effect of inertia from strain rate sensitivity, simulations were done with the JC plasticity model (Eq. (4.1)) considering $C = 0$ for all the three materials. It should be mentioned that the assumption $C = 0$ is purely numerical, that suppresses the strain rate sensitivity in Eq. (4.1). These two types of simulation results were then compared with static response (in absence of time dependent part of Eq. (4.2)) of the material under the same loading condition of σ_H and d_H, where both the inertial and strain rate sensitive effects are absent. As an example in the case of A-2205, Fig. 4.3 shows the variation of pit depth (h_P) with t_H for a constant value of $\sigma_H = 3$ GPa and $d_H = 40$ μm. As can be seen, with increase in t_H both the dynamic solutions, with (C = 0.031) and without (C = 0) the strain rate sensitivity effect, the dynamic solution converges towards the static solution and in both the cases a peak has been observed.

In both the dynamic cases, with or without strain rate sensitivity, pit depth initially increases with increase in t_H, reaches a peak, then again decreases and thereafter for strain rate insensitive behavior the pit depth remains unchanged, whereas for strain rate sensitive behavior pit depth continues to increase again, until the hardening due to strain rate sensitivity is diminished. With the inclusion of strain rate sensitivity, the characteristic time t_H at which the peak is observed decreased from 0.05 to 0.02 μs. This could be due to the natural frequency of the material, which increases with increase in stiffness and there by reduces the characteristic time or natural period of the material.

One important phenomenon to be noticed, after $t_H \geq 0.5$ μs, the dynamic solution with C = 0 is identical i.e. the inertial effect becomes insignificant with respect to the pit dimension. Similar behavior was also observed in Al-7075 and NAB with the occurrence of peak at values of t_H close to 0.05 μs (orange dashed line in Fig. 4.3). Thus in the case of real cavitation hydrodynamic impact, if the impact duration is in the order of microsecond, we can possibly avoid the dynamic effect due to inertia for the inverse calculation of σ_H and d_H from cavitation pit geometry, as done by Roy *et al.* [2,3,145]. However, it should be emphasized that time dependent strain rate sensitivity of the material should be considered for accurate estimations using such inverse method. Although it is difficult to accurately measure the impact duration by using pressure transducer, some observations suggest that impact duration generally varies in the order of microsecond [48,81,107].

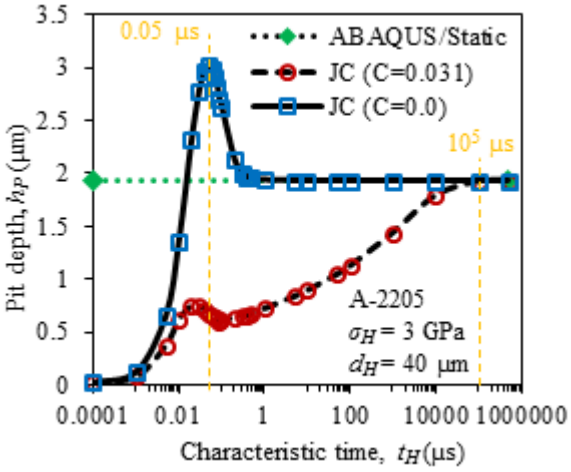

Fig. 4.3 Variation of pit depths (h_P) with characteristic impact rise duration t_H(log-scale). Material: A-2205, $\sigma_H = 3$ GPa, $d_H = 40$ µm and t_H ranges from 1×10^{-4} to 5×10^5 µs. Static solutions is time independent and the virtual dotted line highlights the same.

In presence of positive strain rate sensitivity, as shown in Fig. 4.3 (by JC (C = 0.031)), the material becomes harder and the pit depth gets reduced, especially in the time domain where the strain rate sensitivity is effective in the deformation mechanism. For characteristic impact rise duration $t_H > 10^5$ µs (orange dashed line in Fig. 4.3), the strain rate sensitivity is also found to disappear from the deformation behavior. As 10^5 µs is a quite large value for impact rise duration, it can be considered that for metal subjected to cavitation erosion, strain rate sensitivity would always play a key role in the erosion mechanism. As the strain rate sensitivity reduces the pit depth, it can be assumed that, in case of high strain rate sensitive material (like A-2205), less volume of the material will be affected by a similar hydrodynamic impact compared to that of a less strain rate sensitive material (like Al-7075). For example, Al-7075 and NAB have almost the same level of yield strength, but the strain rate sensitivity of NAB is 1.75 times more than Al-7075, and it was experimentally observed that cavitation erosion damage in Al-7075 is significantly higher than NAB [63]. For A-2205, the minimum erosion rate was observed as both the yield strength and strain rate sensitivity for A-2205 is the highest among the three materials. Thus we could say if a material has higher yield strength as well as higher strain rate sensitivity, the erosion resistance of that material would be greater.

One more important observation can be drawn from Fig. 4.3, as t_H approaches to zero, the pit depth also approaches to zero in both the cases of dynamic simulations. As an example, for $t_H = 10^{-4}$ µs, the pit depth h_P is estimated to be ~0.01µm. This indicates that even if the impact pressure is high (here $\sigma_H = 3$ GPa), the hugely dynamic impacts for which the impact duration is in the order of less than a nanosecond, might not be able to produce any detectable pit. This phenomenon imposes a limitation to the target material, if used as a pressure sensor in cavitation pitting like authors did in [3,145], the material will not reveal impacts of very small duration. Reason of such behavior could be related to the natural frequency of the materials and is discussed in details in Sec. 4.4. It can also be assumed that, when the impact duration is very short, the rate of deformation is very high and hence most of the impact energy is transformed into kinetic energy, less energy remains available for work-done in terms of material deformation.

Fig. 4.4 shows the effect of t_H on the pit shape for constant values of $\sigma_H = 3$ GPa and $d_H = 40$ µm. Pit shapes have been plotted for some selected values of t_H to highlight the evolution pattern. Fig. 4.4(a) shows the variation of pit shapes in absence of strain rate sensitivity, whereas Fig. 4.4(b) shows the same in presence of strain rate sensitivity. In both the cases, pit shape, especially the depth, changes with t_H and ultimately attains the pit shape obtained by static simulation, after 0.5 µs in the case $C = 0$ and after 10^5 µs in the case $C = 0.031$. As can be seen in Fig. 4.4(a), for $t_H = 0.05$ µs pit volume is maximum and it decreases with both increase or decrease in t_H. Thus it can be considered that for such impacts, when a material has minor strain rate sensitivity, cavitation erosion damage could also be enhanced by the increased volume of deformation, whereas strain rate sensitivity would always reduce the volume of deformation, as can be seen in Fig. 4.4(b).

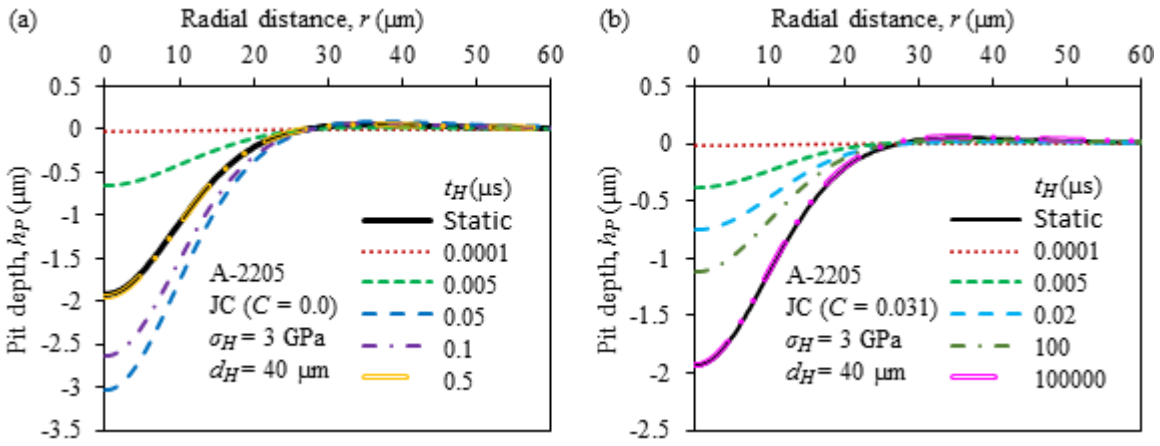

Fig. 4.4 Variation of pit shape with characteristic impact rise duration t_H shown for A-2205, $\sigma_H = 3$ GPa and $d_H = 40$ µm. (a) in case of strain rate insensitive behavior (C = 0) and (b) in case of strain rate sensitive behavior (C = 0.031). Static Shape represent the pit shape obtained by ABAQUS static analysis with the same values of σ_H and d_H.

4.3.3. Effect of σ_H and d_H on the dynamics of cavitation pitting

Here the analyses are focused on the dynamic behavior of the material with the highest strain rate sensitivity: A-2205. To analyze the effect of d_H, simulations were done with different values of d_H (10, 20, 40, 80 & 160 µm) keeping a constant value of $\sigma_H = 3$ GPa, while in each case t_H was varied from 0.001 to 1 µs. This range of t_H is chosen as the dynamic behavior is crucial in this time domain, as can be seen in Fig. 4.3. Pit depth, h_P versus characteristic time t_H has been plotted on a log-log graph as shown in Fig. 4.5 for all the simulations. The values of t_H at which the peak in pit depth h_P occurs, increases with d_H as shown by the arrow connecting the peaks and Sec. 4.4 explains a probable reason for this.

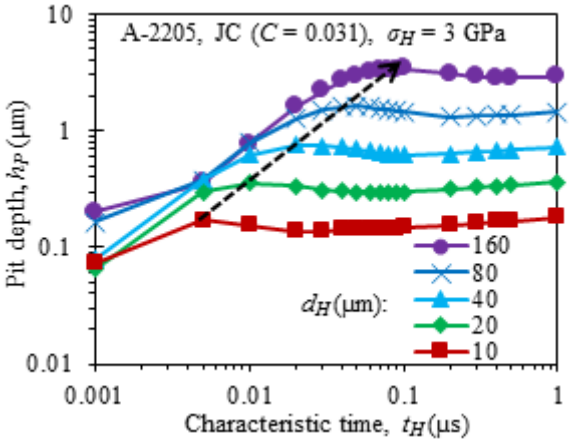

Fig. 4.5 Variation of pit depth, h_P with characteristic impact rise duration t_H with $\sigma_H = 3$ GPa and d_H = 10, 20, 40, 80 & 160 µm. The data for A-2205 is plotted on log-log scale.

To analyze the effect of σ_H, simulations were done with different values of σ_H (2, 3, 4, 5 & 6 GPa) keeping a constant value of $d_H = 40$ µm, while in each case t_H was varied from 0.001 to 1 µs. The values of t_H at which the peak in pit depth h_P occurs, increases with σ_H as shown by the arrow connecting the peaks in Fig. 4.6.

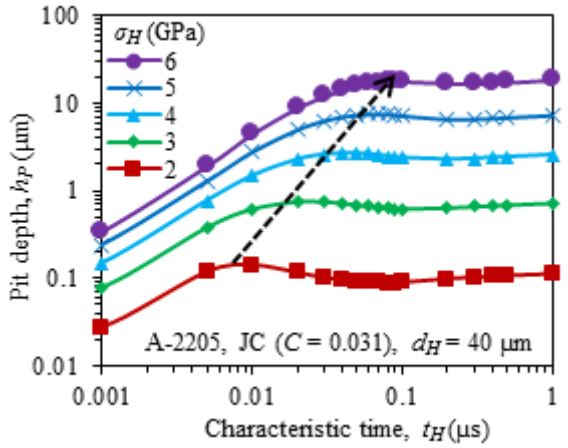

Fig. 4.6 Variation of pit depth, h_P with characteristic impact rise duration t_H with $\sigma_H = 2, 3, 4, 5$ & 6 GPa and d_H = 40 µm. The data for A-2205 is plotted on log-log scale.

Based on the observations from Fig. 4.5 and Fig. 4.6, it can be concluded that all the three parameters σ_H, d_H and t_H of hydrodynamic impact influence the dynamics of cavitation pitting, and thereby cavitation erosion. Pit depth increases with increase in both σ_H and d_H, whereas with t_H the variation is complex.

4.4. Discussion

4.4.1. Mechanism of cavitation pitting

In cavitation pitting the target material size is infinite compared to the size of the hydrodynamic impact and it is difficult to know the real volume of the material which is affected by the impact. One option would be the

numerical analysis of the stress or strain field into the material using certain criterion, for example yield stress or 0.2% plastic strain. Fig. 4.7 shows the schematic of the applied Gaussian pressure load and, the strain field in A-2205 material while impacted with $\sigma_H = 3$ GPa and $d_H = 40$ µm for a rise duration of $t_H = 0.02$ µs. As can be seen, maximum strain occurs inside the material on the axis of symmetry and the plastic domain is confined into a small region. The plastically deformed volume of the material could be confined into a cylinder of radius, r_d and length, l_d as shown in Fig. 4.7. The values of r_d and l_d will depend on the values of σ_H, d_H and t_H of the impact load and also on the material constitutive laws.

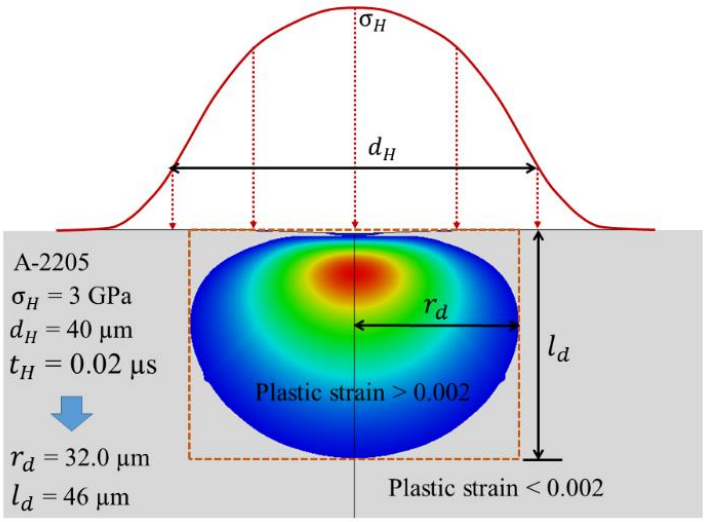

Fig. 4.7 Schematic of the applied Gaussian pressure field and the strain field in A-2205 material, impacted with $\sigma_H = 3$ GPa and $d_H = 40$ µm for a period of $t_H = 0.02$ µs. plastic strain > 0.2% is used for determining the domain size.

The dependencies of the plastic strain field size (strain > 0.2%) on σ_H and d_H has been analyzed. When σ_H and t_H both are constant, the ratio of l_d/d_H remains almost constant for any value of d_H. Whereas, when d_H and t_H both are constant, as shown in Fig. 4.8 (a log-log plot), the ratio of l_d/d_H varies with σ_H which can be expressed by a power law equation as shown in Eq. (4.3).

$$l_d/d_H = C_{12}\,{\sigma_H}^{C_{13}} \tag{4.3}$$

In Eq. (4.3), $C_{12}$and C_{13} are two fitting parameters which depend on the material properties. As shown in Fig. 4.8, when $t_H \geq 0.01$ µs the plots of l_d/d_H versus σ_H are almost identical which can be represented by a single curve (dashed line). Therefore, for the sake of simplicity, time dependencies of $C_{12}$and C_{13} are not considered here and the values are estimated to be S_1 = 0.0002 and S_2 = 1.0563, as shown in Fig. 4.8. The benefit of using a power law is, when $\sigma_H = 0$ or $d_H = 0$, the value of $l_d = 0$.

Using the estimated values of C_{12} and C_{13} , we can estimate the approximate values of l_d corresponding to each data in Fig. 4.5 and Fig. 4.6. These estimated values will be used to adimensionalize the plots in Fig. 4.5 and Fig. 4.6 in the following section.

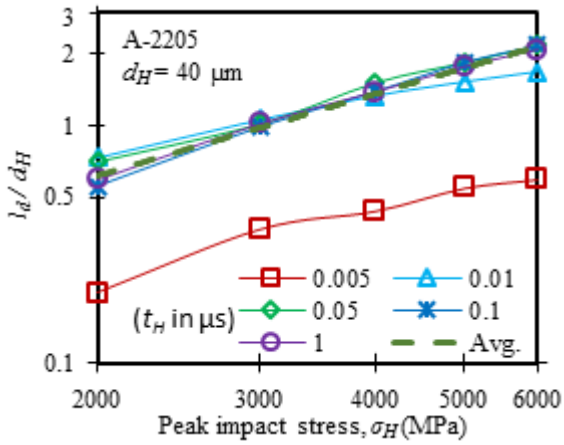

Fig. 4.8 Variation of normalized plastic strain domain size (l_d/d_H) with peak impact stress (σ_H) is plotted on a log-log scale. Material: A-2205, $d_H = 40\ \mu m$ and $t_H = 0.005$ to $1\ \mu s$.

The objective here is to find out if the peaks observed in Fig. 4.3, Fig. 4.5 & Fig. 4.6 are related to the natural frequency of the material or not, as it is well know that, when the applied load frequency is close to the natural frequency of the material then the maximum deflection occurs.

For a spring mass damper system under the external force (F) of sinusoidal form as shown in Fig. 4.9(a), the equation of motion based on Newton's second law can be written as Eq. (4.4).

$$m.\ddot{X}(t) + b.\dot{X}(t) + S.X(t) = F_0.\cos(\omega t) \tag{4.4}$$

Where, m is the mass, b is the damping coefficient of the damper, S is the stiffness of the spring. The $X(t)$ represents the time variation of the displacement and its first derivative is $\dot{X}(t)$ and second derivative is $\ddot{X}(t)$. The magnitude F_0 of the applied force has an angular frequency of ω.

From Eq. (4.4), the amplitude of oscillation (X) of the steady state response can be derived as given by the following Eq. (4.5) (detailed illustration of deriving Eq. (4.5) from Eq. (4.4) can be found in chapter-4 in [146]).

$$X = \frac{F}{S}\frac{1}{\sqrt{(1-\bar{\omega}^2)^2 + 4\xi^2\bar{\omega}^2}} \tag{4.5}$$

In Eq. (4.5), $\bar{\omega} = \omega/\omega_n$ (i.e. the ratio of angular frequency of the applied load ω to the angular natural frequency ω_n where, $\omega_n = \sqrt{S/m} = 2\pi f_n$ (f_n represents the natural frequency in Hz)) and the damping ratio is $\xi = b/(2\sqrt{Sm})$.

The analytical plot of the amplitude of oscillation X as a function of $1/\bar{\omega}$ using Eq. (4.5) and assuming constants $F/S = 1$ and $\xi = 0.4$ is shown in Fig. 4.9(b). Assumptions of $F/S = 1$ is arbitrary as it is insignificant in the current context, and $\xi = 0.4$ is also arbitrary but represents an under-damped system ($\xi < 1$). It should be emphasized that as the current study is conducted on metallic alloys, the assumption of $\xi < 1$ (under-damped) is physically or scientifically valid.

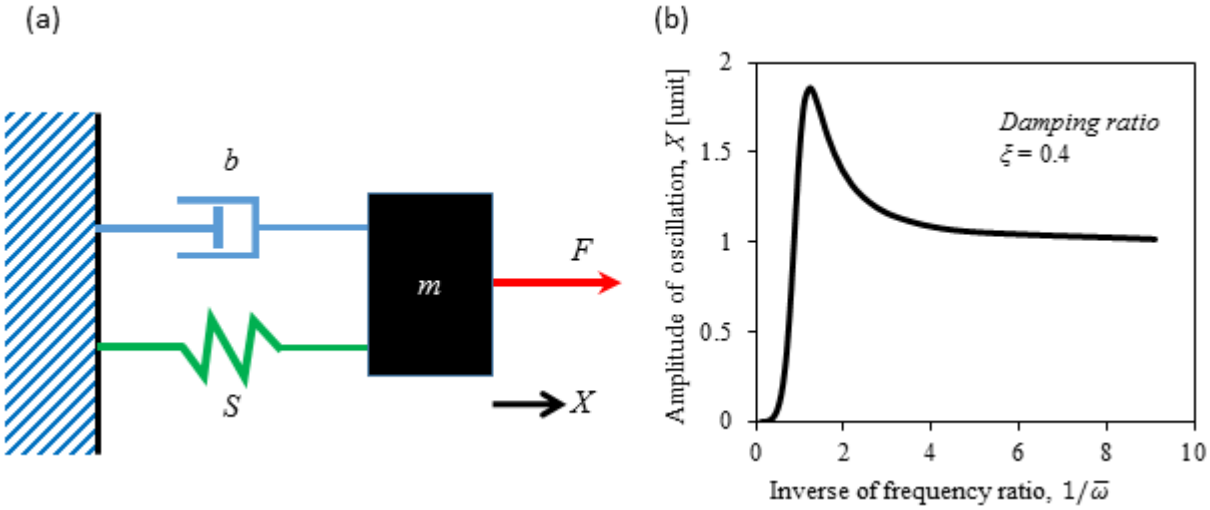

Fig. 4.9 (a) Illustration of a frictionless spring (S)-mass (m)-damper (b) system under external force (F) and, (b) Amplitude of oscillation X as a function of inverse of frequency ratio $1/\bar{\omega}$ of a spring mass damper system under external force of sinusoidal form, plotted using Eq. (4.5).

In cavitation pitting, the presence of plasticity would change the stiffness and damping coefficient of the impact affected region of the material with time, leading to potential changes in natural frequency. The dynamic response of the spring mass damper system as shown in Fig. 4.9(b) however interestingly resembles very well the dynamic behavior of the material under cavitation pitting as shown in Fig. 4.3, Fig. 4.5 & Fig. 4.6. As stated, it can be noticed in Fig. 4.3 that the strain rate sensitivity changes the dynamic behavior significantly, however, the basic behavior remains the same with the occurrence of a peak.

Now by comparing the dynamics of cavitation pitting with that of spring mass damper system we shall try to find out some kind of natural frequency for the material under cavitation impact. It should be emphasized here that Eq. (4.5) is mainly derived from the equation of motion for elastic response of spring or wire system. The purpose here is to qualitatively understand the mechanism of cavitation pitting rather than estimating something very precise.

For the representative cylinder in Fig. 4.7 the stiffness can be estimated as $S = \pi r_d^2 E/l_d$ and mass as $m = \pi r_d^2 l_d \rho$ where, E is the Young's modulus, ρ is the density of the material. An approximate estimation of the natural frequency of the material under cavitation impact can then be done based on the representative cylindrical volume of radius, r_d and length, l_d as shown in Fig. 4.7 and can be written as given by Eq. (4.6).

$$f_n = \frac{1}{2\pi}\sqrt{\frac{S}{m}} = \frac{1}{2\pi l_d}\sqrt{\frac{E}{\rho}} \tag{4.6}$$

From Eq. (4.6), the natural period of the material t_{mat} in cavitation pitting can be estimated as $t_{mat} = 1/f_n$. Using Eq. (4.3), the values of l_d have been estimated for all the data in Fig. 4.5 and Fig. 4.6, and corresponding t_{mat} have also been estimated by using the estimated values of l_d in Eq. (4.6). Fig. 4.5 and Fig. 4.6 have been re-plotted by normalizing h_P with l_d and t_H with t_{mat} as shown in Fig. 4.10 and Fig. 4.11 respectively. Unlike

before, $2 \times t_H$ is considered instead of t_H, as it could be considered as impact duration which includes both the rise and fall duration of the hydrodynamic impact.

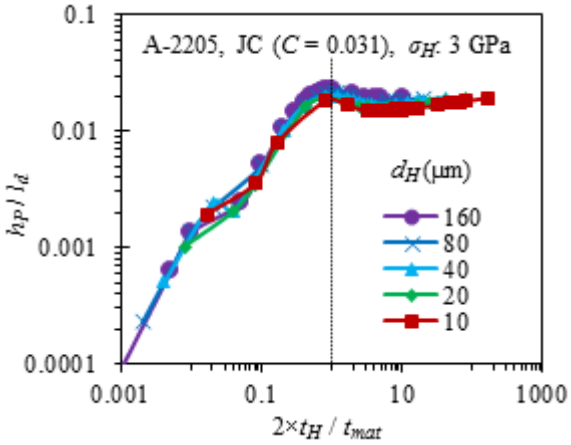

Fig. 4.10 Variation of pit depth h_P normalized by plastic strain field size l_d versus impact duration $2 \times t_H$ normalized by natural period of the material t_{mat} for different values of impact diameters $d_H = 10 - 160\ \mu m$ at the same peak impact stress $\sigma_H = 3$ GPa. Both the axes are on log scale.

As can be seen in the Fig. 4.10, all the peaks for different values of d_H at constant value of σ_H are now aligned at the same point ($2 \times t_H / t_{mat} \approx 1$, as shown by the dotted line) on the horizontal axis. This indicates that the peaks are indeed related to the frequency of the impact load, which is close to the natural frequency of the material. As can be seen, the ratio of h_P / l_d is also almost independent of d_H when σ_H is constant.

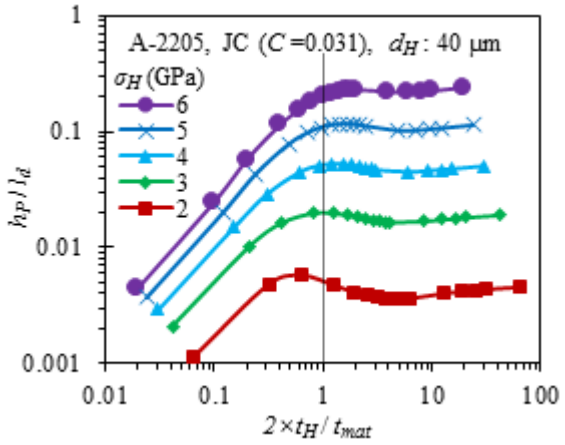

Fig. 4.11 Variation of pit depth h_P normalized by plastic strain field size l_d versus impact duration $2 \times t_H$ normalized by the natural period of the material t_{mat} for different values of peak impact stresses $\sigma_H = 2 - 6$ GPa at the same impact diameter $d_H = 40\ \mu m$. Both the axes are on log scale.

Unlike Fig. 4.6, in Fig. 4.11 also, all the peaks for different values of σ_H at constant value of d_H are now aligned close to 1 on the horizontal axis as shown by the dotted line, though the deviation is more for $\sigma_H = 2$ GPa. Unlike Fig. 4.10, the ratio of h_P / l_d is not independent of σ_H when d_H is constant.

Thus based on the above analyses we could state that the dynamics of cavitation pit formation under cavitation hydrodynamic impact is similar to the steady state response of a spring mass damper system under external

force. When the impact duration is very short, the frequency of the impact load is very high, hence inertia of the material controls the deformation rather than the stiffness of the material and, most of the energy is converted into kinetic energy leading to very shallow pit depth, as seen in Fig. 4.3. When the impact duration or frequency is close to the natural time or frequency of the target material the deformation is maximum leading to a maximum pit depth. If the impact duration is higher than the natural time of the material, solution moves towards the static condition and stiffness of the material starts to control the deformation. Depending on the strain rate sensitivity of the material pit depth varies but most of the energy is spent on work-done.

4.4.2. Analysis of cavitation pit dimensions

A simulation campaign of 425 simulations has been conducted for different values of σ_H (2 to 6 GPa), d_H (10 to 160 μm) and t_H (0.001 to 1 μs) of the Gaussian pressure field and using the strain rate sensitive material properties defined by the JC plasticity model, as in Eq. (4.1). As an example, Fig. 4.12 shows the distribution of pit depth h_P and diameter d_P for a characteristic impact rise duration $t_H = 0.05$ μs and different values of σ_H and d_H. Point to be noted, pit diameter is always measured at mid-pit depth to be consistent with the experimental measurement of pit diameter to avoid surface noise effect and cut-off depth dependence as described in Sec. 2.4 in Chapter-2 (or in [2]). One interesting fact to be noticed in Fig. 4.12 is that for a pit of given depth and diameter (h_P, d_P) there is only one set of impact load parameters (σ_H, d_H) that can produce the pit when the impact duration is known. This kind of bijective behavior or one-to-one correspondence between the pit dimensions and the hydrodynamic impact parameters has earlier been reported by Roy *et al.* [2] within the framework of FEM static analysis of cavitation pitting. This one-to-one correspondence is very essential for estimating hydrodynamic impact loads from pit geometries by the inverse FEM technique as described in [2,3].

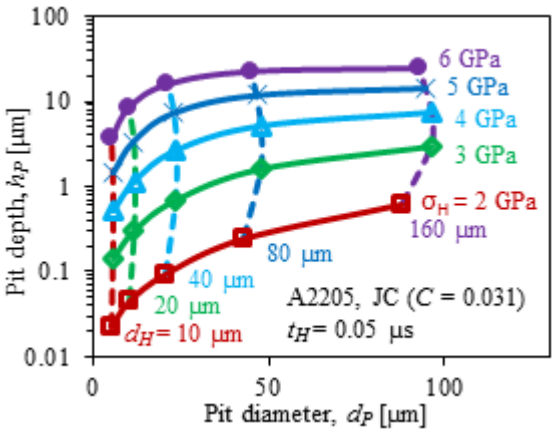

Fig. 4.12 Distribution of pit depth h_P and diameter d_P in A-2205 for a characteristic impact rise duration $t_H = 0.05$ μs and different values of σ_H and d_H. The vertical axis is plotted on log-scale for better readability.

Note that in Fig. 4.12 the impact rise duration is assumed to be the same, irrespective of the impact diameter d_H, which seems to be a little bit unrealistic from the fluid dynamics point of view. The reason for this assumption is that, although experimental measurements of impact duration due to cavitation bubble collapse are available

in the literature, no method is available to derive the impact duration corresponding to a given cavitation pit, at least by the current state of art. Computational fluid dynamics (CFD) simulation of cavitation bubble collapse has been the common practice to correlate collapse duration with bubble size and/or collapse standoff distance [81], but still there is no useable relationship between pit shape and impact duration. In [6] Franc and Michel have stated that the impact duration of cavitation bubble collapse is on the order of the ratio of bubble radius (r_b) to the speed of sound in the liquid medium (c_l). When the microjet resulting from bubble collapse hits the wall, a very high pressure is applied to the material that can be estimated from the classical water hammer formula $\rho_l c_l v_l$ where v_l is the velocity of the microjet and ρ_l is the density of the liquid. Outside the jet, a relatively small pressure is applied corresponding to the ambient pressure in the flow. As a result, a pressure discontinuity or shock wave is generated at the boundary of the jet that propagates inwards at the speed of sound in the liquid. During wave propagation, the wall is progressively unloaded until the shock wave reaches the microjet center, which corresponds to complete unloading. The propagation of the wave from the boundary of the jet to its center requires the time (r_b/c_l) that can then be considered as the rise time of the impact pressure. Thus, we could estimate the characteristic impact rise duration t_H based on the impact diameter d_H using $2 \times t_H = d_H/(2 \times c_l)$. This is what is done in Fig. 4.13. Unlike Fig. 4.12 where t_H was kept constant, in Fig. 4.13 the characteristic impact rise duration t_H is estimated from d_H as stated above. Now also, very interestingly, there exists the one-to-one correspondence between the pit dimensions and the hydrodynamic impact parameters. This opens up a new opportunity for implementing the inverse FEM technique as described in [2,3] for estimating the hydrodynamic impact loads from the cavitation pit geometries by considering the complete dynamic behavior of the target materials. This remains the subject of future research which might give us more accurate estimation of the hydrodynamic impact loads for better quantification of flow aggressiveness.

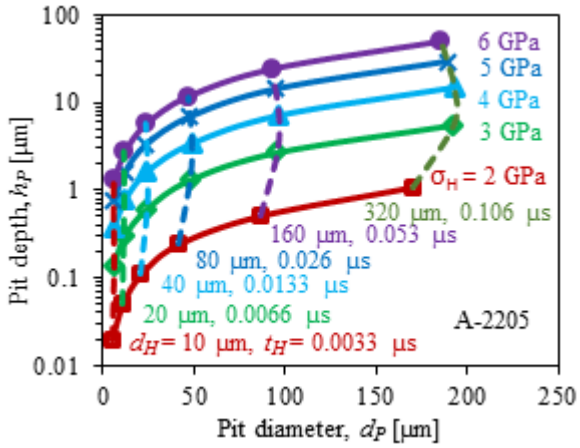

Fig. 4.13 Distribution of pit depth h_P and diameter d_P in A-2205 for different values of σ_H and d_H. The characteristic impact rise duration t_H is estimated from d_H. The vertical axis is plotted on log-scale for better readability.

The limitations of such a method would be in selecting a proper material and adequately characterizing its mechanical properties, particularly if the material behavior is size or microstructure dependent. Although the Gaussian pressure field is used for simplicity, the real pressure load applied during bubble collapse is often

more complex in both space and time [81]. Knowledge of impact duration corresponding to a given pit, required by the inverse FEM technique for accurate estimation of impact loads, is a big challenge for the time being.

In Fig. 4.12, it is clear that pit depth h_P increases with increase in both σ_H and d_H, whereas pit diameter d_P increases essentially with increase in d_H. In Fig. 4.14, pit shape factor (h_P/d_P) is plotted as a function of peak impact stress σ_H (2-6 GPa) on log-log scale for different values of d_H (10–60 µm) and t_H = 0.01, 0.05 & 0.5 µs. Different types of points indicate different characteristic impact diameters (d_H) and different types of lines, each of which joins the iso-d_H data points, indicate different characteristic impact rise durations (t_H). As can be been seen, for a given value of d_H and t_H, pit shape factor h_P/d_P follows a power law behavior with σ_H. When t_H is ≥ 0.05 µs (dotted and dashed lines), h_P/d_P becomes almost independent of d_H and t_H and, follows almost a unique curve (for example dashed lines). This type of unique behavior was studied by Roy *et al.* [2] with FEM static analysis. The analytical method they proposed to predict the peak impact stress from the cavitation pit geometry is here extended to complete dynamic behavior of the target material under cavitation pitting.

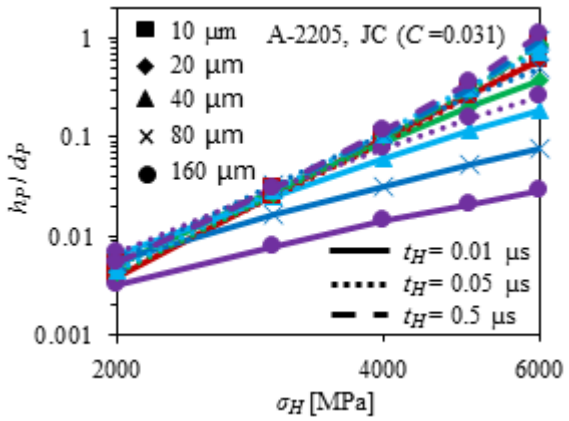

Fig. 4.14 Pit shape factor (h_P/d_P) as a function of peak impact stress σ_H for different values of d_H (10–60 µm) and t_H = 0.01, 0.05 & 0.5 µs. Each line joins the iso-d_H data points where different line types indicate different values of t_H and different point types indicate different d_H. Linear behavior on log-log graph indicate power law behavior.

In Fig. 4.15 the ratio of pit diameter to impact diameter (d_P/d_H) is plotted as a function of the impact diameter d_H for different values of σ_H, which shows d_P/d_H remains almost constant irrespective of the value of σ_H, though the error limit increased from ± 5.0% at d_H= 10 µm to ± 12.0% at d_H= 160 µm. It should be remembered that unlike d_H, the pit diameter d_P is measured at mid-pit depth, hence the ratio d_P/d_H is close to 0.5. This indicates that actual pit diameter and impact diameter are very close to each other. Earlier by FEM static analysis Roy *et al*. [2] have seen a similar behavior, which seems to be true if inertial and strain rate sensitivity are included into the simulation. This could be used to predict impact diameter from cavitation pit geometry for a given target material.

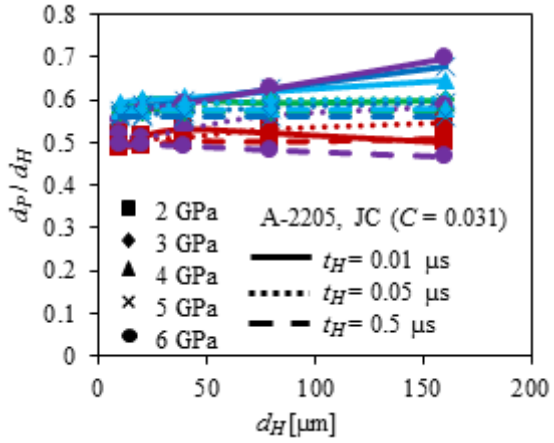

Fig. 4.15 Ratio of pit diameter to impact diameter (d_P/d_H) as a function of impact diameter d_H for different values of σ_H (2-6 GPa) and t_H = 0.01, 0.05 & 0.5 µs. Each line joins the iso-σ_H data points where different line types indicate different values of t_H and different point types indicate different σ_H.

4.4.3. Strain rate during cavitation pit formation

Knowledge of strain rate involved in pit formation due to cavitation bubble collapse is important for mass loss prediction [6,81,147] or quantification of flow aggressiveness [3,67,145]. Though there is no solid way to justify, generally strain rate of 10^3 s^{-1} or more is used [6,67,147]. With the current state of art, to the best of our knowledge, we cannot measure it experimentally. Numerical approach (FEM) has been adopted here to estimate the maximum strain rate achieved during pitting.

The deformation in cavitation pitting is not homogeneous around a pit (Fig. 4.7), so that the strain rate would be different at different points into the material. Hence, the determination of maximum strain rate would be a good indicator. As shown in Fig. 4.16, maximum of maximum principal strain rates ($\dot{\epsilon}$) into the materials is plotted as a function of the characteristic impact rise duration t_H for constant values of σ_H= 3 GPa and d_H= 40 µm. For all the three materials, in a log-log graph $\dot{\epsilon}$ versus t_H follows a linear behavior. Thus we could conclude that for metallic alloys, maximum of maximum principal strain rate ($\dot{\epsilon}$) follows a power law behavior with impact rise duration t_H as given by the Eq. (4.7) (plotted by dashed line in Fig. 4.16).

$$\dot{\epsilon} = C_{14} t_H^{C_{15}} \tag{4.7}$$

In Eq. (4.7), C_{14} and C_{15} are fitting constants and can be obtained by numerical cavitation pitting analysis of the target material. These two constants would depend on the material properties and impact loading condition (i.e. σ_H and d_H). The estimated values of C_{14} and C_{15} estimated from Fig. 4.16 are given in Table 4.2.

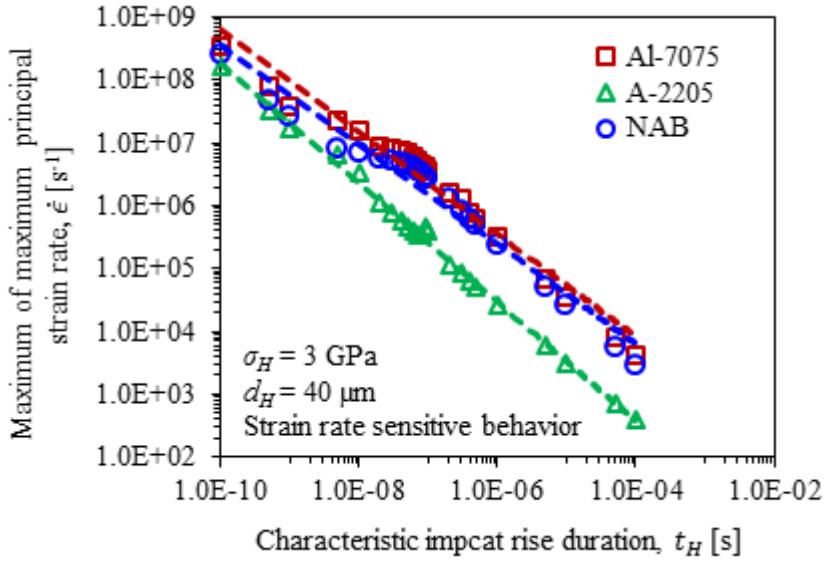

Fig. 4.16 Plot of maximum of maximum principal strain rates ($\dot{\epsilon}$) into the material versus characteristic impact rise duration t_H (on log-log scale) for constant values of σ_H = 3 GPa and d_H = 40 µm is plotted for all three materials Dotted line represents the power law fitting.

Table 4.2 Values of C_{14} and C_{15} estimated from Fig. 4.16

Material	C_{14} **[s^{-1}]**	C_{15}
Al-7075	4.6783	-0.813
A-2205	0.0604	-0.948
NAB	4.3102	-0.793

From Fig. 4.16, it is clear that strain rate in cavitation pitting depends on the impact duration and may be very high. Now if we consider an impact of size $d_H = 2$ mm and the speed of sound in water $c_l \approx 1500$ m/s, then the characteristic impact rise duration t_H can be estimated as stated in [6] using $2 \times t_H = d_H/(2 \times c_l)$. This yields $t_H \approx 0.333$ µs for which the strain rate would be ~10^5 s^{-1} in A-2205. Probability of such a large impact of 2 mm size would be very rare in cavitation pitting. From our earlier experiences [2,3,145]] on cavitation pitting test, the characteristic mean size of hydrodynamic impacts is close of 50 µm, for which the corresponding impact rise time $t_H \approx 0.0166$ µs and strain rate would be ~10^6 s^{-1} in A-2205 material. Thus Fig. 4.16 gives us a more reliable indication of level of strain rate into a metal subjected to cavitation hydrodynamic impact. It should be re-emphasized here that the analytical measurement of t_H as stated in [6] using $2 \times t_H = d_H/(2 \times c_l)$ is not universal. It is used here to have a rough idea of the strain rate. Though it is debatable, impact duration in cavitation pitting is assumed to be of the order of microsecond [35], for which the strain rate would be about 10^5-10^6 s^{-1}.

4.5. Summary and conclusions

Dynamic behavior of cavitation pitting has been analyzed in this paper in details and some interesting phenomena have been observed. It is well established that if the peak stress of the hydrodynamic impact is less than a certain value for which the local stress into the target material is smaller than the yield stress, then no cavitation pit will form. The current study shows that, even if the peak stress is significantly high but the impact duration very short compared to the characteristic time of the material defined on the basis of its natural frequency, no detectable pit will form into the material. This is because of the dynamic behavior of the material under the hydrodynamic impact load at very high frequency. At high frequency, the dynamic behavior is controlled by the inertia of the material as the velocity or acceleration of the deformation is very high. Most of the supplied energy is converted into as kinetic energy and less energy remains available for deformation or work-done. When the impact duration is high, the frequency is less and the deformation is controlled by the stiffness of the material rather than inertia and sufficient amount of the energy is spent on work-done in terms of elastic-plastic deformation.

Inertia and strain rate sensitivity both influence the pit dimensions in cavitation pitting. In metals, at least for the three materials investigated here, the inertial effect on pit dimension becomes insignificant if the impact duration is greater than about one microsecond, while the strain rate effect is inevitable in cavitation pitting since it affects any impact whatever may be its duration up to about 10^5 μs. With increase in strain rate sensitivity the pit becomes shallow, thus the affected volume of the material under hydrodynamic impact gets reduced. Hence the strain rate sensitivity could be considered beneficial since it would reduce the size of deformed region and thereby mass-loss rate due to cavitation erosion.

It is observed that there exists a one-to-one correspondence between the hydrodynamic impact load and the cavitation pit shape. This is a very important conclusion that would enable us to estimate the hydrodynamic impact load from cavitation pit geometry by numerically reproducing the cavitation pit considering the complete dynamics of the material behavior. This remains the subject of future research.

Rate of strain of material deformation during cavitation pitting depends on the hydrodynamic impact duration and accurate estimation of impact duration either by experimental or numerical method remains a big challenge for the researchers. Current study shows that, in metals the strain rate could vary in the range of 10^4 to 10^7 s^{-1} when the loading time varies between 1 μs and 0.001 μs.

4.6. Some highlights and remarks

Some highlights of the chapter:

- Dynamics of cavitation impact on Al-7075, A-2205 and NAB materials have been studied.
- Dynamic explicit analysis of cavitation pitting was conducted with a doubly Gaussian type of pressure field versus space and time.
- Along with the yield strength, the strain rate sensitivity provides additional resistance to cavitation erosion.
- Strain rate sensitivity of a material greatly influences the cavitation pit dimensions.
- Dynamic behavior of a metallic alloy under cavitation impact is similar to a spring-mass-damper system.
- Natural frequency of the target material greatly influences the energy transfer between the cavitation impact due to bubble collapse and the target material.
- Cavitation impact of very high magnitude compared to that of yield strength of the material may not be able to produce a cavitation pit if the impact duration is very short compared to its natural period.
- At lower frequency of impact loading, the deformation is controlled by the stiffness and most of the impact energy is spent on plastic deformation or pit formation.
- At higher frequency of impact loading, the inertial effect becomes dominant and most of the impact energy transform into kinetic energy, less energy remains for plastic work.
- One-to-one correspondence between cavitation pit and impact load has been observed. This provides the background to implement the inverse FE technique along with dynamic behavior of material to estimate impact load from cavitation pit geometry.
- The analytical method proposed in Chapter-2 for the prediction of impact load from pit geometry (in static analysis) has been confirmed to be valid when accounting for the dynamic behavior of the materials.
- Strain rate in cavitation pitting is very high, in the order of 10^4 to 10^7 s^{-1}.

Remarks:

In this chapter (Chapter-4) a few of the primary objectives (a part of item number 2 and item number (ii) as discussed in Sec. 1.5) have been achieved. Apart from that some interesting conclusions have been drawn. The rest of the aims are dealt with in the following chapters.

Chapter-5

5. Modeling of damage due to cavitation erosion and mass loss prediction

This chapter contains the results of a journal paper [5] whose details are given below. However, additional data and results are included which could not be included in the paper. Some data are also removed to avoid unnecessary repetition of any dialogue, figures or tables etc. that were already presented in the thesis. The paper has been published in the journal "Interface Focus" in 2015.

M. Fivel, J. -P. Franc, S. C. Roy, "Towards numerical prediction of cavitation erosion," Interface Focus, 5, 20150013. http://dx.doi.org/10.1098/rsfs.2015.0013

Towards numerical prediction of cavitation erosion

Marc Fivel[1], Jean-Pierre Franc[2] and **Samir Chandra Roy[1]**

[1]SIMaP, and [2]LEGI, Université Grenoble Alpes, Grenoble, France

Corresponding authors e-mail: jean-pierre.franc@legi.cnrs.fr

Abstract

This paper is intended to provide a potential basis for a numerical prediction of cavitation erosion damage. The proposed method can be divided into two steps. The first step consists in determining the loading conditions due to cavitation bubble collapses. It is shown that individual pits observed on highly polished metallic samples exposed to cavitation for a relatively small time can be considered as the signature of bubble collapse. By combining pitting tests with an inverse finite-element modelling (FEM) of the material response to a representative impact load, loading conditions can be derived for each individual bubble collapse in terms of stress amplitude (in gigapascals) and radial extent (in micrometres). This step requires characterizing as accurately as possible the properties of the material exposed to cavitation. This characterization should include the effect of strain rate, which is known to be high in cavitation erosion (typically of the order of several thousands s^{-1}). Nanoindentation techniques as well as compressive tests at high strain rate using, for example, a split Hopkinson pressure bar test system may be used. The second step consists in developing an FEM approach to simulate the material response to the repetitive impact loads determined in step 1. This includes a detailed analysis of the hardening process (isotropic versus kinematic) in order to properly account for fatigue as well as the development of a suitable model of material damage and failure to account for mass loss. Although the whole method is not yet fully operational, promising results are presented that show that such a numerical method might be, in the long term, an alternative to correlative techniques used so far for cavitation erosion prediction.

Keywords: *Cavitation, Erosion, Bubble*

5.1. Introduction

A well-known consequence of cavitation is erosion of neighboring solid walls caused by the impact of high velocity liquid jets and/or shock waves. Prediction of such erosion is required for calculating service life of a hydraulic component for successful operation. Fig. 5.1 shows a typical example of cavitation erosion damage observed in a gear pump. Several regions of erosion with a different amount of damage are visible in Fig. 5.1 from limited damage characterized by an orange peel appearance to more serious damage characterized by significant material removal.

Fig. 5.1 Typical example of cavitation erosion damage in a gear pump circulating mercury (LEGI photograph).

Cavitation damage depends on both the liquid flow conditions and the material properties. On the liquid side, a key issue is to define the so-called flow aggressiveness or cavitation intensity. An attempt is made in Chapter-2 to quantify the cavitation intensity in terms of the loading conditions due to bubble collapses.

On the material side, damage depends upon the mechanical properties of the material. As discussed in Sec. 1.4.2.1, various correlative techniques are available in the literature for predicting cavitation damage (see e.g. [7]). They generally relate the resistance to erosion often defined as the inverse of the erosion rate (typically in μm/h) to some relevant material property (e.g. hardness). A major difficulty is that such correlative techniques are not universal and depend upon the class of material and the type of the cavitating flow. It is then hazardous using such correlative techniques to predict cavitation damage for materials or cavitating conditions that deviate from the ones used for establishing the correlation.

Because of the lack of versatility of the correlative techniques, alternative methods are being developed, that make greater use of numerical simulation. They are based on a physical analysis of the phenomena involved in cavitation erosion and require modelling as accurately as possible each step of the erosion process for both the fluid and the material. The objective of this paper is to provide an outline of such an analysis.

The proposed method can be broken up into two main steps. The first step consists in determining the impact loads due to cavitation bubble collapses. The idea behind this is that any simulation of cavitation erosion requires firstly a thorough knowledge of the loads applied to the material. A method have been proposed in Chapter-2 ([2]) to determine the spectrum of impact loads from joint pitting tests and finite element modelling (FEM).

The second step consists in simulating the response of the material to repetitive impact loads. The objective is to predict the behavior of the material as a function of the exposure time i.e. for an increasing number of impact loads. The model should be able to account for the various stages of the erosion process. This includes the incubation period where no significant mass loss is observed and the more advanced stages of erosion where material is progressively removed by the collapsing bubbles. For such a simulation, the impact loads identified in the first step should be applied repetitively and randomly on the material surface.

This computational numerical is based on the stress-strain relationship of the material that should include the effect of strain rate and density since the strain rate is quite high in cavitation because of the small duration of the impact loads. It also requires an appropriate modelling of the hardening mechanism in order to account for fatigue behavior that is observed during the incubation period. Finally, it also requires modelling the damage process including failure that leads to mass loss.

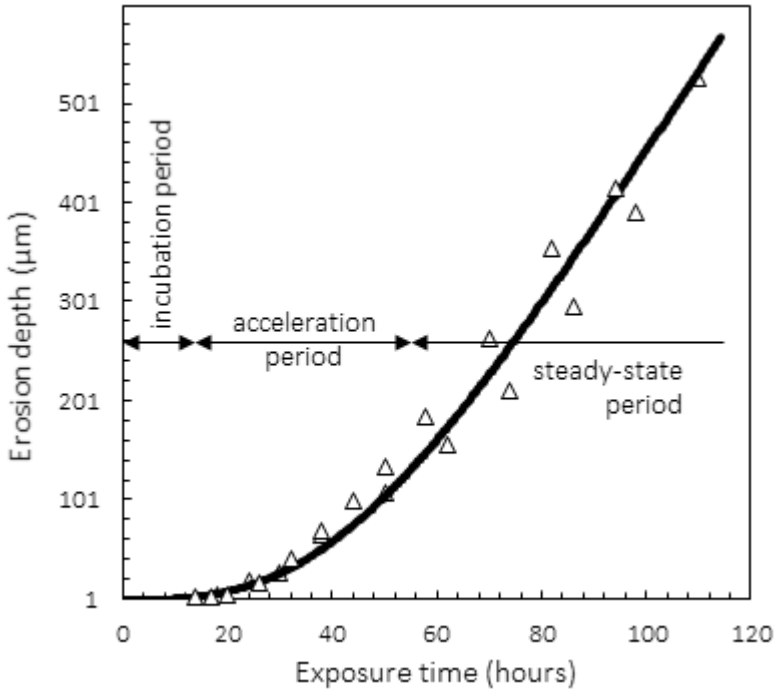

Fig. 5.2 Typical example of the kinetics of cavitation erosion damage. The curve shows the evolution of the erosion depth as a function of the exposure time for a Nickel Aluminum Bronze alloy. Results obtained in a cavitation erosion tunnel [7,38,62,63].

The approach proposed here is a one-way simulation since the impact loads are supposed to be unchanged by the erosion of the solid wall. In other words, it is assumed that the change in the wall geometry does not significantly affect the cavitating flow and the impact loads. The model is then supposed to reach a steady-

state regime of erosion characterized by a constant erosion rate beyond a given exposure time (Fig. 5.2). It is not able to predict the longer term behavior that require a more complicated time evolution of mass loss such as an attenuation period [6] which is generally interpreted in terms of a reduction of flow aggressiveness because of a modification of the flow due to the change in wall geometry.

It may be, however, necessary that the impact loads determined in the first step include the damping effect due to the fluid structure interaction. This is particularly important in the case of soft materials such as polymeric coatings that may undergo a significant deformation during bubble collapses, resulting in a reduction of the amplitude of the impact loads in comparison to a perfectly rigid wall. A simple model is briefly described in this chapter to account for the fluid structure interaction.

Various laboratory devices have been developed in order to investigate cavitation erosion, as described in Sec. 1.2 in Chapter-1. The approach presented in this paper is supported by experimental data (in particular pitting test data) obtained in a cavitation erosion tunnel using a radial divergent test section [7,38,62,63].

The two steps mentioned above are addressed in separate sections. Sec. 5.2 is devoted to the determination of the cavitation impact loads using pitting tests combined with inverse FEM simulations. Section 5.3 is devoted to an analysis of the response of the material to repetitive impact loads with a special emphasis on the most relevant material properties to be considered for damage prediction. In Sec. 5.4 some preliminary results of a large number of impacts on a three dimensional material surface, applied randomly and repetitively to track the mass-loss with time, have been discussed. It should be emphasized that the FEM simulations of fatigue and damage presented in Section 5.3 are very preliminary results that need further research developments before the proposed method is effective for real applications.

5.2. Cavitation impact loads

In Chapter-2 (or in [2]) a new method called “numerical inverse method” or “inverse FE technique” is proposed to estimate the impact loads due to cavitation bubbles collapses in a high speed liquid. The method is based on cavitation pitting tests and FEM simulations of material response. The feasibility and limitations of the proposed method, to take into account the dynamic behavior (especially inertial and strain rate effect) of the material (used as a pressure sensor in the proposed method) into the FEM simulations, have been discussed in Chapter-4 (or in [4]. In Chapter-3 (or in [3]) the method was further implemented on three different materials under the same flow condition to verify the accuracy of the impact loads estimated. However the proposed method has some scope for further improvements, the material independence of the estimated impact loads using different materials as pressure sensors depicts about the accuracy. The same method is also adopted here for estimating the statistical population of the cavitation impact loads and a summary in brief is given below.

Pitting tests are short duration tests conducted on the three ductile metallic materials namely 7075 Aluminum alloy (Al-7075), 2205 duplex stainless steel (A-2205), Nickel-Aluminum Bronze (NAB) at different flow pressures of 10, 20 and 40 bar. The sample surface is mirror polished prior to exposure to cavitation in order

to reveal the tiny plastic deformations or pits due to bubble collapses. Fig. 5.3 presents a typical example of the surface of a stainless steel sample exposed to cavitation for a relatively short time. The exposure time should be adjusted in order to have a sufficient number of pits to enable a statistical analysis, on the one hand, and to limit pit overlapping that would bias the analysis, on the other hand.

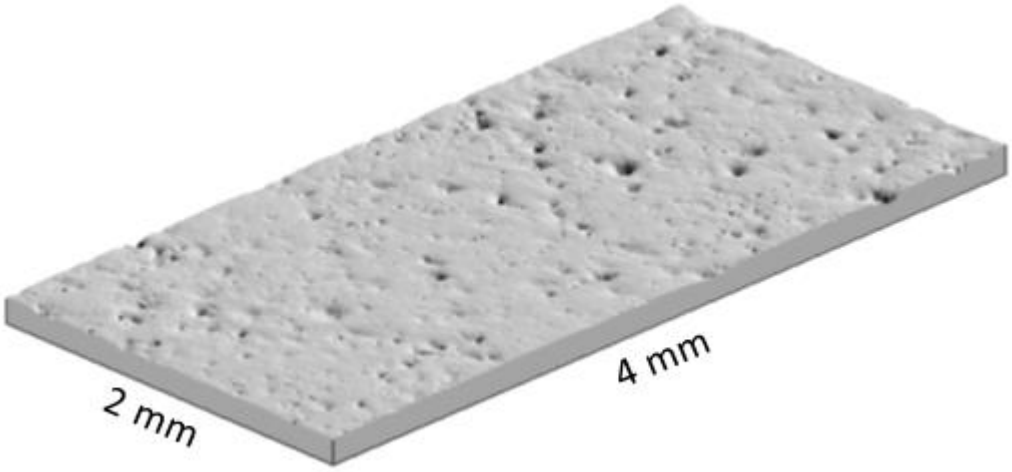

Fig. 5.3 Typical view of a pitting test. Material is stainless steel A2205. The surface (2 mm x 4 mm) was scanned using a contact profilometer with a precision of 1 µm in both horizontal directions. Operating conditions [62] for cavitation erosion test: upstream pressure 2 MPa (20 bar), flow velocity 60 m/s, cavitation number 0.9, exposure time 6 minutes.

As proposed in [2] (or in Sec. 2.4 in Chapter-2) and in the present study as well, the resulting pit is characterized by two geometrical parameters, namely its residual maximum depth h_P and residual diameter d_P measured at mid-depth (Fig. 5.4(b)).

The impact load corresponding to a bubble collapse is assumed to have a Gaussian type of distribution (Eq. (5.1)) with two parameters as shown in Fig. 5.4(a).

$$\sigma = \sigma_H \exp\left(-\left(\frac{2r}{d_H}\right)^2\right) \tag{5.1}$$

where r is the radial distance along the wall from the bubble axis as shown in Fig. 5.4(a). This equation gives the space distribution of the hydrodynamic impact load in terms of amplitude σ_H and radial extent d_H. The load given by Eq. (5.1) is the normal component of the applied stress tensor.

The Gaussian law used here is a simplified model of the actual loading conditions. It is well known that several phenomena occur during the collapse of a bubble near a wall including the development of a microjet and shockwaves [7]. As a result, the actual loading is much more complicated than the one described by Eq. (5.1). In addition, unsteadiness in loading and unloading is ignored in Eq. (5.1) since no time dependence is included. To include time dependency into the proposed "numerical inverse method", impact duration corresponding to each pit has to be known, which is difficult to measure experimentally [2–4]. Then, there is obviously room for improving the present approach. Even though the time variation of loading is ignored, the high strain rate encountered in cavitation is here taken into account to some extent by using, in FEM computations, stress strain relationships obtained at high strain rate (10^6 s^{-1}) as opposed to quasi-steady stress strain relationships.

The choice of this value for strain rate is explained in Sec. 4.4.3 in Chapter-4 (or in [4]) which corresponds to an impact duration of as short as 1 µs for all the three materials.

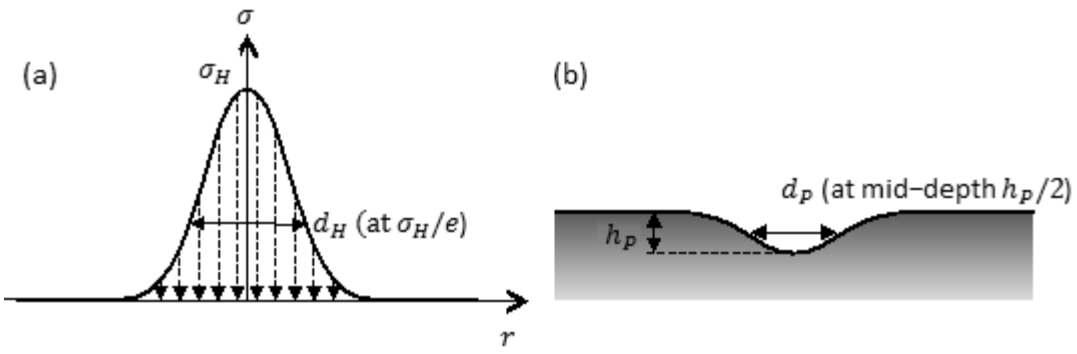

Fig. 5.4 Schematic representation of the impact load due to the collapse of a cavitation bubble using a Gaussian law (left). Definition of the two main characteristics of a pit (right).

All aspects of the numerical inverse method are presented in details in [2–4]. A two dimensional axisymmetric model as shown in Fig. 4.1 in Chapter-4 is used. The mesh is parameterized by the hydrodynamic parameter d_H. The minimum element size is 0.123 µm and size of the model domain is 1500 µm for $d_H = 20$ µm. Zero vertical displacement condition is imposed on the bottom boundary of the model. The mesh has been validated by applying the reference Hertzian loading on a purely elastic material for which the analytical solution is available. Computations are made using Abaqus standard. Although the numerical model is quasi-steady, it should be emphasized that the effect of strain rate on the material behavior is, to some extent, included by considering a stress-strain relationship at high strain-rate (see Sec. 3.2 in Chapter-3). The material properties were characterize by nanoindentation tests and, the strain rate sensitivities required to extrapolate the stress-strain relationships at high strain rate were estimated by compression and split Hopkinson pressure bar tests, as explained in Sec. 3.2 in Chapter-3 [3]. Typical results of an inverse calculation are shown in Fig. 5.5 and Fig. 5.6.

Fig. 5.5 shows the evolution of the frequency of impact loads as a function of their amplitude σ_H. Two curves are plotted that correspond to two different ranges in impact diameter d_H. The vertical axis is the frequency of impact loads (N) per unit surface area exposed to cavitation. In addition, it has been divided by the two bandwidths in σ_H and d_H to get the frequency insensitive to bandwidths. This explains the presence of MPa and µm in the unit.

As shown in Fig. 5.5, each material allows investigating a different range in stress amplitude. Soft materials (such as the aluminum alloy) permit the determination of the impact load spectrum for relatively low stress amplitude whereas harder materials (such as stainless steels) permit investigating higher amplitudes. The interest of using several materials is to broaden the range in stress amplitude. It is clear that the material used for pitting tests must not be harder than the one for which the prediction of long-term erosion is desired. If it is harder, a fraction of the impact loads of small amplitude will not be detected by pitting tests whereas they actually contribute to damage.

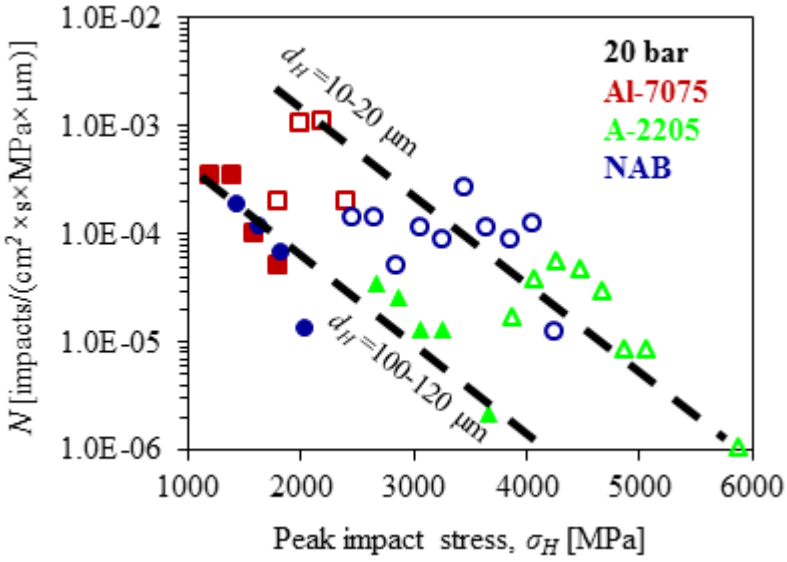

Fig. 5.5 Frequency of impact loads as a function of amplitude for two different bandwidths in impact load diameter 10 - 20 µm and 100 – 120 µm. The data are well represented by straight lines in the above log – linear scales so that it can be assumed that the impact load frequency decays exponentially with amplitude. The frequency is expressed in impacts/cm^2/s/MPa/µm. It represents the frequency of impacts per unit surface area exposed to the cavitating flow and per unit bandwidth in both amplitude and diameter.

Since the impact loads are here characterized by two parameters, namely the impact stress σ_H and impact diameter d_H, it should be interesting to represent the spectrum of frequency of impact loads versus both parameters using a three dimensional picture as shown in Fig. 5.6. The surface thus obtained is considered in this paper as a measure of the cavitation intensity or flow aggressiveness.

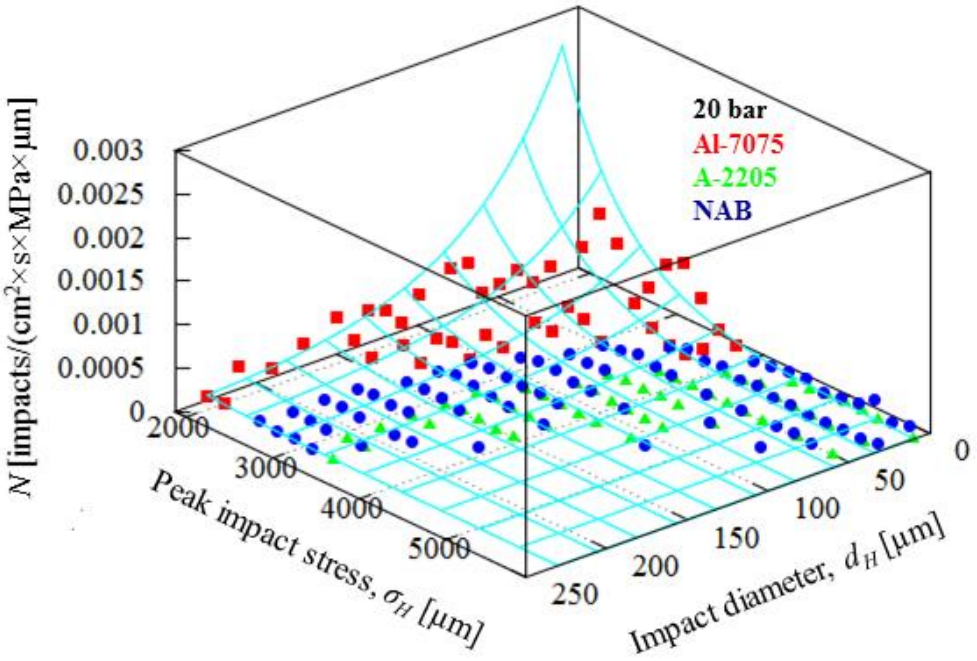

Fig. 5.6 Representation of flow aggressiveness in terms of a spectrum of impact loads vs. impact stress and impact diameter.

Other parameters may be considered in addition to σ_H and d_H for a more accurate description of each impact such as the duration of impact. If so, additional axis should be added in Fig. 5.6 and flow aggressiveness would be characterized by a hypersurface. The larger the number of parameters the more accurate the model of flow aggressiveness is.

Next step is to simulate the response of the material to the so-defined flow aggressiveness in order to predict cavitation damage.

It should be underlined here that the fluid-structure interaction was not considered for determining the impact loads in Section 5.2. This is because the pitting tests from which the impact loads were derived are made using metallic materials that are generally quite stiff. As a result, the hydrodynamic impact loads are only weakly damped by the recoil effect of the wall. This is no longer the case for soft materials that may significantly reduce the impact stress in comparison to rigid walls. In this case, the fluid-structure interaction must be taken into account in order to update the impact loads. This is especially the case for soft coatings such as paints or polymeric coatings.

In a first approach, the importance of the fluid-structure interaction can be estimated using a simple one-dimensional model of the impact of a high velocity liquid jet on an elastic material. The shock of the liquid on the material surface is supposed to generate two plane shock waves, one propagating forward into the solid and the other one backward in the liquid. The impact pressure is given by [6]:

$$P_{imp} = \left(\rho_l c_l v_{jet}\right)/\left(1 + \left(\rho_l c_l/\rho_s c_s\right)\right) \tag{5.2}$$

The numerator is the impact pressure of a liquid jet of velocity v_{jet} on a perfectly rigid wall. It is derived from the common water hammer formula. The quantity ρc is the acoustic impedance of the liquid (subscript l) or solid (subscript s). The acoustic impedance of the solid is connected to Young's modulus E by $\rho_s c_s = \sqrt{\rho_s E}$.

Equation (5.2) shows that the actual pressure on an elastic material is smaller than that on a rigid wall. According to this model, the damping effect is directly connected to the ratio of the acoustic impedances $\alpha' = \rho_s c_s/\rho_l c_l$. Fig. 5.7 shows the influence of α' on the non-dimensional pressure $\mathrm{P_{imp}}/\rho_l c_l v_{jet}$. The perfectly rigid wall corresponds to an infinite value of α' whereas the compliant wall corresponds to $\alpha' = 0$ for which the impact pressure vanishes.

As an example, let us consider a coating made of Ultra High Molecular Weight Polyethylene (UHMWPE) exposed to a cavitating water flow. In this particular case, mechanical properties are the following [52]:

$\rho_{UHMWPE} \cong 945$ kg/m^3	$c_{UHMWPE} \cong 2000$ m/s	$(\rho c)_{UHMWPE} \cong 1.9 \times 10^6$ kg/m^2/s
$\rho_{water} \cong 1000$ kg/m^3	$c_{water} \cong 1500$ m/s	$(\rho c)_{water} \cong 1.5 \times 10^6$ kg/m^2/s

The ratio of acoustic impedances is then $\alpha' = \rho_s c_s/\rho_l c_l \cong 1.26$. As a result, the impact pressure given by Eq. (5.2) is only 56% of the impact pressure in the perfectly rigid case.

This simple model of fluid structure interaction shows that the amplitude of impact loads may quite significantly be reduced in the case of a compliant wall. The same conclusion is obtained when considering a stiffer liquid such as cavitating mercury. In the case of a compliant wall or a stiff liquid, the impact stresses as determined in Section 5.2 must be updated to account for the damping effect due to the fluid-structure interaction for a right prediction of cavitation damage.

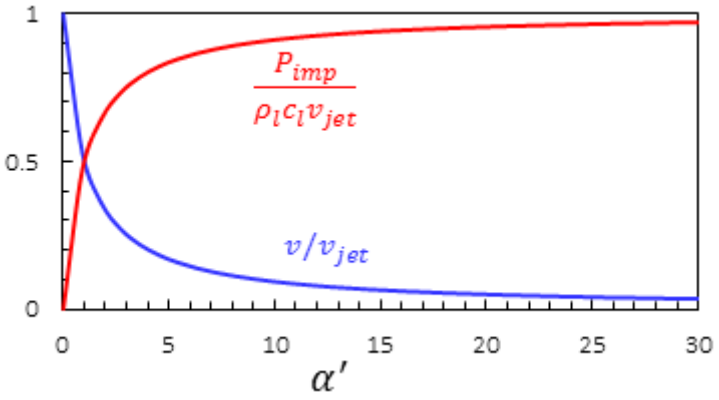

Fig. 5.7 Simple model of the fluid-structure interaction in the case of a jet impacting a solid wall with a velocity v_{jet}. The amplitude of impact load (in red) is made non-dimensional using the water hammer formula and is plotted vs. the ratio α' of acoustic impedances between the solid and the liquid. The plot also shows the influence of α' on the velocity v of the solid wall made non-dimensional using the liquid jet velocity v_{jet} (in blue).

5.3. Material response to cavitation impact loads

This section provides a rough outline of a potential approach for a numerical prediction of cavitation damage. It is based upon a FEM method that aims at simulating the response of the material to the cavitation intensity defined in Sec. 5.2. The goal is to simulate mass loss with time i.e. with the number of impacts, where the estimated statistical population of the impact loads will be applied repetitively and randomly on the material surface. Although, the impact loads were estimated in Chapter-2 by using static finite element (FE) analysis, here dynamic explicit finite element (FE) analysis has to be considered in order to be able to track mass-loss with time. In that case, the Gaussian pressure defined by Eq. (5.1) is not sufficient as it has no time dependence parameter. Time dependency of the impact load is also considered to be of Gaussian type and the impact load is given by the Eq. (5.3) as proposed in Chapter-4.

$$\sigma = \sigma_H \exp\left(-\left(\frac{2r}{d_H}\right)^2\right)\exp\left(-\left(\frac{t - t_{max}}{t_H}\right)^2\right) \tag{5.3}$$

Here, t_H is a characteristic impact duration and t_{max} is the instantaneous time when the load is maximum.

An important issue is to determine the material properties in order to account for the phenomena involved in cavitation erosion. As discussed in Sec. 1.1.5 in Chapter-1, fatigue aspects of cavitation is more complex than that of conventional low cycle fatigue (LCF) or high cycle fatigue (HCF) behavior of materials, especially because of variable amplitudes, sizes, time durations and locations of the impact loadings. Thus it is necessary

to establish an appropriate hardening law that properly characterizes the fatigue behavior. This can be done by numerical simulation of the material response to multiple impacts and analyzing the strain accumulation with different parameters relevant to the real scenario of cavitation fatigue as discussed below in this section. Moreover, it is also required to determine an appropriate damage law or criteria to simulate damage accumulation and propagation leading to failure or mass-loss.

FEM simulation of cavitation damage is still the subject of research and the results presented in this section are very preliminary that need to be confirmed and improved before a consolidated approach for cavitation damage prediction is actually available.

- **Cavitation fatigue: mechanism of strain accumulation**

An essential input of FEM simulations is the material parameters related to the chosen constitutive law. For cavitation applications, it must include the effect of strain rate that generally results in an increase in flow stress for ductile materials. As discussed in Sec. 3.2 in Chapter-3, the Johnson-Cook (JC) plasticity model is widely used for characterizing high strain rate, hence also used for the current study as given by Eq. (5.4).

$$\bar{\sigma} = \left(\sigma_y + K\varepsilon_p^n\right)\left(1 + C\ln\frac{\dot{\varepsilon}_p}{\dot{\varepsilon}_0}\right) \tag{5.4}$$

The materials parameters of the Johnson-Cook plasticity model (Eq. (5.4)) are estimated in Sec. 3.2 in Chapter-3 and are given here in Table 5.1.

Table 5.1 Nanoindentation mechanical properties at strain rate 0.05 s^{-1}, strain rater sensitivity obtained by compression and split Hopkinson pressure bar tests, and physical properties of the materials.

Material	σ_y **[MPa]**	K **[MPa]**	n	C	E **[GPa]**	ν	ρ **(kg/m^3)**
Al-7075	335	396	0.3	0.0068	71.9	0.33	2810
A-2205	508	832	0.51	0.0310	186	0.30	7805
NAB	300	1150	0.58	0.0119	122	0.32	7580

The next step after determining the potential constitutive law and material parameters is to verify the ability of the constitutive law to model cavitation fatigue mechanism. A specificity of cavitation erosion is the repetitive loading that induces fatigue, although there is no reversal of the exerted load due to bubble collapse. The load varies between zero and a compressive peak for each cavitation impact. Fatigue is particularly obvious during the incubation period since cavitation bubbles collapse repetitively on the material surface without producing any mass loss. During the incubation period, the cumulated plastic strain progressively increases within the material until damage occurs. The occurrence of damage determines the end of the incubation period and the onset of the acceleration period.

The conventional model of isotropic hardening (i.e. Eq. (5.4) without considering the strain rate sensitive part) is not appropriate to model the incubation period. This is explained in Fig. 5.8(a) where it is assumed, for simplicity, that the material has a bilinear behavior and the impacts have all the same amplitude σ_H. After the first impact, the material is in state B and its yield stress has increased from σ_y to σ_H. It should be emphasized

here that the local stress into the material is significantly less than the peak impact stress (as discussed in Sec. 2.3 in Chapter-2), however, for simplicity in explanation both are assumed to be same. If a second impact with the same (or smaller) amplitude hits the surface at the same point, the material has a purely elastic behavior and its representative point moves during loading and unloading along path BC. Thus, the second impact and all subsequent impacts have a purely reversible elastic effect but do not deposit additional energy into the material, thus making this hardening model inappropriate for cavitation erosion modelling.

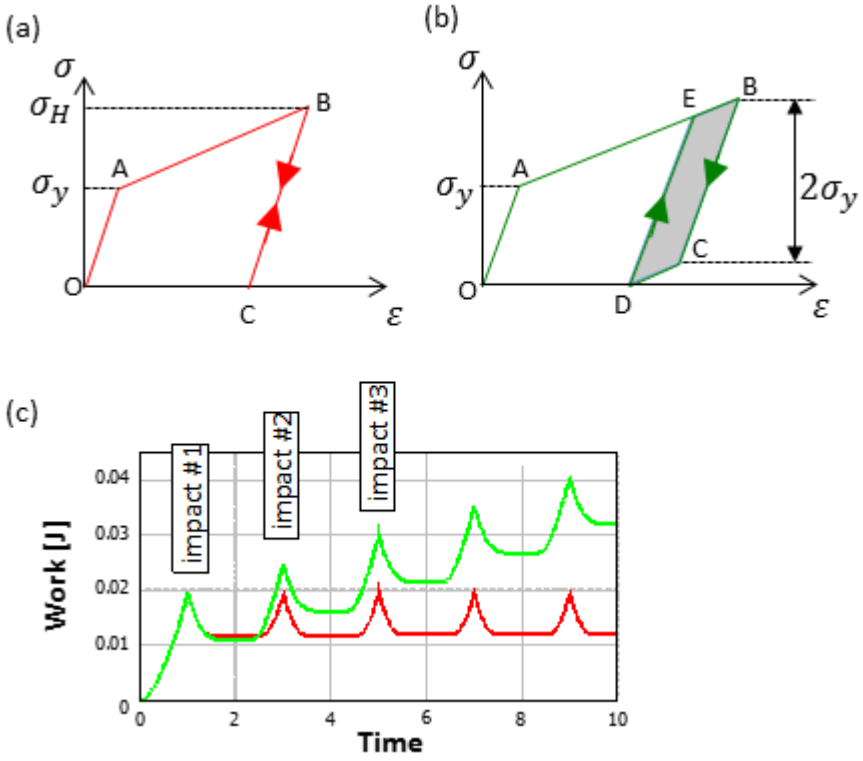

Fig. 5.8 Isotropic (red) vs. kinematic (green) hardening. Typical path in the stress-strain diagram for repetitive impacts in the simple case of a bilinear material (a) isotropic hardening (b) kinematic hardening. (c) Variation of the plastic energy stored by the material as a function of number of impacts for both isotropic and kinematic hardening.

On the other hand, kinematic hardening (i.e. Eq. (5.4) without considering the strain rate sensitive part) allows to account for fatigue. The loading phase OAB for the first impact is exactly the same as for isotropic hardening. However, during unloading, the material follows path BCD which comprises an elastic part BC but also an additional plastic deformation CD. The stress difference between points B and C is twice the initial yield stress σ_y since the yield surface is translated but keeps the same size in kinematic hardening as opposed to isotropic hardening for which it expands.

During the second impact, the material representative point describes the loop DEBCD that has a non-zero thickness. As a result, additional energy corresponding to the area of loop DEBCD is deposited into the material after each new impact. This is confirmed by Fig. 5.8(c) that compares the evolution of work after successive impacts for both hardening models. In the case of isotropic hardening, the work after unloading and elastic recovery remains constant whatever may be the number of impacts. In the case of kinematic hardening,

work increases step by step after each impact. This behavior is consistent with fatigue that develops during the incubation period. However, the point to be noticed in Fig. 5.8(b) is that the above explanation for damage accumulation by kinematic hardening law works only when the flow stress (i.e. stress corresponding to the point B) is more than two times the initial yield strength of the material. Otherwise the material would behave like isotropic hardening. Moreover, the physical relevance of this phenomenon is also questionable, especially for materials like Al-7075 which has low kinematic component in its hardening stage.

These two observations indicate that there is a need for a detailed study of damage accumulation to explore the basic mechanism of damage accumulation from solid mechanics point of view. Particular emphasis is given on the strain rate sensitivity to take into account the dynamic aspect of cavitation and Fig. 5.9 explains the possible mechanism of damage accumulation in cavitation erosion. Here it is assumed that the same impact load, both in space and time, is being applied repetitively at the same location.

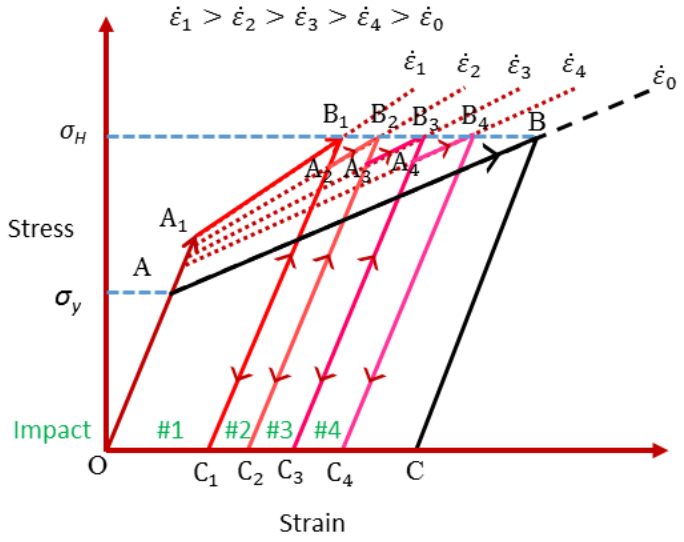

Fig. 5.9 Mechanism of strain accumulation explained by a simple bilinear isotropic hardening model with strain rate sensitivity. The solid lines (color) represent the evolution of the flow stress with the number of impacts for a strain rate sensitive material and the solid lines (black) represent the same for a strain rate insensitive material.

In absence of strain rate sensitivity (at strain rate $\dot{\varepsilon}_0$) if the material is impacted by σ_H, the flow stress would reach B through the path OAB as shown by the black curve in Fig. 5.9. But in presence of strain rate sensitivity, assuming the strain rate is $\dot{\varepsilon}_1$ the flow stress will follow the path OA_1B_1 to reach the same level of stress at B_1. The point to be noted that because of strain rate sensitivity the accumulated strain is reduced from B to B_1. During the second impact, as some work has already been done or energy is stored into the material, the induced plastic deformation will not be the same as for the first impact (most probably less). As a result the plastic strain rate would be different, most probably less compared to the first impact loading. Now by definition, a strain rate sensitive material has no fixed yield strength. Thus, during the second impact, the yield stress of the material would be less than the maximum flow stress (B_1) reached during the first impact, and the material would follow a stress-strain path $C_1A_2B_2$ leading to additional strain accumulation. Similarly, for the

third impact the material would follow a stress-strain path as $C_2A_3B_3$ leading to more strain accumulation. Thus with the number of impacts the strain would accumulates into the material.

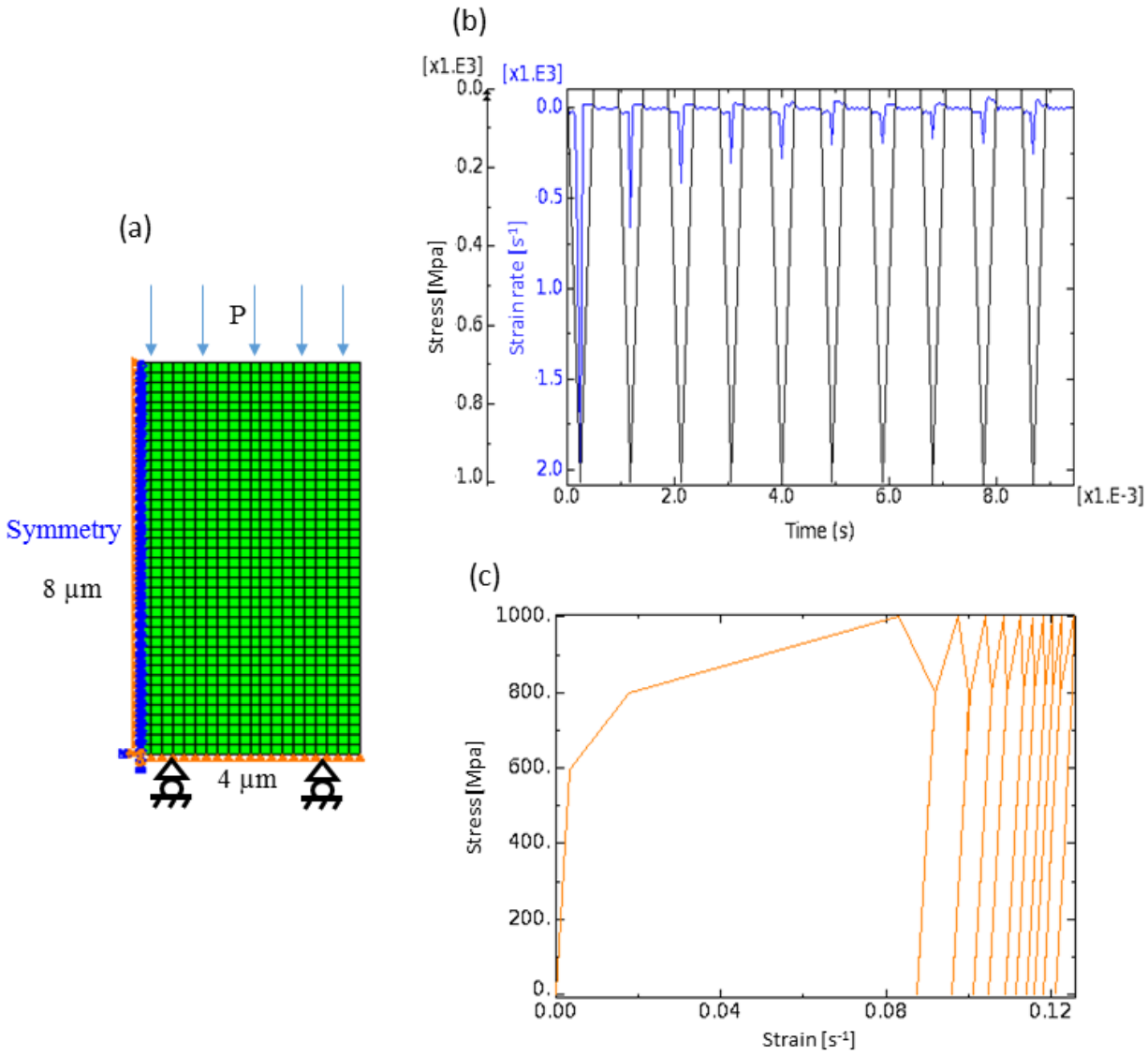

Fig. 5.10 Numerical simulation of dynamic uniaxial fatigue test. (a) The 2D axisymmetric model has a size of 8 µm × 4 µm. (b) Variation of applied pressure and strain rate with time or number of impacts and (c) The stress-strain curve shows strain accumulation with number of impacts.

This mechanism of strain accumulation is verified by conducting numerical simulation of uniaxial compressive fatigue test. The material constitutive behavior was characterized by the Johnson-Cook plasticity model (Eq. (5.4)) that takes into account strain rate sensitivity. Material properties are those of A-2205 stainless steel given in Table 5.1. A two dimensional axisymmetric mesh as shown in Fig. 5.10(a) is used. A pressure load of 1000 MPa has been applied repetitively 10 times with a constant duration of impact of about 0.0004 s. As can be seen in Fig. 5.10(b) during the first impact the maximum strain rate was about 2000 s^{-1} and during the second impact it is drastically reduced to about 700 s^{-1} and follows to decrease with the number of impacts, however small increase is also noticed during the 9^{th} and 10^{th} impacts. The corresponding strain accumulation is plotted in Fig. 5.10(c) that resembles the mechanism explained in Fig. 5.9. These results, in a sense, validate the

proposed mechanism of strain accumulation for cavitation erosion presented above, and also the applicability of JC plasticity model for mass-loss simulation of cavitation erosion. Although phenomenological explanation and numerical evidences have been provided, the experimental verification of this mechanism remains to be done.

Now the effects of impact duration and interval between the successive impacts have been investigated by numerical simulations with the JC plastic model to reveal the fatigue aspects of cavitation. Multiple impacts (10 impacts) on the same location were simulated. As an example Fig. 5.11 shows the effect of characteristic impact duration t_H on the accumulation of plastic energy in the case of A-2205. As can be seen, the plastic strain accumulates with the number of impacts and the amount of strain accumulation varies with impact duration.

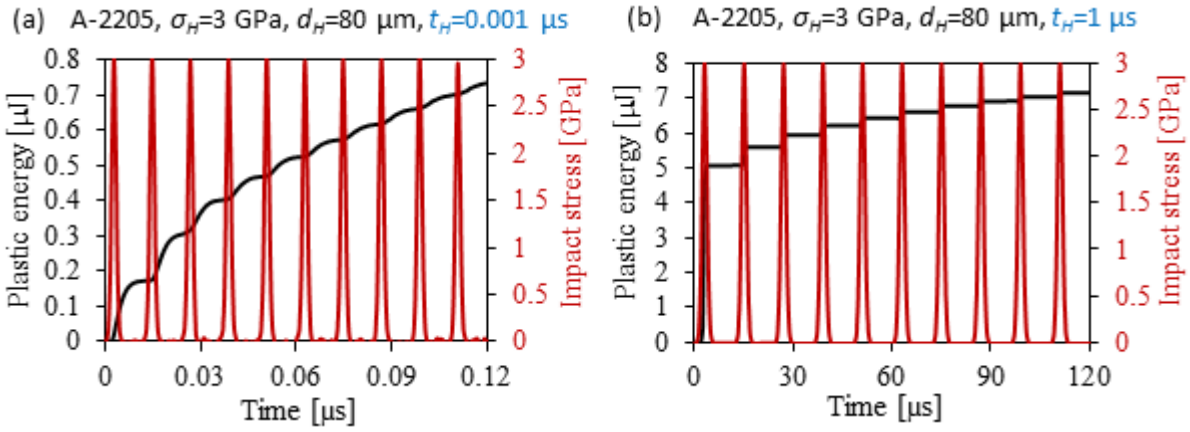

Fig. 5.11 Effect of cavitation impact duration on strain accumulation is shown for A-2205, $\sigma_H = 3$ GPa, $d_H = 80$ µm, (a) $t_H = 0.001$ µs and (b) $t_H = 1$ µs.

In contrary, the interval between two successive impacts has almost a negligible effect. For example, as shown in Fig. 5.12, the interval has been changed from 6 times of t_H in (a) to 60 times in (b), but PE or plastic strain accumulation remains almost the same.

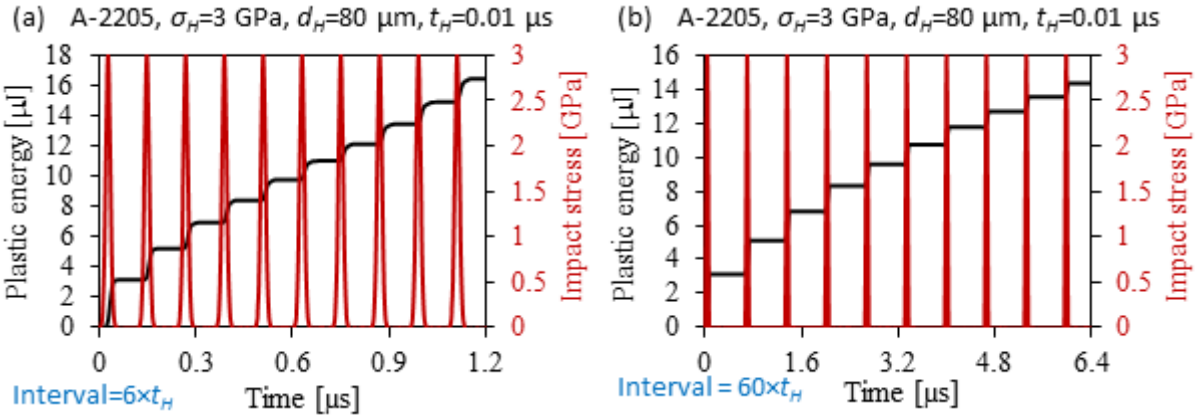

Fig. 5.12 Effect of interval between cavitation impacts on strain accumulation is shown for A-2205, $\sigma_H = 3$ GPa, $d_H = 80$ µm, $t_H = 0.01$ µs and (a) interval = $6 \times t_H$ and (b) interval = $60 \times t_H$.

- **Modeling of cavitation damage**

After establishing the constitutive law and material properties that properly account for hardening behavior of the material under cavitation fatigue, the next step is to establish an appropriate damage model i.e. criteria for damage initiation and damage evolution. As already mentioned, FEM simulation of cavitation damage is still an opened subject of research; rarely any literature can be found that explains the damage criteria for cavitation erosion.

In ductile material, the damage initiation is generally attributed to the shear band localization or void nucleation, growth and coalescence. The equivalent plastic strain at the damage initiation is defined as a function of the shear stress ratio [148] and strain rate for the former one, and stress triaxiality and strain rate for the latter one [148]. With respect to cavitation, the selection of a proper damage initiation creation as well as a damage evolution criterion remains to be a subject of research. However, in a first step forward, a simple ductile damage criterion as explained in Fig. 5.13(a) has been used for the current study. The general framework of ductile damage modeling is- elasto-plastic deformation, damage initiation, damage propagation and failure. For an elastic-plastic material, the damage is characterized by both the degradation of the elastic stiffness and the yield strength (Fig. 5.13(a)). The damage initiation is given by a scalar variable (ω_D) [148] as shown in the following Eq. (5.5). A value of $\omega_D > 0$ indicates the onset of plastic strain accumulation and $\omega_D = 1$ indicates damage initiation, after which the stiffness starts to degrade.

$$\omega_D = \int \frac{d\varepsilon_p}{\varepsilon_p^i} \tag{5.5}$$

In Eq. (5.5), ε_p^i is the critical cumulated plastic strain at the damage initiation that requires experimental determination. Depending on the material, geometry and loading condition it could depend on the stress triaxiality, strain rate, temperature, shear stress ratio etc. Future research should be directed towards the estimation of ε_p^i for cavitation erosion. Nanoindentation or single bubble collapse experiments could potentially be utilized along with metallurgical examinations of the tested specimen. The possibility of such future research is discussed in details in Chapter-6.

A common approach to account for damage evolution is introducing a scalar damage variable D. Undamaged material corresponds to D=0 whereas D=1 means complete failure with the occurrence of fracture. FEM codes generally correlate the damage variable D to the cumulative plastic strain [148]. Several models are available. A simple version is given by a linear correlation between the two as shown in Fig. 5.13(b). For which the damage variable can be defined as-

$$D = \int \frac{d\varepsilon_p'}{\Delta\varepsilon_p^f} \tag{5.6}$$

Where, $\varepsilon_p' = \varepsilon_p - \varepsilon_p^i$ and $\Delta\varepsilon_p^f = \varepsilon_p^f - \varepsilon_p^i =$ constant. Here, ε_p^i and ε_p^f are equivalent plastic strain at damage initiation (D>0 or $\omega_D = 1$) and complete failure (D=1) respectively, and ε_p is the instantaneous or current value of plastic strain. The values of ε_p^i and ε_p^f can be estimated experimentally and introduced into the numerical modeling.

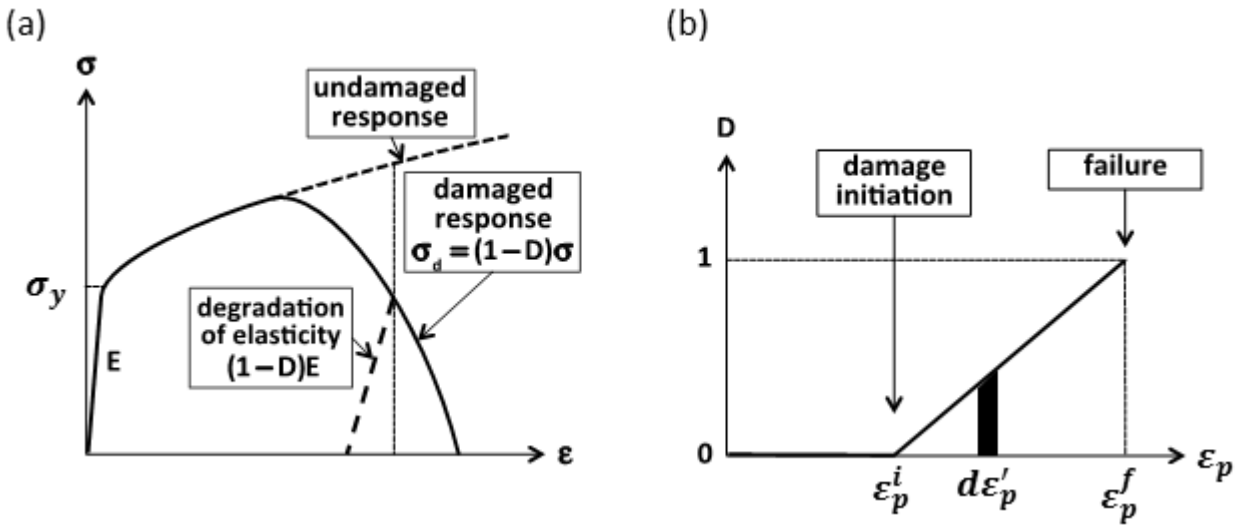

Fig. 5.13 Principle of the damage model. Left: Typical stress-strain curves for damaged and undamaged material. Right: Typical correlation of the damage variable D with the cumulative plastic strain ε_p showing the critical strains for damage initiation and failure.

In order to demonstrate the feasibility of such an approach to model or simulate cavitation erosion, multiple impacts of same loading conditions (for example, $\sigma_H = 4$ GPa, $d_H = 80$ µm and $t_H = 0.01$ µs) on the same location were simulated, for example on A-2205 material. The equivalent plastic strains at the damage initiation and failure are assumed to be 15% and 20% respectively, along with a linear evolution of the damage variable versus the cumulated plastic strain as depicted in Fig. 5.13(b). The results are shown in Fig. 5.14, on the left the frames (#1 to #8) show the accumulation of plastic strain with time, whereas the frames on the right show the corresponding equivalent stresses. As can be seen, from frame #1 to #3 strain accumulates without any failure or mass-loss. This behavior corresponds to the incubation period of cavitation erosion. On frame #4, damage initiates from inside the material where the cumulative strain reaches the failure strain. Upon damage, the elements are deleted from the material, which means these elements do not provide any stiffness any more into the material. The damage after initiation initially propagates along the sharp edges of the cracked region (frame #5) and ultimately a piece of material is removed from the surface (frame #6). Then afterwards the material removal occurs from the surface, as can be seen from frame #6 to #8, with the successive impacts.

The corresponding mass-loss with time or number of impacts for the above cavitation erosion simulation is plotted in Fig. 5.15. As can be seen, only after 6 impacts the damage is initiated and then propagated very fast. This shape of the mass-loss curve qualitatively resembles the experimental cavitation erosion curve (Fig. 5.2). However, these two are completely different in a sense that the experimental data represent the cumulative mass-loss of a material induced by a large number of impacts occurring randomly at different locations, the similarity in shape indicates that a three dimensional cavitation erosion simulation with the cavitation aggressiveness as estimated in Sec. 5.2 in a long term would give a similar erosion curve. For doing that the impact load randomly chosen from the statistical population of the estimated flow aggressiveness has to be applied repeatedly and randomly on the material surface. However, this remains to be a challenging issue and some highlights are given in the next section.

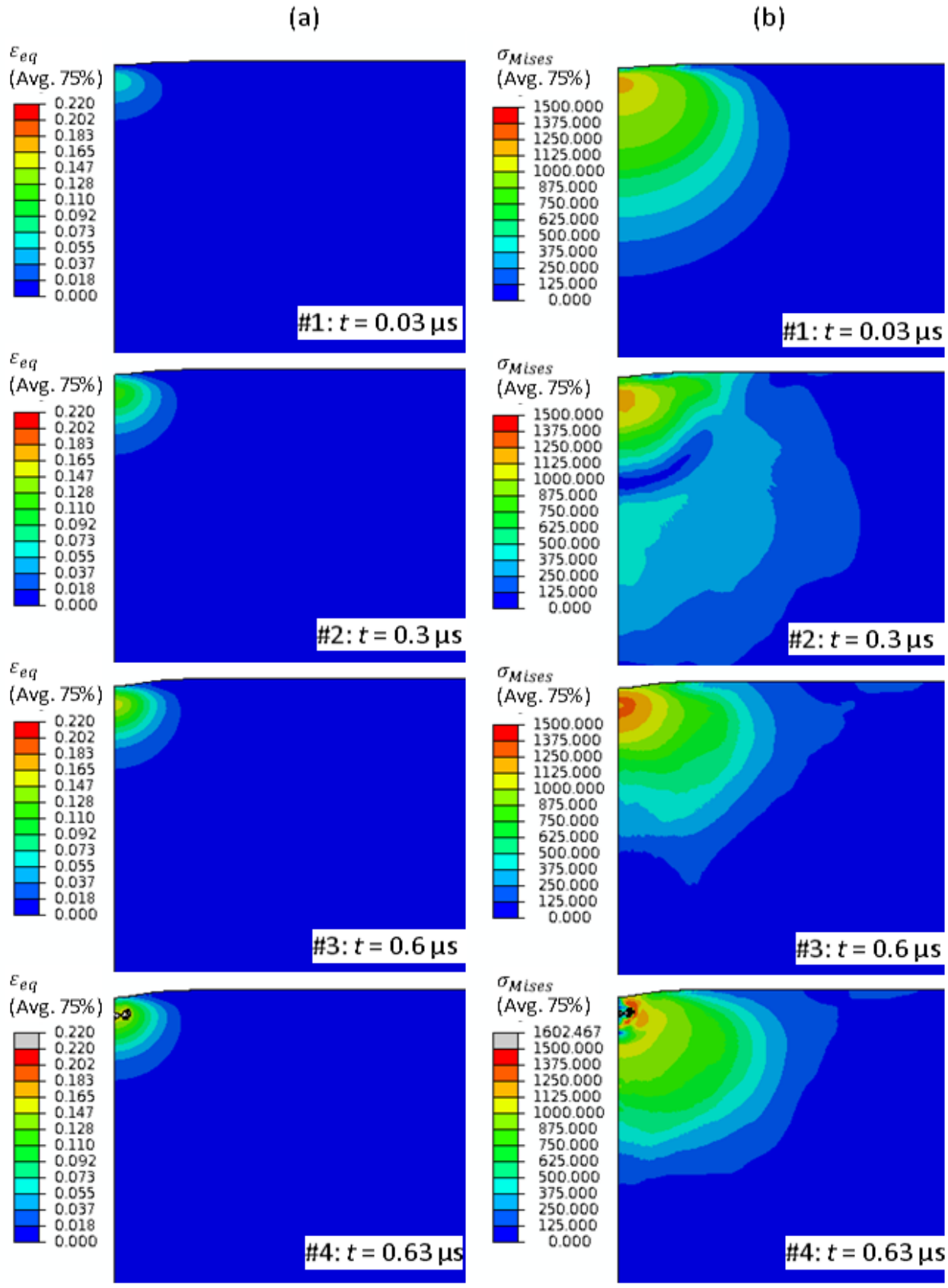
(a)
(b)
ε_{eq}
(Avg. 75%)
0.220
0.202
0.183
0.165
0.147
0.128
0.110
0.092
0.073
0.055
0.037
0.018
0.000
#1: t = 0.03 µs
σ_{Mises}
(Avg. 75%)
1500.000
1375.000
1250.000
1125.000
1000.000
875.000
750.000
625.000
500.000
375.000
250.000
125.000
0.000
#1: t = 0.03 µs
#2: t = 0.3 µs
#2: t = 0.3 µs
#3: t = 0.6 µs
#3: t = 0.6 µs
1602.467
#4: t = 0.63 µs
#4: t = 0.63 µs

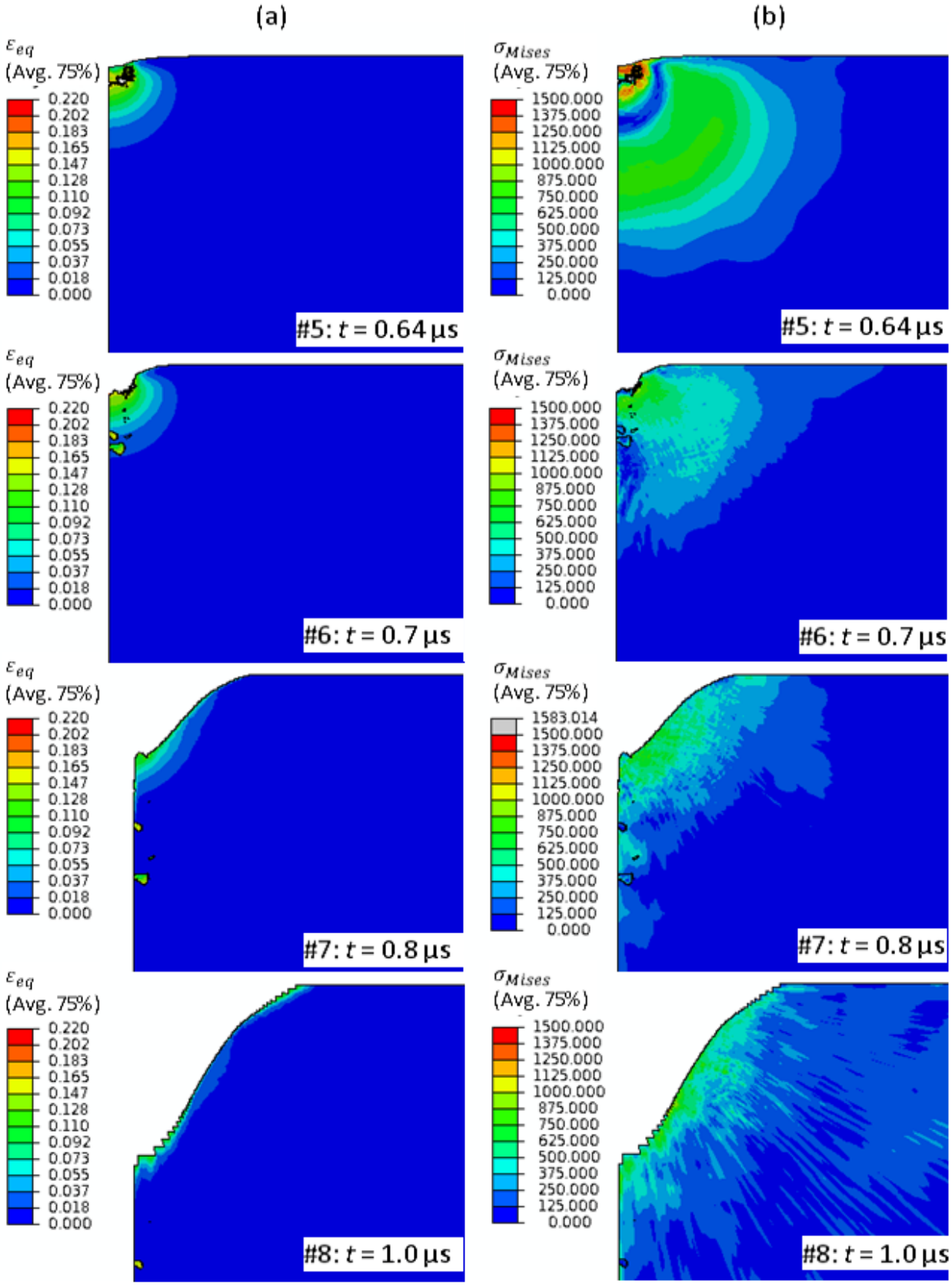

Fig. 5.14 Simulation of cavitation erosion. Multiple impacts of the same impact load ($\sigma_H = 4$ GPa, $d_H = 80$ µm and $t_H = 0.01$ µs) on the same location shows fatigue behavior of cavitation that lead to strain accumulation and damage in A-2205 material. Frames (#1-#8) on the left show plastic strain accumulation with time, whereas the corresponding equivalent stresses are shown in frames on the right. The debris on the figures are the damaged materials.

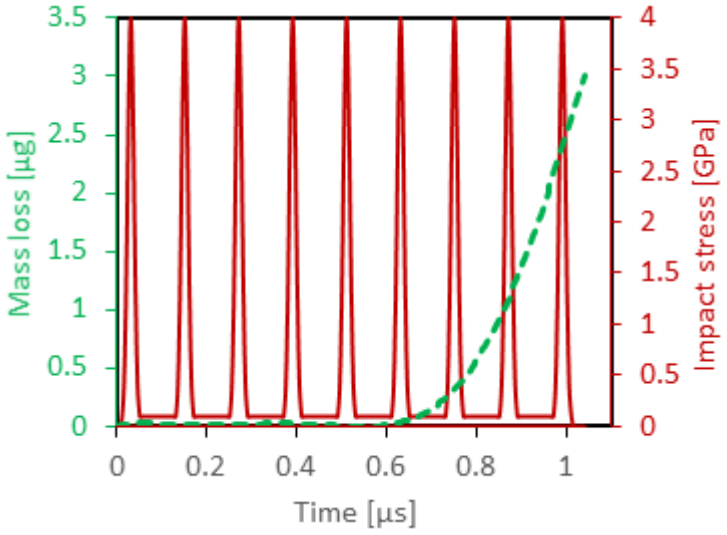

Fig. 5.15 Mass-loss versus time of the cavitation erosion simulation conducted on A-2205 material. Nine impacts of the same impact load ($\sigma_H = 4$ GPa, $d_H = 80$ µm and $t_H = 0.01$ µs) on the same location shows fatigue behavior of cavitation that lead to strain accumulation and damage. Till 6 impacts there were no mass-loss, but afterwards damage initiated and propagated very fast. Interval between impacts is equal to total duration of an impact (i.e. summation of impact rise and fall duration).

Based on the above studies we can conclude that, by introducing a suitable hardening mechanism together with a damage model, one should be able to model the fatigue mechanism that takes place during the incubation period as well as in the more advanced stages of erosion characterized by material removal and mass loss. In particular, it is expected that the usual mass loss curve that characterizes the kinetics of cavitation erosion damage could be predicted from such a numerical approach.

5.4. 3D numerical simulation of cavitation erosion: random impacts

In this section some preliminary results are shown that highlight the possibility and difficulties to implement the three dimensional simulation of cavitation erosion, where the impact loads chosen randomly from the statistical population of flow aggressiveness are applied repeatedly at random locations on the material surface. The geometrical model and meshing used for the simulations are shown in Fig. 5.16. The meshing is done with 8-node brick elements (C3D8R). The xy-planar geometries of all the elements are similar through the thickness. The elements have a tetragonal shape in the region ABCD-through thickness, whereas the mesh shape is free in the surrounding region. The xy-planar dimension of the elements in the ABCD region is 3.33 µm × 3.33 µm, however the dimensions along thickness (z) varies from 3.33 µm on the top to 33.33 µm on the bottom face. Thus, the smallest elements on the top surface have cubic shape of 3.33 µm dimension. The impact loads were applied on the surface within the region ABCD, whereas the total domain size is kept much bigger to avoid the effect of wave reflection from the boundaries. Displacement of the bottom face along z-direction was restricted, along with a fixed (all degrees of freedom are zero) boundary condition at one corner. No boundary conditions were applied on the vertical faces. The total number of elements in the target material is 632920. It should be mentioned that the model and meshing used for this study is elementary and could be

much improved. As an example, a better model could be used with periodical boundary conditions on the vertical faces of a small volume delimited by the target area ABCD, which would reduce the number of elements. This point is not investigated here any further.

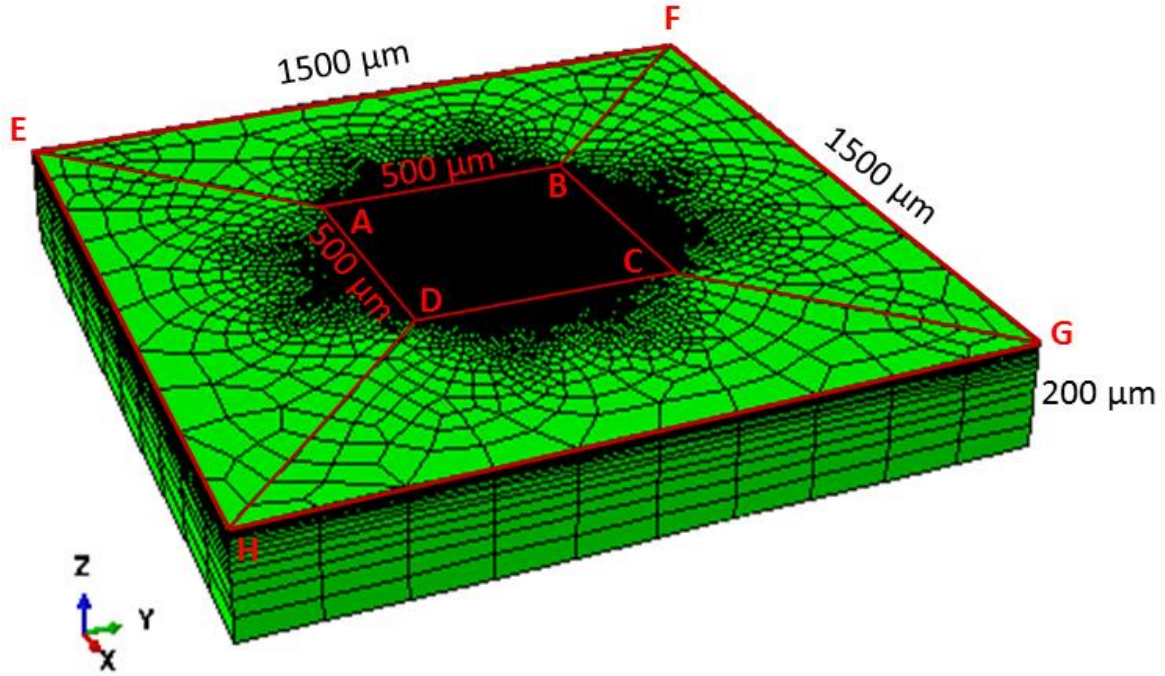

Fig. 5.16 Three dimensional (3D) geometrical model and meshing used for cavitation erosion simulation. Maximum domain size is 1500 µm × 1500 µm × 200 µm. Total 632920 numbers of 8-node brick elements on the target material. Total number of elements on the thin layer is 62438.

It should be mentioned that the FEM code ABAQUS is used for the numerical simulation. Once the elements on the surface get deleted upon meeting the damage criterion, the impact load cannot be applied any more in absence of those elements. Hence to overcome this difficulty a thin elastic layer (0.1 µm thickness) of the same material is modeled on the surface of the target material, as shown by EFGH. The thin layer is modeled with 4-node shell (S4R) elements and the meshing pattern is identical to the target material. The total number of S4R elements on the thin layer is 62438. Frictionless contact is defined between the thin layer and the target material. The use of this very thin layer does not provide any significant resistance to the impact load to reach the target material. Similar thin layer has been applied in Sec. 5.3 as well to simulate cavitation damage.

As an example, in the case of A-2205 material, Fig. 5.17 shows the strain accumulation and propagation of pressure waves with the number of impacts at different locations. The impact loads were chosen randomly from the statistical population of the impact loads shown in Fig. 5.6. Since the impact duration corresponding to each of the impact loads in Fig. 5.6 is not known, the dynamic FE explicit analysis is conducted with a unique characteristic of the impact duration $t_H = 0.01$ µs and $t_{max} = 3 \times t_H$ used in the Gaussian pressure field defined by Eq. (5.3), irrespective of the values of σ_H and d_H.

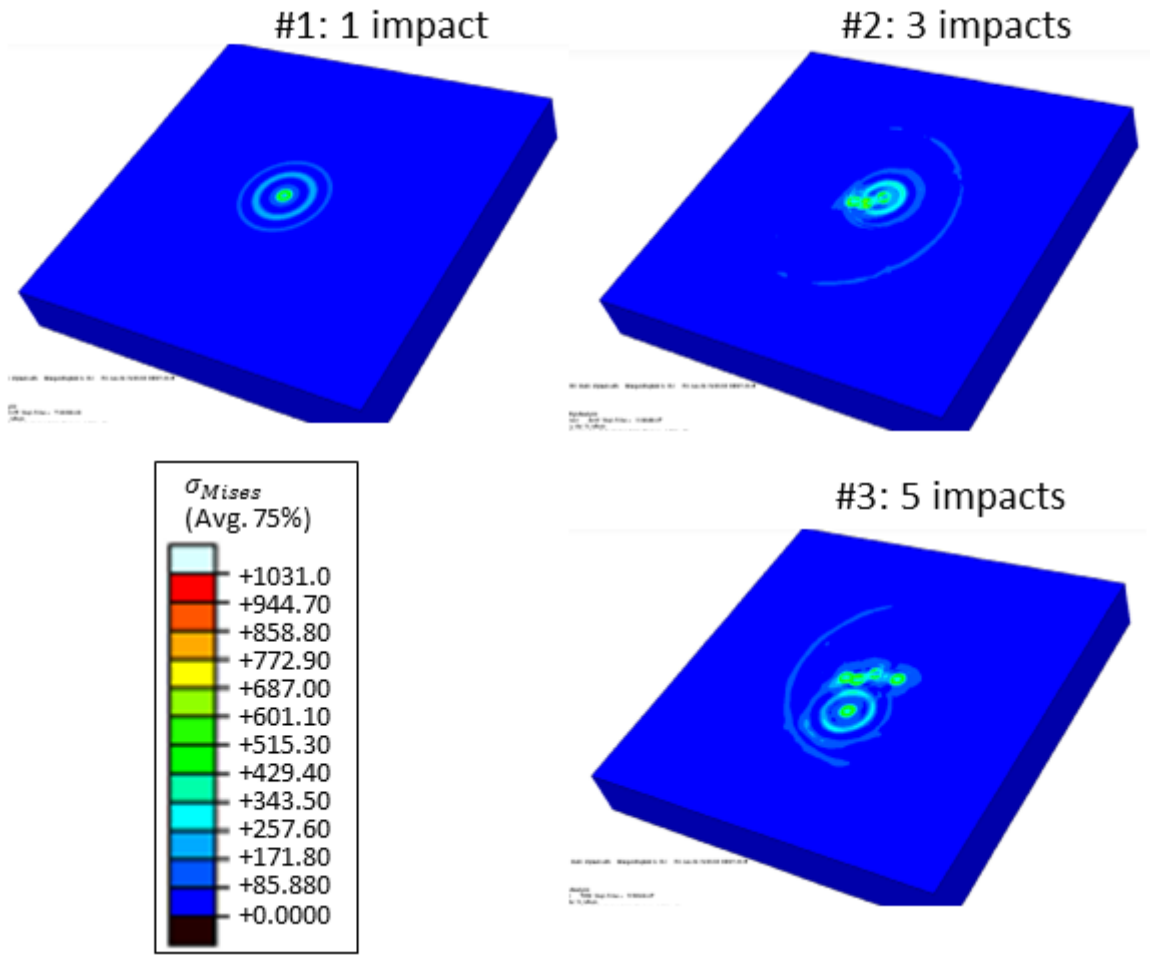

Fig. 5.17 Strain accumulation and propagation of pressure waves with the number of impacts. Spherical pressure waves propagate away from the point of impact. Only up to five impacts are shown here, which were randomly selected from the statistical population of impact loads given in Fig. 5.6. Material: A-2205. Characteristic impact duration $t_H = 0.01$ μs and $t_{max} = 3 \times t_H$ are assumed.

As an example, Fig. 5.18 shows the damage initiation after 360 impacts and the simulation was continued till 420 impacts. Total CPU time taken for the simulations was about 10 days on a computer system with 24 GB ram and 2.8 GHz Intel X5660 processor. It should be mentioned that the mass-loss after 360 impacts for A-2205 material is quite unrealistic from an experimental point of view since the incubation period for A-2205 at 20 bar (that corresponds to Fig. 5.6) is about 6 minutes, whereas for 360 impacts the total impact duration is about $360 \times 6t_H \cong 21.6$ µs. This discrepancy highlights the complex nature of the sequence of the impact loadings, even if they are random. Just applying the loads randomly is probably not sufficient, as it is well know that the frequency of occurrence of higher amplitude impacts are less compared to that of lower amplitudes [7]. Thus this aspect should be replicated when applying the impact loads randomly, in order to avoid mass-loss in the beginning of the simulation. Moreover, the spatial size of the impacted region modeled in the simulation is in the order of a few hundreds of micrometers (~500 µm). Thus this small volume may not be big enough to be representative of the actual geometry so that the mass loss is artificially over estimated. Moreover, the number of impacts at which the mass-loss initiates also depends on the mesh and damage criteria used. Since in the current study the mesh is quite coarse (the minimum size is 3.33 µm) compared to that of

the impact loads of 5 or 10 μm, some numerical errors are also involved. To get more reliable and realistic results, a very fine mesh along with a realistic spatial size of the model have to be considered, and doing that would require a very high performance computer with a large number of processors, as the total number of element would become very high compared to the current number of 685358.

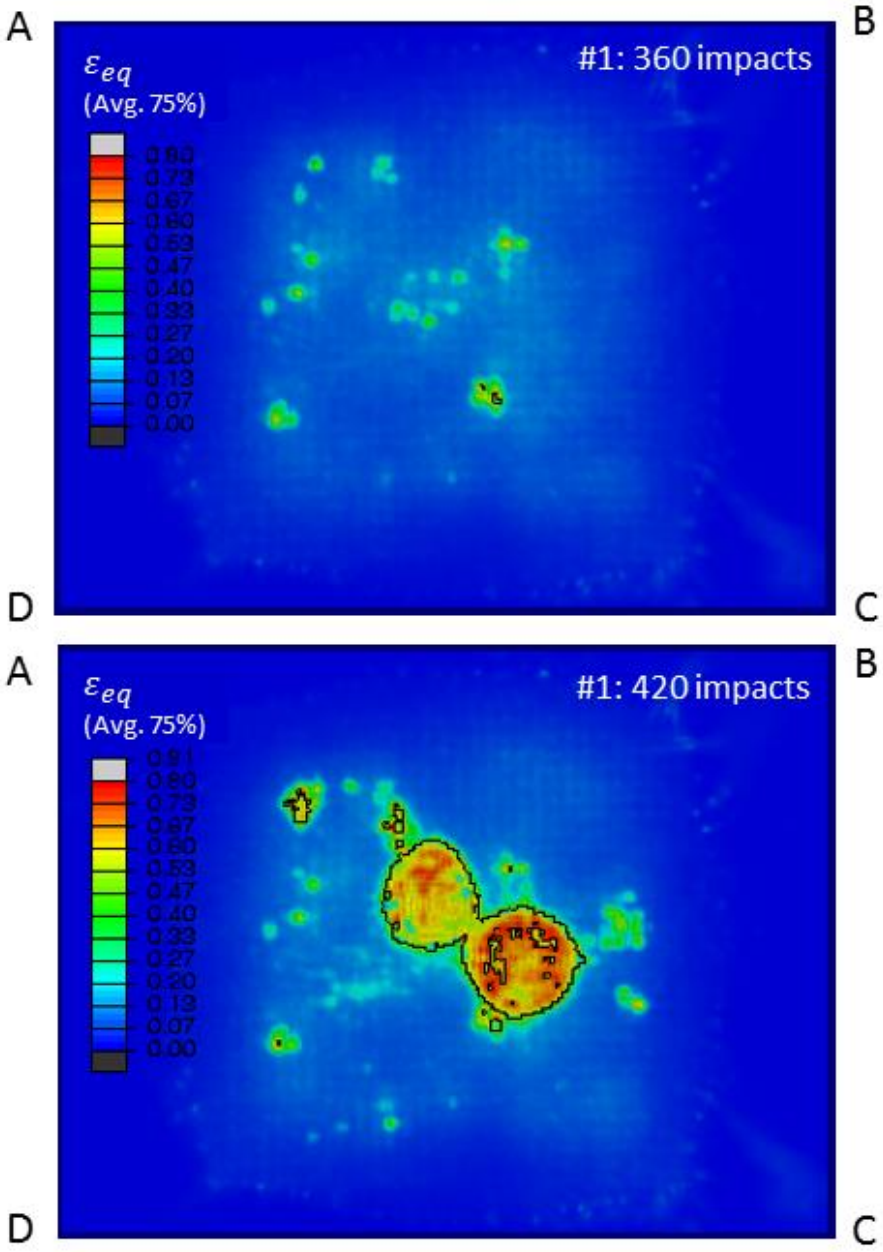

Fig. 5.18 Cavitation erosion simulation on A-2205 material. Characteristic impact duration $t_H = 0.01$ μs and $t_{max} = 3 \times t_H$ are assumed. Mass-loss started after 360 impacts at some locations. The plastic strain at the damage initiation and failure is defined as 80% and 90% respectively, along with a linear evolution. This choice is arbitrary. As the mesh is coarse (minimum size is 3.33 μm) compared to the smaller impact diameters of 5 or 10 μm, a higher value of strain was required to use to avoid numerical problems. Only the region ABCD on of the mesh is shown here. As can be seen, the regions from where the material has been removed is surrounded by black lines.

A simple linear damage law has been used for the current study without considering the dependency of damage initiation on the stress triaxiality, strain rate or temperature. In cavitation however, the strain rate is very high,

in the order of ~10^6 s^{-1} [4,6], and for such a high strain rate, adiabatic heating would definitely change the local temperature of the material. Thus for proper modeling of cavitation damage these two factors must be considered, which require experimental determination.

It should be recalled here that the Johnson-Cook dynamic failure model [120] has the ability to take into account the effect of strain rate ($\dot{\varepsilon}_p$), temperature (T) and stress triaxiality (η'). According to the model the damage initiation strain (ε_p^i) is given as Eq. (5.7).

$$\varepsilon_p^i = [D_1 + D_2 \exp(-D_3\eta')]\left[1 + D_4 \ln\left(\frac{\dot{\varepsilon}_p}{\dot{\varepsilon}_0}\right)\right]\left(1 + D_5\bar{T}^{m'}\right) \tag{5.7}$$

Here, $\eta' = p/\sigma_{eq}$ is the stress triaxiality, p is the pressure and σ_{eq} is the Mises equivalent stress, variables D_1 to D_5 and m' are material constants determined experimentally, $\dot{\varepsilon}_p$ and $\dot{\varepsilon}_0$ are the strain rate and reference strain rate respectively. The non-dimensional temperature $\bar{T}$ is the same as previously defined in Eq. (3.3), the temperature dependence of ε_p^i arises when the specimen temperature T is above the transition temperature $T_{transition}$. It should be mentioned that the negative sign in front of D_3 is due to the fact that ε_p^i decreases with the increase in η' as suggested in [148].

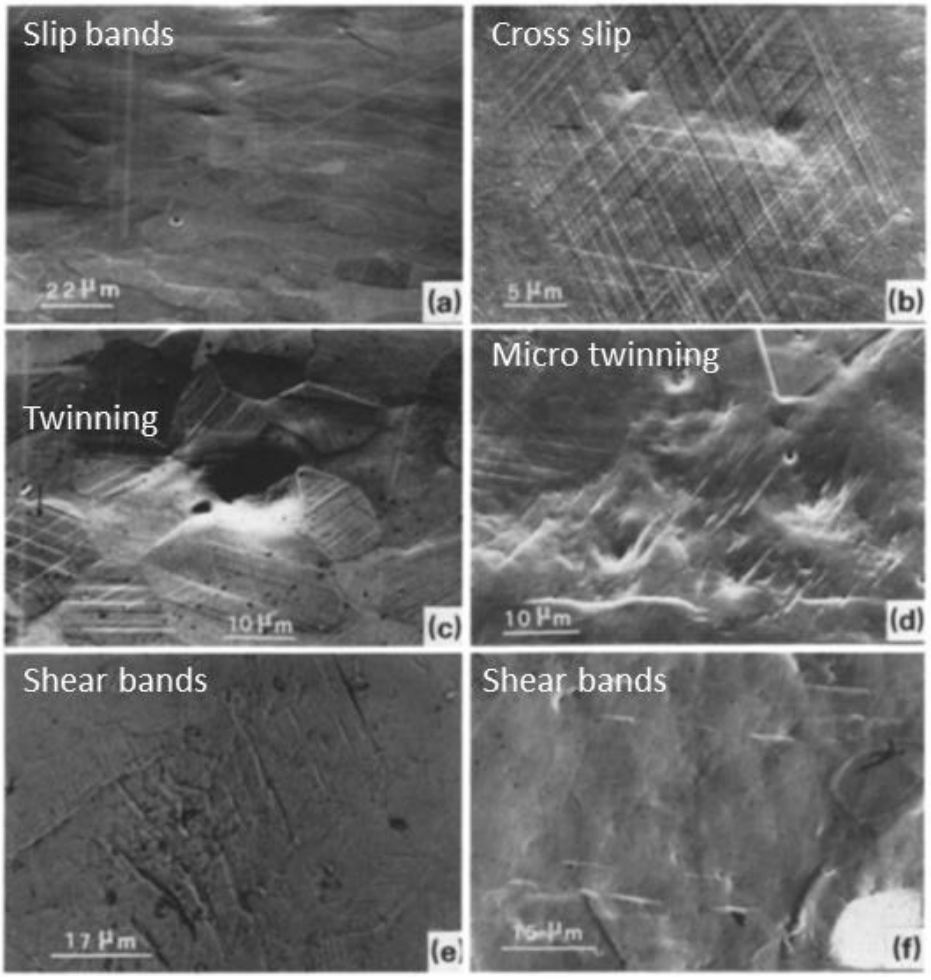

Fig. 5.19 Mechanism of cavitation erosion related to twinning, slip bands, cross slip, shear bands etc. as observed on duplex stainless steel by Karimi [43].

The above model can be used, but the model is totally empirical. The stress triaxiality may not be an important issue in the case of cavitation erosion since it accounts for void nucleation, growth and coalescence. The loading being compressive in nature, the void nucleation is probably not the dominant mechanism for damage, rather shear bend localization, twinning etc. could play a vital role. As shown in Fig. 5.19, Karimi [43] and many others as well [7], have shown the evidences of slip bands, cross slips, shear bands and twinnings etc. on the material surface exposed to cavitation erosion. These observations indicate the need of a suitable fatigue and damage model for cavitation erosion, which can quantitatively explain all the physical phenomena involved.

Although, the results presented here for the moment are quantitatively unrealistic, the consistency in qualitative nature (i.e. no mass-loss until 360 impacts) of the material behavior under the random impacts at random location gives a strong indication that such a method could be useful in the future for cavitation erosion prediction. However a lot of work remains to be done. Results presented here are nevertheless encouraging, considering the current state of art of the cavitation erosion prediction methods.

5.5. Conclusion

Although much remains to be done to apply this approach to cavitation erosion and to validate it, the preliminary results presented in this paper tend to prove that the prediction of cavitation erosion damage is now within the reach of numerical simulation.

The proposed method requires first estimating the distribution of impact loads due to cavitation bubble collapses. This could be done from pitting tests carried out on ductile materials. It was shown in Section 5.2 that an inverse FEM computation could be developed in order to determine both the stress amplitude and the radial extent of the hydrodynamic impact responsible for each pit.

Once the impact load spectrum is determined, the method consists in simulating the response of the material to these impacts of various amplitudes and sizes hitting randomly the wall. This could be achieved by a finite element modelling (FEM) of the material response. By using an appropriate hardening model completed by a damage model, it can be expected that the incubation period as well as the evolution of mass loss as a function of exposure time could be numerically predicted.

The approach requires a precise characterization of the material properties that is suited to the physics of cavitation erosion. This includes characterizing the material response including high strain rate effect. It is also essential to characterize the fatigue mechanism that takes place in the material during the repetitive loading by collapsing bubbles, which requires using a hardening law that accounts for strain rate sensitivity of the material. If possible the kinematic hardening behavior of the material should also be included. In addition, an appropriate damage model should be used in order to predict material removal and mass loss. All these models introduce material properties such as critical strains for damage initiation and material failure that need to be determined.

Such an approach is a priori applicable to any material provided the mechanical properties are available. In particular, it could be applied to compliant materials, coatings and multi layers materials of interest for cavitation erosion mitigation. Such a numerical approach could be very helpful for optimization purposes.

The method presented here is not a purely numerical method since it relies on the pitting tests for estimating the impact loads. It can however be guessed that this experimental step could be replaced in the future by a numerical step. The idea is to predict the impact loads from computational fluid dynamics (CFD). Recent results (see e.g. [85,87]) are quite promising regarding the numerical prediction of impact load spectra due to the collapse of cavitating structures. As a long-term vision, the CFD could be directly coupled to the FEM in order to better account for the fluid structure interaction and have a fully numerical approach of cavitation damage.

5.6. Some highlights and remarks

Some highlights of the chapter:

- The framework for a new method of cavitation erosion prediction has been established.
- The importance of relative acoustic impedances of the liquid and target material for cavitation erosion prediction has been discussed.
- The fatigue aspects of cavitation erosion have been discussed in details and it was found that the strain rate effect plays a vital role in the fatigue mechanism of cavitation erosion. Kinematic hardening is also found to be able to explain the fatigue aspect.
- A mechanism of strain accumulation based on the reduction of the strain rate with the number of impacts is proposed and validated by the numerical simulation of dynamic compressive fatigue test.
- Cavitation damage is found to initiate from inside the material. However, depending on the sequence of stress amplitudes of the repeated impacts damage may initiate from the surface layer as well.
- Simple linear damage evolution law is also found to provide a realistic interpretation of fatigue occurs under cavitation impacts.
- More investigation is required to identify more accurate hardening law and damage law to properly account for cavitation erosion mechanism, in order to be able to track mass-loss with time.
- The qualitative nature of the preliminary results presented by 2D and 3D mass-loss simulations gives a strong indication that such a method could be useful in the future for long term cavitation erosion prediction.

Remarks:

In this chapter (Chapter-5) a few of the primary objectives (item numbers 6 and 7 as discussed in Sec. 1.5) have been achieved. Apart from that some interesting conclusions have been drawn. The rest of the aims are dealt with in the previous chapters. In the following chapter (Chapter-6) a few scopes for future work have been highlighted.

Chapter-6

6. Scope of future work

- **Estimation of impact duration:**

  In this thesis (or in [2,4,49]) we have proposed and validated a numerical inverse method to estimate the cavitation impact load (especially the peak pressure and radial extent) from a cavitation pit geometry. The method is based on cavitation pitting tests and finite element (FE) simulations of the material response to a representative pressure profile. The method provides a better definition of the flow aggressiveness compared to what was available in the literature [7]. The flow aggressiveness is defined by the statistical distribution of the impact loads of given peak pressure and radial extent. This definition of the flow aggressiveness can be improved if the impact durations corresponding to such impact loadings are known. As the method uses the cavitation pit geometry obtained by pitting test, the experimental estimation of the impact duration corresponding to each pit is difficult. *There is scope for future work to investigate, if it is possible to derive the cavitation impact duration from a pit geometry, at least when the pit is generated in a controlled experimental condition.*

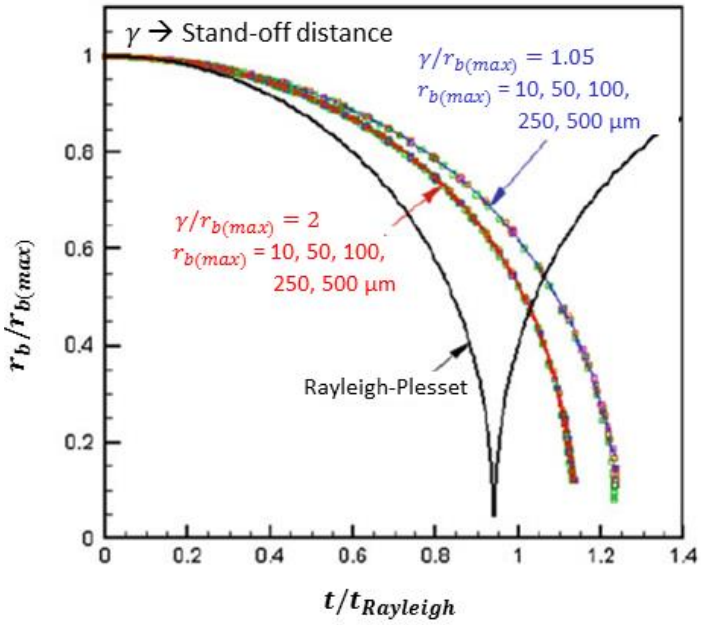

Fig. 6.1 Comparison of the time history of the normalized bubble equivalent radius for initial bubble maximum radii of 10, 50, 100, 250 and 500 µm at $\gamma/r_{b(max)}$ = 1.05 (blue line) and $\gamma/r_{b(max)}$ = 2.0 (red line). All the bubbles have an initial gas pressure of 1 atm (~1.01 bar) and are subjected to an ambient pressure of 34.5 atm (~ 34.95 bar) to simulate the bubble collapse. The bubble equivalent radius is normalized by $r_{b(max)}$ while the time scale is normalized by the Rayleigh time [81].

Like Harrison [22], Chahine [81] has shown using a fluid-structure interaction simulation of a single bubble collapse near a solid boundary (see Fig. 6.1) that the ratio of the instantaneous bubble radius to the maximum radius (i.e. $r_b/r_{b(max)}$) versus the ratio of instantaneous time to the characteristic (Rayliegh) collapse duration (i.e. $t/t_{Rayleigh}$) is independent of $r_{b(max)}$. Although minor dependence on stand-off distance (γ) is observed, if the values of r_b(at collapse) and $r_{b(max)}$ corresponding to each pit are known the impact duration can be estimated from the knowledge of $t_{Rayleigh}$. The characteristic bubble collapse duration $t_{Rayleigh}$ can be estimated form the relationship [19,21] in Eq. (6.1).

$$r_{b(max)} = \frac{1}{0.915}\left(\frac{p - p_V}{\rho}\right)^{1/2} . t_{Rayleigh} \tag{6.1}$$

Where, ρ and p_V are density and vapor pressure of the test liquid. In a controlled test environment it should be possible to know the approximate value of the collapse driving pressure (p), which in the case of cavitation tunnel apparatus must be related to the upstream and downstream pressures. Moreover, in the current study we have shown that there is a geometrical relationship between the impact radius (r_H) and the pit radius (r_P) by some constant factor (see Eq. (2.9) in chapter-2), and the impact radius (r_H) must be related to the bubble radius (r_b) by some factor, which requires investigation. The question is how to estimate $r_{b(max)}$? This needs investigation, however it can be expected that some relationship could possibly be established among the collapse driving pressure, the bubble radius at collapse (r_b) and the maximum bubble radius ($r_{b(max)}$). *All these facts motivate for investigating all these aspects in order to be able to estimate the cavitation impact duration form a pit geometry, when the pitting test is done under controlled environment*. Moreover Franc and Michel [6] have also stated that the impact duration of a bubble collapse is related to the ratio of the bubble radius to the speed of sound through the test liquid. This point should also be considered.

- **Material as a pressure sensor with dynamic explicit analysis:**

In the proposed method of cavitation impact load measurement, the target material is used as a pressure sensor. The method can be successfully used for materials like 7075 Aluminum alloy which has minor strain rate sensitivity, however some errors are inevitable when the material is strongly strain rate sensitive like 2205 duplex stainless steel. The limitations arise from the fact that the impact durations corresponding to the cavitation pits obtained by pitting test are unknown. Hence, dynamic explicit analysis of the material response could not be conducted to estimate the impact loads, rather static analysis had to be conducted. As stated in Chaper-2 and Chapter-4, the dynamic effect on the material properties was simply extrapolated to a high strain rate relevant to cavitation erosion conditions. *Thus this remains to be a future challenge to implement the proposed "numerical inverse method" to estimate cavitation impact loads from pit geometry, where the dynamic behavior of the material that include the inertia and strain rate effect would be included into the numerical simulation.* However, for that impact duration corresponding to a given pit must be known.

- **Better estimation of cavitation impact load: single bubble collapse experiment**

  In Chapter-5, by the extrapolated nanoindentation material properties at higher strain rate, the estimated impact loads were found be statistically material independent. The material independence of the estimated loads itself in a sense validates the method and the accuracy of the estimated impact loads. However, the following investigation proposed here would give a very precise and accurate answer to the question- whether the target material can be used as a pressure sensor in cavitation pitting or not. A preliminary roadmap for conducting such a research is explained below.

  The idea is, if we can produce a cavitation pit on a smooth material surface by controlled experimental collapse of a single cavitation bubble, we would have access to the bubble collapse parameters like bubble size, standoff distance, collapse driving pressure gradient etc. and also we can measure the impact duration and micro-jet size by using high speed photographic technique. It has already been established that a single bubble collapse in a controlled manner is possible, a few examples are presented in [18,19,22,24,27]. With such measurments, we can then relate the shape, depth and diameter of the cavitation pit to the impact duration corresponding to that same pit. The latter could be obtained by using a piezo-electric transducer of a suitable size. Okada *et al*. [75] have indeed shown that it is possible to make a transducer mounted with the test specimen, which enables the simultaneous measurement of the cavitation erosion and the impact loads due to the single bubble collapse.

  When everything is under control we can reproduce the same bubble collapse condition resulting in a similar pit. The purpose would be to produce a cavitation pit as clear as possible (as shown in Fig. 6.2), without any effect of surface roughness so that the pit dimensions can be measured precisely and unambiguously.

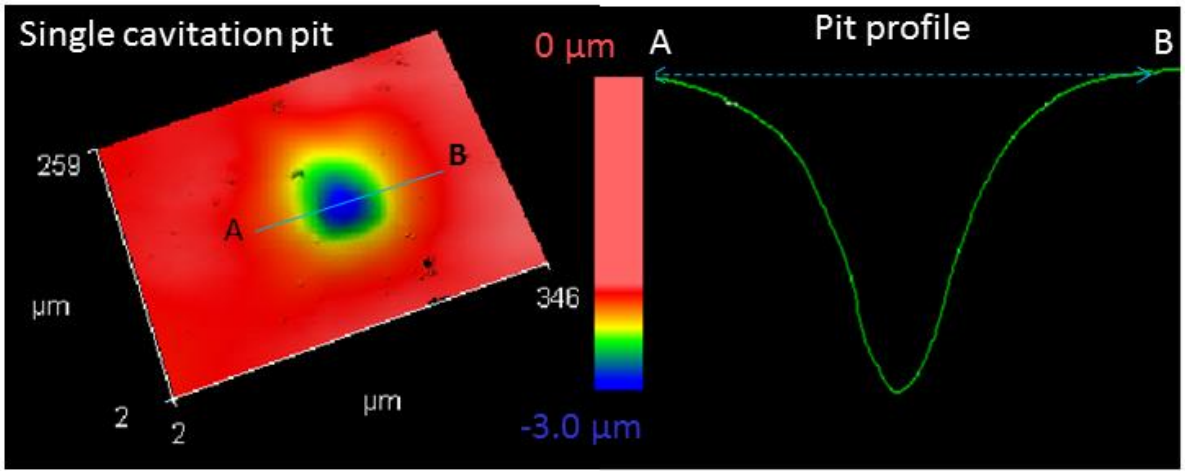

Fig. 6.2 A cavitation pit obtained by optical profilometry. Cavitation pitting tested on NAB material in a high speed cavitation tunnel. An ideal pit for the inverse calculation should have a symmetrical shape with smooth profile.

Then by numerically reproducing the cavitation pit (characterized by at least three parameters: depth, diameter and a shape factor) with a representative pressure field (characterized by at least three parameters: peak stress, radial extent and a shape factor) we would be able to estimate the impact force. Then, since the impact duration is known, dynamic explicit FE analysis can be used to estimate the impact load by the proposed "numerical inverse method". Once the parameters of the representative pressure field are obtained, the impact force can be estimated and compared to that obtained experimentally by the pressure transducer. Comparing the impact force rather than the impact stress is beneficial, as the error associated with the conversion of impact force recorded by transducer to impact stress can be avoided. This type of research has not yet been done to the best of our knowledge. It would be a valid or proper method to say that the target material can be used as a pressure sensor in cavitation pitting.

This method requires setup an instrument to produce high intense bubble collapse in a controlled manner. Such a device is not available yet for large enough impact that could plastically deform common engineering materials with a high yield strength. Generally the spark or laser induced bubble collapse cannot produce an impact of more than a few MPa [18,19,22,24,27]. One option would be to use a soft pure material or single crystal (Cu, Al, Ni). In that case we may have to develop new constitutive laws to accurately characterize the material behavior, including high strain rate effect and crystal plasticity aspects, if the signature id observed in the resulted pit.

Another difficulty would come from the experiments to be conducted to characterize the materials behavior, especially with regards to the high strain rate and compressive nature of the deformation confined into a micron size region. But for simplicity we can start with the Johnson-cook plasticity model or any other suitable model (like the Mechanical Threshold Stress (MTS), Zerillli-Armstrong (ZA) model discussed in Sec. 3.2.1 in Chapter-3) that take into account strain rate sensitivity effect. For the material property characterization we can probably use nanoindentation as used by many authors [49,68] for cavitation study. To get an indication of the strain rate sensitivity of the material we can probably use compression test with strain jump along with split Hopkinson pressure bar (SHPB) test, as done in the current study, since nanoindentation tests cannot be conducted at very high strain rates. It should be mentioned that all these factors may lead to some error in the numerical estimation of impact force.

- **Characterization of confined high rate deformation:**

There is also a scope for future work to develop a new technique to characterize high rate deformation behavior of material where the deformation is confined into a small region (in the order of micrometers or millimeters) and is not uniform. Simple uniaxial tension or compression type of tests do not represent the actual behavior of material under such condition of deformation. This is not a requirement for the field of cavitation alone, many other areas such as cold spray technique, impact problems, particle impingement fatigue failure of aircraft structures, rain erosion and so on also require such a technique to properly characterize the material behavior.

- **Location of crack initiation:**

  There is always a discrepancy when we compare the simulated results of cavitation pitting with experimental observation of cavitation erosion. Simulated data show that the maximum strain occurs in the subsurface region which is compressive in nature (as can be seen in Fig. 5.14 in Chapter-5), but the experimental observations show that the fatigue damage starts at the surface. There are a couple of papers saying the damage or cracks initiate from the surface [32,43,45]. This point should be investigate in details to get a clear answer to the underlying reason for such discrepancy. In order to do that three dimensional numerical simulation of a large number of impacts on a material surface applied repeatedly and randomly could be investigated and compared with cavitation pitting/erosion test results. Especially by comparing the hardening profile along the thickness. This could in fact prove that the discrepancy is rather apparent or virtual. Under a large number of impacts both the behavior would become similar or may be not…! Moreover, such kind of numerical study would definitely help to understand the cavitation fatigue mechanism.

- **Cavitation damage criterion:**

  A simple damage criterion for damage initiation and propagation has been used in the numerical simulations of mass loss presented in Chapter-5. This criterion is a key parameter to develop an accurate model. Experimental investigation of the material response under repeated single bubble collapse seems to be an appropriate option to define this criterion. In absence of such facilities, repeated nanoindentation test can probably be used. Metallurgical examination of the tested specimen should reveal the information about damage controlling mechanism and other information.

- **Compliant materials:**

  Once the cavitation erosion prediction method is established, the following question arises is how to protect the material from cavitation erosion. It has been shown that compliant materials like ultra-high molecular weight polyethylene (UHMWPE) has excellent cavitation erosion resistance over metallic alloy [52], which essentially comes from high damping ability of the polymeric material to the dynamic impact loading. Thus these materials provide a potential basis to be used as a coating for cavitation erosion protection of metallic structure, however, currently not being used in marine application for its weak adhesion to metallic alloys. Thus it would be interesting to numerically study the cavitation erosion behavior of such compliant material. The numerical

investigation of cavitation erosion of coating of such material on metallic substrate should be of particular interests, as these type of investigations would provide very useful information about the usefulness and performance of these materials as a coating under cavitation erosion. Moreover, recent investigation of cavitation erosion of UHMWPE tested in a high speed cavitation tunnel has shown that the cavitation erosion resistance of UHMWPE coatings on a metallic alloy substrate increases with increase in molecular weight [52]. The underlying reason is not very clear. The numerical study of such composite system along with proper constitutive laws could be able to explain some aspect of such behavior under the huge dynamic loading of cavitation impact.

Appendix-A

A. Split Hopkinson Pressure Bar (SHPB) test

Split Hopkinson Pressure Bar (SHPB) test is generally used for characterization of compressive material properties at high strain rates (>100 s^{-1}) [3]. In this thesis, all the SHPB tests were conducted at the ENSAM Laboratory PIMM in Paris, France. The SHPB testing method is also known as Kolsky pressure bar testing method, as Kolsky was the person who invented the apparatus [149] in its split form. The Figure A.1(a) shows the schematic of a split Hopkinson pressure bar test setup, whereas Figure A.1(b) shows the actual setup of the SHPB test apparatus used in the current study, and Figure A.1(c) shows the geometry of the test specimen. The test specimen in held firmly in-between the two elastic pressure bars, the incident bar and the output bar. The elastic striker bar, driven by air gun, explosion or other means, produces a high velocity impact onto the incident bar. As a result, an elastic compressive wave is generated within the incident bar that propagates towards the output bar. At the interface between the incident bar and the specimen, the wave is partially reflected back to the incident bar and partially transmitted into the specimen. The reflected wave is tensile in nature. The transmitted wave propagates through the output bar. The evolution of strain into the incident pressure bar due to the incident and reflected waves are recorded by the strain gage A, whereas the same strain evolution in the transmitted bar is measured by strain gage B. As an example, Figure A.2 shows the strain signals recorded by the two strain gages. The data obtained from these two strain gages can be used for establishing the stress-strain response of the specimen and strain rate of deformation [150,151]. However, these data are useful only if the following conditions are satisfied by the particular apparatus setup being used- (1) the wave propagation should be uniaxial, (b) the deformation of the specimen should be uniform, and (3) during the test period the specimen should be in dynamic equilibrium. Generally in SHPB apparatus these three conditions are achieved very easily, however smooth specimen with parallel faces should be prepared carefully to maintain uniform deformation and all the calibrations should be carried out before conducting any actual test. To verify the dynamic equilibrium of the tests conducted, as an example shown in Figure A.3, the temporal evolution of stress-strain at the incident bar/specimen interface (entry side) and specimen/output bar interface (exit side) have been checked. Theoretically these two stress have opposite sign, but the equal magnitudes validate the dynamic equilibrium. Very interestingly the dynamic equilibrium condition is reached at a strain of about 1%. It should be mentioned that maximum strain rates of < 2000 s^{-1} has been achieved during all the tests on all the three metallic alloys. For which, theoretically, the onset strain for equilibrium would be about 0.6% [149], thus in the current study the strain rate sensitivity measured at 1.5% of plastic

[3] For higher strain rates, Taylor impact test and Laser shock are other options that could be used for strain rates as high as (~10^5 - $10^6 s^{-1}$).

strain is completely justified. Now, in the following section the data analysis techniques to deduce the stress-strain curve form the strain gage signals have been discussed.

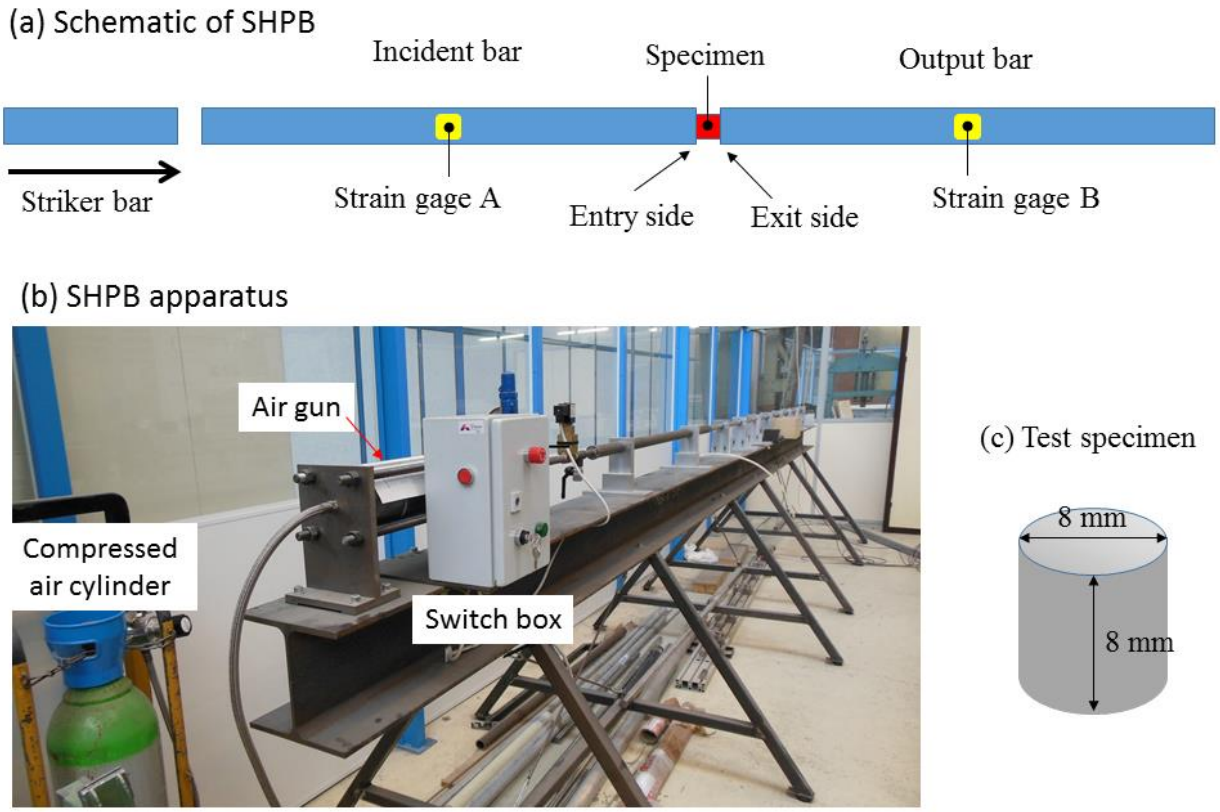

Figure A.1 (a) Schematics of split Hopkinson pressure bar apparatus, (b) the real split Hopkinson pressure bar test apparatus available at PIMM used for the current study and (c) the test specimen geometry.

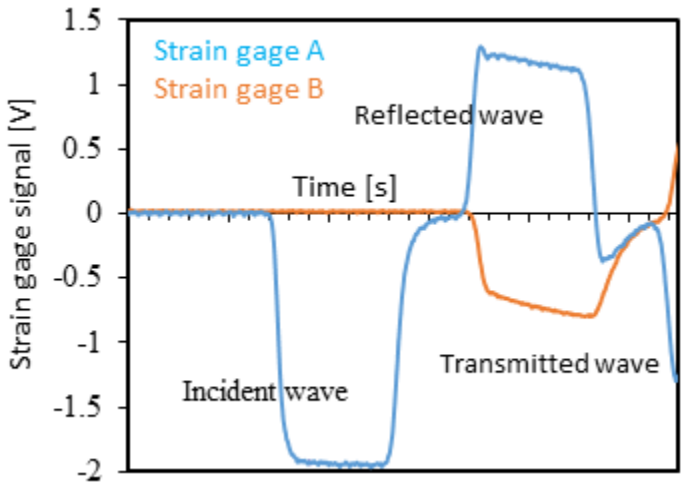

Figure A.2 Temporal evolution of strain recorded by the two strain gages (A and B), Strain gage A was attached to the incident bar and B was attached to the output bar.

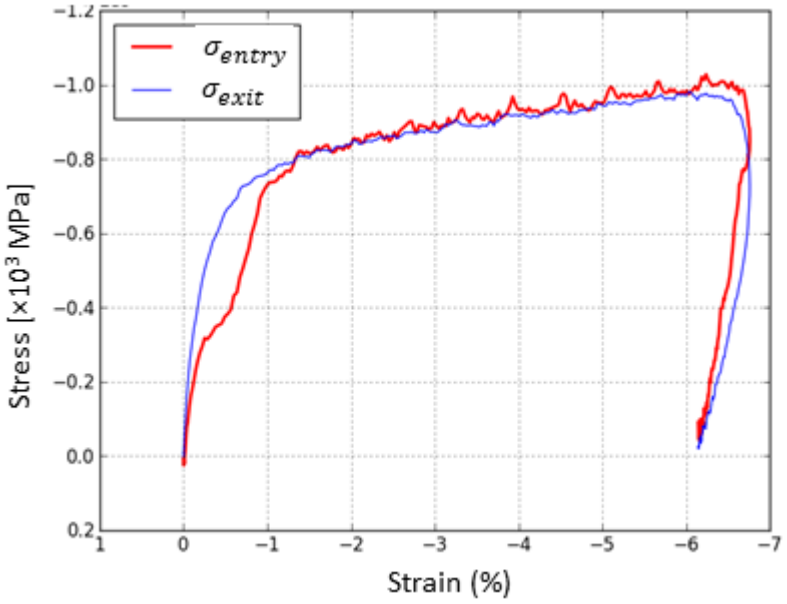

Figure A.3 Verification of dynamic equilibrium of the test specimen. The σ_{entry} is stress at the input bar/specimen interface and σ_{exit} is stress at the specimen/output bar interface. In principle σ_{entry} and σ_{exit} has opposite sign.

Based on the assumption that all the above-mentioned conditions are satisfied, the strain rate ($\dot{\varepsilon}$) for the test specimen can written as-

$$\dot{\varepsilon} = \frac{d\varepsilon(t)}{dt} = \frac{V_{entry}(t) - V_{exit}(t)}{l_{initial}} \tag{A.1}$$

Where, $l_{initial}$ is the initial length of the specimen, $V_{entry}(t)$ is the velocity of deformation of the specimen at the entry side (input bar/specimen interface) and $V_{exit}(t)$ is the velocity of deformation of the specimen at the exit side (specimen/output bar interface). Now these velocities can be estimated as-

$$V_{entry}(t) = \left(-\varepsilon_{incident}(t) + \varepsilon_{reflected}(t)\right) \times c_{bar} \tag{A.2}$$

$$V_{exit}(t) = -\varepsilon_{transmitted}(t) \times c_{bar} \tag{A.3}$$

Where, $\varepsilon_{incident}(t)$, $\varepsilon_{reflected}(t)$ and $\varepsilon_{transmitted}(t)$ are incident, reflected and transmitted strains signals recorded by the strain gages, respectively. And c_{bar} is the velocity of sound in the bar.

Eq. (A.1) can be written as-

$$\dot{\varepsilon} = \frac{d\varepsilon(t)}{dt} = \frac{c_{bar}}{l_{initial}}\left(-\varepsilon_{incident}(t) + \varepsilon_{reflected}(t) - \varepsilon_{transmitted}(t)\right) \tag{A.4}$$

Now from the equilibrium condition, considering the forces acting on the entry face is $F_{entry}(t)$ and exit face is $F_{exit}(t)$ we can write-

$$F_{entry}(t) = F_{exit}(t) \Longrightarrow \sigma_{entry}(t) \times A_{bar} = -\sigma_{exit}(t) \times A_{bar} \tag{A.5}$$

or,

$$\left(\varepsilon_{incident}(t) + \varepsilon_{reflected}(t)\right) \times A_{bar} \times E_{bar} = -\varepsilon_{transmitted}(t) \times A_{bar} \times E_{bar} \tag{A.6}$$

or,

$$\varepsilon_{incident}(t) + \varepsilon_{reflected}(t) = -\varepsilon_{transmitted}(t) \tag{A.7}$$

From Eq. (A.4) we can now write

$$\dot{\varepsilon} = \frac{d\varepsilon(t)}{dt} = 2\frac{c_{bar}}{l_{initial}}\varepsilon_{reflected}(t) \tag{A.8}$$

By definition, Eq. (A.8) gives an estimation of the engineering strain, which can easily be converted to true strain as $\ln(1 + \int \dot{\varepsilon}\, dt)$.

The average stress into the specimen is given as-

$$\sigma(t) = \frac{F_{entry}(t) + F_{exit}(t)}{2 \times A_{specimen}} = E_{bar}\frac{A_{bar}}{A_{specimen}}\varepsilon_{transmitted}(t) \tag{A.9}$$

In Eq. (A.9), if $A_{specimen}$ is considered to be the initial cross section of the specimen, then this equation gives a measure of the engineering stress which can be converted to true stress as $\sigma(t) \times (1 + \int \dot{\varepsilon}\, dt)$.

Thus, unlike conventional compression testing method, by using the SHPB testing method the stress-strain properties of a material can be estimated from the elastic responses of the pressure bars, without measuring the instantaneous dimensions of the specimen. The estimated stress-strain curves of all the three materials obtained by using the above-mentioned SHPB apparatus have been shown in Figure A.4(a)-(c) along with the stress-strain curves obtained by using conventional serve-hydraulic compression testing machine (as shown in Fig. 3.1). The curves for strain rates < 10 s^{-1} are conventional compression test data, whereas the curves for strain rates >100 s^{-1} are SHPB data. These data have been used in Sec. 3.2 in Chapter-3 to the estimate strain rate sensitivity coefficient of the materials involved in the Johnson-Cook plasticity model. As an example to verify the estimated strain rate sensitivities of the materials, the experimental stress-strain curves at maximum strain rates for all the three materials are compared with the predicted stress-strain curves, as shown in Figure A.4(d). Compression stress-strain curves (at strain rate 1 s^{-1}) were predicted by using the Johnson-Cook plasticity model with the estimated strain rate sensitivities. Overall, the correlations are very good, which validates the estimated strain rate sensitivities of the materials. However it should be mentioned that the little discrepancy at higher strain is due to the modified Johnson-Cook plasticity model (as shown in Eq. (3.6) in Chapter-3) which does not consider thermal softening due to adiabatic heating that is inevitably present in the experimental data.

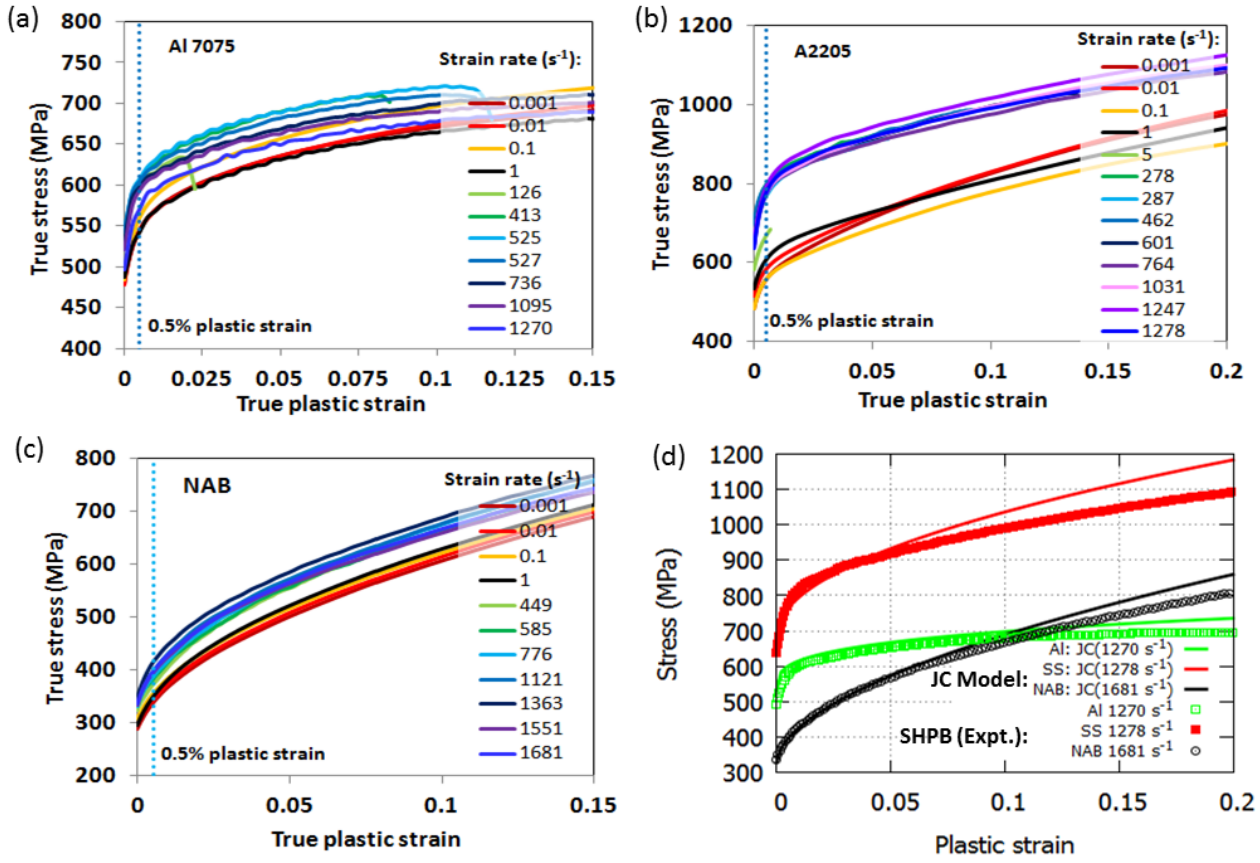

Figure A.4 (a)-(c) Stress-strain curves obtained by SHPB tests are plotted together along with compression tests curves. Stress-strain curves at strain rates < 10 s^{-1} are obtained by servo-hydraulic compression testing machine, whereas curves at strain rates >100 s^{-1} are SHPB data.

Appendix-B

B. Traditional method of analysis of nanoindentation test results to obtain uniaxial stress-strain curve

With the development of continuous stiffness measurement (CSM) system, the accuracy in determining material properties by nanoindentation has improved. In the current study, nanoindentation tests were conducted using MTS-NanoXP nanoindenter (Force resolution: 50 nN, displacement resolution: 0.1 nm, maximum force limit: 0.7 N, maximum displacement limit: 700 µm) with continuous stiffness measurement (CSM) with harmonic displacement of 2 nm. All the tests were done to a predefined maximum load limit (200 or 300 mN) under controlled strain rate of 0.05 s^{-1}. The testing method adopted here is similar to that of Oliver and Pharr [152]. All the test samples were mirror-polished following the conventional metallurgical polishing technique to a final polishing with 0.03 µm colloidal silica gel. A spherical diamond indenter of 9.46 µm nominal radius (R_{ind}) has been used.

The primary output data obtained from the nanoindentation test are load or force (F), displacement (h) and contact harmonic stiffness (S). Typical load-displacement curves are shown in Fig. 3.5 (Chapter-3, Sec. 3.2.5).

Step-1: The contact depth (h_c) can be estimated [152,153] as $h_c = h - \epsilon\frac{F}{S}$, where $\epsilon = 0.75$ for a spherical indenter.

Step-2: The area function should be derived to estimate the contact area as a function of the contact depth i.e. $A_c = f(h_c)$. The area function given by Juliano *et al*. [154], as shown below in Eq. (B.1), can be used.

$$A_c = \sum_{0}^{n} \Omega_n h_c^{2/2^n} \tag{B.1}$$

where, Ω_n represents the area coefficients.

Step-3: The contact radius a_c can be determined from A_c as $A_c = \pi a_c^2$.

Step-4: The indentation stress (σ_{ind}) can be estimated as-

$$\sigma_{ind} = \Psi\frac{F}{\pi a_c^2} \tag{B.2}$$

where, Ψ is a constant which depends on λ as follows [154]-

$$\lambda = 0.9\left(\frac{h}{h_c} - 1\right) \tag{B.3}$$

Based on the values of λ the constant Ψ can be estimated [155] as follows-

$$\Psi = \left\{ \begin{array}{lll} \lambda & if & 0.278 < \lambda < 0.89 \\ 0.278 & & \lambda < 0.278 \\ 0.890 & & \lambda > 0.89 \end{array} \right\} \quad \text{(B.4)}$$

Step-5: The indentation strain (ε_{ind}) can be estimated, by using Tabors equation [77], as-

$$\varepsilon_{ind} = 0.2 \times a_c / R_{ind} \quad \text{(B.5)}$$

The indenter radius R_{ind} is known and provided by the manufacturer as shown in Figure B.1, but often the indenter geometry is not perfect.

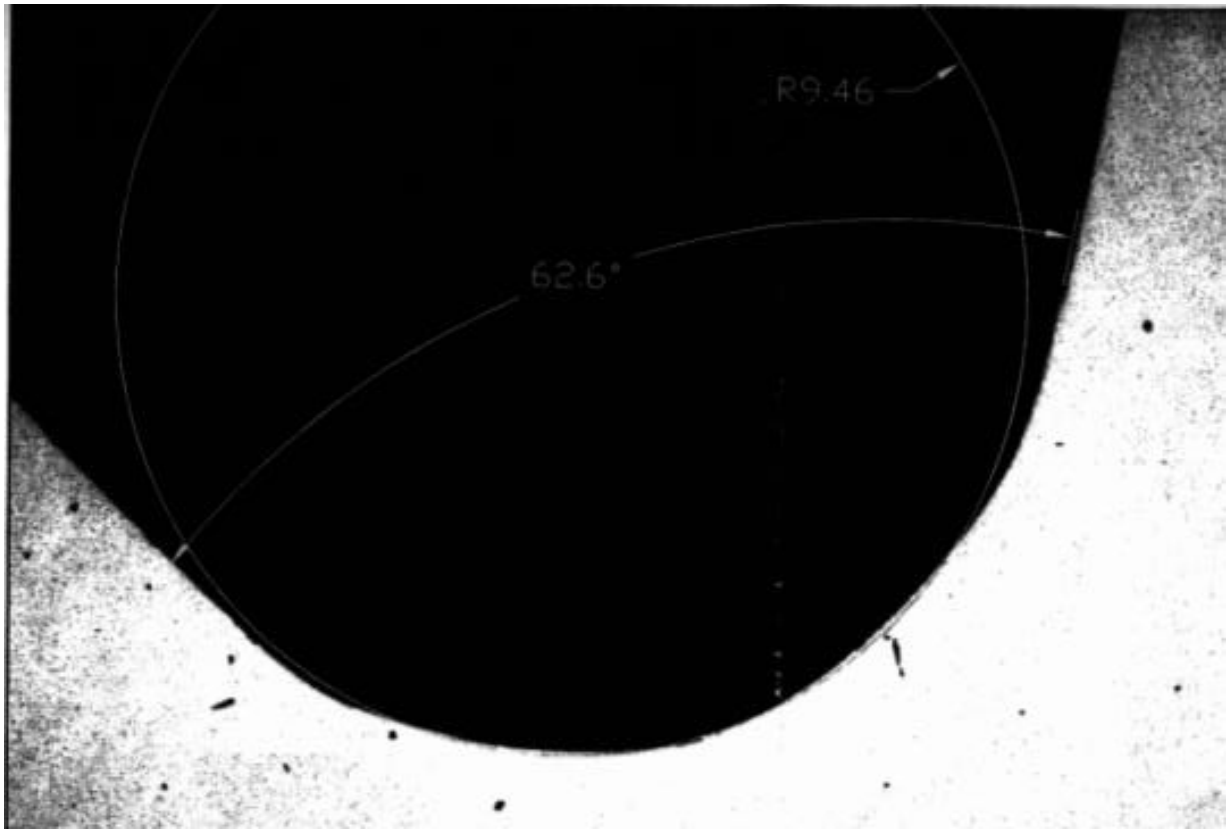

Figure B.1 TEM profile (Magnification x6337) of the 10µm spherical tip used in all our nanoindentation tests.

Therefore it is better to estimate R_{ind} using a geometrical relationship from the contact depth and contact radius as follows-

$$R_{ind} = \frac{a_c^2 + h_c^2}{2h_c} \quad \text{(B.6)}$$

However, as presented through Step-1 to Step-5, the method looks pretty simple and straight-forward to estimate the nanoindentation stress-strain curve. But, the calibration required in Step-1 and Step-2 makes the method a little bit ambiguous and difficult to implement. The measured displacement (h) from the indentation testing machine is actually the total displacement of the sample/indenter tip, testing machine or frame and the indenter. Thus, a calibration is required to get only the indenter tip displacement by excluding the load frame and indenter compliance from the measure displacement (h). Moreover, the calibration of the area function is

also required in Step-2 and is tiresome. For calibration generally nanoindentation tests are done on a standard specimen (usually fused silica) with known mechanical properties. Details of such a calibration can be found in [156] or in [152,153,157]. Apart from the above mentioned difficulties, the constant 0.2 in Eq. (B.5) and constants in Eq. (B.3) and Eq. (B.4) are not universal, thus lead to some error in the estimation of indentation strain. And also the equations do not take into account pile-up (or sink-in) behavior of material, which has great influence on the estimated values. Therefore, in the current study this traditional method of nanoindentation stress-strain curve determination has not been used, and no further details have been given regarding the calibration techniques. Instead, as discussed in Sec. 3.2.5 in Chapter-3, the nanoindentation material properties were estimated by using finite element simulation, optimizing the materials properties to reproduce the experimental load-displacement curves.

Appendix-C

C. Numerical details

All the numerical analyses in this thesis, related to cavitation impact using Gaussian type of pressure field, were done using high deformation and high strain formulation available in the most commonly used commercial finite element method (FEM) code ABAQUS. All the details about the FEM method/procedure can be found in 'Abaqus Theory Manual [158],' however the method is discussed below in brief. Any bold symbol denotes a tensor or matrix.

Assuming a material of volume V_* and surface area of S_* is under action of a surface force $\boldsymbol{t}_*$ per unit area and a body force $\boldsymbol{f}_*$ per unit volume, the force equilibrium gives-

$$\int_{S_*} \boldsymbol{t}_* \, dS_* + \int_{V_*} \boldsymbol{f}_* \, dV_* = 0 \tag{C.1}$$

The "true" or Cauchy stress matrix $\boldsymbol{\sigma}_*$ at any point on S_* is then-

$$\boldsymbol{t}_* = \boldsymbol{n}_* . \boldsymbol{\sigma}_* \tag{C.2}$$

where $\boldsymbol{n}_*$ is the unit outward normal to S_* at the point of consideration. Now, Eq. (C.1) can be rewritten as-

$$\int_{S_*} \boldsymbol{n}_* . \boldsymbol{\sigma}_* \, dS_* + \int_{V_*} \boldsymbol{f}_* \, dV_* = 0 \tag{C.3}$$

Now using Gauss theorem to the surface integral we can write the first term as-

$$\int_{S_*} \boldsymbol{n}_* . \boldsymbol{\sigma}_* \, dS_* = \int_{V_*} \left(\frac{\partial}{\partial \boldsymbol{x}}\right) . \boldsymbol{\sigma}_* \, dV_* \tag{C.4}$$

Since the Eq. (C.3) is valid at any material point ($\boldsymbol{x}$), the equilibrium equation can be written as-

$$\left(\frac{\partial}{\partial \boldsymbol{x}}\right) . \boldsymbol{\sigma}_* + \boldsymbol{f}_* = \boldsymbol{0} \tag{C.5}$$

These are the three familiar differential equations of force equilibrium.

Now, if the material at any point at any time is imagined to have a "virtual" velocity field, $\delta \boldsymbol{v}_*$, the dot product of this with the equilibrium force field then represents the "virtual" work rate (also known as an equivalent "weak form" of Eq. (C.5)), which can be written as –

$$\int_{V_*} \left[\left(\frac{\partial}{\partial \boldsymbol{x}}\right) . \boldsymbol{\sigma}_* + \boldsymbol{f}_*\right] . \delta \boldsymbol{v}_* \, dV_* = 0 \tag{C.6}$$

Using chain rule and Gauss theorem the Eq. (C.6) can be expressed as follows (for detailed explanation see ref. [158])-

$$\int_{S_*} \boldsymbol{t}_* . \delta \boldsymbol{v}_* \, dS_* + \int_{V_*} \boldsymbol{f}_* . \delta \boldsymbol{v}_* \, dV_* = \int_{V_*} \boldsymbol{\sigma}_* : \left(\frac{\partial \delta \boldsymbol{v}_*}{\partial \boldsymbol{x}} \right) dV_* \tag{C.7}$$

The virtual velocity gradient can be decomposed symmetrical and asymmetrical parts as-

$$\frac{\partial \delta \boldsymbol{v}_*}{\partial \boldsymbol{x}} = \frac{1}{2}\left(\frac{\partial \delta \boldsymbol{v}_*}{\partial \boldsymbol{x}} + \left[\frac{\partial \delta \boldsymbol{v}_*}{\partial \boldsymbol{x}} \right]^T \right) + \frac{1}{2}\left(\frac{\partial \delta \boldsymbol{v}_*}{\partial \boldsymbol{x}} - \left[\frac{\partial \delta \boldsymbol{v}_*}{\partial \boldsymbol{x}} \right]^T \right)$$

Since $\boldsymbol{\sigma}_*$ is symmetrical, $\boldsymbol{\sigma}_* = \boldsymbol{\sigma}_*^{\boldsymbol{T}}$, then $\boldsymbol{\sigma}_* : \frac{1}{2}\left(\frac{\partial \delta \boldsymbol{v}_*}{\partial \boldsymbol{x}} - \left[\frac{\partial \delta \boldsymbol{v}_*}{\partial \boldsymbol{x}} \right]^T \right) = 0$ and the Eq. (C.7) can be written as-

$$\int_{S_*} \delta \boldsymbol{v}_* . \boldsymbol{t}_* \, dS_* + \int_{V_*} \delta \boldsymbol{v}_* . \boldsymbol{f}_* \, dV_* = \int_{V_*} \boldsymbol{\sigma}_* : \delta \boldsymbol{D}_* \, dV_* \tag{C.8}$$

Or

$$\int_{V_*} \boldsymbol{\sigma}_* : \delta \boldsymbol{D}_* \, dV_* = \int_{S_*} \delta \boldsymbol{v}_* . \boldsymbol{t}_*^T \, dS_* + \int_{V_*} \delta \boldsymbol{v}_* . \boldsymbol{f}_*^T \, dV_* \tag{C.9}$$

Where, $\delta \boldsymbol{D}_* = \frac{1}{2}\left(\frac{\partial \delta \boldsymbol{v}_*}{\partial \boldsymbol{x}} + \left[\frac{\partial \delta \boldsymbol{v}_*}{\partial \boldsymbol{x}} \right]^T \right)$.

The Eq. (C.8) or Eq. (C.9) is called classical virtual work equation i.e. the "weak form" of the equilibrium equations which is used as the basic statement for finite element formulation in ABAQUS.

The left-hand side of the Eq. (C.9) is the internal virtual work rate and can be replaced by any conjugate pairing of stress ($\boldsymbol{\tau}_*^C$) and strain ($\boldsymbol{\varepsilon}_*$) of the material of reference volume V_*^0 as follows-

$$\int_{V_*^0} \boldsymbol{\tau}_*^C : \delta \boldsymbol{\varepsilon}_* \, dV_*^0 = \int_{S_*} \delta \boldsymbol{v}_* . \boldsymbol{t}_*^T \, dS_* + \int_{V_*} \delta \boldsymbol{v}_* . \boldsymbol{f}_*^T \, dV_* \tag{C.10}$$

The finite element interpolator, using summation convention, can be written in general as-

$$\boldsymbol{u}_* = N_{*_N} \boldsymbol{u}_*^N \tag{C.11}$$

Where N_{*_N} is interpolation function that depends on material coordinate system, $\boldsymbol{u}_*^N$ are nodal varialbles, and subscripts and superscripts indicate nodal variables.

Now similarly the $\delta \boldsymbol{v}_*$ can be defined as-

$$\delta \boldsymbol{v}_* = N_{*_N} \delta \boldsymbol{v}_*^N \tag{C.12}$$

Thus $\delta \boldsymbol{v}_*$ for the continuum of the material is approximated by a variation of over the set $\delta \boldsymbol{v}_*^N$.

Again, $\delta \boldsymbol{\varepsilon}_*$ can also be defined as-

$$\delta \boldsymbol{\varepsilon}_* = \boldsymbol{\beta}_{*_N} \delta \boldsymbol{v}_*^N \tag{C.13}$$

The matrix $\boldsymbol{\beta}_*$ depends on the current position of the material point and defines the strain variations from the kinematic variables.

Now Eq. (C.10) can be approximated as-

$$\int_{V_*^0} \boldsymbol{\beta}_{*_N} : \boldsymbol{\tau}_*^C \, dV_*^0 = \int_{S_*} \boldsymbol{N}_{*_N}^T . \, \boldsymbol{t}_* \, dS_* + \int_{V_*} \boldsymbol{N}_{*_N}^T . \boldsymbol{f}_* \, dV_* \tag{C.14}$$

This above systems of equations defines the "nonlinear equilibrium equations" and forms the basis for the ("standard/implicit") displacement finite element analysis procedure and has the form-

$$F_*^N(u_*^M) = 0 \tag{C.15}$$

Where, F_*^N is the force component conjugate to the N^{th} variable and u_*^M is the value of the M^{th} variable.

ABAQUS standard/implicit analysis:

The Jacobian of the equilibrium equations required for the Newton Algorithm or linear perturbation commonly used in standard/implicit analysis is given as (See [158] for more detailed explanation)-

$$K_{*_{MN}} = \int_{V_*^0} \boldsymbol{\beta}_{*_M} : \boldsymbol{H}_* : \boldsymbol{\beta}_{*_N} \, dV_*^0 + \int_{V_*^0} \boldsymbol{\tau}_*^C : \partial_N \boldsymbol{\beta}_{*_M} \, dV_*^0 - \int_{S_*} \boldsymbol{N}_{*_M}^T . \boldsymbol{Q}_{*_N}^{S_*} \, dS_* - \int_{V_*} \boldsymbol{N}_{*_M}^T . \boldsymbol{Q}_{*_N}^{V_*} \, dV_* \tag{C.16}$$

Where,

$$\partial_N = \partial / \partial u_*^N \tag{C.17}$$

Assuming that the constitutive theory allows to write

$$d\boldsymbol{\tau}_*^C = \boldsymbol{H}_* : d\boldsymbol{\varepsilon}_* + \boldsymbol{g}_* \tag{C.18}$$

where $\boldsymbol{H}$ and $\boldsymbol{g}$ depend on the material constitutive laws, current state and direction of straining etc. and the kinematic assumptions used in forming the generalized strains (as discussed below). Now-

$$\partial_N \boldsymbol{\varepsilon}_* = \partial \boldsymbol{\varepsilon}_* / \partial u_*^N = \boldsymbol{\beta}_{*_N}$$

$$\partial_N \boldsymbol{\tau}_*^C = \boldsymbol{H}_* : \boldsymbol{\beta}_{*_N}$$

$$\delta \boldsymbol{\varepsilon}_* = \partial_M \boldsymbol{\varepsilon}_* \, \delta u_*^M = \boldsymbol{\beta}_{*_M} \delta u_*^M$$

And

$$\partial_N \boldsymbol{t}_* + \boldsymbol{t}_* \frac{1}{A_r} \partial_N A_r = \boldsymbol{Q}_{*_N}^{S_*}$$

where, $A_r = |dS_* / dS_*^0|$ is the ratio between the current area and the reference area of the material volume under consideration.

And

$$\partial_N \boldsymbol{f}_* + \boldsymbol{f}_* \frac{1}{J} \partial_N J = \boldsymbol{Q}_{*_N}^{V_*}$$

where $J = |dV_* / dV_*^0|$ is the ratio between the current volume and the reference volume of the material part under consideration.

The Eq. (C.14) and Eq. (C.16) provide the basis for Newton incremental solution.

The basic problem of ABAQUS standard/implicit analysis is to solve the Eq. (C.15) for the u_*^M throught out the history of interest. Newton's method as the numerical technique for solving the nonlinear equilibrium equations is used, which is as follows-

Assuming $u_{*(i)}^M$ is the solution obtained after i^{th} iteration and the difference between this solution and the exact solution is $c_{*(i+1)}^M$ it can be written-

$$F_*^N\left(u_{*(i)}^M + c_{*(i+1)}^M\right) = 0 \tag{C.19}$$

Now using Taylor series expansion to the left-hand side and assuming $c_{*(i+1)}^M$ is small, it can be shown that-

$$K_{*(i)}^{NP} c_{*(i+1)}^P = -F_{*(i)}^N \tag{C.20}$$

where

$$K_{*(i)}^{NP} = \frac{\partial F_*^N}{\partial u_*^P}\left(u_{*(i)}^M\right)$$

is the Jacobian matrix (similar to Eq. (C.16)) and $F_{*(i)}^N = F_*^N\left(u_{*(i)}^M\right)$.

The next approximation to the solution is then

$$u_{*(i+1)}^M = u_{*(i)}^M + c_{*(i+1)}^M$$

And the iteration continues.

ABAQUS dynamic/explicit analysis:

The explicit analysis procedure is based on the implementation of an explicit integration rule along with the use of 'lumped' mass matrix. For dynamic explicit analysis the inertial contribution is considered separately and Eq. (C.15) is defined as-

$$\boldsymbol{M}_*^{NM}\ddot{\boldsymbol{u}}_*^M + \boldsymbol{F}_*^N(\boldsymbol{u}_*^M) = 0 \tag{C.21}$$

$$\ddot{\boldsymbol{u}}_*^M = -\frac{1}{\boldsymbol{M}_*^{NM}}\boldsymbol{F}_*^N(\boldsymbol{u}_*^M) \tag{C.22}$$

Where $\boldsymbol{M}_*^{NM}$ represents "lumped' mass matrix.

In ABAQUS explicit analysis the equations of motion for the body are integrated using explicit central difference integration rule (Forward Euler Rule)-

$$\dot{\boldsymbol{u}}_{*\left(i+\frac{1}{2}\right)} = \dot{\boldsymbol{u}}_{*\left(i-\frac{1}{2}\right)} + \frac{\Delta t_{(i+1)} + \Delta t_{(i)}}{2}\ddot{\boldsymbol{u}}_{*(i)}$$

$$\boldsymbol{u}_{*(i+1)} = \boldsymbol{u}_{*(i)} + \Delta t_{(i+1)}\dot{\boldsymbol{u}}_{*\left(i+\frac{1}{2}\right)}$$

Where $\dot{\boldsymbol{u}}_*$ and $\ddot{\boldsymbol{u}}_*$ are velocity and acceleration respectively and subscript i refers to the increment number. Thus the explicit procedure requires no iterations or no tangent stiffness matrix like implicit, hence time

increment should be sufficiently small for better accuracy. Unlike in implicit, time in explicit analysis is a physical quantity. The central difference integrator is conditionally stable and the stable time increment is defined as-

$$\Delta t_{\text{stable}} \leq \frac{2}{\omega_{*(\max)}}\left(\sqrt{1+\xi^2}-\xi\right)$$

Where, $\omega_{*(\max)}$ is the highest eigenvalue in the system and ξ is the damping ratio.

A conservative estimation of stability limit is obtained as-

$$\Delta t_{\text{stable}} = \min\left(\frac{L_{*e}}{c_{*d}}\right)$$

Where, L_{*e} is the minimum element dimension in the model and c_{*d} is the speed of sound through the material.

Material and constitutive models:

In elasto-plastic model the deformation ($\boldsymbol{B}_*$) is generally divided into elastic ($\boldsymbol{B}_*^e$) and plastic ($\boldsymbol{B}_*^e$) parts-

$$\boldsymbol{B}_* = \boldsymbol{B}_*^e \,.\, \boldsymbol{B}_*^p$$

In terms of strain rate this decomposition is written in additive manner as-

$$\dot{\varepsilon}_* = \dot{\varepsilon}_*^e + \dot{\varepsilon}_*^p$$

where, $\dot{\varepsilon}_*$ is the total strain rate, $\dot{\varepsilon}_*^e$ is the elastic strain rate and $\dot{\varepsilon}_*^p$ is the plastic strain rate. The strain rate can be measured as-

$$\dot{\varepsilon}_* = \text{sym}\left(\frac{\partial \boldsymbol{v}_*}{\partial \boldsymbol{x}}\right) = \frac{1}{2}\left(\frac{\partial \boldsymbol{v}_*}{\partial \boldsymbol{x}} + \left[\frac{\partial \boldsymbol{v}_*}{\partial \boldsymbol{x}}\right]^T\right)$$

For the elastic part the response of the material is obtained as-

$$\boldsymbol{\sigma}_* = \frac{\partial U}{\partial \varepsilon_*^e}$$

where, U is the strain energy density potential.

The limit of elastic response is defined by yield function f as-

$$f(\boldsymbol{\sigma}_*, T, H_\alpha) < 0$$

where, T is temperature and H_α are set of hardening parameters as indicated by subscript α.

For rate-independent plastic deformation-

$$f(\boldsymbol{\sigma}_*, T, H_\alpha) = 0$$

For rate-dependent plastic deformation-

$$f(\boldsymbol{\sigma}_*, T, H_\alpha) \geq 0$$

During plastic deformation the material flow rule is defined as-

$$d\varepsilon_*^p = d\lambda_* \frac{\partial g}{\partial \boldsymbol{\sigma}_*}$$

where, $g(\boldsymbol{\sigma}_*, T, H_\alpha)$ is the flow potential and $d\lambda_*$ is the rate of change of time, dt, for rate-independent model or a measure of plastic flow rate (scalar quantity) for rate-dependent model.

For some rate-independent models the direction of flow is towards the direction of outward normal to the yield surface and is expressed as-

$$\frac{\partial g}{\partial \boldsymbol{\sigma}_*} = c \frac{\partial f}{\partial \boldsymbol{\sigma}_*}$$

Where c is a scalar. Such models are called "associate flow" plasticity models and useful for material where the deformation mechanism is driven by dislocations motion.

Axisymmetric model:

For a cylindrical coordinate system as shown in below (Figure C.1) the stress ($\boldsymbol{\sigma}_*$) and strain ($\boldsymbol{\varepsilon}_*$) tensors can be expressed as-

$$\boldsymbol{\sigma}_* = \begin{bmatrix} \sigma_{rr} & \sigma_{rz} & \sigma_{r\theta} \\ \sigma_{rz} & \sigma_{zz} & \sigma_{z\theta} \\ \sigma_{r\theta} & \sigma_{z\theta} & \sigma_{\theta\theta} \end{bmatrix}, \quad \boldsymbol{\varepsilon}_* = \begin{bmatrix} \varepsilon_{rr} & \varepsilon_{rz} & \varepsilon_{r\theta} \\ \varepsilon_{rz} & \varepsilon_{zz} & \varepsilon_{z\theta} \\ \varepsilon_{r\theta} & \varepsilon_{z\theta} & \varepsilon_{\theta\theta} \end{bmatrix}$$

For an axisymmetric element, because of symmetry $\sigma_{r\theta}$ and $\sigma_{z\theta}$ vanishe, and-

$$\boldsymbol{\sigma}_* = \begin{bmatrix} \sigma_{rr} & \sigma_{rz} & 0 \\ \sigma_{rz} & \sigma_{zz} & 0 \\ 0 & 0 & \sigma_{\theta\theta} \end{bmatrix}$$

Similarly,

$$\boldsymbol{\varepsilon}_* = \begin{bmatrix} \varepsilon_{rr} & \varepsilon_{rz} & 0 \\ \varepsilon_{rz} & \varepsilon_{zz} & 0 \\ 0 & 0 & \varepsilon_{\theta\theta} \end{bmatrix}$$

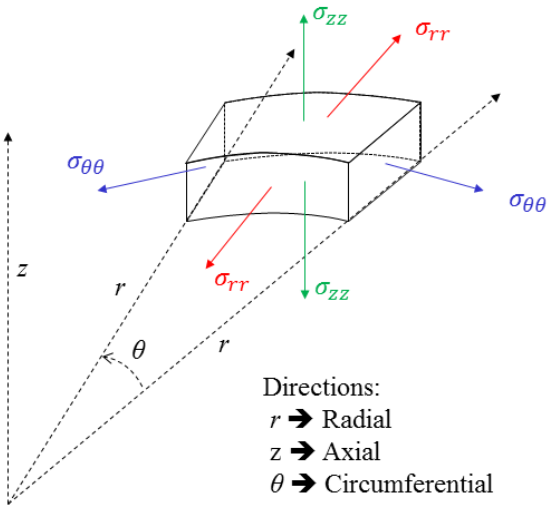

Figure C.1 Cylindrical coordinate system and axisymmetric element.

Isotropic elasto-plasticity:

For simple isotropic elasto-plasticity modeling the strain decomposition is-

$$d\boldsymbol{\varepsilon}_* = d\boldsymbol{\varepsilon}_*^e + d\boldsymbol{\varepsilon}_*^p$$

Volumetric strain is given as- $\varepsilon_{*_{vol}} = \text{trace}(\boldsymbol{\varepsilon}_*)$ and the deviatoric strain is $\boldsymbol{e}_* = \boldsymbol{\varepsilon}_* - \frac{1}{3}\varepsilon_{*_{vol}}\boldsymbol{I}$, where $\boldsymbol{I}$ is a unit matrix. The elasticity is written in terms of volumetric and deviatoric components as-

Volumetric part:

$$p_* = -K_* \varepsilon_{*_{vol}}$$

Where, $p_* = -\frac{1}{3}\text{trace}(\boldsymbol{\sigma}_*)$ is the equivalent pressure stress causes only elastic deformation, and $K_* = \frac{E}{3(1-2\nu)}$ is the bulk modulus, function of Young's modulus (E) and Poisson ratio (ν).

Deviatoric part:

$$\boldsymbol{\sigma}'_* = 2G\boldsymbol{e}^e_*$$

Where, $G = \frac{E}{2(1+\nu)}$ is the shear modulus and the deviatoric stress ($\boldsymbol{\sigma}'_*$) is expressed as

$$\boldsymbol{\sigma}'_* = \boldsymbol{\sigma}_* + p_*\boldsymbol{I}$$

The associative plastic flow rule is given as-

$$d\boldsymbol{e}^p_* = d\bar{e}^p_*\,\boldsymbol{n}$$

where, $\bar{e}^p_*$ is the scalar equivalent plastic strain and

$$\boldsymbol{n} = \frac{3}{2}\frac{\boldsymbol{\sigma}'_*}{\sigma_{eq}}$$

Where, the von Mises equivalent stress (σ_{eq}) is given as-

$$\sigma_{eq} = \sqrt{\frac{3}{2}\boldsymbol{\sigma}'_* : \boldsymbol{\sigma}'_*}$$

The corresponding equivalent plastic strain rate is given as-

$$\dot{\varepsilon}^p_{eq} = \sqrt{\frac{2}{3}\dot{\boldsymbol{\varepsilon}}^p_* : \dot{\boldsymbol{\varepsilon}}^p_*}$$

The yield function for **rate-independent material** is givens as-

$$f = \sigma_{eq} - \sigma^0 = 0$$

Where $\sigma^0(\bar{e}^p_*, T)$ is the material yield stress and a user input.

When the material is strain **rate dependent** then the yield criteria is written as-

$$f = \sigma_{eq} - \bar{\sigma} = 0$$

where, $\bar{\sigma}(\bar{e}^p_*, \dot{\bar{e}}^p_*, T)$ is the material yield strength and for the Johnson-Cook plasticity model (without considering the thermal softening part) is expressed as-

$$\bar{\sigma} = \left(\sigma_y + K\varepsilon_p^n\right)\left(1 + C\ln\frac{\dot{\varepsilon}_p}{\dot{\varepsilon}_0}\right)$$

Nomenclature

In this thesis for any symbol whether italic or no-italic has the same meaning, however upper-case and lower-case letters or symbols stand for different variable.

Symbol	Description
P	Pressure
T	Temperature
γ	Bubble's stand-off distance
T_r	Triple point temperature of water
T_c	Critical point temperature of water
σ_{ca}	Cavitation number
Δp	Pressure drop
E_k	Kinetic energy
p_V	Vapor pressure of liquid (water)
p_l	Local pressure in liquid (water)
ρ_l	Density of liquid (water)
v_l	Velocity of liquid (water)
σ_i	Incipient cavitation number
P_{imp}	Water hammer impact pressure
v_{jet}	Velocity of water jet
ρ_s	Density of solid
c_s	Speed of sound in solid
c_l	Speed of sound in liquid
E_s	Young's modulus of solid
Φ	Indicates diameter
p_u	Upstream pressure
p_d	Downstream pressure
ε	True strain
a_c	Indentation contact radius
R_{ind}	Indenter radius
d_P	Pit diameter
h_P	Pit depth
ε_P	Pitting strain
σ_P	Pitting stress
MDER	Mean depth of erosion rate
HV	Hardness Vickers

MDE	Mean depth of erosion
A and B	Fitting constants of Eq. (1.9)
N_{imp}	Number of mechanical impact cycles
A' and B'	Fitting constants of Eq. (1.10)
Δm	Non-dimensional mass loss
Δt	Non-dimensional exposure time
N_i	Total number of cavitation impacts of force F_i to cavitation failure, classified by i
F_i	Impact force of a particular amplitude, classified by i
$\alpha \; and \; C_1$	Empirical constants depend on material (Eq. (1.11))
n_i	Number of impacts of force F_i , classified by i
D	Damage variable
ΔD	Damage increment
t_{incb}	Incubation period
σ	Stress
σ_y	Yield strength
σ_u	Ultimate strength
ε_u	Ultimate strain
σ_R	Rupture stress
ε_R	Rupture strain
t_{cov}	Coverage time
σ_{mean}	Mean impact stress
ε_{mean}	Mean impact strain
A_{mean}	Mean impacted area
$\dot{N}$	Pitting rate
ε_s	Strain at the surface (Eq. (1.15))
x	Distance from the surface into the material (Eq. (1.15))
θ	Steepness of hardening gradient of material (Eq. (1.15))
L	Thickness of the hardened layer (Eq. (1.15))
ΔL	Thickness of eroded material layer (Eq. (1.15))
$K \; and \; n$	Strain hardening coefficient and exponent respectively
$MDPR$	Mean depth of penetration rate
E_{wave}	Energy of incident wave
V_{pit}	Pit volume
C_2	A material constant (Eq. (1.22))
ΔE	Increment of internal energy density

ΔE_{max}	Maximum increment of internal energy
N_r	Number of cavitation impacts at failure
β *and* C_3	Constants that depends on the test material (Eq. (1.23))
N_i	Number of impacts at failure for a particular load level, categorized by i
η	Fraction of impacted shock-wave energy utilized for plastic deformation to form a cavitation pit
$\overline{\gamma}$	A correction factor account for cyclic hardening or softening under repeated cavitation impacts
L'	Parameter related to the distance between metal surface and the source of the shock wave emission
r	Radial direction for an axisymmetric element
z	Longitudinal direction for an axisymmetric element
θ	Circumferential direction for an axisymmetric element
R	Maximum radial size of the simulated volume
H	Vertical size along z axis of the simulated volume
P_0	Maximum Hertz pressure at the center of symmetry
r_c	Hertzian contact radius
δ'	Hertzian depth of indentation
E	Young's modulus
E^*	Effective modulus of Hertz contact
ν	Poisson's ratio
ν_1 *and* ν_2	Poison's ratio of substrate and indenter respectively
E_1 *and* E_2	Young's modulus of substrate and indenter respectively
F	Force
τ	Shear stress along depth, z on the axis of symmetry
τ_{max}	Maximum shear stress under Herzian contact
z_{max}	Depth of maximum shear stress under Herzian contact
σ_H	Peak pressure of hydrodynamic impact
r_H	Radial extent of hydrodynamic impact
d_H	Diameter of hydrodynamic impact
h_P	Pit depth
d_P	Pit diameter at 50% of pit depth
r_P	Pit radius at 50% of pit depth
ε_e	Elastic strain
ε_P	Plastic strain
m_y *and* K_y	Parameter of the Ramberg–Osgood constitutive equation (Eq. (2.8))
k	Material constant (Eq. (2.9))

σ^*, β'	Material constants (Eq. (2.10))
σ_{eq} *or* σ_{mises}	Von Mises equivalent stress
ε_{eq}	Equivalent plastic strain
σ_{rr} , σ_{zz} *and* $\sigma_{\theta\theta}$	Normal stresses on radial, longitudinal and circumferential faces respectively
σ_{rz}	Shear stress on the radial face and longitudinal direction
CCOD	Constant cut-off depth
FCOD	Fractional cut-off depth
h	Depth (Eq. (2.12))
d	Diameter (Eq. (2.12))
h_{max}	Maximum pit depth (Eq. (2.12))
d_{max}	Maximum pit diameter (Eq. (2.12))
$\langle a', b', c' \rangle$	Normal vector ($\overrightarrow{ON}$) (Eq. (2.13) and Fig. 2.19)
d'	A constant related to the 3D plane (Fig. 2.19)
(x, y, y)	Represent three Cartesian coordinates
h_{cut}	Cut-off depth (Eq. (2.14))
$\sigma_{H_{min}}$	Minimum value of peak pressure require to form a pit (Eq. (2.14))
δ	Characteristic pit diameter
$\dot{\varepsilon}$	Strain rate
$\dot{\varepsilon}_p$	Plastic strain rate
C_4 *and* C_5	Material constant in Eq. (3.1)
$\bar{\sigma}$	Flow stress at high strain rate
$\dot{\varepsilon}_0$	Reference strain rate of Johnson-Cook plasticity model
C	Strain rate sensitivity parameter of Johnson-Cook plasticity model
$\bar{T}$	Non-dimensional temperature
T_{melt}	Melting temperature
$T_{transition}$	Transition temperature
$\Delta\sigma_G'$	Material constant in Eq. (3.4)
C_6	Microstructural stress intensity
l'	Average grain diameter
C_7 *to* C_{11}	Are material constants in Eq. (3.4) and Eq. (3.5)
ρ	Density
t	Time
t_H	Characteristic impact duration
t_{max}	Instantaneous time when the impact load reaches the peak value
R'	Stress ratio

N	Normalized impact frequency (impacts/cm^2/sec/μm/MPa)
N^*, σ_H^* *and* d_H^*	Three fitting constants in Eq. (3.9)
r_d	Radius of the representative cylinder for the deformed region of material under cavitation impact (Fig. 4.7)
l_d	Length or height of the representative cylinder for the deformed region of material under cavitation impact (Fig. 4.7)
C_{12}*and* C_{13}	Material constants in Eq. (4.3)
m	mass
b	Damping coefficient
$X(t)$	Amplitude of oscillation of spring-mass-damper system (Fig. 4.9(a))
$\dot{X}(t)$	Velocity of oscillation of spring-mass-damper system (Fig. 4.9(a))
$\ddot{X}(t)$	Acceleration of oscillation of spring-mass-damper system (Fig. 4.9(a))
F_0	Magnitude of external force to the spring-mass-damper system (Fig. 4.9(a))
ω	Angular frequency in radians per second
ω_n	Angular natural frequency
$\overline{\omega}$	Frequency ratio (=Angular frequency/ Angular natural frequency)
f_n	Natural frequency
ξ	Damping ratio
S	Stiffness or contact harmonic stiffness
$\dot{\epsilon}$	Maximum of maximum principal strain rates
C_{14} *and* C_{15}	Fitting constants in Eq. (4.7)
α'	Ratio of acoustic impedances ($= \rho_s c_s/\rho_l c_l$)
ω_D	Scalar variable for damage initiation
ε_p^i	Equivalent plastic strain at damage initiation
ε_p^f	Equivalent plastic strain at complete failure
D	Damage variable for damage evolution
ε_p'	Cumulative plastic strain after damage initiation ($= \varepsilon_p - \varepsilon_p^i$)
η'	Stress triaxiality ($= p/\sigma_{eq}$)
D_1 *to* D_5	Material constants in Eq. (5.7)
m'	Material constant in Eq. (3.3) and Eq. (5.7)
r_b	Bubble radius
$r_{b(max)}$	Maximum bubble radius
$t_{Rayleigh}$	Characteristic bubble collapse duration or Rayleigh time
$V_{entry}(t)$	Velocity of incident bar/specimen interface in SHPB test
$V_{exit}(t)$	Velocity of specimen/incident bar interface in SHPB test

$l_{initial}$	Initial length of SHPB test specimen
$\varepsilon_{incident}(t)$	Incident strain in the pressure bar in SHPB apparatus
$\varepsilon_{reflected}(t)$	Reflected strain in the pressure bar in SHPB apparatus
$\varepsilon_{transmitted}(t)$	Transmitted strain in the pressure bar in SHPB apparatus
c_{bar}	Speed of sound in the pressure bars in SHPB apparatus
$F_{entry}(t)$	Force at the incident bar/specimen interface in SHPB test
$F_{exit}(t)$	Force at the specimen/incident bar interface in SHPB test
$\sigma_{entry}(t)$	Stress at the incident bar/specimen interface in SHPB test
$\sigma_{exit}(t)$	Stress at the specimen/incident bar interface in SHPB test
A_{bar}	Cross sectional area of the pressure bars in SHPB apparatus
E_{bar}	Young's modulus area of the pressure bars in SHPB apparatus
$A_{specimen}$	Initial cross section of a test specimen for SHPB test
h_c	Contact depth
A_c	Contact area
Ω_n	Indenter area coefficients (Eq. (B.1))
Ψ	Constant in Eq. (B.2)
λ	Constant in Eq. (B.3)
σ_{ind}	Indentation stress
ε_{ind}	Indentation strain

References

[1] L. Euler, Theorie plus compiette des machines qui sont mises en mouvement par la reaction de l'eau, Mémoires L'académie Des Sci. Berlin. 10 (1954) 227–295.

[2] S.C. Roy, J.-P. Franc, C. Pellone, M. Fivel, Determination of cavitation load spectra – Part 1: Static finite element approach, Wear. In Press (2015). doi:10.1016/j.wear.2015.09.006.

[3] S.C. Roy, J.-P. Franc, M. Fivel, Cavitation Erosion: Using the Target Material as a Pressure Sensor, J. Appl. Phys. Accepted (2015).

[4] S.C. Roy, J.-P. Franc, N. Ranc, M. Fivel, Determination of cavitation load spectra—Part 2: Dynamic finite element approach, Wear. In Press (2015). doi:10.1016/j.wear.2015.09.005.

[5] M. Fivel, J.P. Franc, S.C. Roy, Towards Numerical Prediction of Cavitation Rrosion, Interface Focus. 5 (2015) 20150013 (1–10).

[6] J.-P. Franc, J.-P. Michel, eds., Fundamentals of Cavitation, Kluwer Academic Publishers, 2004. doi:10.1007/1-4020-2233-6.

[7] K.-H. Kim, G. Chahine, J. Franc, A. Karimi, eds., Advanced Experimental and Numerical Techniques for Cavitation Erosion Prediction, Springer, 2014.

[8] R.T. Knapp, J.W. Daily, F.G. Hammitt, Cavitation, 1970.

[9] R.E.A. Arndt, Cavitation in fluid machinery and hydraulic structures, Annu. Rev. Fluid Mech. 13 (1981) 273–328.

[10] G.J. Ball, B.P. Howell, T.G. Leighton, M.J. Schofield, Shock-induced collapse of a cylindrical air cavity in water: a Free-Lagrange simulation, (2000) 265–276. doi:10.1007/s001930000060.

[11] T.B. Benjamin, A.T. Ellis, The collapse of cavitation bubbles and the pressure thereby produced against solid boundaries, Philos. Trans. R. Soc. London A. 260 (1966) 221–240.

[12] J.P. Best, The formation of toroidal bubbles upon the collapse of transient cavities, J. Fluid Mech. 251 (1993) 79–107.

[13] G.L. Chahine, Y.T. Shen, Bubble Dynamics and Cavitation Inception in Cavitation Susceptibility Meters, J. Fluids Eng. 108 (1986) 444. doi:10.1115/1.3242602.

[14] J.R. Blake, B.B. Taib, G. Doherty, Transient cavities near boundaries. Part 1. Rigid boundary, J. Fluid Mech. 170 (1986) 479–497. doi:10.1017/S0022112086000988.

[15] N.K. Bourne, J.E. Field, Shock-induced collapse of single cavities in liquids, J. Fluid Mech. 244 (21992) 225–240. doi:10.1017/S0022112092003045.

[16] M. Kornfeld, L. Suvorov, On the Destructive Action of Cavitation, J. Appl. Phys. 15 (1944) 495. doi:10.1063/1.1707461.

[17] C.F. Naudé, A.T. Ellis, On the Mechanism of Cavitation Damage by Nonhemispherical Cavities Collapsing in Contact With a Solid Boundary, J. Basic Eng. 83 (1961) 648. doi:10.1115/1.3662286.

[18] L.A. Crum, Surface Oscillations and Jet Development in Pulsating Bubbles, Le J. Phys. Colloq. 40 (1979) C8–285–C8–288. doi:10.1051/jphyscol:1979849.

[19] A. Philipp, W. Lauterborn, Cavitation erosion by single laser-produced bubbles, J. Fluid Mech. 361 (1998) 75–116. doi:10.1017/S0022112098008738.

[20] A. Vogel, W. Lauterborn, R. Timm, Optical and acoustic investigations of the dynamics of laser-produced cavitation bubbles near a solid boundary, J. Fluid Mech. 206 (1989) 299–338.

[21] Lord Rayleigh, On the pressure developed in a liquid during the collapse of a spherical cavity, Philos. Mag. Ser. 6. 34 (1917) 94–98. doi:10.1080/14786440808635681.

[22] M. Harrison, An Experimental Study of Single Bubble Cavitation Noise, J. Acoust. Soc. Am. 24 (1952) 776. doi:10.1121/1.1906978.

[23] Y. Tomita, A. Shima, Mechanisms of impulsive pressure generation and damage pit formation by bubble collapse, J. Fluid Mech. 169 (1986) 535–564. doi:10.1017/S0022112086000745.

[24] O. Lindau, W. Lauterborn, Cinematographic observation of the collapse and rebound of a laser-produced cavitation bubble near a wall, J. Fluid Mech. 479 (2003) 327–348. doi:10.1017/S0022112002003695.

[25] M.S. Plesset, R.B. Chapman, Collapse of an initially spherical Vapor Cavity in the Neighborhood of a solid Boundary, J. Fluid Mech. 47 (1971) 283–290. doi:10.1017/S0022112071001058.

[26] E. Johnsen, T. Colonius, Numerical simulations of non-spherical bubble collapse, J. Fluid Mech. 629 (2009) 231. doi:10.1017/S0022112009006351.

[27] A. Jayaprakash, C.-T. Hsiao, G. Chahine, Numerical and Experimental Study of the Interaction of a Spark-Generated Bubble and a Vertical Wall, J. Fluids Eng. 134 (2012) 031301. doi:10.1115/1.4005688.

[28] C.-T. Hsiao, A. Jayaprakash, A. Kapahi, J.-K. Choi, G.L. Chahine, Modelling of material pitting from cavitation bubble collapse, J. Fluid Mech. 755 (2014) 142–175. doi:10.1017/jfm.2014.394.

[29] N.D. Shutler, R.B. Mesler, A Photographic Study of the Dynamics and Damage Capabilities of Bubbles Collapsing Near Solid Boundaries, J. Basic Eng. 87 (1965) 511. doi:10.1115/1.3650589.

[30] V.F.J. Bjerknes, Fields of Force, Colombia University Press, New York, 1906.

[31] A. Vogel, W. Lauterborn, R. Timm, Optical and acoustic investigations of the dynamics of laser-produced cavitation bubbles near a solid boundary, Jounral Fluid Mech. 206 (1989) 299–338.

[32] S.M. Ahmed, K. Hokkirigawa, R. Oba, Fatigue failure of SUS 304 caused by vibratory cavitation erosion, Wear. 177 (1994) 129–137. doi:10.1016/0043-1648(94)90238-0.

[33] I.R. Jones, D.H. Edwards, An experimental study of the forces generated by the collapse of transient cavities in water, J. Fluid Mech. 7 (1960) 596–690. doi:10.1017/S0022112060000311.

[34] T. Momma, A. Lichtarowicz, A study of pressures and erosion produced by collapsing cavitation, Wear. 186-187 (1995) 425–436. doi:10.1016/0043-1648(95)07144-X.

[35] ASM Handbook, Volume 11, Failure analysis and prevention, ASM International, 2002.

[36] B. V Hubballi, V.B. Sondur, A Review on the Prediction of Cavitation Erosion Inception in Hydraulic Control Valves, 3 (2013) 110–119.

[37] W. Pfitsch, S. Gowing, D. Fry, M. Donnelly, S. Jessup, Development of measurement techniques for studying propeller erosion damage in severe wake fields, in: Proc. 7th Int. Symp. Cavitation, Ann Arbor, Michigan, USA, 2009: pp. 1–9.

[38] J.-P. Franc, M. Riondet, A. Karimi, G.L. Chahine, Impact Load Measurements in an Erosive Cavitating Flow, J. Fluids Eng. 133 (2011) 121301. doi:10.1115/1.4005342.

[39] R.I. Stephens, A. Fatemi, R.R. Stephens, H.O. Fuchs, Metal Fatigue in Engineering, John Wiley & Sons, 2000.

[40] G.E. Dieter, Mechanical Metallurgy, McGraw-Hill, 1988.

[41] S. Hattori, T. Itoh, Cavitation erosion resistance of plastics, Wear. 271 (2011) 1103–1108. doi:10.1016/j.wear.2011.05.012.

[42] J.F. Santa, J. a. Blanco, J.E. Giraldo, A. Toro, Cavitation erosion of martensitic and austenitic stainless steel welded coatings, Wear. 271 (2011) 1445–1453. doi:10.1016/j.wear.2010.12.081.

[43] A. Karimi, Cavitation erosion of a duplex stainless steel, Mater. Sci. Eng. 86 (1987) 191–203. doi:10.1016/0025-5416(87)90452-6.

[44] R. Fortes Patella, T. Choffat, J.-L. Reboud, A. Archer, Mass loss simulation in cavitation erosion: Fatigue criterion approach, Wear. 300 (2013) 205–215. doi:10.1016/j.wear.2013.01.118.

[45] S. Hattori, N. Mikami, Cavitation erosion resistance of stellite alloy weld overlays, Wear. 267 (2009) 1954–1960. doi:10.1016/j.wear.2009.05.007.

[46] A. Karimi, Cavitation erosion of austenitic stainless steel and effect of boron and nitrogen ion implantation, Acta Metall. 37 (1989) 1079–1088. doi:10.1016/0001-6160(89)90104-1.

[47] B. Vyas, C.M. Preece, Cavitation erosion of face centered cubic metals, Metall. Trans. A. 8 (1977) 915–923. doi:10.1007/BF02661573.

[48] J.-K. Choi, A. Jayaprakash, A. Kapahi, C.-T. Hsiao, G.L. Chahine, Relationship between space and time characteristics of cavitation impact pressures and resulting pits in materials, J. Mater. Sci. 49 (2014) 3034–3051. doi:10.1007/s10853-013-8002-5.

[49] F. Pöhl, S. Mottyll, R. Skoda, S. Huth, Evaluation of cavitation-induced pressure loads applied to material surfaces by finite-element-assisted pit analysis and numerical investigation of the elasto-plastic deformation of metallic materials, Wear. 330-331 (2015) 618–628. doi:10.1016/j.wear.2014.12.048.

[50] H. Soyama, Y. Sekine, K. Saito, Evaluation of the enhanced cavitation impact energy using a PVDF transducer with an acrylic resin backing, Meas. J. Int. Meas. Confed. 44 (2011) 1279–1283. doi:10.1016/j.measurement.2011.03.027.

[51] Y.C. Wang, C.H. Huang, Y.C. Lee, H.H. Tsai, Development of a PVDF sensor array for measurement of the impulsive pressure generated by cavitation bubble collapse, Exp. Fluids. 41 (2006) 365–373. doi:10.1007/s00348-006-0135-8.

[52] T. Deplancke, O. Lame, J. Cavaille, M. Fivel, M. Riondet, J. Franc, Outstanding cavitation erosion resistance of Ultra High Molecular Weight Polyethylene (UHMWPE) coatings, Wear. 328-329 (2015) 301–308. doi:10.1016/j.wear.2015.01.077.

[53] G.L. Chahine, P. Courbière, Noise and Erosion of Self-Resonating Cavitating Jets, J. Fluids Eng. 109 (1987) 429–435.

[54] X. Escaler, F. Avellan, E. Egusquiza, Cavitation erosiion prediction from inferred forces using material resistance data, in: 4th Int. Symp. Cavitation, 2001: pp. 1–9.

[55] F.G. Hammitt, Damage to solids caused by cavitation, Philos. Trans. A. 260 (1966) 245–255.

[56] M.K. Lee, W.W. Kim, C.K. Rhee, W.J. Lee, Liquid impact erosion mechanism and theoretical impact stress analysis in TiN-coated steam turbine blade materials, Metall. Mater. Trans. A. 30 (1999) 961–968. doi:10.1007/s11661-999-0149-y.

[57] ASTM G32-06, Standard Test Method for Cavitation Erosion Using Vibratory Apparatus, ASTM International, West Conshohocken, PA, 2006, www.astm.org, n.d.

[58] ASTM G32-10, Standard Test Method for Cavitation Erosion Using Vibratory Apparatus, ASTM International, West Conshohocken, PA, 2010, www.astm.org, n.d.

[59] ASTM G134-95(2001)e1, Standard Test Method for Erosion of Solid Materials by a Cavitating Liquid Jet, ASTM International, West Conshohocken, PA, 2001, www.astm.org, n.d.

[60] R.F. Patella, J.L. Reboud, a. Archer, Cavitation damage measurement by 3D laser profilometry, Wear. 246 (2000) 59–67. doi:10.1016/S0043-1648(00)00446-4.

[61] M. Dular, B. Bachert, B. Stoffel, B. Širok, Relationship between cavitation structures and cavitation damage, Wear. 257 (2004) 1176–1184. doi:10.1016/j.wear.2004.08.004.

[62] J.-P. Franc, Incubation Time and Cavitation Erosion Rate of Work-Hardening Materials, J. Fluids Eng. 131 (2009) 021303. doi:10.1115/1.3063646.

[63] J.-P. Franc, M. Riondet, A. Karimi, G.L. Chahine, Material and velocity effects on cavitation erosion pitting, Wear. 274-275 (2012) 248–259. doi:10.1016/j.wear.2011.09.006.

[64] R. Fortes-Patella, G. Challier, J. Reboud, A. Archer, Cavitation Erosion Mechanism: Numerical Simulations of the Interaction Between Pressure Waves and Solid Boundaries, in: Proc. 4th Int. Symp. Cavitation, Pasadena, CA, 2001: pp. 1–8.

[65] X. Escaler, E. Egusquiza, M. Farhat, F. Avellan, M. Coussirat, Detection of cavitation in hydraulic turbines, Mech. Syst. Signal Process. 20 (2006) 983–1007. doi:10.1016/j.ymssp.2004.08.006.

[66] R. Xu, R. Zhao, Y. Cui, J. Lu, X. Ni, The collapse and rebound of gas-vapor cavity on metal surface, Optik (Stuttg). 120 (2009) 115–120. doi:10.1016/j.ijleo.2007.06.017.

[67] D. Carnelli, A. Karimi, J.P. Franc, Evaluation of the hydrodynamic pressure of cavitation impacts from stress-strain analysis and geometry of individual pits, Wear. 289 (2012) 104–111. doi:10.1016/j.wear.2012.04.009.

[68] D. Carnelli, A. Karimi, J.-P. Franc, Application of spherical nanoindentation to determine the pressure of cavitation impacts from pitting tests, J. Mater. Res. 27 (2012) 91–99. doi:10.1557/jmr.2011.259.

[69] R.T. Knapp, Recent Investigations of the Mechanics of Cavitation and Cavitation Damage, Trans. ASME. 77 (1955) 1045–1054.

[70] R.T. Knapp, Accelerated Field Tests of Cavitation Intensity, Trans. Am. Soc. Mech. Eng. 80 (1958) 91–102.

[71] B. Belahadji, J.P. Franc, J.M. Michel, A Statistical Analysis of Cavitation Erosion Pits, J. Fluids Eng. 113 (1991) 700–706. doi:10.1115/1.2926539.

[72] S.M. Ahmed, K. Hokkirigawa, Y. Ito, R. Oba, Scanning electron microscopy observation on the incubation period of vibratory cavitation erosion, Wear. 142 (1991) 303–314. doi:10.1016/0043-1648(91)90171-P.

[73] T. Okada, Y. Iwai, K. Awazu, A Study of Cavitation Bubble Collapse Pressures and Erosion Part 1: A Method for Measurement of Collapse Pressures, Wear. 133 (1989) 219–232.

[74] S. Hattori, T. Hirose, K. Sugiyama, Prediction method for cavitation erosion based on measurement of bubble collapse impact loads, Wear. 269 (2010) 507–514. doi:10.1016/j.wear.2010.05.015.

[75] T. Okada, S. Hattori, M. Shimizu, A fundamental study of cavitation erosion using a magnesium oxide single crystal (intensity and distribution of bubble collapse impact loads), Wear. 186-187 (1995) 437–443. doi:10.1016/0043-1648(95)07162-8.

[76] Y.C. Wang, Y.W. Chen, Application of piezoelectric PVDF film to the measurement of impulsive forces generated by cavitation bubble collapse near a solid boundary, Exp. Therm. Fluid Sci. 32 (2007) 403–414. doi:10.1016/j.expthermflusci.2007.05.003.

[77] D. Tabor, The Hardness of Metals, Clarendon Press, 1951.

[78] X. Liu, J. Katz, Instantaneous pressure and material acceleration measurements using a four-exposure PIV system, Exp. Fluids. 41 (2006) 227–240. doi:10.1007/s00348-006-0152-7.

[79] M. Unal, J. Lin, D. Rockwell, Force prediction by PIV imaging: a momentum-based approach, J. Fluids Struct. 11 (1997) 965–971. doi:10.1006/jfls.1997.0111.

[80] X. Liu, J. Katz, Measurements of Pressure Distribution in a Cavity Flow by Integrating the Material Acceleration, in: Vol. 3, ASME, 2004: pp. 621–631. doi:10.1115/HT-FED2004-56373.

[81] G.L. Chahine, Modeling of Cavitation Dynamics and Interaction with Material, in: K.-H. Kim, G.L. Chahine, J.-P. Franc, A. Karimi (Eds.), Adv. Exp. Numer. Tech. Cavitation Eros. Predict. Fluid Mech. Its Appl. Vol. 106, Springer, 2014: pp. 123–161.

[82] E. Johnsen, Numerical Simulations of Shock Emission by Bubble Collapse Near a Rigid Surface, in: K.-H. Kim, G. Chahine, J.-P. Franc, A. Karimi (Eds.), Adv. Exp. Numer. Tech. Cavitation Eros. Predict., Springer, Berlin, 2014: pp. 373–396.

[83] M. Fukaya, Y. Tamura, Y. Matsumoto, Prediction of Cavitation Intensity and Erosion Area in Centrifugal Pump by Using Cavitating Flow Simulation with Bubble Flow Model, Trans. Japan Soc. Mech. Eng. Ser. B. 74 (2008) 2116–2123. doi:10.1299/kikaib.74.2116.

[84] M. Fukaya, Y. Tamura, Y. Matsumoto, Prediction of Impeller Speed Dependence of Cavitation Intensity in Centrifugal Pump Using Cavitating Flow Simulation with Bubble Flow Model, in: Proc. 7th Int. Symp. Cavitation, Ann Arbor, Michigan, USA, 2009: pp. 1–7.

[85] M.S. Mihatsch, S.J. Schmidt, M. Thalhamer, N.A. Adams, Quantitative Prediction of Erosion Aggressiveness through Numerical Simulation of 3-D Unsteady Cavitating Flows, Proc. 8th Int. Symp. Cavitation. (2012) 1–6. doi:10.3850/978-981-07-2826-7.

[86] M.S. Mihatsch, S.J. Schmidt, M. Thalhamer, N.A. Adams, Numerical Prediction of Erosive Collapse Events in Unsteady Compressible Cavitating Flows, in: Mar. 2011, IV Int. Conf. Comput. Methods Mar. Eng., Springer Netherlands, Dordrecht, 2013: pp. 187–198. doi:10.1007/978-94-007-6143-8.

[87] S.J. Schmidt, M.S. Mihatsch, M. Thalhamer, N.A. Adams, Assessment of Erosion Sensitive Areas via Compressible Simulation of Unsteady Cavitating Flows, in: K.-H. Kim, G.L. Chahine, J.-P. Franc, A. Karimi (Eds.), Adv. Exp. Numer. Tech. Cavitation Eros. Predict., Springer, 2014: pp. 329–344.

[88] C. Hsiao, J. Ma, G.L. Chahine, Simulation of Sheet and Tip Vortex Cavitation on a Rotating Propeller Using a Multiscale Two-Phase Flow Model, in: Fourth Int. Symp. Mar. Propulsors, Austine, Texas, USA, 2015.

[89] R. Singh, S.K. Tiwari, S.K. Mishra, Cavitation Erosion in Hydraulic Turbine Components and Mitigation by Coatings: Current Status and Future Needs, J. Mater. Eng. Perform. 21 (2011) 1539–1551. doi:10.1007/s11665-011-0051-9.

[90] M. Futakawa, H. Kogawa, C. Tsai, S. Ishikura, Y. Ikeda, Off-line tests on pitting damage in Mercury target, Japan, 2003.

[91] M.. D. Kass, J.. H. Whealton, N.E. Clapp Jr., J.R. DiStefano, J.H. DeVan, J.R. Haines, et al., Nonlinear cavitation erosion of stainless steel in mercury versus applied power ∗, Tribol. Lett. 5 (1998) 231–234.

[92] H. Soyama, M. Futakawa, Estimation of incubation time of cavitation erosion for various cavitating conditions, Tribol. Lett. 17 (2004) 27–30. doi:10.1023/B:TRIL.0000017415.79517.8c.

[93] S. Hattori, Recent Investigations on Cavitation Erosion at the University of Fukui, in: K.-H. Kim, G.L. Chahine, J.-P. Franc, A. Karimi (Eds.), Adv. Exp. Numer. Tech. Cavitation Eros. Predict., Springer, 2014: pp. 257–282.

[94] T. Okada, Y. Iwai, S. Hattori, N. Tanimura, Relation between impact load and the damage produced by cavitation bubble collapse, Wear. 184 (1995) 231–239. doi:10.1016/S0301-9322(97)88613-2.

[95] A. Karimi, W.R. Leo, Phenomenological model for cavitation erosion rate computation, Mater. Sci. Eng. 95 (1987) 1–14. doi:10.1016/0025-5416(87)90493-9.

[96] H. Kato, A. Konno, M. Maeda, H. Yamaguchi, Possibility of Quantitative Prediction of Cavitation Erosion Without Model Test, Trans. ASME. 118 (1996) 582–588.

[97] N. Berchiche, J.P. Franc, J.M. Michel, A Cavitation Erosion Model for Ductile Materials, J. Fluids Eng. 124 (2002) 601. doi:10.1115/1.1486474.

[98] J. Steller, International cavitation erosion test and quantitative assessment of material resistance to cavitation, Wear. 233-235 (1999) 51–64. doi:10.1016/S0043-1648(99)00195-7.

[99] J. Steller, P. Kaczmarzyk, Phenomenological models of cavitation erosion progress, Int. Cavitation Eros. Test Semin. l (2000) 1–2.

[100] M. Dular, B. Stoffel, B. Širok, Development of a cavitation erosion model, Wear. 261 (2006) 642–655. doi:10.1016/j.wear.2006.01.020.

[101] R.F. Patella, J.-L. Reboud, A New Approach to Evaluate the Cavitation Erosion Power, J. Fluids Eng. 120 (1998).

[102] C.E. Brennen, Cavitation and Bubble Dynamics, Oxford University Press, New York, 1995.

[103] C.E. Brennen, Hydrodynamics of Pumps, Oxford University Press and Concepts ETI Inc., 1994.

[104] S. Hattori, H. Mori, T. Okada, Quantitative Evaluation of Cavitation Erosion, J. Fluids Eng. 120 (1998) 179–185. doi:10.1115/1.2819644.

[105] H. Soyama, A. Lichtarowicz, T. Momma, E.J. Williams, A New Calibration Method for Dynamically Loaded Transducers and Its Application to Cavitation Impact Measurement, J. Fluids Eng. 120 (1998) 712–718. doi:10.1115/1.2820728.

[106] A.C. Fischer-Cripps, Nanoindentation, Springer, New York, 2004.

[107] G.L. Chahine, J.-P. Franc, A. Karimi, Cavitation Impulsive Pressures, in: K.-H. Kim, G.L. Chahine, J.-P. Franc, A. Karimi (Eds.), Adv. Exp. Numer. Tech. Cavitation Eros. Predict. Fluid Mech. Its Appl. Vol. 160, Springer, 2014: pp. 71–95.

[108] S. Singh, J.-K. Choi, G.L. Chahine, Characterization of Cavitation Fields From Measured Pressure Signals of Cavitating Jets and Ultrasonic Horns, J. Fluids Eng. 135 (2013) 091302–1 – 091302–11. doi:10.1115/1.4024263.

[109] K.L. Johnson, Contact Mechanics, Cambridge University Press, 1985.

[110] R.T. Knapp, J.W. Daily, F.G. Hammitt, Cavitation, McGraw Hil Book Col, New York, 1970.

[111] J. Lemaitre, J.L. Chaboche, Mécanique des matériaux solides, Dunod, 1996.

[112] K. Ludwik, Element der technologischen mechanik, J. Springer. 32 (1909).

[113] G.E. Totten, ed., Handbook of residual stress and deformation of steel, ASM international, 2002.

[114] M. Fivel, J.-P. Franc, S.C. Roy, Towards Numerical Prediction of Cavitation Erosion, Interface Focus. Accepted (2015) xx.

[115] N.K. Bourne, J.E. Field, A high-speed photographic study of cavitation damage, J. Appl. Phys. 78 (1995) 4423–4427. doi:10.1063/1.359850.

[116] A. Karimi, J.L. Martin, Cavitation erosion of materials, Int. Met. Rev. 31 (1986) 1–26.

[117] R. Liang, A.S. Khan, A critical review of experimental results and constitutive models for BCC and FCC metals over a wide range of strain rates and temperatures, Int. J. Plast. 15 (1999) 963–980. doi:10.1016/S0749-6419(99)00021-2.

[118] G.R. Cowper, P.S. Symonds, Strain-hardening and strain-rate effects in the impact loading of cantilever beams, USA, 1957.

[119] G. Johnson, W. Cook, A constitutive model and data for metals subjected to large strains, high strain rates and high temperatures, Proc. 7th Int. Symp. Ballist. (1983) 541–547.

[120] G.R. Johnson, W.H. Cook, Fracture characteristics of three metals subjected to various strains, strain rates, temperatures and pressures, Eng. Fract. Mech. 21 (1985) 31–48. doi:10.1016/0013-7944(85)90052-9.

[121] F.J. Zerilli, R.W. Armstrong, Dislocation-mechanics-based constitutive relations for material dynamics calculations, J. Appl. Phys. 61 (1987) 1816–1825. doi:10.1063/1.338024.

[122] A.S. Khan, S.S. Huang, Experimental and theoretical study of mechanical behavior of 1100 Aluminum in the strain rate range 10^-5-10^4 s^-1, Int. J. Plast. 8 (1992) 397–424.

[123] P.S. Follansbee, U.F. Kocks, A constitutive description of the deformation of copper based on the use of the mechanical threshold stress as an internal state variable, Acta Metall. 36 (1988) 81–93. doi:10.1016/0001-6160(88)90030-2.

[124] Z. Xin-ming, L. Hui-jie, L. Hui-zhong, G. Hui, G. Zhi-guo, L. Ying, et al., Dynamic property evaluation of aluminum alloy 2519A by split Hopkinson pressure bar, Trans. Nonferrous Met. Soc. China. 18 (2008) 1–5.

[125] S. Erturk, D. Steglich, J. Bohlen, D. Letzig, W. Brocks, Modelling and Simulation of Extrusion of Magnesium Alloys, Int. J. Mater. Form. 1 (2008) 419–422.

[126] J.R. Pothnis, Y. Perla, H. Arya, N.K. Naik, High Strain Rate Tensile Behavior of Aluminum Alloy 7075 T651 and IS 2062 Mild Steel, J. Eng. Mater. Technol. 133 (2011) 021026. doi:10.1115/1.4003113.

[127] N.S. Brar, V.S. Joshi, B.W. Harris, Constitutive model constants for Al7075-T651 and Al7075-T6, AIP Conf. Proc. 1195 (2009) 945–948. doi:10.1063/1.3295300.

[128] E.A. Starke, J.T. Staleyt, Application of Modern Aluminum Alloys to Aircraft, 32 (1996) 131–172.

[129] C. Herrera, D. Ponge, D. Raabe, Characterization of the microstructure, crystallographic texture and segregation of an as-cast duplex stainless steel slab, Steel Res. Int. (2008) 10–12. doi:10.2374/SRI08SP014-79-2008-482.

[130] F. Hasan, a. Jahanafrooz, G.W. Lorimer, N. Ridley, The morphology, crystallography, and chemistry of phases in as-cast nickel-aluminum bronze, Metall. Trans. A. 13 (1982) 1337–1345. doi:10.1007/BF02642870.

[131] K.S. Tan, J. a. Wharton, R.J.K. Wood, Solid particle erosion-corrosion behaviour of a novel HVOF nickel aluminium bronze coating for marine applications - Correlation between mass loss and electrochemical measurements, Wear. 258 (2005) 629–640. doi:10.1016/j.wear.2004.02.019.

[132] J.M. Collin, G. Mauvoisin, O. Bartier, R. El Abdi, P. Pilvin, Experimental evaluation of the stress-strain curve by continuous indentation using different indenter shapes, Mater. Sci. Eng. A. 501 (2009) 140–145. doi:10.1016/j.msea.2008.09.081.

[133] E.G. Herbert, W.C. Oliver, G.M. Pharr, On the measurement of yield strength by spherical indentation, Philos. Mag. 86 (2006) 5521–5539. doi:10.1080/14786430600825103.

[134] B. Xu, X. Chen, Determining engineering stress–strain curve directly from the load–depth curve of spherical indentation test, J. Mater. Res. 25 (2010) 2297–2307. doi:10.1557/jmr.2010.0310.

[135] G.T. Gray, Classic Split-Hopkinson Pressure Bar Testing, in: ASM Handbook, Vol. 8, Mech. Test. Eval., ASM International, Materials Park, OH, 2000: pp. 1027–1068.

[136] C. Moussa, X. Hernot, O. Bartier, G. Delattre, G. Mauvoisin, Evaluation of the tensile properties of a material through spherical indentation: definition of an average representative strain and a confidence domain, J. Mater. Sci. 49 (2014) 592–603. doi:10.1007/s10853-013-7739-1.

[137] M. Dao, N. Chollacoop, K.J. Van Vliet, T. a. Venkatesh, S. Suresh, Computational modeling of the forward and reverse problems in instrumented sharp indentation, Acta Mater. 49 (2001) 3899–3918. doi:10.1016/S1359-6454(01)00295-6.

[138] M. El Mehtedi, S. Spigarelli, P. Ricci, C. Paternoster, E. Quadrini, Caratterizzazione meccanica delle fasi dell'acciaio Duplex 2205 mediante nanoindentazione, Metall. Ital. 102 (2010) 11–16.

[139] J. Hay, Mapping the Mechanical Properties of 2205 Duplex Stainless Steel, Appl. Note, Agil. Technol. Inc. 2013. (2013) 1–4.

[140] A. Jahanafrooz, F. Hasan, G.W. Lorimer, N. Ridley, Microstructural development in complex nickel-aluminum bronzes, Metall. Trans. A. 14 (1983) 1951–1956. doi:10.1007/BF02662362.

[141] A. Al-Hashem, W. Riad, The role of microstructure of nickel-aluminium-bronze alloy on its cavitation corrosion behavior in natural seawater, Mater. Charact. 48 (2002) 37–41. doi:10.1016/S1044-5803(02)00196-1.

[142] S.S. Singh, C. Schwartzstein, J.J. Williams, X. Xiao, F. De Carlo, N. Chawla, 3D microstructural characterization and mechanical properties of constituent particles in Al 7075 alloys using X-ray synchrotron tomography and nanoindentation, J. Alloys Compd. 602 (2014) 163–174.

[143] Y. Xue, H. El Kadiri, M.F. Horstemeyer, J.B. Jordon, H. Weiland, Micromechanisms of multistage fatigue crack growth in a high-strength aluminum alloy, Acta Mater. 55 (2007) 1975–1984. doi:10.1016/j.actamat.2006.11.009.

[144] A.D. Rollett, R. Campman, D. Saylor, Three Dimensional Microstructures: Statistical Analysis of Second Phase Particles in AA7075-T651, Mater. Sci. Forum. 519-521 (2006) 1–10. doi:10.4028/www.scientific.net/MSF.519-521.1.

[145] S.C. Roy, M. Fivel, J.-P. Franc, C. Pellone, Cavitation Induced Damage : FEM Inverse Modeling of the Flow Aggressiveness, in: Elev. Int. Conf. Flow Dyn., Sendai, Japan, 2014.

[146] A.P. French, ed., Vibrations and Waves: the M.I.T introductory physics series, W.W. Norton & Company Inc., New York, 1971.

[147] A. Karimi, J.-P. Franc, Modeling of Material Response, in: K. –H. Kim, G.L. Chahine, J. –P. Franc, A. Karimi (Eds.), Adv. Exp. Numer. Tech. Cavitation Eros. Predict. Fluid Mech. Its Appl. Vol. 160, Springer, 2014: pp. 163–181.

[148] Progressive Damage and Failure, in: Abaqus Anal. User's Man. (Abaqus 6.12), Dassault Systèmes, RI, USA, 2012.

[149] S. Nemat-Nasser, Introduction to High Strain Rate Testing, in: ASM Handbook, Vol. 8, Mech. Test. Eval., ASM international, Materials Park, OH, 2000: pp. 939–943.

[150] G. Ravichandran, A.J. Rosakis, J. Hodowany, P. Rosakis, On the Conversion of Plastic Work into Heat During High-Strain-Rate Deformation, in: Shock Compression Condens. Matter, 2001.

[151] U.S. Lindholm, Some Experiments With the Split Hopkinson Pressure Bar∗, J. Mech. Phys. Solids. 12 (1964) 317–335.

[152] W.C. Oliver, G.M. Pharr, Measurement of hardness and elastic modulus by instrumented indentation : Advances in understanding and refinements to methodology, J. Mater. Res. (2004).

[153] W.C. Oliver, G.M. Pharr, An improved technique for determining hardness and elastic modulus using load and displacement sensing indentation experiments, J. Mater. Res. 7 (2011) 1564–1583. doi:10.1557/JMR.1992.1564.

[154] T.F. Juliano, M.R. Vanlandingham, T. Weerasooriya, P. Moy, Extracting Stress-Strain and Compressive Yield Stress Information From Spherical Indentation, MD, USA, 2007.

[155] H.A. Francis, Phenomenological Analysis of Plastic Spherical Indentation, J. Eng. Mater. Technol. 98 (1976) 272–281. doi:10.1115/1.3443378.

[156] Rapid Calibration of Area Function and Frame Stiffness with Express Test1. Application Note (5991-1453EN). Keysight Technologies., USA, n.d.

[157] G.M. Pharr, W.C. Oliver, F.R. Brotzen, On the generality of the relationship among contact stiffness, contact area, and elastic modulus during indentation, J. Mater. Res. 7 (1992) 613–617. doi:10.1557/JMR.1992.0613.

[158] Introduction and Basic Equations (Section 1), in: Abaqus Theory Man. (ABAQUS 6.11), Dassault Systèmes, 2011.

Articles from the Thesis

Journal papers

1. S.C. Roy, J.-P. Franc, C. Pellone, M. Fivel, "Determination of cavitation load spectra – Part 1: Static finite element approach," *WEAR*, In Press, 2015.
2. S.C. Roy, J.-P. Franc, N. Ranc, M. Fivel, "Determination of cavitation load spectra – Part 2: Dynamic finite element approach," *WEAR*, In Press, 2015.
3. S.C. Roy, J.-P. Franc, M. Fivel, "Cavitation erosion: using the target material as a pressure sensor", *Journal of Applied Physics*, Accepted, 2015.
4. M. Fivel, J.-P. Franc, S.C. Roy, "Towards Numerical Prediction of Cavitation Erosion", *Interface Focus*, 5, 20150013, 2015.
5. S.C. Roy, J.-P. Franc, M. Fivel, "Mechanism of cavitation fatigue and numerical prediction of cavitation erosion", In Preparation, 2015.

Conference papers/proceedings

6. S.C. Roy, M. Fivel, and J.-P. Franc, C. Pellone, "Finite Element Analysis of cavitation pits to estimate bubble collapse pressure", in the Proceedings of SHF Conference on Hydraulic Machines and Cavitation/Air in water pipes, 2013.
7. S.C. Roy, M. Fivel, and J.-P. Franc, C. Pellone, "Cavitation induced damage: FEM inverse modeling of the flow aggressiveness", in the Proceedings of 11th International Conference on Flow Dynamics, 2014, Sendai, Japan.
8. S.C. Roy , M. Fivel, J.-P. Franc, C. Pellone, N. Ranc, Numerical estimation of impact load and prediction of material loss in cavitation erosion, in the Proceedings of 1st International Conference on Mechanics of Complex Solids and Fluids (ICMCSF), May 17-22, 2015, Lille, France.
9. S.C. Roy, M. Fivel, J.–P. Franc, C. Pellone, M. Verdier, Cavitation Pitting: Using the Target Material as a Sensor, 13th U.S. National Congress on Computational Mechanics (USNCCM13), July 26-30, 2015, San Diego, California, USA.

Abstract

Numerical prediction of cavitation erosion requires the knowledge of flow aggressiveness, both of which have been challenging issues till-date. This thesis proposes to use an inverse method to estimate the aggressiveness of the flow from the observation of the pits printed on the surface in the first moments of the cavitation erosion. Three materials were tested in the same experimental conditions in the cavitation tunnel PREVERO available LEGI Grenoble. The geometry of the pits left on the surface is precisely measured using a systematic method to overcome the roughness effect. Assuming that each pit was generated by a single bubble collapse whose pressure field is treated as a Gaussian shape, finite element calculations are run for estimating the load that created each residual imprint. It is shown that the load distribution falls on a master curve independent of the tested material; the softer material (aluminum alloy) measuring the lowest impacts while the most resistant material (duplex stainless steel) provides access to the largest impact pressures. It is concluded that the material can be used as a pressure sensor measuring the level of aggressiveness of the flow. The inverse method is based on a material characterization taking into account strain rate effects. It is shown that nanoindentation tests are more suitable than compression tests to determine the parameters of the behavior law, particularly for the aluminum alloy for which the microstructure is very heterogeneous. High-speed compression tests with split Hopkinson pressure bars complement the constitutive law giving the sensitivity to the strain rate. Simulations considering the dynamic loading show that impacts of strong amplitude but applied in a short time do not leave any residual pit if the frequency is higher than the natural frequency of the material treated as a damped oscillator. A dynamic mechanism of plastic strain accumulation that could eventually lead to fatigue failure is proposed. Finally, the mass loss curve of cavitation erosion is simulated by applying randomly on a 3D mesh, the impact force population estimated by the inverse method.

Key Words: Cavitation erosion; Numerical modeling; Material characterization, Impact load measurement; Cavitation fatigue, Mass-loss prediction.

Résumé

A ce jour il n'est toujours pas possible de prédire avec exactitude le phénomène d'érosion par cavitation. La raison principale est qu'il est difficile de caractériser l'agressivité de l'écoulement. Cette thèse propose d'utiliser une méthode inverse pour estimer l'agressivité de l'écoulement à partir de l'observation des cratères (pits) imprimées sur la surface dans les premiers instants de l'érosion de cavitation. Trois matériaux ont été testés dans la veine d'écoulement PREVERO disponible au LEGI de Grenoble dans les mêmes conditions expérimentales. La géométrie des pits laissés sur la surface est précisément mesurée à l'aide d'une méthode systématique permettant de s'affranchir de l'effet de rugosité. Supposant que chaque pit a été généré par une bulle unique dont le champ de pression est assimilé à une forme Gaussienne, des calculs par éléments finis permettent d'estimer le chargement qui a créé l'empreinte résiduelle. On montre que la distribution des chargements suit une loi universelle indépendante du matériau testé ; le matériau le plus tendre (alliage d'aluminium) mesurant les plus faibles impacts tandis que le matériau le plus résistant (Acier inoxydable) donne accès aux plus grandes pressions d'impact. On en conclu que le matériau peut être utilisé comme capteur de pression mesurant le niveau d'agressivité de l'écoulement. La méthode inverse repose sur une caractérisation mécanique des matériaux prenant en compte la sensibilité de la contrainte à la vitesse de déformation. On montre que les essais de nanoindentation sont mieux adaptés que les essais de compression pour déterminer les paramètres de la loi de comportement, notamment pour l'alliage d'aluminium pour lequel la microstructure est très hétérogène. Des essais de compression à haute vitesse par barres de Hopkinson complètent la loi de comportement en donnant la sensibilité à la vitesse de déformation. Des simulations prenant en compte la dynamique du chargement montrent que des impacts de fort amplitude mais appliqués sur un temps court ne laissent pas d'empreinte résiduelle si la fréquence est plus élevée que la fréquence naturelle du matériau assimilé à un oscillateur amorti. Un mécanisme d'accumulation dynamique de la déformation plastique pouvant conduire à la rupture par fatigue est proposé. Finalement, la courbe de perte de masse est simulée en appliquant aléatoirement sur un maillage 3D, la population d'impacts estimée par la méthode inverse.

Mots Clefs: Erosion de cavitation; Simulation numérique; Eléments Finis; Caractérisation Mécanique; Perte de masse.